



HAL
open science

Quantum atom optics with metastable helium atoms

Quentin Marolleau

► **To cite this version:**

Quentin Marolleau. Quantum atom optics with metastable helium atoms. Optics [physics.optics]. Université Paris-Saclay, 2022. English. NNT : 2022UPASP166 . tel-04059502

HAL Id: tel-04059502

<https://pastel.hal.science/tel-04059502>

Submitted on 5 Apr 2023

HAL is a multi-disciplinary open access archive for the deposit and dissemination of scientific research documents, whether they are published or not. The documents may come from teaching and research institutions in France or abroad, or from public or private research centers.

L'archive ouverte pluridisciplinaire **HAL**, est destinée au dépôt et à la diffusion de documents scientifiques de niveau recherche, publiés ou non, émanant des établissements d'enseignement et de recherche français ou étrangers, des laboratoires publics ou privés.

Optique atomique quantique avec hélium métastable

Quantum atom optics with metastable helium

Thèse de doctorat de l'université Paris-Saclay

École doctorale n°572, Ondes et matière (EDOM)

Spécialité de doctorat : Physique

Graduate School : Physique. Référent : Institut d'Optique

Thèse préparée au **Laboratoire Charles Fabry**
(Université Paris-Saclay, Institut d'Optique Graduate School, CNRS),
sous la direction de **Denis BOIRON**, Professeur des universités,
et le co-encadrement de **Christoph WESTBROOK**, Directeur de recherche.

Thèse soutenue à Paris-Saclay, le 13 décembre 2022, par

Quentin MAROLLEAU

Composition du jury

Membres du jury avec voix délibérative

M. Alberto BRAMATI Professeur des universités à Sorbonne Université (Laboratoire Kastler Brossel)	Président
M. Laurent VERNAC Maître de conférence à l'Université Paris 13 (Laboratoire de Physique des Lasers)	Rapporteur
M. William Guerin Chargé de recherche à l'Université Côte d'Azur (Institut de Physique de Nice)	Rapporteur
Mme. Rosa Tualle-Broui Professeure des universités à l'Université Paris-Saclay (Laboratoire Charles Fabry)	Examinatrice

Disclaimer

I hereby declare that this thesis represents my own work, which has been done after registration for the degree of PhD of the University Paris-Saclay. It has not been previously included in a thesis or dissertation submitted to this or any other institution for a degree, diploma or other qualifications, unless otherwise stated with due reference to the literature, or acknowledgment of collaborative research and discussions.

Colophon

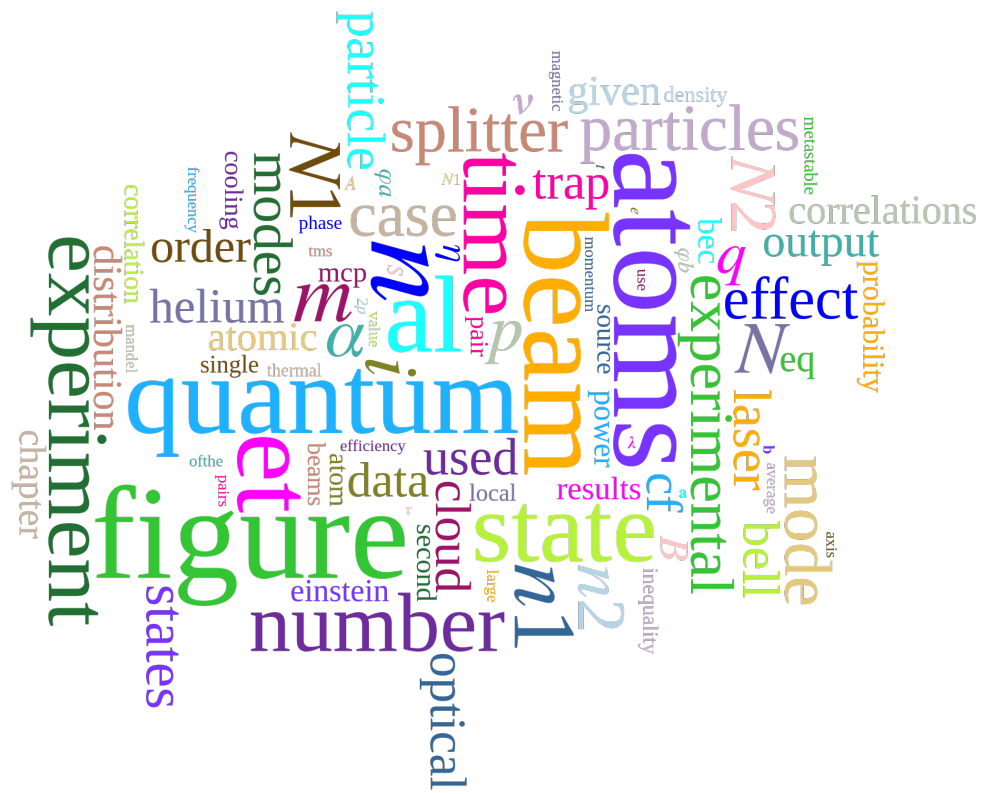
This document was typeset with the help of *KOMA-Script* and \LaTeX using the *kaobook* class.

The source code of this class is available at:

<https://github.com/fmarotta/kaobook>

Publisher

Third edition published Tuesday the 21th February, 2023.



This manuscript in 100 words...

Remerciements

Le travail présenté dans ce manuscrit a été rendu possible grâce à l'aide précieuse (et au soutien) d'un certain nombre de collègues, de partenaires de laboratoire, et d'encadrants, à qui je souhaite renouveler ici l'expression de mes sincères remerciements.

J'adresse ces premiers mots à Denis BOIRON, qui a été le principal directeur des travaux que j'ai menés au sein de l'équipe. Je le remercie très chaleureusement pour son dévouement au projet, mais aussi – et surtout – pour sa présence et son implication soutenue auprès des thésards de l'équipe : aussi bien dans les bureaux pour les problèmes théoriques, que dans la salle de manip (et tous les défis techniques qui l'accompagnent). Denis est un physicien et un pédagogue qui m'aura énormément appris durant ces presque 4 années, et dont je saurai continuer de m'inspirer dans la suite de ma carrière.

Je souhaite remercier en second lieu, le binôme – pour le moins hétéroclite – de thésards qui me succèdent sur l'expérience : Charlie LEPRINCE et Victor GONDRET*, avec qui j'ai eu énormément de plaisir à travailler. Outre leur grandes qualités humaines, c'est grâce à l'engagement et aux efforts ininterrompus de Charlie et Victor que la jouvence de la plateforme expérimentale réalisée pendant ma thèse a été rendue possible. Un grand merci à eux. Pour le reste, du fait de leur compétences d'expérimentateurs – très complémentaires – et de leur remarquable efficacité, je suis certain qu'ils sauront très prochainement obtenir le meilleur de cette expérience. Bon courage à vous !

Je remercie également Chris WESTBROOK, qui m'a accueilli dans l'équipe, et avec qui les nombreuses discussions scientifiques m'ont toujours été très profitables. Sur le plan expérimental Chris a toujours l'imagination fertile, et sa connaissance formidablement étendue en matière de physique atomique et d'optique quantique m'a indéniablement permis de beaucoup progresser.

Merci ensuite à mes prédécesseurs sur l'expérience: Maxime PERRIER, Ziyad AMODJEE et Alexandre DAREAU, qui m'ont permis de débiter dans le domaine parfois frustrant de la physique des atomes ultra-froids sereinement, et dans la bonne humeur ! Une part importante du savoir-faire expérimental se transmet de thésards et postdocs expérimentés à thésards novices, je leur suis reconnaissant d'avoir assumé cette responsabilité à mon égard.

Je remercie enfin les autres thésards, postdocs et chercheurs permanents du groupe gaz quantique, avec qui j'ai été heureux d'avoir pu échanger aussi bien des arguments de physique que du matériel expérimental... Merci en particulier à Marc CHENEAU qui jusqu'à très récemment a joué un rôle actif dans notre projet, et qui n'est jamais avare de conseils et d'astuces techniques ; ainsi qu'à Alain ASPECT, qui a toujours su trouver le temps de participer à nos séminaires hebdomadaire, et d'y partager aussi bien sa vision de la physique, qu'une foule de conseils expérimentaux acquis au cours d'une carrière proprement exceptionnelle.

* GONDRE ?

Mes derniers mots sont réservés à Diane, à qui je ne saurais exprimer ma gratitude en un seul paragraphe. Je te dois tant. Je ne sais à quoi l'avenir nous prédestine, mais ce sera heureux tant que nous y serons ensemble.

Quentin Marolleau — Février 2023

Résumé en français

N.B. *Le présent résumé est inspiré de la seconde section du chapitre d'introduction (en anglais) de ce manuscrit.*

Contexte et motivation

Notre équipe de recherche¹ a développé une technique de détection à 3 dimensions, résolue pour des atomes individuels. Cela donne accès à de nombreuses informations qui sont généralement difficile d'accès dans les expériences de physique atomique, notamment les propriétés de corrélation entre atomes spatialement séparés. Cette capacité à mesurer des particules individuelles est une grande force de notre dispositif expérimental. En effet, les corrélations entre atomes peuvent comporter la signature d'effets purement quantiques : les propriétés d'intrication et de non-localité de l'information quantique en sont des exemples particulièrement marquants [1–4].

Parallèlement à cela, depuis le milieu des années 2000 notre équipe a exploré différentes procédures de préparation de paires d'atomes corrélés (émis au sein de jets atomiques) [5–7]. Dans certains régimes de paramètres expérimentaux, de telles paires atomiques peuvent constituer un état quantique intriqué, et grâce à l'interaction lumière-matière ceci ouvre des perspectives intéressantes pour réaliser de nombreuses expériences inspirées de l'optique quantique.

Relativement récemment, l'équipe a été en mesure d'observer l'analogue atomique de l'effet Hong-Ou-Mandel [8]. Elle a également montré une preuve de principe d'interféromètre à deux particules, qui pourrait être exploité pour mettre en œuvre une expérience de violation des inégalités de Bell portant sur la vitesse des atomes [9]. Un tel test de non-localité quantique pour des particules massives n'a encore jamais été observé² et constitue à ce jour un des objectifs principaux de notre équipe. Cette mesure révélerait la nature non-classique d'un degré de liberté purement mécanique, ce qui marquerait le franchissement d'une étape importante sur le plan épistémologique. Par ailleurs, comme les particules mises en jeu sont *massives* (et donc assujetties à l'interaction gravitationnelle), cette expérience réaliserait un pas supplémentaire vers l'étude du couplage entre mécanique quantique et relativité générale,

1: cette thèse a été conduite au sein de l'équipe « *Optique Atomique Quantique* » (sous constituante du groupe « *Gaz quantiques* ») du laboratoire Charles Fabry.

[1]: Reid et al. (1986), “Violations of Classical Inequalities in Quantum Optics”

[2]: Kheruntsyan et al. (2012), “Violation of the Cauchy-Schwarz Inequality with Matter Waves”

[3]: Volovich (2016), “Cauchy–Schwarz Inequality-Based Criteria for the Non-Classicality of Sub-Poisson and Antibunched Light”

[4]: Wasak et al. (2016), “Cauchy–Schwarz Inequality for General Measurements as an Entanglement Criterion”

[5]: Perrin et al. (2007), “Observation of Atom Pairs in Spontaneous Four-Wave Mixing of Two Colliding Bose-Einstein Condensates”

[6]: Jaskula et al. (2012), “Acoustic Analog to the Dynamical Casimir Effect in a Bose-Einstein Condensate”

[7]: Bonneau et al. (2013), “Tunable Source of Correlated Atom Beams”

[8]: Lopes (2015), “An Atomic Hong-Ou-Mandel Experiment”

[9]: Dussarrat et al. (2017), “Two-Particle Four-Mode Interferometer for Atoms”

2: en considérant l'impulsion des atomes comme paramètre quantique.

[10]: Penrose et al. (1998), “Quantum computation, entanglement and state reduction”

sur le plan expérimental [10].

Durant cette thèse, j’ai contribué à la modernisation et la jouvence de nos installations expérimentales, qui souffraient depuis plus de cinq ans de nombreux problèmes techniques, inhibant fortement l’obtention de nouveaux résultats scientifiques. Ces multiples évolutions ont conduit à l’obtention d’un condensat de Bose-Einstein d’hélium métastable dans un piège optique. À partir de ce condensat, nous avons été en mesure de produire des paires atomiques corrélées dans un régime « intense » qui n’avait pas été exploré dans les stades antérieurs de l’expérience.

J’ai également effectué une courte étude théorique traitant d’une version généralisée des expériences de type Hong-Ou-Mandel, en considérant une situation où plus de deux particules entrent en jeu. Cette étude prend en considération les effets d’efficacité quantique finie des détecteurs utilisés. Une telle expérience pourrait être mise en place dans notre laboratoire dans un futur proche.

Résumé rapide de chaque chapitre

Ce manuscrit est organisé en cinq chapitres, répartis dans deux grandes parties :

Considérations théoriques

Chapitre 1 : de l’effet Hong-Ou-Mandel à deux particules, à sa version généralisée à N particules.

L’effet Hong-Ou-Mandel est bien connu en optique quantique : observé pour la première fois en 1987, il a été reproduit avec des atomes par notre équipe en 2015. Après quelques rappels concernant l’effet Hong-Ou-Mandel « original » à deux particules, on démontre dans ce chapitre un ensemble de résultats analytiques qui présentent de l’intérêt pour la mise en œuvre d’une expérience que l’équipe souhaiterait réaliser ultérieurement. En particulier les propriétés d’indiscernabilité et de non-classicité révélées par certaines observables y sont discutées.

Chapitre 2 : inégalités de Bell pour des atomes intriqués en impulsion.

Le début du second chapitre expose les idées essentielles de l'argument EPR, et montre comment les inégalités de Bell permettent d'en vérifier expérimentalement les conclusions.

Après une introduction à la question du théorème de Bell, on détaille dans une seconde section le sujet d'intérêt principal pour l'équipe de recherche : la réalisation d'une expérience de test des inégalités de Bell concernant la vitesse des atomes. Il est en particulier montré qu'un traitement astucieux des données expérimentales de corrélation permet d'accroître le rapport signal à bruit pour une telle mesure.

Réalisations expérimentales

Chapitre 3 : détection et obtention d'un condensat de Bose-Einstein d'hélium métastable.

Ce chapitre commence par rappeler comment le caractère métastable de l'hélium présente un avantage pour la détection de particules individuelles. Dans une seconde partie, il détaille les différentes étapes de refroidissement du gaz, vers le seuil de condensation.

Chapitre 4 : évolution et changements technologiques pendant la thèse.

Ce chapitre expose les différentes pannes et problèmes rencontrés sur l'expérience, avant et pendant la thèse. Il est expliqué en quoi ces difficultés ont ralenti la production scientifique, ainsi que les décisions et mesures prises pour les résoudre.

Chapitre 5 : étude de la source de paires d'atomes corrélés.

Le chapitre final présente les récents résultats scientifiques, obtenus pendant la thèse. Les données exposées n'ont cependant pas été acquises dans la perspective d'une communication scientifique, mais plutôt pour dresser une caractérisation préliminaire de la source de paires fonctionnant dans un nouveau régime.

Après approximativement trois mois de bon fonctionnement de l'expérience, l'acquisition de ces données a de nouveau été stoppé par une série de problèmes techniques, survenus à la toute fin de la thèse. Ce chapitre propose néanmoins un traitement aussi complet que possible des données les plus prometteuses, obtenues avant ces nouvelles pannes.

En complément, des rappels théoriques sur le processus de création de paires servent d'introduction au chapitre.

Contents

Remerciements	v
Résumé en français	vii
Contents	xi
Introduction	I
1 Entanglement: from the early 20 th century to nowadays	2
1.1 The origins: EPR paradox	2
1.2 John Bell and the emergence of the quantum information theory	3
1.3 Quantum technologies	5
2 Quantum atom optics with metastable helium	6
2.1 Context and motivation	6
2.2 Outline of this manuscript	7
THEORETICAL CONSIDERATIONS	9
I Hong-Ou-Mandel effect	II
Introduction	12
1 Two-particle HOM effect	13
1.1 History and presentation	13
1.2 Theory	15
1.2.1 Lossless beam splitter model	15
1.2.2 Derivation and interpretation of the two-particle HOM effect	17
1.2.3 Classical limit	21
1.3 Experimental results with metastable helium	22
2 N-particle HOM effect	24
2.1 Theoretical generalities	25
2.1.1 Notations used	25
2.1.2 Transformation of a quantum system by a beam splitter	26
2.2 Classification of the interference patterns for different input states	31
2.2.1 Twin-Fock states and mixing with vacuum	31
2.2.2 Coherent states	36
2.2.3 Thermal states	40
2.2.4 Two-mode squeezed vacuum state	47
Conclusion	65
2 Bell inequalities	67
Introduction	68

1	General considerations	68
1.1	EPR argument	68
1.2	Bell's theorem	72
1.2.1	Main idea	72
1.2.2	CHSH inequality & violation	72
2	Rarity-Tapster interferometer	78
2.1	Introduction to the problem	78
2.2	General description	81
2.2.1	Topology	81
2.2.2	Bragg diffraction in brief	82
2.2.3	Formal effect of the deflector and beam splitters	84
2.3	Well-suited Bell inequalities	89
2.3.1	First natural approach	90
2.3.2	Second approach: projection onto two-outcome events observables	92
2.3.3	Third approach based on the CH inequality	94
	Conclusion	97

EXPERIMENTAL WORKS 99

3	Preparation of a Bose-Einstein condensate and single atom detection 101
	Introduction 102
1	Metastable helium 103
1.1	Spectroscopy 103
1.2	Collision theory 106
1.2.1	Elastic collision 107
1.2.2	Inelastic & ionising collisions 108
2	Detecting individual atoms in the momentum space 112
2.1	Microchannel plate 112
2.2	Generation of 3D data: delay lines, electronics & software 114
2.2.1	Delay lines & electronics 114
2.2.2	Reconstruction algorithm 120
2.2.3	From timestamps to velocities 123
2.2.4	A word about the resolution 124
2.2.5	Comparison between performances 125
3	Cooling of the metastable helium cloud: down to the BEC 127
3.1	Source of metastable helium 127
3.2	Cooling procedure 128
3.2.1	Transverse optical molasses and Zeeman slower 130
3.2.2	Magneto-optical trap & optical molasses 131
3.2.3	Magnetic trap 133

	3.2.4	Optical dipole trap (ODT)	139
	3.2.5	Recap	145
4		Technology changes	147
		Introduction	148
1		Status of the experiment in 2019	149
2		Problems and workarounds during my PhD	150
	2.1	Holes in the MCP	151
	2.1.1	Genesis of the breakdown	151
	2.1.2	Pushing the cloud with a Raman kick	152
	2.1.3	Protecting the MCP with a copper plate	154
	2.2	A new cooling laser	159
	2.2.1	Why do it?	159
	2.2.2	The new laser	160
	2.2.3	Obtained effects	161
	2.3	Instabilities of the magnetic trap	163
	2.4	A next-gen sequencer and software control	164
	2.4.1	GUS and the old hardware	164
	2.4.2	ADwin sequencer and the QControl3 project	166
	2.4.3	QControl3 structure	166
	2.4.4	A word about HAL	169
5		Pair production and experimental results	173
		Introduction	174
1		Source of momenta-correlated atoms	175
	1.1	Generalities	175
	1.1.1	Parametric down conversion	175
	1.1.2	Four-wave mixing	176
	1.1.3	Extension to the atomic case	176
	1.2	A bit of formalism	177
	1.2.1	Four-wave mixing in a BEC	177
	1.2.2	Phase-matching condition in a periodic potential	179
	1.2.3	Dynamics, density and correlations	181
	1.2.4	Turning on and off the optical lattice	185
2		Experimental results	187
	2.1	Optical setup	187
	2.2	Generation of pairs	188
	2.2.1	First characterisation of the pair creation's behaviour	188
	2.2.2	Density of pairs	193
	2.3	Probing the correlation	195
	2.3.1	Short definition reminder	196
	2.3.2	Second-order correlations: 2D map	197

2.3.3	1D analysis: correlation amplitude and modes' width	199
2.4	Emission statistics	203
	Conclusion	206
	General conclusion	209
	APPENDIX	211
	A Raman lattice	215
	B Imaging camera settings	217
	C Magnetic trap	219
1	Coils and IGBT setup	219
2	Bias measurements and calibration	220
	D Blueprints	223
	Bibliography	227
	List of Terms	243

List of Figures

1.1	Schematic of the single-photon anti-correlation experiment	13
1.2	Classical outcomes of a HOM-like experiment	14
1.3	Outcomes of a HOM experiment	14
1.4	Historical result of the HOM	15
1.5	Quantum-mechanical depiction of a beam splitter.	15
1.6	Notations for the input and output states of the beam splitter in first quantisation	19
1.7	Schematic drawing of the atomic HOM experiment	22
1.8	Two-particle HOM anti-correlation measured with helium atoms	24
1.9	Twin-Fock states interferences at a 50-50 beam splitter	32
1.10	Twin-Fock states interferences: effect of the beam splitter transmittance on the width of the probability distribution	33
1.11	Twin-Fock states interferences: schematic of an experiment	33
1.12	Twin-Fock states interferences at a 50-50 beam splitter, with a finite quantum efficiency	34
1.13	Twin-Fock states interferences: comparison with the equivalent distinguishable case	35
1.14	Twin-Fock states interferences: comparison with the equivalent distinguishable case	36
1.15	Output joint probability distribution for indistinguishable thermal states interfering at a 50-50 beam splitter	43
1.16	Output joint probability distribution for distinguishable thermal states interfering at a 50-50 beam splitter	46
1.17	Expected joint probability distribution of a TMS state, when it is measured <i>directly</i>	50
1.18	Graphical proof of the equivalence of two double summation patterns	52
1.19	Output probability distribution for a TMS interfering at a 50-50 beam splitter	54
1.20	Effect of the 50-50 beam splitter on a two-mode squeezed vacuum state	54
1.21	Output joint probability distribution for a TMS interfering at a 50-50 beam splitter with finite quantum efficiency	59
1.22	Output joint probability distribution for a “distinguishable TMS” interfering at a 50-50 beam splitter	62
1.23	Output joint probability distribution for a “distinguishable TMS” interfering at a 50-50 beam splitter with finite quantum efficiency	63
1.24	$P_0^{1\text{ch}}$ as a function of the average population per mode	64
2.1	Principle of an EPRB experiment	70
2.2	Rotation of the basis of detection of a two-level system	76
2.3	Schematic of a polarisation CHSH inequality violation experiment	79
2.4	Schematic of the atomic Rarity-Tapster two-particle four modes interferometer	81
2.5	Principle of Bragg diffraction	82

2.6	Schematic of the optical lattice used for Bragg diffraction. θ is defined as the half-angle between the beams. The coordinate system $(\vec{e}_x, \vec{e}_y, \vec{e}_z)$ is given for consistency with the Figure 3.19 (cf. Chapter 3).	83
2.7	Pairing of the modes in two configurations of the Rarity-Tapster interferometer	84
2.8	Schematic of the atomic Rarity-Tapster two-particle four modes interferometer in the large separation configuration	85
2.9	Bell parameter as a function of the population ν , using Ralph et al. correlator	91
2.10	Bell parameter as a function of the population ν , using the correlator based on the sgn function	93
2.11	Bell parameter as a function of the population ν , using the correlator based on the sgn function with vacuum postselection	96
2.12	Saturation of the Bell inequality as a function of the population	96
3.1	Energy level diagram of the ^4He	105
3.2	Two-body elastic, ionisation and inelastic collisions constant rates as a function of the temperature	107
3.3	Elastic collision rate constant as a function of temperature	107
3.4	Schematic structure of a MCP	112
3.5	Schematic of the electronic cascade inside a microchannel	112
3.6	Schematic of a cross-sectional view of a microchannel	113
3.7	Micrometer scale photograph of the surface of standard and “funnel” MCPs	113
3.8	MCP and mounting assembly photographs	114
3.9	Schematic of the electronic cascade inside a microchannel	115
3.10	Threshold controlled TDC	115
3.11	Principle of the CFD	115
3.12	Block diagram of the electronic chain used for the detection	116
3.13	Pulses amplitude histograms (after pre-amplification)	119
3.14	Diagrammatic representation of the reconstruction algorithm	121
3.15	Schematic of the far field regime detection with an MCP	123
3.16	Comparison of the gain/resolution maps between the old and new detection system	126
3.17	Minimal Zeeman slower length for helium, as a function of atoms velocity	127
3.18	Representation of the helium plasma source	128
3.19	Schematic of the experiment apparatus	129
3.20	Measurement of the magnetic field along the Zeeman solenoid	130
3.21	Bias measurement in the magnetic trap	136
3.22	Competition between the doppler cooling in the magnetic trap, and the heating due to the longitudinal optical molasses	137
3.23	Schematic of the RF coupling used to perform evaporative cooling in the MT	137
3.24	Temporal profile of the power of the ODT beams	140
3.25	Histograms of BECs arrival times with and without the horizontal ODT	140
3.26	Potential seen by the atoms during the loading	143
3.27	Potential seen by the atoms at the end of the evaporation	143

3.28	Overview of the different cooling steps of the procedure	146
4.1	Schematic of the camera set-up	149
4.2	Image of the hole in the old Burle MCP	151
4.3	Evolution of the diameter of the MCP's hole	152
4.4	Raman transfer towards the $m_J = 0$ magnetic sublevel	153
4.5	Top view of the Raman beams, and of the kick given to the BEC	153
4.6	MCP: raman kick applied to a BEC trapped in the MT	154
4.7	Integration over the Y axis of the figure Figure 4.6	154
4.8	Top view of the protective copper plate	155
4.9	Side view of the protective copper plate	156
4.10	Detectivity map of the MCP protected with the copper plate	156
4.11	Detectivity map obtained with $m_J = 0$ atoms coming out of an ODT	157
4.12	Example of drift of the number of atoms in a Doppler cloud	159
4.13	Picture of the new NKT Photonics [®] fibered laser	160
4.14	Laser frequency locking: optical schematic	161
4.15	Stability of number of atoms in a Doppler cloud with the new NKT [®] laser	161
4.16	Day-to-day evolution of the position of the centre of a cloud trapped in the magnetic trap	163
4.17	Picture of the ADwin-Pro II - light sequencer frame	166
4.18	Chartflow diagram of the coarse architecture of the QControl3 program	167
4.19	HAL's logo	169
4.20	User interface of HAL	170
4.21	Example of visualisations generated with HAL	171
5.1	Pair creation process in the lowest energy band of the optical lattice	180
5.2	First three bands of the modified dispersion relation, for $V_0 = 0.8 E_{lat}$	180
5.3	First three bands of the modified dispersion relation, for $V_0 = 4 E_{lat}$	181
5.4	Profile of the density for the multi-mode emission	183
5.5	Schematic representation of the pair creation lattice	188
5.6	Rabi oscillations with the pair creation lattice	189
5.7	Quasi-momenta of the pairs as a function of the BEC's quasi-momentum	190
5.8	3D pairs' density iso-surfaces in the momentum space	191
5.9	2D histograms of the pairs' density in the momentum space	192
5.10	1D pairs' density histogram in the momentum space	192
5.11	Average number of particle per mode as a function of the centre q_z of the mode (with different boxes' size for the two modes)	194
5.12	Average number of particle per mode as a function of the centre q_z of the mode (with the same boxes' size for the two modes)	195
5.13	2D map of the second-order correlation function	198
5.14	1D local correlations as a function of $\delta q = q_1 - q_2$	200
5.15	1D crossed correlations as a function of $q_x^1 + q_x^2$	202
5.16	Counting statistics of the two modes modes emitted by the source (with different boxes' size for the two modes)	204

5.17	Counting statistics of the two modes modes emitted by the source (with the same boxes' size for the two modes)	205
A.1	Rabi oscillations of the Raman coupling observed with fluorescence imaging	215
A.2	Rabi oscillations of the Raman coupling observed with the MCP	215
A.3	Two-photon Rabi frequencies for different powers and detuning of the Raman beams	216
B.1	Chain of conversions for fluorescence imaging: from a number of atoms to the greyscale of a PNG file	217
C.1	General electrical network of the Ioffe-Pritchard magnetic trap	219
C.2	MOT configuration of the IGBTs circuit	219
C.3	MT configuration of the IGBTs circuit	219
C.4	Ferromagnetic hysteresis cycle of the bias	220
C.5	Calibration of the bias \bar{B}_0 in MHz as a function of the current in the two PSUs	220
D.1	Blueprint of the protective copper plate	224
D.2	Blueprint of the new Oswald [®] clusters of coils.	225

List of Tables

3.1	Physical properties of metastable helium	104
3.2	Cooling transition $2^3P_2 \rightarrow 2^3S_1$ characteristics	106
3.3	MCP comparison	114
3.4	Slowing and trapping characteristics	129
3.5	Characteristics of the Zeeman and transverse molasses beams	130
3.6	Characteristics of the MOT beams, and the pulses performed with it.	131
3.7	Characteristics of the pumping and Doppler pulses	136
3.8	Characteristics of the ODT during the loading	139
3.9	Characteristics of the ODT at the end of the evaporation	139
4.1	Characteristics of the copper plate	155
4.2	New fibered laser reference	160
4.3	Typical duty cycles of different types of clouds	168
5.1	Parameters of the lattice	188
5.2	Sequence reference and informations about the dataset chosen to measure densities and correlation	189
5.3	Estimation of the number of atomic modes emitted along each direction	193
5.4	Comparison between expected and measured amplitudes the local correlations	202

Introduction

Introduction's table of contents

1. Entanglement: from the early 20th century to nowadays	2
1.1 The origins: EPR paradox	2
1.2 John Bell and the emergence of the quantum information theory	3
1.3 Quantum technologies	5
2. Quantum atom optics with metastable helium	6
2.1 Context and motivation	6
2.2 Outline of this manuscript	7

1 Entanglement: from the early 20th century to nowadays

After more than forty years of experiments, and twice as long of meta-physical debates, it is now largely admitted –even by the layman– that quantum entanglement is one of the most remarkable features of quantum theory. Even though it seems to be an obvious component of quantum formalism of many body systems, the question of its physical meaning remains the subject of many heated debates: it is one aspect of the well-known question of *quantum reality*[11, 12].

[11]: Tegmark (1998), “The Interpretation of Quantum Mechanics”

[12]: Laloë (2011), “Comprenons-nous vraiment la mécanique quantique ?”

1.1 The origins: EPR paradox

Historically, quantum entanglement was put in the spotlight for the first time back in 1935, thanks to the extremely famous [Einstein, Polsky and Rosen \(EPR\)](#)’s article[13]. A fundamental element of the EPR reasoning is the principle of *locality*, which is the idea that any physical description of a natural phenomenon[†] should involve local parameters only. This means that all the information needed to describe an event –as accurately as possible– is contained in an infinitesimal space-time volume, centred on that event. Einstein was obviously very much attached to the locality hypothesis, which is the core pillar of the theory of relativity. Through their work, EPR proved that if we assume the principle of locality to be correct, quantum theory is therefore incomplete¹, and requires additional *hidden* and *local* elements, so as to cover the whole reality of Nature. Such a theory is usually named *local-realistic theory*.

[13]: Einstein et al. (1935), “Can Quantum-Mechanical Description of Physical Reality Be Considered Complete?”

1: a more complete wording of the EPR theorem will be given in the next chapter.

[14]: Bohr (1935), “Can Quantum-Mechanical Description of Physical Reality be Considered Complete?”

2: that is an aspect of the *Copenhagen interpretation* of quantum mechanics.

Bohr is known to be one of the major opponents to EPR’s position, and quickly objected (in an article of the same name)[14] that the conclusion of the EPR theorem –which he did not disprove– should not have been the idea that quantum physics were an incomplete constituted theory, but that local realism must collapse. In this paradigm, entangled systems must be considered as a whole: it no longer makes any sense to deal with the alleged physical properties of its sub-components² (without loss of information at least). In Bohr’s mind, the nonseparability of quantum states means that some part of quantum information can be carried in a nonlocal way, and individual particles should not systematically be considered as the ultimate substrates to the physical properties of Nature.

[†] considered to be an *event* in the sense of special relativity.

It is nevertheless worth noticing that both visions agree on the validity of the predictions of quantum theory (to argue against it would have been quite a tough position to defend considering the unprecedented series of experimental successes this theory provided¹). The essential difference between these two schools of thought consists in the belief –or disbelief– in a deeper theory, involving additional local degrees of freedom.

1.2 John Bell and the emergence of the quantum information theory

Apart from Einstein, Bohr and Schrödinger², few physicists of the first half of the 20th century seemed to show a legitimate interest in the question of the interpretation of entangled states. Since it does not put the roots of quantum mechanics at stake, it was quickly relegated to the list of metaphysical issues, thus making it a matter for debates in epistemological circles.

The physical essence of the question was revived by John S. Bell, in an article published in 1964 with thunderous consequences^[15]. Thanks to an ingenious use of correlators³, Bell pinpointed the fact that an “extended” version of quantum mechanics incorporating local hidden variables could not reproduce *all* predictions of the “standard” quantum theory. In particular, if one would consider a two-body system, entangled with respect to a given observable quantity \mathcal{O} –e.g. two spin- $\frac{1}{2}$ particles⁴– one could pay attention to the *correlations* between the measurements of \mathcal{O} made upon one particle by a first operator (commonly called *Alice*), and the same measurements made upon its entangled partner by a second operator (*Bob*). Bell proved that due to the locality hypothesis, the degree of correlation between the observations of Alice and Bob is bound to some numerical limit, that can be overcome in the purely quantum realm. In other words, quantum theory predicts an *excess of correlations*, to be compared with the intrinsic constraints imposed by locality.

Thus, we have two different *classes* of theories at our disposal, that exhibit two different experimental results. The question of the existence of Einstein’s hidden variables is therefore experimentally accessible. Multiple formal alternatives of the Bell inequalities were proposed in the following years^[17–19]. After a pioneering realisation by Clauser and Freedman ^[20], the first convincing measurements of a Bell inequalities violation were published in the early 1980s by Alain Aspect

1: Franck-Hertz’s electron collision experiment (1914). Stern-Gerlach experiment (1920). Compton scattering experiment (1923). Davisson-Germer electron diffraction experiment (1927). Anderson’s discovery of positron (1932)...

2: to whom we owe the term *entanglement*...

[15]: Bell (1964), “On the Einstein Podolsky Rosen paradox”

3: a more detailed derivation of the Bell inequalities will be given in the next chapter

4: this is the example proposed by D. Bohm^[16] to simplify the original EPR argument, historically dealing with particles spatially entangled. It is now often called an **EPRB** experiment.

[17]: Clauser et al. (1969), “Proposed Experiment to Test Local Hidden-Variable Theories”

[18]: Bell (1971), “Introduction to the hidden-variable question”

[19]: Clauser et al. (1974), “Experimental consequences of objective local theories”

[20]: Freedman et al. (1972), “Experimental Test of Local Hidden-Variable Theories”

[21]: Aspect (1976), “Proposed experiment to test the nonseparability of quantum mechanics”

[22]: Aspect et al. (1981), “Experimental Tests of Realistic Local Theories via Bell’s Theorem”

[23]: Aspect et al. (1982), “Experimental Realization of Einstein-Podolsky-Rosen-Bohm *Gedankenexperiment*”

[24]: Aspect et al. (1982), “Experimental Test of Bell’s Inequalities Using Time-Varying Analyzers”

[25]: Shih et al. (1988), “New Type of Einstein-Podolsky-Rosen-Bohm Experiment Using Pairs of Light Quanta Produced by Optical Parametric Down Conversion”

[26]: Kiess et al. (1993), “Einstein-Podolsky-Rosen-Bohm experiment using pairs of light quanta produced by type-II parametric down-conversion”

[27]: Rarity et al. (1990), “Experimental violation of Bell’s inequality based on phase and momentum”

[28]: Hensen et al. (2015), “Loophole-free Bell inequality violation using electron spins separated by 1.3 kilometres”

[29]: Giustina et al. (2015), “Significant-Loophole-Free Test of Bell’s Theorem with Entangled Photons”

[30]: Shalm et al. (2015), “Strong Loophole-Free Test of Local Realism”

1: strategy based on sharing a set entangled particles between several participants to a given game, making possible to the player to beat the optimal classical limit achieving a collective win.

2: allows the communication of a large number of classical bits via the transmission a smaller amount of entangled *qubits*.

and his coworkers[21–24]. The tour de force of these experiments was to take extra care in keeping a spacelike separation between Alice’s and Bob’s detections, which is a crucial point in order to put the substantial nonlocality of entangled states to the test. A violation was indeed observed, with statistical confidence better than 240 standard deviation! More than constituting the verdict in a conceptual opposition between Bohr and Einstein –that endured for almost fifty years– the joint contributions of Bell and Aspect are a notable milestone in the advent of modern quantum physics.

Many similar experiments have been achieved since then. Amongst many others, let us cite the works of Shih et al. [25, 26] that popularised the process of parametric excitation to induce the creation of entangled particles, and Rarity-Tapster[27] that designed an interferometer whose topology is well-adapted to the probing of the entanglement of velocities. Concerning the epistemological validity of the conclusions to those experiments, the final piece of this work was obtained in a concomitant manner by three independent groups –respectively in Delft, Vienna and Boulder– through the realisation of the so-called *loophole-free experiments* [28–30], carefully avoiding any possible local-realistic interpretation of the inequalities.

Even though entanglement could be considered to be a mainstream feature in experimental quantum physics nowadays, it became clear that the ability to prepare those highly non-classical states in various contexts is one of the most burning issues for our century. With regard to the manipulation of information, it is indeed entanglement that is at the root of the advantage of quantum computing over its classical counterpart. On a purely formal point of view, it is no difficult task to convince oneself of the upgraded possibilities offered by quantum information. In the wake of John Bell, many theorists with fertile imaginations came upon various situations that can be efficiently handled by quantum systems: quantum *pseudo-telepathy*¹ in game theory [31–33], superdense coding [34, 35] in communication protocols², quantum teleportation of states [36–38], quantum computing [39, 40], etc.

To some extent, the prodigious booming of research activity in quantum information fields which has been witnessed in the last decades (and, more recently, strongly stimulated by remarkable financial investments), can be considered to be a legacy of Bell’s avant-garde contribution. This era of vigorous scientific progress, carried out by the prominent *quantum technologies*, is sometimes called “*second quantum revolution*”[41].

1.3 Quantum technologies

In 1948, the discovery of the transistor effect by Bardeen, Shockley and Brattain paved the way to the technological development of computers, that propelled the world in the new age of information processing and digital communication. This major contribution was awarded by the Nobel prize in 1956.

Very recently, the Nobel prize in physics 2022 was awarded jointly to Alain Aspect, John F. Clauser and Anton Zeilinger “for experiments with entangled photons, establishing the violation of Bell inequalities and pioneering quantum information science”. In addition to the great epistemological significance of the work conducted by these three physicists, this prize is also the recognition that the second quantum revolution —initiated in laboratories during the early 80s— gave birth to a radically new way to manipulate and exchange information. Indeed, during the last three decades, people have identified a number of situations where the coherent superposition and entanglement of states can provide a quantum advantage. Just to name a few, we can mention prime numbers factorisation (and the subsequent question of quantum cryptography) [42], the speed up search of an element in a list [43] or the secured quantum-key distribution for telecommunications [44, 45]. The concrete implementations of this new kind of protocols requires the use of technical platforms able to generate, store, transport, and interact with qubits¹. Various quantum systems seem to be available to realise qubits²: photons [46], neutral atoms [47], superconductors [48], trapped ions [49] etc. These platforms constitute an important facet of modern quantum technologies.

Another aspect is focused on the enhanced possibilities offered by quantum physics concerning the metrology and high performance sensors. It is widely known that quantum systems may have an extreme sensitivity to their surroundings, that can be used to advantage to interferometry above the shot noise limit [50], or even direct measurements (for instance magnetometers based on nitrogen-vacancy [51]).

Quantum technologies have now invested the industrial sector during the last few years, gathered in what is sometimes called the *quantum deeptech*, and which is heavily supported by public policies: in France with the Plan Quantique (since 2021), but also in Europe with the Quantum Flagship program (since 2018) or the QuantERA call (since 2017).

[42]: Shor (1999), “Polynomial-Time Algorithms for Prime Factorization and Discrete Logarithms on a Quantum Computer”

[43]: Grover (1996), “A Fast Quantum Mechanical Algorithm for Database Search”

[44]: Bennett et al. (1984), “Quantum Cryptography”

[45]: Ekert (1991), “Quantum Cryptography Based on Bell’s Theorem”

1: the quantum elementary unit of information, consisting in a two-level quantum system.

2: it is perhaps not yet clear which one will be the most sustainable.

[46]: Wein et al. (2022), “Photon-Number Entanglement Generated by Sequential Excitation of a Two-Level Atom”

[47]: Browaeys et al. (2020), “Many-Body Physics with Individually Controlled Rydberg Atoms”

[48]: Lescanne et al. (2020), “Exponential Suppression of Bit-Flips in a Qubit Encoded in an Oscillator”

[49]: Debnath et al. (2016), “Demonstration of a Small Programmable Quantum Computer with Atomic Qubits”

[50]: Marciniak et al. (2022), “Optimal Metrology with Programmable Quantum Sensors”

[51]: Kuwahata et al. (2020), “Magnetometer with nitrogen-vacancy center in a bulk diamond for detecting magnetic nanoparticles in biomedical applications”

2 Quantum atom optics with metastable helium

2.1 Context and motivation

Our team in the Laboratoire Charles Fabry has developed a detection method for individual atoms, in three dimensions. It gives access to many information that are usually difficult to capture in atomic physics experiments, such as the correlations between spatially separated particles. This feature is a significant strength of our apparatus, because correlations can contain the signature of purely quantum effects and nonlocality properties of multiple-particles systems [1–4].

Along with this, since the mid-2000s the team has explored different way to generate correlated pairs of atomic beams [5–7], that —under specific experimental conditions— may constitute an entangled system. With the assistance of light-matter interplay, this opens up the possibility to realise many experiments, inspired by quantum optics.

Fairly recently, the team achieved the atomic analogue of the Hong-Ou-Mandel effect [8], as well as a proof of principle of a two-particle interferometer that could be used in the future to enable a test of a Bell inequality for atoms’ entangled in momenta [9]. Such a test of quantum nonlocality with massive particles has not been obtained yet, and it is currently one of the main goals of our team. By demonstrating non-classical state of mechanical¹ degrees of freedom, such an experiment would constitute an important philosophical milestone. In addition, since it involves *massive* particles —subjected to gravitational coupling— in a highly *quantum* state, it would also be a first step towards a new generation of experiment soliciting both quantum mechanics and general relativity [10].

During this PhD I contributed to the modernisation of the experimental setup, who suffered during the last five years of many technical issues, inhibiting the production of new scientific results. These evolutions conducted to the obtention of a metastable helium Bose-Einstein condensate in an optical trap, and thereafter the production of correlated atomic pairs in a regime that was not explored in the early states of the experimental platform.

I also achieved a short theoretical study, dealing with a generalised version of Hong-Ou-Mandel like experiments, involving more than two particles, and taking into account finite quantum efficiency effects of

[1]: Reid et al. (1986), “Violations of Classical Inequalities in Quantum Optics”

[2]: Kheruntsyan et al. (2012), “Violation of the Cauchy-Schwarz Inequality with Matter Waves”

[3]: Volovich (2016), “Cauchy-Schwarz Inequality-Based Criteria for the Non-Classicality of Sub-Poisson and Antibunched Light”

[4]: Wasak et al. (2016), “Cauchy-Schwarz Inequality for General Measurements as an Entanglement Criterion”

[5]: Perrin et al. (2007), “Observation of Atom Pairs in Spontaneous Four-Wave Mixing of Two Colliding Bose-Einstein Condensates”

[6]: Jaskula et al. (2012), “Acoustic Analog to the Dynamical Casimir Effect in a Bose-Einstein Condensate”

[7]: Bonneau et al. (2013), “Tunable Source of Correlated Atom Beams”

[8]: Lopes (2015), “An Atomic Hong-Ou-Mandel Experiment”

[9]: Dussarrat et al. (2017), “Two-Particle Four-Mode Interferometer for Atoms”

¹: and therefore having a clear classical meaning.

[10]: Penrose et al. (1998), “Quantum computation, entanglement and state reduction”

the detector. Such an experiment could be performed in our laboratory in a near future.

2.2 Outline of this manuscript

The manuscript is organised in five chapters, divided in two parts:

Theoretical considerations

Chapter 1: from the two-particle Hong-Ou-Mandel effect, to its generalised version with N particles.

The Hong-Ou-Mandel effect is famous in quantum optics: it has been demonstrated experimentally in 1987, and reproduced with atoms in our team in 2015. In this chapter, after giving some reminders about the original two particle Hong-Ou-Mandel experiment, I will derive a number of theoretical results that could be useful in the prospect of an upcoming experiment that we would like to achieve in our team: an experiment similar to the Hong-Ou-Mandel one, but with a large number of indiscernible particles.

Chapter 2: Bell inequalities with momentum-entangled atoms.

At the beginning of this second chapter, I shall recall the essential ideas of the [EPR](#) argument, and show how the Bell's inequalities allow to verify experimentally its conclusions.

After this fairly well known introduction to the question Bell's theorem, I will dive more precisely into the topic the currently interests us in the team: the realisation of a Bell inequality test with respect to the velocities of helium atoms. Such an experiment would be an important milestone in nowadays quest to engineering new type of entangled states, and exploring quantum mechanics in different regimes.

Experimental achievements

Chapter 3: detecting and obtaining a Bose-Einstein condensate of helium.

In this chapter I will start by showing how the metastable state of helium can be used as an advantage to perform a single-particle resolved detection of atoms. I will then go through the different experimental steps that we apply to an helium cloud so as to obtain a metastable Bose-Einstein condensate.

Chapter 4: technological changes and evolutions during my PhD.

In this chapter I will expose the various problems that have plagued our apparatus (mostly during my PhD but also a few years before), preventing us from making scientific progress. Then I shall explain the different technological evolutions and workarounds that we decided to implement so as to overcome these issues.

Chapter 5: study of the source of correlated pairs of atoms.

In this final chapter, I will present the main scientific results that I obtained during my PhD. However, the data that I will show were not acquired in the purpose of a scientific communication: we were still testing the generation of pairs, who started to work only recently. Unfortunately, after approximately three months of successful operation, a new set of technical issues struck the experiment, and stopped the acquisition of data. In this chapter, I will propose an analysis—as complete as possible—of the dataset that offered the most satisfying results.

Before doing this, I will also make a short formal introduction to the process of pair creation: it is a summary of several theoretical considerations, that have been treated in the PhD manuscripts of my predecessors on the experiment.

THEORETICAL CONSIDERATIONS

Hong-Ou-Mandel effect

1

Chapter's table of contents

. Introduction	12
1. Two-particle HOM effect	13
1.1 History and presentation	13
1.2 Theory	15
1.2.1 Lossless beam splitter model	15
1.2.2 Derivation and interpretation of the two-particle HOM effect	17
1.2.3 Classical limit	21
1.3 Experimental results with metastable helium	22
2. N-particle HOM effect	24
2.1 Theoretical generalities	25
2.1.1 Notations used	25
2.1.2 Transformation of a quantum system by a beam splitter	26
Heisenberg and Schrödinger representations	26
Effect on a general density matrix	27
Fock states at the input	30
2.2 Classification of the interference patterns for different input states	31
2.2.1 Twin-Fock states and mixing with vacuum	31
Indiscernible case: twin-Fock states	31
Distinguishable case: mixing with the vacuum	34
2.2.2 Coherent states	36
2.2.3 Thermal states	40
Indiscernible case	41
Distinguishable case	44
2.2.4 Two-mode squeezed vacuum state	47
Motivation	47
Probability distribution of a TMS	48
Indiscernible case	52
Distinguishable case	59
Distinguishable and indiscernible comparison	64
. Conclusion	65

Introduction

1: mainly in 2020.

In this chapter, I will report the analytical and numerical calculations that I performed¹ concerning an extension of the famous Hong-Ou-Mandel (HOM) experiment to a domain in which the total number of particles involved can be much larger than two.

In the first section of this chapter, I will provide a general review of the HOM experiment, from its origins in quantum optics (back in 1987) to a more recent realisation of its atomic equivalent, that has been demonstrated by our team in 2015.

I will insist in particular on the fact that this experiment is genuinely quantum, and provides interesting information about the indistinguishability properties of the particles that are involved.

2: and also to take advantage of the 2020 lockdown period...

Due to recent technical issues that we have encountered with our apparatus (and that will be at the core of Chapter 4), we have not been able to reconduct this type of interferometry experiment since 2017 (two years before my arrival in the team). However, in anticipation of the time when the experiment will be functional again², I have studied what could be interesting in setting up a similar experiment, in which a more complex initial state would be involved.

[52]: Gerry et al. (2005), *Introductory Quantum Optics*

This particular state is widely known as the two-mode squeezed vacuum state (TMS). We will see that this entangled state provides remarkable results when it used in an HOM-like experiment. This state is quite famous, at least in quantum optics, as it can be prepared with the spontaneous parametric down conversion with a nonlinear crystal [52]. It interests us particularly, because we have several reasons to believe that our experimental platform is able to generate it with helium atoms: this will be discussed in details in the last chapter of this manuscript.

1 Two-particle HOM effect

1.1 History and presentation

Since the early 1970s, and the appearance of single-photon sources, the optical testing of quantum mechanics is a fertile field of activity in experimental physics. From an epistemological point of view, one of the goals of quantum optics experiments is to exhibit effects which can in no way be explained by classical physics. Important milestones have been reached in the 1980s, for example with the pioneering contribution of Clauser et al. and Aspect et al. who revealed the nonlocal nature of certain states of light [20, 22] (we will come back to this type of measurement in Chapter 2). In 1987 Chung Ki Hong, Zheyu Ou, and Leonard Mandel experimentally demonstrated a two-particle interference effect, involving the bosonic nature of the light field [53]. This effect — now commonly known as the **Hong-Ou-Mandel (HOM)** effect — is also the signature of the intrinsic indiscernibility property of single photons, and cannot be explained classically. Before giving the outline of this experiment, we will present first a simpler version of the optical setup, that was used at the Institut d’Optique d’Orsay one year before the **HOM** experiment.

Indeed, in 1986, Grangier et al. obtained direct experimental evidence of the existence of photons (defined as the quantised excitations of the electrical field) [54]. The idea was to collect one of the photons emitted by the radiative cascade¹ of a calcium atom and place it at the input of a 50-50 beam splitter. One can then look at the coincident detections between both output sides of the beam splitter: if a single photon is indeed emitted, it should never be detected at both output sides of the beam splitter, meaning that no coincidence should be measured. A schematic of the experiment is given in Figure 1.1. The experiment resulted in strong quantum anti-correlation effect, which is the signature of a single photon emission from the source: a manifestation of the *particle-like* behaviour of light. With the wording of quantum statistics and correlation functions, this is known as the *photon anti-bunching* effect.

Even though the previous experiment revealed the quantum statistics of the emission of light by an atom, it does not involve interferences of any kind. During each realisation only one photon is propagating, and it never interferes until its detection. To witness quantum interference effects, one can complete the optical setup of Figure 1.1 by adding two mirrors and one beam splitter and realise a *single photon Mach-*

[20]: Freedman et al. (1972), “Experimental Test of Local Hidden-Variable Theories”

[22]: Aspect et al. (1981), “Experimental Tests of Realistic Local Theories via Bell’s Theorem”

[53]: Hong et al. (1987), “Measurement of Subpicosecond Time Intervals between Two Photons by Interference”

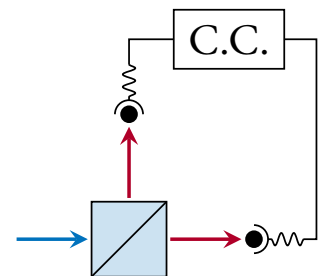


Figure 1.1: Simplified drawing of the single-photon anti-correlation experiment. This design was proposed by Grangier et al. [54] The blue arrow represents a single photon input, in front a 50-50 beam splitter. The red arrows represent the two possible outcome channels of the photon. The detections are then correlated with a coincidence counter (C.C.) device.

[54]: Grangier et al. (1986), “Experimental Evidence for a Photon Anticorrelation Effect on a Beam Splitter”

¹: a process in which an atom successively emits several photons, by deexciting itself in several successive steps, going from an excited state to lower energy states.

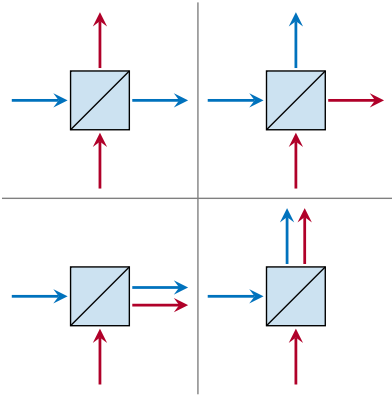


Figure 1.2: Classical outcomes of a HOM-like experiment. Classically, photons are distinguishable, and we are allowed to label them with specific colours (red and blue). Each arrow represents a single photon, and four possible outcomes can be considered, weighed by the same probability $1/4$ (in the case of a 50-50 beam splitter).

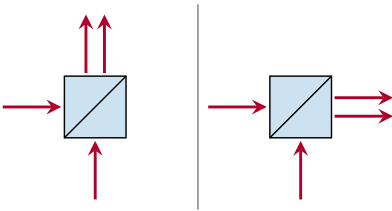


Figure 1.3: Outcomes of a HOM experiment. Photons are indistinguishable, and we are not allowed to label them. Each arrow represents a single photon. In contrast to the classical picture in Figure 1.2, the bosonic nature of photons, and interferences lead to only two possible outcomes: both photons leaving the beam splitter on the same side.

¹: let us say the same polarisation, same frequency, and same spatial mode.

[55]: Cohen-Tannoudji et al. (2017), *Mécanique quantique - Tome 3*

Zehnder interferometer. This work has also been done by Grangier et al. (published in the same paper [54]) and the team observed (statistically) the well known fringes at the output of the interferometer, being interpreted as the self-interference of the photon wave function.

The idea of HOM is to consider again the design of the experiment in Figure 1.1 and to extend it to the domain of two-particle physics. Considering the schematic in Figure 1.1, one can indeed wonder what happens when *two* single photons are placed at the inputs of the beam splitter, with one on each side. With a classical approach, there is no notion of indiscernibility: the two photons can be labelled, and depending on which one is reflected or transmitted, four possible outcomes may be considered, which are represented in Figure 1.2 (the beam splitter is assumed to be lossless). With a 50-50 beam splitter the configurations are equiprobable, meaning that if an experimentalist monitors the coincident detections of particles of the output channels, a coincidence should be found half of the time (corresponding to the two configurations at the top of Figure 1.2).

When considering a quantum treatment of this experiment, the situation is very different. First, if the photons are in the same mode¹, and reach the beam splitter at the same date t , they are properly **indiscernible** and their labelling does not make any sense. To capture efficiently the notion of indiscernibility of particles in quantum formalism (and the subsequent notion of symmetry of the states) the best practice is to work with the second-quantisation (that is presented in details in [55]). Denoting $|n, m\rangle_{\text{in}}$ the state corresponding to n photons placed at one of the inputs of the beam splitter and m photons on the other one, the initial quantum state corresponding of the HOM experiment reads:

$$|\Psi\rangle_{\text{in}} = |1, 1\rangle_{\text{in}} \tag{1.1}$$

Due to indiscernibility, the two configurations with crossed outputs represented at the top of Figure 1.2 are completely identical in quantum mechanics. With similar notations as before, the output state of the HOM experiment is a priori written as the following coherent superposition:

$$|\Psi\rangle_{\text{out}} = \alpha_{20} |2, 0\rangle + \alpha_{11} |1, 1\rangle + \alpha_{02} |0, 2\rangle \tag{1.2}$$

where the hypothesis of absence of losses at the beam splitter has been used, and

$$|\alpha_{20}|^2 + |\alpha_{11}|^2 + |\alpha_{02}|^2 = 1 \tag{1.3}$$

Now the spectacular result of the HOM effect is that if two indiscernible photons reach the beam splitter, the α_{11} term turns out to be

zero, and we end up with the output probabilities (with Born's rule):

$$|\alpha_{20}|^2 = |\alpha_{02}|^2 = \frac{1}{2} \quad (1.4)$$

This is not mathematically difficult to prove, and we will give a justification of this in the next subsection. For now let us just highlight the fact that the HOM experiment reveals a quantum effect that is very different from the one that we presented in the two previous experiments. Indeed, in the first experiment of photon anti-correlation that we presented (Grangier et al.) the vanishing of the coincident detection probability was sourced by the particle-like nature of photons. On the contrary, in the case of the HOM effect, it is the destructive interference between the output probability amplitudes of the photons that imposes the two photons to leave the beam splitter on the same channel: it is therefore the manifestation of the *wave-like* nature of photons. Actually, HOM experiments probe the level of indiscernibility of the particles that interfere: this property is sometimes called *purity*, and it is a major concern in modern quantum optics [56, 57].

1.2 Theory

1.2.1 Lossless beam splitter model

First, let us offer some reminders about the representation of a beam splitter (BS), in the formalism of second quantisation. Since it will be also useful to Section 2 of this chapter, we will keep fairly general notations in this subsection.

Input and output channels of the BS, and the associated creation/annihilation operators, are written in compliance with Figure 1.5. Denoting $|vac\rangle$ the vacuum state, and using the second quantisation we have:

$$\left\{ \begin{array}{l} |n_1, n_2\rangle_{\text{in}} = \frac{\hat{a}_1^{n_1} \hat{a}_2^{n_2}}{\sqrt{n_1! n_2!}} |vac\rangle \\ |N_1, N_2\rangle_{\text{out}} = \frac{\hat{b}_1^{N_1} \hat{b}_2^{N_2}}{\sqrt{N_1! N_2!}} |vac\rangle \end{array} \right. \quad (1.5)$$

$$\left\{ \begin{array}{l} |n_1, n_2\rangle_{\text{in}} = \frac{\hat{a}_1^{n_1} \hat{a}_2^{n_2}}{\sqrt{n_1! n_2!}} |vac\rangle \\ |N_1, N_2\rangle_{\text{out}} = \frac{\hat{b}_1^{N_1} \hat{b}_2^{N_2}}{\sqrt{N_1! N_2!}} |vac\rangle \end{array} \right. \quad (1.6)$$

In this manuscript, we will only consider perfect lossless beam splitters. At first glance this hypothesis may seem questionable: indeed, we will show in the next chapter that in our experiment the beam splitters

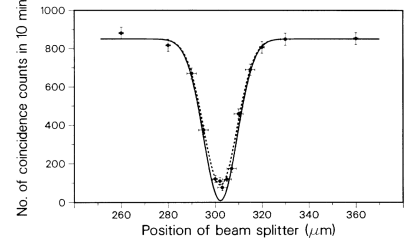


Figure 1.4: Historical result of the HOM copied from [53]. This profile is nowadays widely known as the “HOM dip”. When the beam splitter is positioned such that both photons reach it at the same time, the coincident detections counting vanishes.

[56]: Somaschi et al. (2016), “Near-Optimal Single-Photon Sources in the Solid State”

[57]: Wang et al. (2019), “Towards optimal single-photon sources from polarized microcavities”

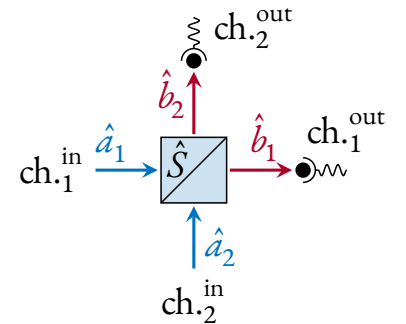


Figure 1.5: Parametrisation of the beam splitter. The input (respectively output) channels are denoted as ch_i^{in} (respectively ch_i^{out}), and are provided with the annihilation operators \hat{a}_i (respectively \hat{b}_i). A detector is placed at each of the two output channels.

are realised with short light pulses (performing Rabi coupling) and cannot have 100 % quantum efficiency. Nonetheless, it is useful to treat the problem with this assumption, because the defects of the beam splitter can be embedded into the finite quantum efficiency of the detectors. It does not make much of a difference to an experimentalist to know whether a particle was lost in the interferometer or during the detection. However, an accurate description of the lossy beam splitter would require the use of non-unitary operators, that could lead to lengthy calculations, without much interest for the current discussion.

1: in the case of metastable helium, the internal state is obviously crucial, but we only propagate atoms polarised in the same $m = 0$ magnetic sublevel in the interferometer. The assumption is therefore experimentally legitimate.

2: meaning that when a detector is placed at an output channel it cannot distinguish whether the particle has been emitted from the opposite side (and therefore transmitted across the beam splitter), or reflected by the beam splitter.

[58]: Campos et al. (1989), “Quantum-Mechanical Lossless Beam Splitter”

In this chapter we will also ignore the internal degrees of freedom of the quantum particles¹, and we assume that there is a perfect overlapping of the spatial modes at the output of the beam splitter². Thus, the notion of indistinguishability only relies on the difference of time of arrival of the particles onto the beamsplitter: two particles are indiscernible if they interact with the beam splitter at the same time.

The beam splitter is entirely characterised by the way it couples the modes $\hat{a}_{i \in \{1,2\}}$ with the modes $\hat{b}_{i \in \{1,2\}}$. Assuming the coupling to be linear, it turns out that the lossless hypothesis is enough to determine the nature of the transformation carried out by the beam splitter, thanks to [Theorem 1](#) [58]:

Theorem 1 (Unitarity of the transformation)

We denote \underline{S} the linear operator representing the action of the beam splitter on the input modes:

$$\begin{pmatrix} \hat{b}_1 \\ \hat{b}_2 \end{pmatrix} = \underline{S} \begin{pmatrix} \hat{a}_1 \\ \hat{a}_2 \end{pmatrix} \quad (1.7a)$$

$$\begin{pmatrix} \hat{a}_1 \\ \hat{a}_2 \end{pmatrix} = \underline{S}^\dagger \begin{pmatrix} \hat{b}_1 \\ \hat{b}_2 \end{pmatrix} \quad (1.7b)$$

$U(2)$ is the group of unitary operators of degree 2.

The three following statements are equivalent:

1. $\underline{S} \in U(2)$
2. the number of particles is conserved

$$i.e. \quad n_1 + n_2 = N_1 + N_2 \quad (1.8)$$

(this is the conservation of energy)

3. the bosonic commutation relations are preserved:

$$\left\{ \begin{array}{l} [\hat{a}_i, \hat{a}_j^\dagger] = [\hat{b}_i, \hat{b}_j^\dagger] = \delta_{ij} \end{array} \right. \quad (1.9a)$$

$$\left\{ \begin{array}{l} [\hat{a}_1, \hat{a}_2] = [\hat{b}_1, \hat{b}_2] = 0 \end{array} \right. \quad (1.9b)$$

\underline{S} being unitary, its most general 2×2 matrix representation reads:

$$\underline{S} \equiv e^{i\varphi_0} \begin{bmatrix} \cos(\theta)e^{i\varphi_\tau} & \sin(\theta)e^{i\varphi_\rho} \\ -\sin(\theta)e^{-i\varphi_\rho} & \cos(\theta)e^{-i\varphi_\tau} \end{bmatrix} \in \text{U}(2) \quad (1.10)$$

The global phase φ_0 does not play any role¹ so we can drop it without loss of generality, leaving $\underline{S} \in \text{SU}(2)$.

¹: at least in a simple scheme, with a single beam splitter, and no subsequent interferences after \underline{S} .

It is also often convenient to introduce the transmittance τ and the reflectance ρ :

$$\left\{ \begin{array}{l} \tau \triangleq \cos^2(\theta) \\ \rho \triangleq \sin^2(\theta) = 1 - \tau \end{array} \right.$$

We can therefore represent the beam splitter in the Fock states bases, associated to the annihilation operators $(\hat{a}_1, \hat{a}_2; \hat{b}_1, \hat{b}_2)$, with the 2×2 matrix:

$$\underline{S}(\tau, \varphi_\tau, \varphi_\rho) \equiv \begin{bmatrix} \sqrt{\tau}e^{i\varphi_\tau} & \sqrt{\rho}e^{i\varphi_\rho} \\ -\sqrt{\rho}e^{-i\varphi_\rho} & \sqrt{\tau}e^{-i\varphi_\tau} \end{bmatrix} \quad (1.11)$$

The coefficients of this matrix contain the *amplitude of probabilities* associated to the possible outcomes (transmission or reflection of each particle).

1.2.2 Derivation and interpretation of the two-particle HOM effect

In second quantisation We consider a 50-50 beam splitter ; with previous notations this means $\tau = \frac{1}{2}$:

$$\underline{S} = \frac{1}{\sqrt{2}} \begin{bmatrix} e^{i\varphi_\tau} & e^{i\varphi_\rho} \\ -e^{-i\varphi_\rho} & e^{-i\varphi_\tau} \end{bmatrix} \quad (1.12)$$

we kept the phase terms for generality, but we will shortly see that they do not play any role in the HOM effect². The input state reads

$$|\Psi\rangle = |1, 1\rangle_{\text{in}} = \hat{a}_1^\dagger \hat{a}_2^\dagger |vac\rangle \quad (1.13)$$

²: more generally, we will even see in Subsection 2.1.2 that they do not play any role when working with pure Fock states.

and the coupling of the modes via the beam splitter (1.7b) gives

$$\hat{a}_1^\dagger = \frac{1}{\sqrt{2}} \left(e^{i\varphi_\tau} \hat{b}_1^\dagger - e^{-i\varphi_\rho} \hat{b}_2^\dagger \right) \quad (1.14a)$$

$$\hat{a}_2^\dagger = \frac{1}{\sqrt{2}} \left(e^{i\varphi_\rho} \hat{b}_1^\dagger + e^{-i\varphi_\tau} \hat{b}_2^\dagger \right) \quad (1.14b)$$

leading to

$$\hat{a}_1^\dagger \hat{a}_2^\dagger = \frac{1}{2} \left[e^{i(\varphi_\tau + \varphi_\rho)} (\hat{b}_1^\dagger)^2 - e^{-i(\varphi_\tau + \varphi_\rho)} (\hat{b}_2^\dagger)^2 + \underbrace{\hat{b}_1^\dagger \hat{b}_2^\dagger - \hat{b}_2^\dagger \hat{b}_1^\dagger}_{=0} \right] \quad (1.15)$$

in which the last two crossed terms cancel each other out since $[\hat{b}_1, \hat{b}_2] = 0$.

By denoting $\phi = \varphi_\tau + \varphi_\rho$, we end up with:

$$|\Psi\rangle = \frac{1}{\sqrt{2}} \left(e^{i\phi} |2, 0\rangle_{\text{out}} - e^{-i\phi} |0, 2\rangle_{\text{out}} \right) \quad (1.16)$$

meaning that indeed, when the detectors are placed after the beam splitter, in each realisation there is a 50 % probability to detect two particles on either side, and zero probability to witness a coincident detection on both sides.

Remark 1.1 Let us emphasise the fact that this probabilistic result is completely independent of the phases φ_τ and φ_ρ applied by the beam splitter.

The calculation was very quick, and it clearly shows that the HOM is resulting from a destructive interference between the creation operators \hat{b}_1 and \hat{b}_2 . Another way of interpreting this cancellation of the crossed detections, may be inspired by Feynman's prescription¹:

¹: this interpretation is actually suggested in the textbook of Gerry & Knight [52].

Feynman's rule (simplified): *In order to know the probability associated to a given outcome E_f of an experiment, one can add up the amplitude of probabilities associated to all the paths leading to E_f , and then take its square modulus.*

Here the amplitude of probabilities is directly given by the matrix elements of \underline{S} . Indeed by denoting $A_T[i \in \{1, 2\}]$ the complex amplitude of probability that a particle placed at the input channel ch_i^{in} is transmitted, and $A_R[i]$ the complex amplitude of probability that it is

reflected, we simply have:

$$\underline{S} = \begin{pmatrix} A_T[1] & A_R[2] \\ A_R[1] & A_T[2] \end{pmatrix} \quad (1.17)$$

Now in the HOM experiment, two paths could lead to a coincident detection of the particles on both outputs:

- ▶ both particles being *transmitted* across the beam splitter: the associated amplitude of probability is $A_T[1] \times A_T[2]$;
- ▶ both particles being *reflected* by the beam splitter: the associated amplitude of probability is $A_R[1] \times A_R[2]$;

regarding the matrix elements (1.12) of \underline{S} , and applying Feynman's rule, the probability P_{crossed} of this event is :

$$\begin{aligned} P_{\text{crossed}} &= |A_T[1]A_T[2] + A_R[1]A_R[2]|^2 \\ &= |e^{i\varphi_\tau} e^{-i\varphi_\tau} - e^{-i\varphi_\rho} e^{i\varphi_\rho}|^2 \\ P_{\text{crossed}} &= 0 \end{aligned} \quad (1.18)$$

We end up with the famous HOM effect again, but with the somehow more “*physical*” picture of a destructive interference between the *paths* heading to the crossed exit of the particles.

Role of the symmetry of the bosonic wave function Previous derivations are satisfying, but the fact that we are dealing with indistinguishable bosons did not appear clearly. Actually, in a sense, we could say it was “hidden” in the fact that we were using the second quantisation formalism, that contains by itself the symmetry of the states. To exhibit the crucial role of indiscernibility in the HOM effect, let us (for once) take a look at what happens in first quantisation formalism.

With the notations of Figure 1.6, we denote respectively ($|A\rangle, |B\rangle$) and ($|C\rangle, |D\rangle$) the input and output states of the beam splitter. The evolution operator \underline{S} of the 50-50 beam splitter is the same as before (it is actually the same as in classical wave optics). We already observed that the phase does not matter, so we will assume (for simplicity) that \underline{S} has the well known real form:

$$\begin{cases} r, t \in \mathbb{R} \\ t^2 + r^2 = 1 \end{cases} \quad \underline{S} = \begin{bmatrix} t & r \\ -r & t \end{bmatrix} \quad (1.19)$$

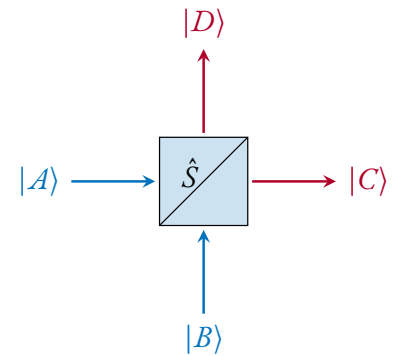


Figure 1.6: Notations for the input and output states of the beam splitter in first quantisation.

If we do not pay attention to the indiscernibility of the particles, then the input state takes the form:

$$|\Psi_{\text{in}}\rangle = |1 : A\rangle \otimes |2 : B\rangle \quad (1.20)$$

where the labellings 1 and 2 of the particles are clearly highlighted. The output state is simply obtained by the application of the evolution operator \underline{S} representing the action of the beam splitter:

$$|\Psi_{\text{out}}\rangle = \underline{S}|1 : A\rangle \otimes \underline{S}|2 : B\rangle \quad (1.21a)$$

$$= (t|1 : C\rangle - r|1 : D\rangle) \otimes (r|2 : C\rangle + t|2 : D\rangle) \quad (1.21b)$$

$$|\Psi_{\text{out}}\rangle = tr|1 : C; 2 : C\rangle + t^2|1 : C; 2 : D\rangle - r^2|1 : D; 2 : C\rangle - rt|1 : D; 2 : D\rangle \quad (1.21c)$$

We therefore have four distinct outcomes: this is the classical result that is depicted in Figure 1.2. When the beam splitter is 50-50, meaning $|r| = |t| = \frac{1}{\sqrt{2}}$, all outcomes are equiprobable, and we find a coincident detection at the output half of the time: there is no HOM effect. This scenario actually corresponds to what would happen if the two particles interact *successively* with the beam splitter, making them effectively distinguishable.

If we consider indiscernible bosons, the only input state that satisfies the symmetry of the two-particle wave function is:

$$|\Psi_{\text{in}}\rangle = \frac{1}{\sqrt{2}} (|A\rangle |B\rangle + |B\rangle |A\rangle) \quad (1.22)$$

then the output state reads:

$$|\Psi_{\text{out}}\rangle = \frac{1}{\sqrt{2}} (\underline{S}|A\rangle \underline{S}|B\rangle + \underline{S}|B\rangle \underline{S}|A\rangle) \quad (1.23a)$$

$$= \frac{1}{\sqrt{2}} \left[(t|C\rangle - r|D\rangle)(r|C\rangle + t|D\rangle) + (r|C\rangle + t|D\rangle)(t|C\rangle - r|D\rangle) \right] \quad (1.23b)$$

$$|\Psi_{\text{out}}\rangle = \frac{1}{\sqrt{2}} \left[2rt|C, C\rangle + (t^2 - r^2)(|C, D\rangle + |D, C\rangle) - 2rt|D, D\rangle \right] \quad (1.23c)$$

This final state is very different from the previous one. The first observation we can make, is that it involves a coherent superposition of only *three* symmetric two-particle states: $|C, C\rangle$, $|D, D\rangle$ and $\frac{1}{\sqrt{2}}(|C, D\rangle + |D, C\rangle)$, this is a consequence of the initial symmetrisation of the state: this has already been discussed in the first subsection.

Secondly, when the beam splitter is symmetric we have $r^2 - t^2 = 0$, thus the crossed term is zero, leading to

$$|\Psi_{\text{out}}\rangle = \frac{1}{\sqrt{2}}(|C, C\rangle + |D, D\rangle) \quad (1.24)$$

Once again, we find the HOM effect, written in first quantisation. With this approach, the role of the symmetry of the two-particle wave function is clearly visible.

Remark 1.2 (Fermionic anti-HOM effect) If we had considered fermions, the Pauli exclusion principle would have directly implied the coincident detections on both detectors, whatever the transmission coefficient τ of the beam splitter is! This is sometime called *anti-HOM* effect.

On the mathematical level, let us recall that the derivation of the formal expression of the beam splitter Eq. (1.11) required the use of the fact that we were considering bosons: it is wrong when considering fermions.

1.2.3 Classical limit

At this stage we have a fairly complete picture of what the quantum HOM effect is. However, we can still legitimately wonder if there a classical analogue to this phenomenon. In other words, we could wonder whether the HOM anti-correlation is the genuine signature of quantum effect.

Keeping the notations (A, B, C, D) for the input and output ports, we can study what happens when we shine two coherent light fields (with the same frequency), with equal intensities $I_0 = E_0^2$, at the entrance of the beam splitter. The corresponding complex amplitudes reads:

$$\begin{cases} \underline{E}_A(\varphi_A) = E_0 e^{i\varphi_A} & (1.25a) \\ \underline{E}_B(\varphi_B) = E_0 e^{i\varphi_B} & (1.25b) \end{cases}$$

Considering the parametrisation (1.12) of the beam splitter, and setting $\phi = \varphi_\tau + \varphi_\rho$, it is a very well-known result of classical wave optics that

1: $\sin^2(x) \times \cos^2(x) = \frac{1}{4} \sin^2(2x)$

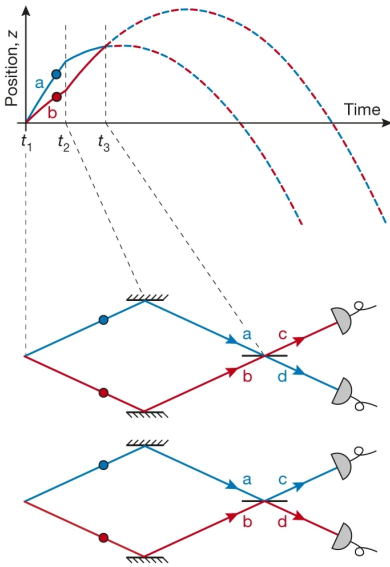


Figure 1.7: Schematic drawing of the atomic HOM experiment. The figure is extracted from the original publication [59]. An atomic source emits pairs of helium atoms (**a** and **b**) along the vertical axis z (cf. Chapter 5). They are subjected to free-fall and their trajectories are parabolas. Bragg diffraction with a resonant optical lattice (cf. Chapter 2) realise the atomic equivalent of a mirror at $t = t_2$, and a beam splitter when the atomic trajectories cross again at $t = t_3$. The lines alternately dashed in red and blue symbolise the indiscernibility of the atoms' trajectories when $t > t_3$. The correlations are probed simply by looking at the arrival times of the atoms on a detector laying beneath the atomic source.

[8]: Lopes (2015), "An Atomic Hong-Ou-Mandel Experiment"

[60]: Perrier (2018), "Interférences multiples avec atomes froids"

the two coherent fields interfere, and give the output intensities

$$I_C(\phi) = 2I_0 \cos^2\left(\frac{\phi_B - \phi_A + \phi}{2}\right) \tag{1.26a}$$

$$I_D(\phi) = 2I_0 \sin^2\left(\frac{\phi_B - \phi_A + \phi}{2}\right) \tag{1.26b}$$

in this framework, the classical equivalent to the coincident detections of particles is given by the product of these intensities¹:

$$I_C(\phi) \cdot I_D(\phi) = I_0^2 \sin^2(\phi_B - \phi_A + \phi) \tag{1.27}$$

The major difference with quantum HOM effect is the phase dependence of above expression. Indeed, even though $I_C \cdot I_D$ can vanish with specific values of ϕ , its quantum counterpart is zero whatever ϕ is. In particular, with classical waves, the average value of the coincident counting rate is given by

$$\frac{1}{I_0^2} \langle I_C(\phi) \cdot I_D(\phi) \rangle_\phi = \frac{1}{2} \tag{1.28}$$

During an experiment, one can therefore randomise the phase ϕ , and compare the coincident counting rate to the classical limit $\frac{1}{2}$ calculated above. Below this value, the experiment reveals an *authentic* quantum effect.

1.3 Experimental results with metastable helium

As it has been mentioned in the introduction, our team demonstrated in 2015 an atomic version of the HOM effect [8]. Let us quickly report here the main features and result of this experiment. More technical details about the atomic interferometer will be given in the following chapter, dealing with a similar experiment (testing a Bell inequality) that we would like to concretely set up in near future.

A schematic representation of the experiment is given in Figure 1.7. Additional details about the Bragg diffraction with a lattice are given in Chapter 2, and an even more complete study of this technique can be found in the PhD manuscript of Maxime Perrier [60].

The observable that is considered is the cross-correlation $G_{cd}^{(2)}$ between both outputs of the beam splitter. By denoting N_c and N_d the number

of atoms counted in time intervals (with a small width Δt) centred onto the arrival times corresponding respectively to the output modes c and d we have¹:

$$G_{cd}^{(2)} = \langle N_c \cdot N_d \rangle \quad (1.29)$$

Contrary to the “pure” HOM experiment in which exactly two particles were emitted at each realisation, here, most of the time, no pair is emitted and the vacuum is detected on both sides of the beam splitter (a pair is emitted approximately 10 % of the time). In addition, the quantum efficiency of the detector was $\eta \approx 25\%$, reducing the amplitude of the obtained signal again, by an η^2 factor (since two particles must be detected).

¹: actually in this paragraph we have simplified a lot what is actually done to the signal to compute the quantity $G_{cd}^{(2)}$: in addition to time filtering, there is also a spatial one. These details will be explained in Chapter 5, but they are not useful to understand the main meaning of the results that are presented in this subsection.

The quantumness of the effect can however be estimated with the *visibility* V of the HOM, which is nothing more than the contrast of the signal (as a function of the time $\tau = t_3 - t_2$ of application of the beam splitter):

$$V = \frac{\max_{\tau} [G_{cd}^{(2)}(\tau)] - \min_{\tau} [G_{cd}^{(2)}(\tau)]}{\max_{\tau} [G_{cd}^{(2)}(\tau)]} \quad (1.30)$$

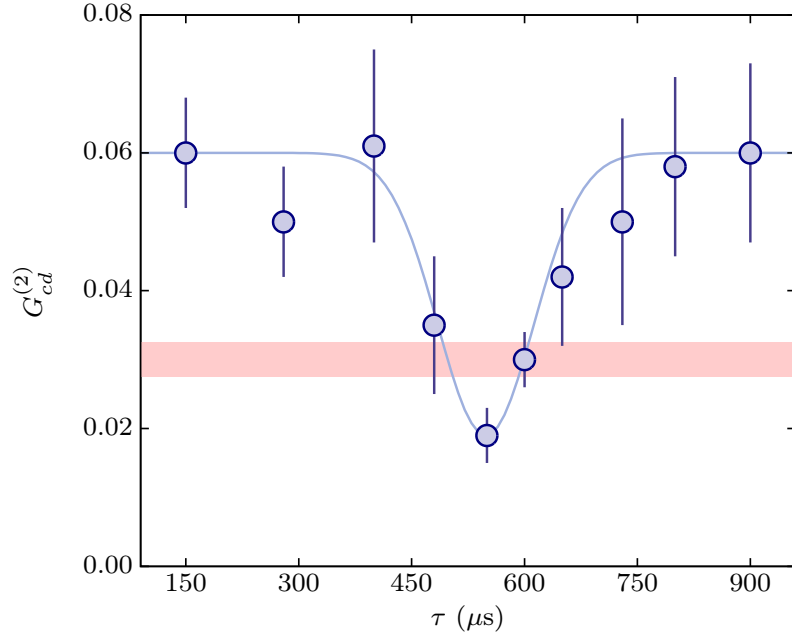
At each experimental realisation, the beam splitter applies a phase ϕ that is intentionally randomised, so that the visibility can be compared to the classical threshold $V_{\text{classical}} = 0.5$.

The result of the experiment is presented in Figure 1.8. The team measured of visibility

$$V = 0.65(7)$$

beating the classical limit by more than two standard deviations.

Figure 1.8: Correlation $G_{cd}^{(2)}$ as a function of time of application $\tau = t_3 - t_2$ of the beam splitter (cf. Figure 1.7). The HOM anti-correlations are maximal when $\tau \approx t_2 - t_1$. The red strip represents the classical limit $V = 0.5$ to HOM dip (taking into account the experimental uncertainties). The limits $\tau \leq 350 \mu\text{s}$ and $\tau \geq 750 \mu\text{s}$, where $G_{cd}^{(2)}$ is maximised, correspond to situations where the particles at the entrance of the beam splitter are distinguishable. $G_{cd}^{(2)}$ is minimised when the particles are indiscernible: when $\tau = 550(50) \mu\text{s}$. The fact that $G_{cd}^{(2)}$ does not reach the value of 0 can be explained by the contribution of some realisations where the total number of particles is larger than 2.



2 N-particle HOM effect

The two-particle HOM experiment obtained in 2015 was an important milestone for our team. In addition to its scientific value, it is also a way of probing the quality of our atomic interferometer.

However, we can wonder whether we are able to extend the HOM experiment to a different regime, where more particles are involved and interfere at the beam splitter. We choose to call this generalised scenario *n*-particle Hong-Ou-Mandel (nHOM) experiments. The aim of this chapter’s second section is to theoretically find a situation –achievable with our apparatus– in which the indiscernibility properties of a collection of particles lead to remarkable effects, and compare it to a classical situation. In this work, taking into account the finite quantum efficiency of the detectors will be crucial: we will see that it has a strong effect onto the expected signal. With the last improvements of our apparatus (cf. Chapter 4) this quantum efficiency is estimated to be roughly 50%: we will use this value in the numerical calculations.

A first simple example of situation that could be considered is the one consisting in an input state that can be written $|n, n\rangle_{\text{in}}$ with $n \geq 2$ ($n = 1$ being the “traditional” HOM experiment). This situation, where the input state is sometimes called a “twin-Fock state” has already been studied theoretically in [58] and tested experimentally in quantum optics [61]. We will present the expected results of an HOM-like experiment using this specific type of state in the Subsection 2.2.1

[58]: Campos et al. (1989), “Quantum-Mechanical Lossless Beam Splitter”

[61]: Yu Spasibko et al. (2014), “Interference of Macroscopic Beams on a Beam Splitter”

of this chapter.

However, we will see in Chapter 5 that our source does not directly provide such a state. Instead, our pair-creation process generates two separated atomic beams, that can be modelled with a so-called “two-mode squeezed vacuum state (TMS)”. The definition of this particular state will be reminded in Subsection 2.2.4, where we will study the interferences resulting of its use in a HOM-like experiment. It turns out that in certain aspects the two-mode squeezed state resembles another one, which is the “thermal” state. Even though the statistical properties of thermal states and TMSs are similar [62], these states are completely different: the first one is a single mode state, whereas the latter is a two-mode entangled state. Therefore we dedicate Subsection 2.2.3 to the study of interferences with thermal states.

[62]: Perrier et al. (2019), “Thermal Counting Statistics in an Atomic Two-Mode Squeezed Vacuum State”

This study will however need some theoretical prerequisites, that are given in Subsection 2.1.

2.1 Theoretical generalities

2.1.1 Notations used

In order to simplify the notations, we will use the following convention:

Notation 1 *When there is no ambiguity, we drop the “in” and “out” indices in the Dirac notation. Kets with capital letters will be referring to output channels. Likewise, kets with lowercase letters will refer to input channels:*

$$\left\{ \begin{array}{l} |n_1, n_2\rangle \equiv |n_1, n_2\rangle_{in} \\ |N_1, N_2\rangle \equiv |N_1, N_2\rangle_{out} \end{array} \right. \quad \begin{array}{l} (1.31) \\ (1.32) \end{array}$$

Concerning the probability distributions, we keep the following notations:

Notation 2 (Joint probability distribution) $k \in \{\text{in}, \text{out}\}$

We denote $P_k(N_1, N_2)$ the joint probability to have exactly N_1 particles at channel ch_1^k and N_2 particles at channel ch_2^k .

Notation 3 (Marginal distributions) $k \in \{\text{in, out}\}$, $i \in \{1, 2\}$

If we focus on a specific channel ch_i^k , we write the marginal probability of detection $\tilde{P}_i^k(N)$ such that:

$$\tilde{P}_1^k(N) = \sum_{N_2=0}^{\infty} P_k(N_1, N_2) \quad (1.33)$$

$$\tilde{P}_2^k(N) = \sum_{N_1=0}^{\infty} P_k(N_1, N_2) \quad (1.34)$$

If the situation is symmetric ($\tilde{P}_1^k = \tilde{P}_2^k$), we will simply write it \tilde{P}^k .

Notation 4 (Conditional probabilities) We use the standard writing $P_{\text{out}}(N_1, N_2 | n_1, n_2)$ to deal with the probability of finding the couple (N_1, N_2) at the output channels knowing that we have the couple (n_1, n_2) at the input channels.

Notation 5 (Finite quantum efficiency) When we need to take into account a finite quantum efficiency η , we simply add the index “ η ”: e.g. $\tilde{P}_\eta^{\text{out}}(N)$, $P_{\text{out}}^\eta(N_1, N_2)$...

2.1.2 Transformation of a quantum system by a beam splitter

Heisenberg and Schrödinger representations So far we have represented the beam splitter with an operator \underline{S} that transforms the creation/annihilation operators, the state vector of the system otherwise remaining fixed. We were thus working in a similar context as the *Heisenberg picture*. We could also consider the equivalent *Schrödinger picture* in order to study the effect of the beam splitter directly on a quantum system (either pure or not). We will need to introduce a different operator \hat{S} , that acts on the kets of the infinite dimensional *Fock space*.

It is important to notice that even though they refer to the same *physical* object (i.e. the actual beam splitter), and involve the same number of degrees of freedom, \underline{S} and \hat{S} are completely different mathematical entities. There is obviously an unequivocal relation between the two, which is provided by the Jordan-Schwinger map for the theory of quantum angular momentum in the Fock space [63, 64].

[63]: Jordan (1935), “Der Zusammenhang der symmetrischen und linearen Gruppen und das Mehrkörperproblem”

[64]: Schwinger (1952), “On angular momentum”

We will not run through the full derivation of the analytical expression of the Schrödinger representation of the beam splitter, for which the interested reader will find more detailed explanations in the references [58, 65]. We will however give here some useful results.

[58]: Campos et al. (1989), “Quantum-Mechanical Lossless Beam Splitter”

[65]: Yurke et al. (1986), “SU(2) and SU(1,1) Interferometers”

In the Jordan-Schwinger map, we introduce the angular-momenta operators:

$$\hat{L}_1 = \frac{1}{2} (\hat{a}_1^\dagger \hat{a}_2 + \hat{a}_2^\dagger \hat{a}_1) \quad (1.35a)$$

$$\hat{L}_2 = \frac{1}{2i} (\hat{a}_1^\dagger \hat{a}_2 - \hat{a}_2^\dagger \hat{a}_1) \quad (1.35b)$$

$$\hat{L}_3 = \frac{1}{2} (\hat{a}_1^\dagger \hat{a}_1 - \hat{a}_2^\dagger \hat{a}_2) \quad (1.35c)$$

for which it is very easy to check they satisfy the $\mathfrak{so}(3)$ Lie algebra relations:

$$[\hat{L}_i, \hat{L}_j] = i\epsilon_{ijk} \hat{L}_k \quad (1.36)$$

\hat{S} is defined without ambiguity by the relation:

$$\hat{b}_j = \hat{S}(\tau, \varphi_\tau, \varphi_\rho) \hat{a}_j \hat{S}^\dagger(\tau, \varphi_\tau, \varphi_\rho) \quad (1.37)$$

This leads to the analytical expression of \hat{S} [58]:

[58]: Campos et al. (1989), “Quantum-Mechanical Lossless Beam Splitter”

$$\hat{S}(\tau, \varphi_\tau, \varphi_\rho) = e^{-i(\varphi_\tau - \varphi_\rho)\hat{L}_3} e^{-2i \arccos[\sqrt{\tau}]\hat{L}_2} e^{-i(\varphi_\tau + \varphi_\rho)\hat{L}_3} \quad (1.38)$$

as well as its formal connection with \underline{S} , since Eq. (1.38) is written so that the parameters $(\tau, \varphi_\tau, \varphi_\rho)$ are the very same as those appearing in Eq. (I.II)!

We have now at our disposal a beam splitter operator that acts on the kets of the entire (and infinite dimensional) Fock space:

$$|\psi_{\text{out}}\rangle = \hat{S}^\dagger(\tau, \varphi_\tau, \varphi_\rho) |\psi_{\text{in}}\rangle \quad (1.39)$$

and, as usual in the Schrödinger picture, the transformation law of the modes is also known:

$$\begin{pmatrix} \hat{b}_1 \\ \hat{b}_2 \end{pmatrix} = \hat{S} \begin{pmatrix} \hat{a}_1 \\ \hat{a}_2 \end{pmatrix} \hat{S}^\dagger, \quad \begin{pmatrix} \hat{a}_1 \\ \hat{a}_2 \end{pmatrix} = \hat{S}^\dagger \begin{pmatrix} \hat{b}_1 \\ \hat{b}_2 \end{pmatrix} \hat{S} \quad (1.40)$$

Effect on a general density matrix The most general description of a quantum system is provided by a density matrix. We will denote ρ_{in} and ρ_{out} the density matrices of the many-body system before and after interacting with the beam splitter. With the bosonic basis states, those matrices can be written:

$$\left\{ \begin{array}{l} \hat{\rho}_{\text{in}} = \sum_{n_1, n_2, n'_1, n'_2=0}^{\infty} \rho_{\text{in}}(n_1, n_2; n'_1, n'_2) |n_1, n_2\rangle\langle n'_1, n'_2| \quad (\text{I.41a}) \\ \hat{\rho}_{\text{out}} = \sum_{N_1, N_2, N'_1, N'_2=0}^{\infty} \rho_{\text{out}}(N_1, N_2; N'_1, N'_2) |N_1, N_2\rangle\langle N'_1, N'_2| \quad (\text{I.41b}) \end{array} \right.$$

The diagonal components of the density matrix (the *populations*) contain information about the joint probability of a given couple of particles' numbers:

$$\left\{ \begin{array}{l} P_{\text{in}}(n_1, n_2) = \langle n_1, n_2 | \hat{\rho}_{\text{in}} | n_1, n_2 \rangle \quad (\text{I.42}) \\ P_{\text{out}}(N_1, N_2) = \langle N_1, N_2 | \hat{\rho}_{\text{out}} | N_1, N_2 \rangle \quad (\text{I.43}) \end{array} \right.$$

It is obviously the $\hat{S}(\tau, \varphi_\tau, \varphi_\rho)$ operator that relates $\hat{\rho}_{\text{out}}$ to $\hat{\rho}_{\text{in}}$. It acts as an evolution operator, which means:

$$\hat{\rho}_{\text{out}} = \hat{S}^\dagger \hat{\rho}_{\text{in}} \hat{S} \quad (\text{I.44})$$

By re-injecting (I.41a), we can expand the matrix elements of $\hat{\rho}_{\text{out}}$:

$$\rho_{\text{out}}(N_1, N_2; N'_1, N'_2) = \langle N_1, N_2 | \hat{\rho}_{\text{out}} | N'_1, N'_2 \rangle \quad (\text{I.45})$$

$$= \langle N_1, N_2 | \hat{S}^\dagger \hat{\rho}_{\text{in}} \hat{S} | N'_1, N'_2 \rangle \quad (\text{I.46})$$

$$= \sum_{n_1, n_2, n'_1, n'_2=0}^{\infty} \rho_{\text{in}}(n_1, n_2; n'_1, n'_2) \underbrace{\langle N_1, N_2 | \hat{S}^\dagger | n_1, n_2 \rangle}_{S_{N_1, N_2}^{(n_1, n_2)}} \underbrace{\langle n'_1, n'_2 | \hat{S} | N'_1, N'_2 \rangle}_{\left(S_{N'_1, N'_2}^{(n'_1, n'_2)} \right)^*} \quad (\text{I.47})$$

where we have introduced the matrix elements $S_{N_1, N_2}^{(n_1, n_2)}$ of \hat{S}^\dagger .

Let us take a look at the different exponential terms in Eq. (I.38): they do not share the same kind of contribution when applied to a Fock state. Indeed, the two exponentials of \hat{L}_3 contribute to a *phase shift*, while the exponential of \hat{L}_2 performs a *rotation* in the Fock space, and as we shall shortly see, the latter plays a crucial role in our topic of interest. Keeping this in mind, it is worth rewriting the matrix elements of \hat{S}^\dagger

so that those two types of contribution appear explicitly [58]:

$$S_{N_1, N_2}^{(n_1, n_2)} = \langle N_1, N_2 | e^{2i \arccos(\sqrt{\tau}) \hat{L}_2} | n_1, n_2 \rangle \times e^{i[\varphi_\tau(N_1 - n_2) + \varphi_\rho(N_1 - n_1)]} \quad (1.48)$$

[58]: Campos et al. (1989), “Quantum-Mechanical Lossless Beam Splitter”

Now, \hat{S} being unitary, all the terms in the sum (1.47) that do not satisfy the conservation of particles (1.8) are zero. N_1 and N_2 being fixed, we can simplify the quadruple sum into a double sum¹, and after a last reindexing step, we end up with the most general form for the joint output probability distribution:

¹: with $n_2 = N_1 + N_2 - n_1$ and $n_2' = N_1 + N_2 - n_1'$

Theorem 2 (Output probabilities for a general input)

Considering a beam splitter represented by an operator $\hat{S} \in \text{SU}(2)$, and a general density matrix $\hat{\rho}_{in}$ at the input channels of this beam splitter,

$$\text{with } \begin{cases} N = N_1 + N_2 \\ n_2 = N - n_1 \\ R_{N_1, N_2}^{(n_1, n_2)} \triangleq \langle N_1, N_2 | e^{2i \arccos(\sqrt{\tau}) \hat{L}_2} | n_1, n_2 \rangle \\ \gamma_k(N_1, N_2) \triangleq \sum_{n_1=0}^N R_{N_1, N_2}^{(n_1, n_2)} R_{N_1, N_2}^{(n_1+k, n_2-k)} \rho_{in}(n_1, n_2; n_1+k, n_2-k) \end{cases}$$

we have:
$$P_{out}(N_1, N_2) = \sum_{k=-N}^N \gamma_k(N_1, N_2) e^{-ik(\varphi_\tau - \varphi_\rho)} \quad (1.49)$$

Let us finish this quite lengthy work with a couple of remarks:

1. it is important to realise that (1.49) is not a useless (although elegant) expression of the joint probability distribution: it can be used for numerical computation. It only requires a formula for the $R_{N_1, N_2}^{(n_1, n_2)}$ (given in the following paragraph);
2. in this case, which was intended to be kept as general as possible, we observe on Eq. (1.49) that the phase difference $\varphi_\tau - \varphi_\rho$ is important. That being said, some special cases exists, where it does not play any role. For instance, with a “pure” statistical mixture –meaning a diagonal density operator– only the $k = 0$ term is non-zero, and we have

$$P_{out}(N_1, N_2) = \sum_{n_1=0}^N P_{in}(n_1, n_2) \underbrace{\left(R_{N_1, N_2}^{(n_1, n_2)} \right)^2}_{P_{out}(N_1, N_2 | n_1, n_2)} \quad (1.50)$$

The interpretation of this equation is very clear: without coherence between the different terms of the input state, there is no interference contribution and we simply sum the conditional probabilities.

Pure Fock states are a particular case of diagonal density operator, and therefore phases are also of no consequence for their resulting output probabilities¹. We will give additional details about it in the following paragraph.

¹: it would not be true in the case of a pure state which is not a *number* state.

Fock states at the input In Theorem 2, we have quite surreptitiously introduced the quantity $R_{N_1, N_2}^{(n_1, n_2)}$. The previous equation (1.50) revealed that it is actually the *amplitude of probability* to measure $|N_1, N_2\rangle_{\text{out}}$ at the output, knowing that we have $|n_1, n_2\rangle_{\text{in}}$ at the input.

Indeed, in the scenario of a pure Fock state $|n_1, n_2\rangle$ at the input, we have

$$\rho_{\text{in}}(n'_1, n'_2; n''_1, n''_2) = \delta_{n'_1}^{n''_1} \delta_{n'_2}^{n''_2} \delta_{n'_1}^{n''_1} \delta_{n'_2}^{n''_2} \quad (1.51)$$

(δ_i^j being the usual Kronecker symbol), $\hat{\rho}_{\text{in}}$ is therefore diagonal in the Fock basis (with just a single 1 somewhere on the diagonal). We are left with the simplest possible case, with just a single element in (1.49) which is not zero, which gives

$$P_{\text{out}}(N_1, N_2) = P_{\text{out}}(N_1, N_2 | n_1, n_2) = \left(R_{N_1, N_2}^{(n_1, n_2)} \right)^2 \quad (1.52)$$

At this stage, we understand the great importance of the R coefficients. We have an analytical expression thereof [58], as a function of the beam splitter's transmittance:

[58]: Campos et al. (1989), "Quantum-Mechanical Lossless Beam Splitter"

$$R_{N_1, N_2}^{(n_1, n_2)} = \sum_{k=0}^{n_1} (-1)^{n_1-k} \sqrt{\binom{N_1}{k} \binom{N_2}{n_1-k} \binom{n_1}{k} \binom{n_2}{N_1-k}} \tau^{2k+n_2-N_1} (1-\tau)^{n_1+N_1-2k} \quad (1.53)$$

Interesting alternative expressions of $R_{N_1, N_2}^{(n_1, n_2)}$, involving Jacobi and Gegenbauer polynomials can be found in reference [58], though Eq. (1.53) is enough for numerical evaluations.

It also satisfies useful symmetry relations:

$$(n_2 \leq N_1 < n_1) \Rightarrow R_{N_1, N_2}^{(n_1, n_2)} = (-1)^{N_1 - n_1} R_{n_1, n_2}^{(N_1, N_2)} \quad (1.54a)$$

$$(n_1 \leq N_1 < n_2) \Rightarrow R_{N_1, N_2}^{(n_1, n_2)} = R_{n_2, n_1}^{(N_2, N_1)} \quad (1.54b)$$

$$(N_1 < n_1, n_2) \Rightarrow R_{N_1, N_2}^{(n_1, n_2)} = (-1)^{N_1 - n_1} R_{N_2, N_1}^{(n_2, n_1)} \quad (1.54c)$$

This is interesting since most of the inputs that we will consider will be *symmetric*, and therefore this symmetry will hold at the output! The set of equations (1.54) combined with Eq. (1.52) indeed gives:

$$P_{\text{out}}(N_1, N_2 | n_1, n_2) = P_{\text{out}}(N_2, N_1 | n_2, n_1) \quad (1.55)$$

whatever transmittance τ is.

2.2 Classification of the interference patterns for different input states

We are now mathematically equipped to undertake the study of the joint output probability distribution, in various scenarios. Just as in the original 2-particles HOM effect, the matter of the discernibility of the quantum systems that we set at the input will necessarily be discussed, as it completely changes the results. The problem of the finite quantum efficiency will also be considered.

The cases of the twin-Fock states, and the coherent states have already been studied before, and can be found in the literature. However, as far as we know, the results that we will demonstrate concerning the thermal, and two-mode squeezed states are new.

2.2.1 Twin-Fock states and mixing with vacuum

i: in particular, the mathematical treatment of the finite quantum efficiency.

We shall begin with the study of the interference effects of twin-Fock states on a beam splitter. Those states read $|n, n\rangle_{\text{in}}$. Even though we are not technically able to prepare those states in our experiment, many results that will be established here will be re-used in the more complex contexts that follow. It will also be sort of an introduction to calculation methods that we will use again afterwards¹

Indiscernible case: twin-Fock states

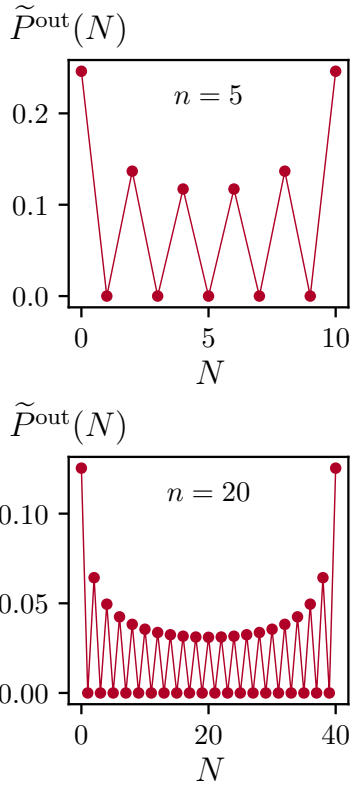


Figure 1.9: Marginal probability distributions for twin-Fock states at the input of a 50-50 beam splitter. n is the number of particles at each input channel. Since $2n$ particles are present in the interferometer, N takes a value between 0 and $2n$.

[66]: Bollinger et al. (1996), “Optimal Frequency Measurements with Maximally Correlated States”

[67]: Gerry (2000), “Heisenberg-Limit Interferometry with Four-Wave Mixers Operating in a Nonlinear Regime”

50-50 beam splitter Considering pure Fock states at the input, in the specific case for which we have $n_1 = n_2 = n$, and with a 50-50 beam splitter, we can do better than the Eq. (1.53). Indeed, the number of particles probability distribution assumes the form:

$$\begin{cases} P_{\text{out}}(2k, 2n - 2k) = \frac{1}{2^n} \sqrt{\binom{2k}{k} \binom{2n - 2k}{n - k}} \\ P_{\text{out}}(2k + 1, 2n - 2k - 1) = 0 \end{cases} \quad (1.56)$$

The situation is completely symmetric, and all the physics can be described by restricting ourselves to the marginal distribution \tilde{P}^{out} (which are the same on both channels). A numerical example is given in Figure 1.9. We can highlight two remarkable properties for the distribution of probability Eq. (1.56):

1. The asymmetrical outputs are much more probable than the other ones (for instance $|0, 2n\rangle$ and $|2n, 0\rangle$ are the most likely output states). This is a manifestation of bosons’ *herd instinct*: they tend to leave the beam splitter on the same side, just as in the two-photon HOM effect case. That distinctive feature explains why this distribution is traditionally named *U-shape distribution* (or sometimes *discrete arcsine law*).
2. Perhaps even more surprisingly, odd output numbers are forbidden! Just like in the two-particle HOM effect, this is a consequence of the symmetry of the input many-body bosonic wavefunction.

Remark 1.3 Regarding the second property above, we could be tempted to define a *parity* operator (e.g. as in references [66, 67])

$$\hat{\mathcal{P}} \triangleq (-1)^{\hat{N}} = \exp(i\pi \hat{b}^\dagger \hat{b}) \quad (1.57)$$

and study its expectation values to evaluate the indistinguishability of the particles at the input. However, it is not something we will be able to observe with our atomic apparatus. So far we have implicitly assumed to have an ideal detector, that can count the correct number of particles with 100% probability. In our experiment we use a detector with roughly 50% detectivity, and we can easily convince ourselves that information about parity vanishes extremely fast with non-perfect quantum efficiency! This effect is visible in Figure 1.12.

Dependence with the reflectivity Eventually, it is interesting to investigate the effect of the reflection/transmission coefficients to the output probabilities. Without the $\rho = \tau$ hypothesis, the analytical simplifications are no longer possible, and we are left with Eq. (1.53) to perform numerical calculations.

Nonetheless, we can have in mind the physical picture for which the 50-50 beam splitter maximises the mixing between modes \hat{a}_1 and \hat{a}_2 , and therefore quantum interference effects. We have already observed (Figure 1.9) that the output probability distribution for the 50-50 beam splitter is quite broad. On the other hand, in the limiting cases for which $\tau = 0$ or $\tau = 1$, the two input modes are completely independent, and we trivially have the state $|n, n\rangle_{out}$ at the output with 100% probability.

Thus, it is quite natural to think that τ has a significant effect on the *width* of the distribution. Concerning the mean number of particles detected, as long as we keep a twin-Fock state $|n, n\rangle_{in}$, each detector will measure $\tau \times n + (1 - \tau) \times n = n$ particles on average: in fact Eq. (1.55) with $n_1 = n_2 = n$ directly implies the symmetry of the output probability distribution (which is a stronger result). For given n and τ , we define the width of the distribution with its standard deviation:

$$\sigma_n(\tau) = \sqrt{\sum_{N=0}^{2n} (N - n)^2 \tilde{P}^{out}(N, \tau)} \quad (1.58)$$

Empirically, one can numerically check that the “normalised” width $\frac{\sigma_n(\tau)}{n}$ is weakly dependent of n , at least as long as $n \geq 4$.

The problem of the finite detectivity Let us imagine the experiment described in Figure 1.11. Following notation 5, we will denote \tilde{P}_γ^{out} the marginal probability distribution after detection.

Assuming that an experimental run returns the number N , due to detection losses, many situations could have led to it:

- the experimentalist could have been lucky, and detected the N particles exactly scattered by the beam splitter into the observed channel, without losing a single one. The probability p_0 of such an event is simple:

$$p_0 = \tilde{P}^{out}(N) \times \eta^N$$

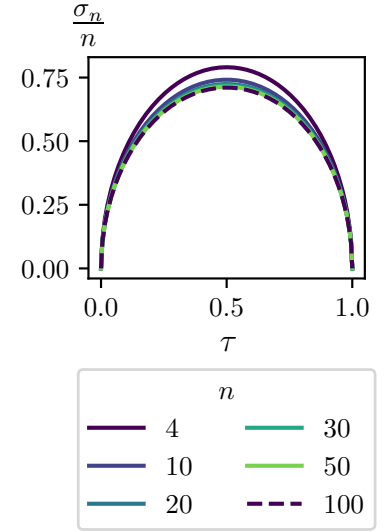


Figure 1.10: Normalised width of the marginal output distributions, plotted as a function of the transmission coefficient τ , for various values of n .

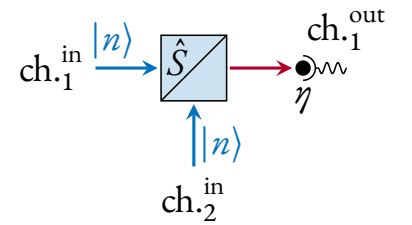


Figure 1.11: Twin-Fock state on a 50-50 beam splitter experiment. The experimentalist uses a detector with finite quantum efficiency η , and collects data from a single output channel, in order to infer the marginal output probability distribution out of statistical averages. At each experimental run, the detector returns a number $N \in \llbracket 0, 2n \rrbracket$.

- ▶ the beam splitter could have scattered $N + 1$ particles in the observed channel, and one of those were lost at the detection: the probability for a particle not to be detected is $(1 - \eta)$. Any of the $N + 1$ particles could have been lost, therefore there is $N + 1$ possibilities for this scenario. The associated probability is

$$p_1 = (N + 1) \times \tilde{P}^{\text{out}}(N + 1) \times \eta^N \times (1 - \eta)$$

- ▶ more generally, the beam splitter could have scattered $N + q$ particles towards the detector, which only counted N of those. The number of possibilities in such a case is obviously combinatorial:

$$p_q = \binom{N + q}{q} \times \tilde{P}^{\text{out}}(N + q) \times \eta^N \times (1 - \eta)^q$$

We are now back to the 50-50 beam splitter case. As it has just been mentioned in the previous remark, if we want a proper prediction of the expected experimental signal, we must take into account the finite quantum efficiency η of the detector.

It is clear that we simply have $\tilde{P}_\eta^{\text{out}}(N) = \sum_q p_q$ which gives the formula:

$$\tilde{P}_\eta^{\text{out}}(N) = \sum_{q=0}^{2n-N} \tilde{P}^{\text{out}}(N + q) \eta^N (1 - \eta)^q \binom{N + q}{q} \quad (1.59)$$

where we recall that $\tilde{P}^{\text{out}}(N)$ is the discrete arcsine law (1.56), which is well-known. Some numerical examples are plotted in Figure 1.12. We can notice how fast the visibility of evenness of the output state washes out when η decreases.

Distinguishable case: mixing with the vacuum In the previous paragraph, we examined a situation where the particles at the input of the beam splitter were perfectly indiscernible. Once again, in our study's framework it mainly means three things:

1. the particles are of the *same kind* (e.g. same atoms, same elementary particles...);
2. the particles share the *same internal state* (e.g. same frequency for photons, same atomic state...);
3. the particles have the same *spatial wave function*;
4. the particles at both input channels *interact with the beam splitter simultaneously*;

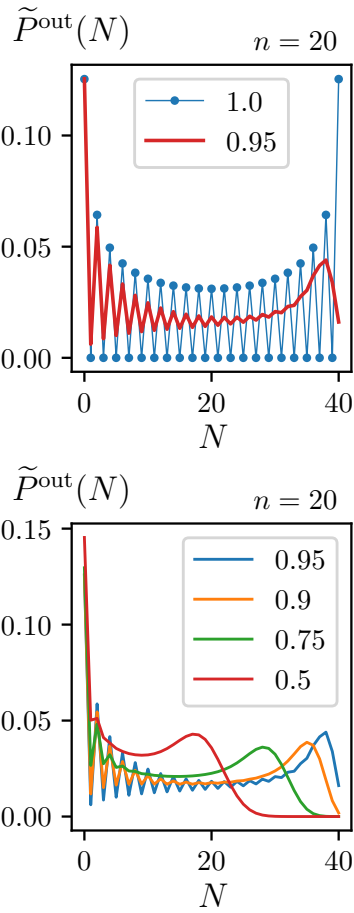


Figure 1.12: Marginal probability distributions for twin-Fock states at the input of a 50-50 BS, using detectors with finite quantum efficiency η (given in the legends). The first plot (on top) compares the ideal detector ($\eta = 1$) to an almost perfect one ($\eta = 0.95$). The second plot (bottom) shows the expected signal, for various values of $\eta < 1$.

We have already discussed that the latter item is often the most important one, in the prospect of an experiment. The delay between the interactions of both inputs with the beam splitter is generally the parameter of control of the degree of indiscernibility in the experiment. It actually makes sense: if two particles arrive on the beam splitter at very different times, they cannot be considered indiscernible since we could label them “first one” and “second one”.

When interacting with the beam splitter, the two modes of the twin-Fock state are therefore perfectly indiscernible. The analogous scenario with complete discernibility between the two input modes would be to send n particles on ch._1^{in} , wait some time, send n particles on ch._2^{in} , and look at the resulting output probabilities. Hence, the input states of interest are $|n, 0\rangle_{\text{in}}$ and $|0, n\rangle_{\text{in}}$.

There is no quantum interference here, $P_{\text{out}}(N_1, N_2|n, 0)$ is actually just a biased¹ Bernoulli trial [68] situation that can be treated classically.

¹: biased if $\tau \neq \frac{1}{2}$

With a perfect detector Again, if no particles are lost during the detection, we can restrict ourselves to the marginal probability distribution, since $N_2 = n - N_1$. The solution of the Bernoulli trial problem is well known:

$$\begin{cases} \tilde{P}^{\text{out}}(N \in \llbracket 0, n \rrbracket | n, 0) = \binom{n}{N} \tau^N (1 - \tau)^{n-N} & \text{(1.60a)} \\ \tilde{P}^{\text{out}}(N \in \llbracket 0, n \rrbracket | 0, n) = \binom{n}{N} \tau^{n-N} (1 - \tau)^N & \text{(1.60b)} \end{cases}$$

they are of course equal for a 50-50 beam splitter.

The final output probability distribution is then obtained by summing all the cases for which the total number of particles received by the detector is equal to N , weighed by the crossed probability:

$$\tilde{P}^{\text{out}}(N \in \llbracket 0, 2n \rrbracket) = \sum_{N'=0}^N \tilde{P}^{\text{out}}(N'|n, 0) \cdot \tilde{P}^{\text{out}}(N - N'|0, n) \quad \text{(1.61)}$$

with $\tilde{P}^{\text{out}}(N' > n|n, 0) = \tilde{P}^{\text{out}}(N - N' < 0|0, n) = 0$

It is very clear –with the numerical example in Figure 1.13– that this distribution is completely different from the one resulting from the interferences of indiscernible twin-Fock states. We notice that the indiscernible distribution is much wider: it is in fact quite general, when making indiscernible bosons interfere on a 50-50 beam splitter we expect

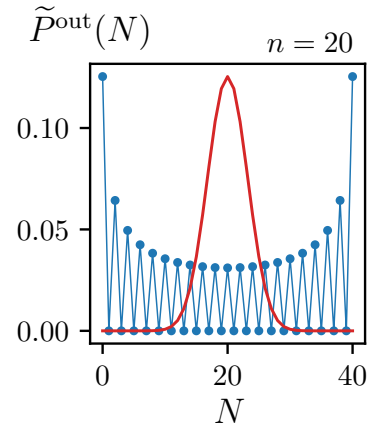


Figure 1.13: (in red) Output probability distribution resulting from the succession of the two equally populated Fock states $|n, 0\rangle$ and $|0, n\rangle$ mixed with vacuum at a 50-50 beam splitter. We have also plotted the equivalent indiscernible twin-Fock state (in blue) for comparison.

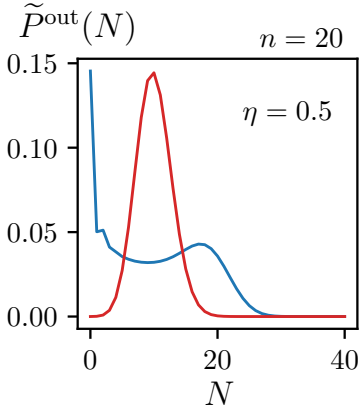


Figure 1.14: Same plot as Figure 1.13, but taking into account a finite quantum efficiency $\eta = 0.5$

to observe a broadening of the output probability distribution.

With a finite quantum efficiency We can now apply the same type of trick as in the paragraph 1 to take into account the finite detectivity. We can see in Figure 1.14 that even with a realistic detector, the distinguishable and indiscernible cases remain very different.

2.2.2 Coherent states

In the rest of this chapter we will deal with distributions consisting in infinite quantum superpositions of Fock states $\sum_{n \geq 0} a_n |n\rangle$, and study the resulting interference pattern after interaction with a 50-50 beam splitter.

In order to be able to discuss the quantum nature of an output probability distribution, it is interesting to first take a look at what happens in a semi-classical context, provided by Glauber’s coherent states [69, 70]. At the end of the chapter, we will discuss the relevant observable to use so as to distinguish a quantum state from a semi-classical state.

[69]: Glauber (1963), “The Quantum Theory of Optical Coherence”
 [70]: Glauber (1963), “Coherent and Incoherent States of the Radiation Field”

Theorem 3 (Transformation of coherent states by a beam splitter)

$|\alpha\rangle_{\hat{a}_1}$ and $|\beta\rangle_{\hat{a}_2}$ being two coherent states placed at the inputs of a beam splitter with transmission coefficient $\sqrt{\tau}e^{i\varphi_\tau}$, and reflection coefficient $\sqrt{\rho}e^{i\varphi_\rho}$. The output state expressed in the \hat{b} modes basis is also a product of coherent states, that writes:

$$|\psi\rangle = |\alpha\sqrt{\tau}e^{i\varphi_\tau} + \beta\sqrt{\rho}e^{i\varphi_\rho}\rangle_{\hat{b}_1} |\beta\sqrt{\tau}e^{-i\varphi_\tau} - \alpha\sqrt{\rho}e^{-i\varphi_\rho}\rangle_{\hat{b}_2} \tag{1.62}$$

Proof We consider a general beam splitter, with the notation of Eq. (1.11) for its parametrisation. Let us first consider two coherent states $|\alpha\rangle_{\hat{a}_1}$ and $|\beta\rangle_{\hat{a}_2}$, placed at the inputs of a beam splitter, and let us write $|\psi\rangle$ the corresponding ket. We denote $\mathcal{N} = \exp\left(-\frac{|\alpha|^2 + |\beta|^2}{2}\right)$ the normalisation factor.

$$\begin{aligned} \frac{|\psi\rangle}{\mathcal{N}} &= \frac{|\alpha\rangle_{\hat{a}_1} |\beta\rangle_{\hat{a}_2}}{\mathcal{N}} \\ &= \exp(\alpha\hat{a}_1^\dagger - \alpha^* \hat{a}_1) \exp(\beta\hat{a}_2^\dagger - \beta^* \hat{a}_2) |vac\rangle \end{aligned}$$

$[\alpha \hat{a}_1^\dagger - \alpha^* \hat{a}_1, \beta \hat{a}_2^\dagger - \beta^* \hat{a}_2] = 0$, we can therefore merge the exponentials, and express the inner terms in the \hat{b} modes basis:

$$= \exp \left(\alpha [\sqrt{\tau} e^{i\varphi_\tau} \hat{b}_1^\dagger - \sqrt{\rho} e^{-i\varphi_\rho} \hat{b}_2^\dagger] - \alpha^* [\sqrt{\tau} e^{-i\varphi_\tau} \hat{b}_1 - \sqrt{\rho} e^{i\varphi_\rho} \hat{b}_2] \right. \\ \left. + \beta [\sqrt{\rho} e^{i\varphi_\rho} \hat{b}_1^\dagger + \sqrt{\tau} e^{-i\varphi_\tau} \hat{b}_2^\dagger] - \beta^* [\sqrt{\rho} e^{-i\varphi_\rho} \hat{b}_1 + \sqrt{\tau} e^{i\varphi_\tau} \hat{b}_2] \right) |vac\rangle$$

$\forall (x, y) \in \mathbb{C}^2$, $[x \hat{b}_1^\dagger - x^* \hat{b}_1, y \hat{b}_2^\dagger - y^* \hat{b}_2] = 0$, we therefore re-factorise the expression above, and split the exponential:

$$= \exp \left([\alpha \sqrt{\tau} e^{i\varphi_\tau} + \beta \sqrt{\rho} e^{i\varphi_\rho}] \hat{b}_1^\dagger - [\alpha^* \sqrt{\tau} e^{-i\varphi_\tau} + \beta^* \sqrt{\rho} e^{-i\varphi_\rho}] \hat{b}_1 \right) \\ \times \exp \left([\beta \sqrt{\tau} e^{-i\varphi_\tau} - \alpha \sqrt{\rho} e^{-i\varphi_\rho}] \hat{b}_2^\dagger - [\beta^* \sqrt{\tau} e^{i\varphi_\tau} - \alpha^* \sqrt{\rho} e^{i\varphi_\rho}] \hat{b}_2 \right) |vac\rangle$$

and we identify two coherent states, with respect to the output modes (the normalisation factor is the same):

$$|\psi\rangle = |\alpha \sqrt{\tau} e^{i\varphi_\tau} + \beta \sqrt{\rho} e^{i\varphi_\rho}\rangle_{\hat{b}_1} |\beta \sqrt{\tau} e^{-i\varphi_\tau} - \alpha \sqrt{\rho} e^{-i\varphi_\rho}\rangle_{\hat{b}_2}$$

Definition 1 (Poisson distribution)
The discrete probability distribution of Poisson with mean value λ is given by:

$$P_p(n; \lambda) \triangleq e^{-\lambda} \frac{\lambda^n}{n!} \quad (1.63)$$

its standard deviation is also λ .

This is a fairly strong result, but it is not surprising either: classical states are stable under the action of a beam splitter. Thus, the output probabilities are Poisson distributions.

In particular, in the **symmetric beam splitter case**, the joint probability distribution is:

$$P_{\text{out}}(N_1, N_2) = P_p \left(N_1; \frac{|\alpha e^{i\varphi_\tau} + \beta e^{i\varphi_\rho}|^2}{2} \right) P_p \left(N_2; \frac{|\beta e^{-i\varphi_\tau} - \alpha e^{-i\varphi_\rho}|^2}{2} \right) \quad (1.64)$$

$$= P_p(N_1; \langle n^1 \rangle + I_{\alpha, \beta}[\Delta\varphi]) P_p(N_2; \langle n^1 \rangle - I_{\alpha, \beta}[\Delta\varphi]) \quad (1.65)$$

where:

- ▶ $\langle n^1 \rangle = \frac{\langle \hat{n}_1 \rangle + \langle \hat{n}_2 \rangle}{2}$ is the single-channel average number of particles;
- ▶ $\Delta\varphi = \varphi_\tau - \varphi_\rho$ is the relative phase;
- ▶ $I_{\alpha, \beta}[\Delta\varphi] = \Re(\alpha \beta^* e^{i\Delta\varphi})$ is the interference term;

In fact, all of this is just a modern rewriting of Michelson's interferometer physics. In particular, just like in the classical version of the two-particle HOM effect, we find a phase dependence of the joint probability distribution. We will see in [Subsection 2.2.4](#) that this is not the

case with a TMS state. During an experiment, one could therefore test the effect of the phase to check the classical nature of state that is involved.

What would happen in a distinguishable case? Just as it was done previously with the Fock states, we should study the successive mixing of each of the two coherent states with the vacuum, and then sum up all of their possible combinations.

Vacuum is just the coherent state with average value 0, so the mixing with vacuum of a coherent state is very simple, since the interference term is 0. We denote $P_{\text{out}}^{1\alpha}$ output distribution after mixing of the coherent state $|\alpha\rangle$ with the vacuum. Since the beam splitter is symmetric, the input channel choice does not matter.

so, with Eq. (1.65)

$$\left\{ P_{\text{out}}^{1\alpha}(N_1, N_2) = P_p \left(N_1; \frac{|\alpha|^2}{2} \right) P_p \left(N_2; \frac{|\alpha|^2}{2} \right) \right. \quad (1.66a)$$

$$\left. P_{\text{out}}^{1\beta}(N_1, N_2) = P_p \left(N_1; \frac{|\beta|^2}{2} \right) P_p \left(N_2; \frac{|\beta|^2}{2} \right) \right. \quad (1.66b)$$

then we just have:

$$P_{\text{out}}(N_1, N_2) = \sum_{N'_1=0}^{N_1} \sum_{N'_2=0}^{N_2} P_{\text{out}}^{1\alpha}(N'_1, N'_2) P_{\text{out}}^{1\beta}(N_1 - N'_1, N_2 - N'_2) \quad (1.67)$$

$$= \overbrace{\left[\sum_{N'_1=0}^{N_1} P_p \left(N'_1; \frac{|\alpha|^2}{2} \right) P_p \left(N_1 - N'_1; \frac{|\beta|^2}{2} \right) \right]}^{\Sigma} \times \left[\sum_{N'_2=0}^{N_2} P_p \left(N'_2; \frac{|\alpha|^2}{2} \right) P_p \left(N_2 - N'_2; \frac{|\beta|^2}{2} \right) \right] \quad (1.68)$$

now we can simplify both sums, e.g.:

$$\Sigma = e^{-\frac{|\alpha|^2 + |\beta|^2}{2}} \frac{1}{2^{N_1}} \sum_{N'_1=0}^{N_1} \frac{|\alpha|^{2N'_1} |\beta|^{2(N_1 - N'_1)}}{N'_1! (N_1 - N'_1)!} \quad (1.69)$$

we identify a binomial identity

$$= e^{-\frac{|\alpha|^2 + |\beta|^2}{2}} \frac{1}{N_1!} \left(\frac{|\alpha|^2 + |\beta|^2}{2} \right)^{N_1} \quad (1.70)$$

and finally:

$$P_{\text{out}}(N_1, N_2) = P_p \left(N_1; \frac{|\alpha|^2 + |\beta|^2}{2} \right) P_p \left(N_2; \frac{|\alpha|^2 + |\beta|^2}{2} \right) \quad (1.71)$$

$$= P_p(N_1; \langle n^1 \rangle) P_p(N_2; \langle n^1 \rangle) \quad (1.72)$$

this is very similar to Eq. (1.65), but with the interference term being 0 (which is reasonable). We actually added intensities: everything works as if we were considering sources to be incoherent between them. This is also exactly the result (1.65) when the phase is randomised during an experiment.

With a finite quantum efficiency The finite detectivity case is actually included in the previous study, thanks to the following remarkable property of the Poisson distribution:

Theorem 4 (Stability of the Poisson distribution with finite detectivity)

We consider the Poisson distribution of average population ν . The corresponding distribution taking into account the finite quantum efficiency η of the detector

1. *is also a Poisson distribution*
2. *its average population is $\eta\nu$*

Proof

$$P_p^\eta(n; \nu) = \sum_{m=n}^{\infty} \binom{m}{n} \eta^n (1-\eta)^{m-n} e^{-\nu} \frac{\nu^m}{m!}$$

expanding the combinatorial term:

$$= \frac{(\eta\nu)^n}{n!} e^{-\nu} \sum_{m=n}^{\infty} \frac{[(1-\eta)\nu]^{m-n}}{(m-n)!}$$

we can make the sum start from $m = 0$:

$$= \frac{(\eta\nu)^n}{n!} e^{-\nu} \underbrace{\sum_{m=0}^{\infty} \frac{[(1-\eta)\nu]^m}{m!}}_{e^{(1-\eta)\nu}}$$

$$P_p^\eta(n; \nu) = P_p(n; \eta\nu)$$

■

Thus, the simple transformation

$$\begin{cases} \alpha \mapsto \sqrt{\eta} \alpha \\ \beta \mapsto \sqrt{\eta} \beta \end{cases}$$

leads to the corresponding joint probability distribution, taking into account the finite quantum efficiency of the detector.

2.2.3 Thermal states

Before treating the case of the TMS state (which is for us the most important one), let us take a look at the thermal one, which has close statistical properties. By “thermal” we actually refer to states for which the probability $P(n)$ to measure n particles follows the *Boltzmann distribution*.

Definition 2 (Thermal state) *We call thermal a monomode state consisting in the following statistical mixture:*

$$\hat{\rho}_{th} = (1 - |\alpha|^2) \sum_{n=0}^{\infty} |\alpha|^{2n} |n\rangle\langle n|, \quad \begin{cases} \alpha \in \mathbb{C} \\ |\alpha| < 1 \end{cases} \quad (1.73)$$

We have indeed

$$P_{th}(n) = (1 - |\alpha|^2) |\alpha|^{2n} \quad (1.74)$$

i: because it can be assimilated to the Boltzmann factor: $|\alpha|^2 \sim e^{-\beta E}$, in the Boltzmann distribution of statistical mechanics. n would play the role of the energy, which is also consistent.

and $|\alpha|^2$ is sometimes called *effective temperature*¹. It is very easy to check that the average population ν of a thermal state is:

$$\nu = \frac{|\alpha|^2}{1 - |\alpha|^2} \quad (1.75)$$

and reciprocally

$$|\alpha| = \sqrt{\frac{\nu}{1 + \nu}} \quad (1.76)$$

It is equally easy to prove that its local second-order degree of coherence is equal to 2:

$$\frac{\langle n^2 \rangle - \langle n \rangle^2}{\langle n \rangle^2} = g_{loc}^{(2)} = 2 \quad (1.77)$$

In fact, the n^{th} -order local correlation function of a thermal source is known [71] and given by

$$g_{loc}^{(n)} = n! \quad (1.78)$$

[71]: Liu et al. (2009), “Nth-Order Coherence of Thermal Light”

Remark 1.4 We will see later that this particular property of the local correlations is also true with two-mode squeezed states.

This is a major difference with semi-classical coherent states, where the correlation function is known to be equal to one.

The second difference being the statistics itself: the coherent state has a Poissonian statistics, whereas that of thermal states is a power law.

We often prefer to write the probability distribution in terms of the average population:

$$P_{tb}(n) = \frac{\nu^n}{(1 + \nu)^{n+1}} \quad (1.79)$$

Let us now investigate what happens when we make thermal states interfere:

Indiscernible case The scenario of two indiscernible thermal states is complex to treat analytically.

With a perfect detector The corresponding density matrix reads:

$$\hat{\rho} = \sum_{n,m=0}^{\infty} \frac{P_{tb}(n)P_{tb}(m)}{n! m!} (\hat{a}_1^\dagger)^n (\hat{a}_2^\dagger)^m |0\rangle\langle 0| (\hat{a}_1)^n (\hat{a}_2)^m \quad (1.80)$$

then we must express the parameters of the beam splitter to expand \hat{a}_i and \hat{a}_i^\dagger in terms of \hat{b}_i and \hat{b}_i^\dagger . The density matrix is not diagonal, therefore the probability distribution a priori depends on the phase (cf. Theorem 2). Thus we should take into account the phases φ_τ and φ_ρ of the beam splitter during the expansion:

$$\left\{ \begin{aligned} \hat{a}_1 &= \frac{1}{\sqrt{2}} \left(e^{-i\varphi_\tau} \hat{b}_1 - e^{i\varphi_\rho} \hat{b}_2 \right) & (1.81a) \\ \hat{a}_2 &= \frac{1}{\sqrt{2}} \left(e^{-i\varphi_\rho} \hat{b}_1 + e^{i\varphi_\tau} \hat{b}_2 \right) & (1.81b) \end{aligned} \right.$$

The calculations being rather heavy, we will just give here a summary of what happens when they are done:

- the binomial expansion of the \hat{a}_i and \hat{a}_i^\dagger terms adds four finite sums to the expression:

$$\hat{\rho} = \sum_{n,m=0}^{\infty} \sum_{p_1,p_2=0}^n \sum_{q_1,q_2=0}^m (\dots) \tag{1.82}$$

Many phase terms are present.

- then, the joint probability is given by $P_{\text{out}}(N_1, N_2) = \langle N_1, N_2 | \hat{\rho} | N_1, N_2 \rangle$, which provides the additional conditions:

$$\begin{cases} m + m = N_1 + N_2 & (1.83a) \\ p_1 + q_1 = N_1 & (1.83b) \\ p_2 + q_2 = N_1 & (1.83c) \end{cases}$$

Therefore, three (out of six) sums disappear. Thankfully all the phase terms cancel out.

- the remaining sums are still difficult to compute (I did not found a satisfying final simplification). However, if we study particular cases we find:

$$\begin{cases} P_{\text{out}}(0, N) = \frac{1}{(1 + \nu)^2} \left(\frac{\nu}{1 + \nu} \right)^N = P_{tb}(0)P_{tb}(N) & (1.84a) \\ P_{\text{out}}(1, N) = \frac{1}{(1 + \nu)^2} \left(\frac{\nu}{1 + \nu} \right)^{N+1} = P_{tb}(1)P_{tb}(N) & (1.84b) \\ P_{\text{out}}(2, N) = \frac{1}{(1 + \nu)^2} \left(\frac{\nu}{1 + \nu} \right)^{N+2} = P_{tb}(2)P_{tb}(N) & (1.84c) \end{cases}$$

$P_{\text{out}}^\gamma(0, N)$ is easy to compute (the binomial sums are trivial), $P_{\text{out}}^\gamma(1, N)$ and $P_{\text{out}}^\gamma(2, N)$ are more difficult (there are some non-trivial sums to compute) but it is still doable.

With the pattern of equations (1.84), we can make the fairly solid conjecture that

$$P_{\text{out}}(N_1, N_2) \stackrel{?}{=} P_{tb}(N_1)P_{tb}(N_2) \tag{1.85}$$

If it is true, everything works as if no beam splitter were present... It is not surprising to find no phase dependence, as the thermal states are the quantum analogue of incoherent fields. We have plotted this profile in [Figure 1.15](#).

This distribution is wider than in the distinguishable case (which is not surprising when dealing with indiscernible boson). But the most remarkable feature of this joint distribution is that it is separable, and that the probability of a given outcome depends only on the total

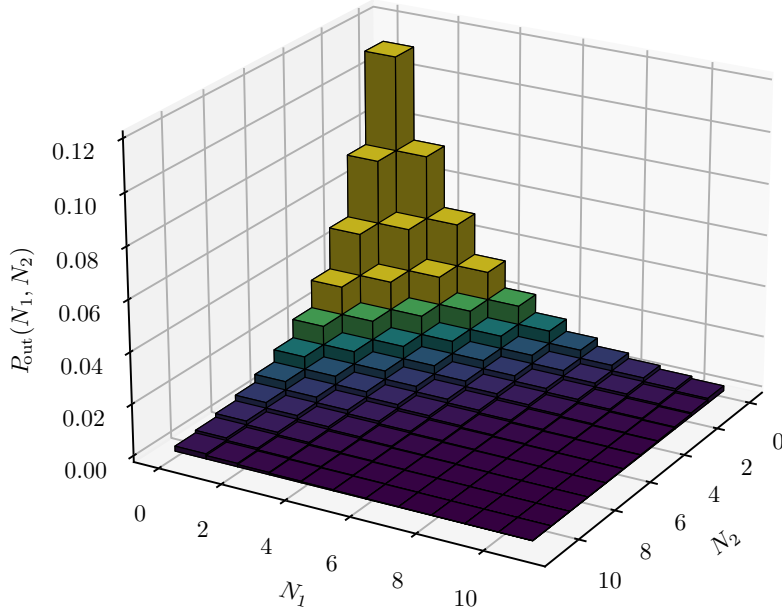


Figure 1.15: Output joint probability distribution for indistinguishable thermal states interfering at a 50-50 beam splitter. We selected an average population per mode $\nu = 2$. We find $P_{\text{out}}(0, 0) \approx 0.111$

number of detected particles. Indeed:

$$P_{\text{out}}(N_1, N_2) = \frac{1}{1 + \nu} P_{tb}(N_1 + N_2) \quad (1.86)$$

We will see in the subsection dedicated to the treatment of TMS states that this property does not hold: this is a distinction criterion between the TMS state (entangled) and the thermal states (not entangled).

With a finite quantum efficiency We have seen in the paragraph above that when two indiscernible thermal distributions of particles interfere on a beam splitter, they behave as if no beam splitter were present. We can therefore solve the question of the finite efficiency very quickly by using the following property of thermal states:

Theorem 5 (Stability of the thermal distribution with finite detectivity)

We consider the thermal distribution of average population ν . The corresponding distribution taking into account the finite quantum efficiency η of the detector:

1. *is also thermal*

2. its average population is $\eta\nu$

Proof first let us recall two useful mathematical identities

$$\left\{ \begin{array}{l} \frac{d^n x^m}{dx^n} = \frac{m!}{(m-n)!} x^{m-n} \quad (1.87a) \\ \frac{d^n}{dx^n} \left[\frac{1}{1-xy} \right] = \frac{n! y^n}{(1-xy)^{n+1}} \quad (1.87b) \end{array} \right.$$

$$P_{tb}^\eta(n) = \sum_{m=n}^{\infty} \binom{m}{n} \eta^n (1-\eta)^{m-n} \frac{\nu^m}{(1+\nu)^{m+1}}$$

using (1.87a) with $x = (1-\eta)$:

$$= \frac{\eta^n}{n!} \frac{1}{1+\nu} \sum_{m=n}^{\infty} \frac{d^n}{d(1-\eta)^n} \left[(1-\eta)^m \left(\frac{\nu}{1+\nu} \right)^m \right]$$

we can make the sum start from $m = 0$ since the first terms would be 0 due to the derivative. We can then switch the sum and the derivative (because the series is geometric):

$$= \frac{\eta^n}{n!} \frac{1}{1+\nu} \frac{d^n}{d(1-\eta)^n} \left[\frac{1}{1 - (1-\eta) \frac{\nu}{1+\nu}} \right]$$

and finally, using (1.87b):

$$P_{tb}^\eta(n) = \frac{(\eta\nu)^n}{(1+\eta\nu)^{n+1}}$$

The resulting joint probability distribution is therefore the same as before (with a perfect detector), just doing the transformation

$$\nu \mapsto \eta\nu$$

Distinguishable case The scenario of distinguishable thermal states is simpler.

With a perfect detector As usual, the first thing to do in the distinguishable case is to study the effect of the mixing of a thermal state with the vacuum. We work in the Heisenberg picture. The corre-

sponding density operator reads:

$$\hat{\rho} = \sum_{n=0}^{\infty} P_{tb}(n) |n\rangle_{\hat{a}_1} \langle n|_{\hat{a}_1} \otimes |0\rangle_{\hat{a}_2} \langle 0|_{\hat{a}_2} \quad (\text{I.88})$$

and we denote $P_{\text{out}}^1(N_1, N_2)$ the output probability distribution.

$$P_{\text{out}}^1(N_1, N_2) = {}_{\hat{b}_1 \hat{b}_2} \langle N_1 N_2 | \hat{\rho} | N_1, N_2 \rangle_{\hat{b}_1 \hat{b}_2} \quad (\text{I.89})$$

$\hat{\rho}$ is a diagonal density operator, thus we already know¹ that the phases of the beam splitter will not contribute to the output probabilities. We can take $\varphi_\tau = 0$ and $\varphi_\rho = \pi$ to simplify the calculations. Therefore, using

$$\hat{a}_1 = \frac{1}{\sqrt{2}} (\hat{b}_1 + \hat{b}_2) \quad (\text{I.90})$$

we can rewrite $\hat{\rho}$ in the \hat{b} -modes basis:

$$\hat{\rho} = \sum_{n=0}^{\infty} \frac{P_{tb}(n)}{2^n n!} (\hat{b}_1^\dagger + \hat{b}_2^\dagger)^n |0\rangle\langle 0| (\hat{b}_1 + \hat{b}_2)^n \quad (\text{I.91})$$

$$= \sum_{n=0}^{\infty} \frac{P_{tb}(n)}{2^n n!} \sum_{k,p=0}^n \binom{n}{k} \binom{n}{p} (\hat{b}_1^\dagger)^k (\hat{b}_2^\dagger)^{n-k} |0\rangle\langle 0| (\hat{b}_1)^p (\hat{b}_2)^{n-p} \quad (\text{I.92})$$

$$= \sum_{n=0}^{\infty} \frac{P_{tb}(n)}{2^n n!} \sum_{k,p=0}^n \binom{n}{k} \binom{n}{p} \sqrt{k! p! (n-k)! (n-p)!} |k, n-k\rangle\langle p, n-p| \quad (\text{I.93})$$

we inject this in Eq. (I.89), the scalar products gives $k = p = N_1$ and $n = N_1 + N_2$. We find:

$$P_{\text{out}}^1(N_1, N_2) = \frac{P_{tb}(N_1 + N_2)}{2^{N_1 + N_2} (N_1 + N_2)!} \binom{N_1 + N_2}{N_1}^2 N_1! N_2! \quad (\text{I.94})$$

$$P_{\text{out}}^1(N_1, N_2) = \frac{P_{tb}(N_1 + N_2)}{2^{N_1 + N_2}} \binom{N_1 + N_2}{N_1} \quad (\text{I.95})$$

The total probability distribution in the distinguishable case is given by the sum of the results when we repeat a mixing with vacuum experiment twice:

$$P_{\text{out}}(N_1, N_2) = \sum_{n_1=0}^{N_1} \sum_{n_2=0}^{N_2} P_{\text{out}}^1(n_1, n_2) P_{\text{out}}^1(N_1 - n_1, N_2 - n_2) \quad (\text{I.96})$$

$$= \sum_{n_1=0}^{N_1} \sum_{n_2=0}^{N_2} \binom{n_1 + n_2}{n_1} \binom{N_1 + N_2 - n_1 - n_2}{N_1 - n_1} \frac{1}{2^{N_1 + N_2}} \frac{1}{(1 + \nu)^2} \left(\frac{\nu}{1 + \nu} \right)^{N_1 + N_2} \quad (\text{I.97})$$

¹: with the second remark on Theorem 2

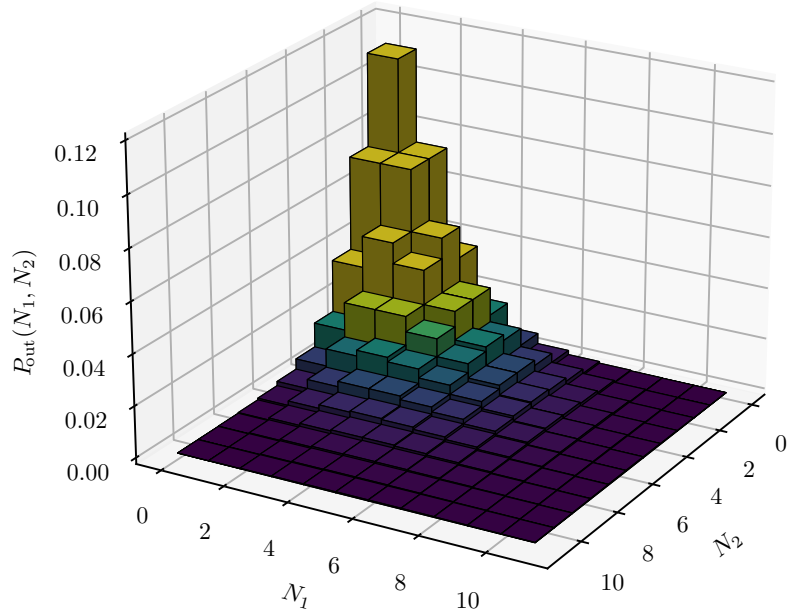


Figure 1.16: Output joint probability distribution for distinguishable thermal states interfering at a 50-50 beam splitter. We selected an average population per mode $\nu = 2$. We find $P_{\text{out}}(0, 0) \approx 0.111$

i: Vandermonde’s identity is

$$\sum_{k=0}^p \binom{m}{k} \binom{n}{p-k} = \binom{m+n}{p} \quad (1.98)$$

Thanks to Vandermonde’s identityⁱ, we can check that:

$$\sum_{n_1=0}^{N_1} \sum_{n_2=0}^{N_2} \binom{n_1+n_2}{n_1} \binom{N_1+N_2-n_1-n_2}{N_1-n_1} = (1+N_1+N_2) \binom{N_1+N_2}{N_1} \quad (1.99)$$

giving:

$$P_{\text{out}}(N_1, N_2) = \frac{(1+N_1+N_2)!}{N_1!N_2!} \frac{1}{2^{N_1+N_2}} \frac{1}{(1+\nu)^2} \left(\frac{\nu}{1+\nu}\right)^{N_1+N_2} \quad (1.100)$$

As always, a numerical example is provided in Figure 1.16. As expected for a distinguishable case, the distribution is quite narrow, and symmetric.

With a finite quantum efficiency The fundamental relation to take the finite detectivity effect into account is still:

$$P_{\text{out}}^\eta(N_1, N_2) = \sum_{m_1=N_1}^{\infty} \sum_{m_2=N_2}^{\infty} \binom{m_1}{N_1} \binom{m_2}{N_2} \eta^{N_1+N_2} (1-\eta)^{m_1+m_2-N_1-N_2} P_{\text{out}}(m_1, m_2) \quad (1.101)$$

which is a priori very difficult to calculate. Actually, it turns out that it can be simplified. So far we have always considered the losses to occur after the interaction with the beam splitter, and before the detection

stage, but with our model – which does not take into account the details of the losses mechanism – we are completely allowed to consider the losses to occur even *before* the application of the beam splitter. In that case, the fact that we are dealing with two *independent* statistical mixtures, and the stability of the thermal distribution with a finite quantum efficiency (Theorem 8) ensures that the treatment of the problem is equivalent to the one with perfect detectors, just replacing the average population of both distribution ν by $\eta\nu$. Therefore:

$$P_{\text{out}}^{\eta}(N_1, N_2; \nu) = P_{\text{out}}(N_1, N_2; \eta\nu) \quad (1.102)$$

We also checked – using a symbolic computation software such as Wolfram Mathematica[®] – that this simplification also occurs by “naively” computing Eq. (1.101). We finally verified numerically that Eq. (1.102) makes sense concerning the mean number of particles that are measured: if we measure $2 \times \nu$ particles on average with a perfect detector, $2 \times \eta\nu$ should be measured on average with a detector of quantum efficiency η .

2.2.4 Two-mode squeezed vacuum state

Motivation As it will be discussed in Chapter 5, our experimental platform offers the opportunity to generate correlated atomic multi-mode fields, for which we expect to witness strong nonclassical effects. In particular, the model that we generally use to describe what our atomic source is producing is the “*two-mode squeezed vacuum state* (TMS)” [52, 72], which is defined as follows:

Definition 3 (two-mode squeezed vacuum state) *a and b being two modes of a bosonic field, we call two-mode squeezed vacuum state and write $|TMS\rangle$ the quantum state:*

$$|TMS\rangle = \sqrt{1 - |\alpha|^2} \sum_{n=0}^{\infty} \alpha^n |n\rangle_a |n\rangle_b, \quad \begin{cases} \alpha \in \mathbb{C} \\ |\alpha| < 1 \end{cases} \quad (1.103)$$

Such a state is obviously entangled, and it involves two modes that can be spatially separated.

If one traces over one of the two modes, it trivially leads to a thermal state (power law) of parameter α .

[52]: Gerry et al. (2005), *Introductory Quantum Optics*

[72]: Heidmann et al. (1987), “Observation of Quantum Noise Reduction on Twin Laser Beams”

It is perfectly feasible to reproduce the analogue of the HOM experiment (discussed in the first section of this chapter) but replacing the two individual atoms –placed at the inputs of the beam splitter– by the two entangled modes a and b of a TMS. One can notice that a TMS is actually a coherent superposition of many twin Fock states, weighted by coefficients following a thermal distribution. Therefore, the output probability distribution resulting of the interferences of a TMS is simply given by the sum of those obtained with twin-Fock states, correctly weighted.

Probability distribution of a TMS (no BS) Before diving into the calculation of the expected results of a HOM-like experiment performed with a TMS, there is a first interesting calculation that we can consider: what distribution of probability do we expect if we measure a TMS with a finite quantum efficiency detector? This question is of special interest for us because even if we have theoretical reasons to believe that our source is indeed emitting two-mode squeezed states¹, it is crucial to gather a maximum of experimental clues indicating that it is *indeed* the case, as well as the validity range of this model. Some of these clues are using the correlations properties of a TMS: those will be discussed and presented in Chapter 5. The statistical distribution of the number of atoms detected when the TMS is measured *directly* is another clue.

1: those arguments will be given in Chapter 5

If the quantum efficiency is perfect, this probability distribution is trivial: Born's rule for expectation values, applied to (1.103), immediately gives

$$\begin{cases} P(n, n) = (1 - |\alpha|^2)|\alpha|^{2n} & (1.104a) \\ P(n_1, n_2 \neq n_1) = 0 & (1.104b) \end{cases}$$

There is a perfect correlation between the number of atoms (a visualisation of this distribution is given in Figure 1.20a on page 54).

We can give an analytical expression to the probability distribution taking into account the finite quantum efficiency of the detector. However, to do this we will need to introduce two rather unusual² functions:

2: in physics at least...

Definition 4 (Rising factorial) We call “rising factorial” (or “Pochhammer function”) the function defined by:

$$\begin{aligned} \mathbb{C} &\rightarrow \mathbb{C} \\ z &\mapsto z^{\bar{n}} = \underbrace{z(z+1)(z+2)\cdots(z+n-1)}_{n \text{ terms}} \end{aligned}$$

The rising factorial being defined, we can introduce the *hypergeometric functions*:

Definition 5 (Hypergeometric function) We call “hypergeometric function” and denote ${}_2F_1$ the complex function defined by:

$$\begin{aligned} {}_2F_1 &: \{z \in \mathbb{C} / |z| < 1\} \rightarrow \mathbb{C} \\ z &\mapsto {}_2F_1(a, b; c; z) = \sum_{n=0}^{\infty} \frac{a^{\bar{n}} b^{\bar{n}} z^n}{c^{\bar{n}} n!} \end{aligned}$$

At first sight, the above-mentioned definition may seem a bit pointless, since it involves an infinite summation. In fact, it is very useful for numerical evaluation, because it is well implemented in computational libraries (for example `scipy` in Python 🐍) allowing for very fast calculations.

Then we have:

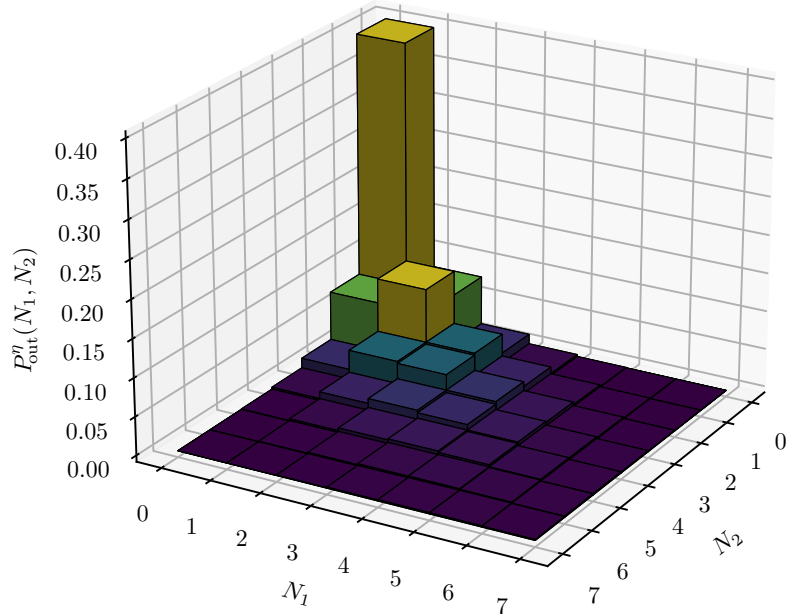
Theorem 6 (Probability distribution of a TMS)

Considering a TMS with an average population per mode $\nu = \frac{|\alpha|^2}{1-|\alpha|^2}$.

When measured with a detector of finite quantum efficiency, the probability $P_\eta(n_1, n_2)$ to count n_1 particles in the first mode and n_2 particles in the second mode is symmetric, and given by:

$$\begin{aligned} P_\eta(n_1, n_2 < n_1) &= (1 - |\alpha|^2) |\alpha|^{2n_1} \eta^{n_1+n_2} (1 - \eta)^{n_1-n_2} \\ &\times \binom{n_1}{n_2} {}_2F_1(n_1 + 1, n_1 + 1; n_1 - n_2 + 1; (1 - \eta)^2 |\alpha|^2) \end{aligned} \tag{1.105}$$

Figure 1.17: Expected joint probability distribution of a TMS state, when it is measured *directly* (no beam splitter). Here the average population per mode is $\nu = 2$ and the detectivity $\eta = 0.5$. We can notice the remarkable property $P_\eta(1, 1) > P_\eta(0, 1) = P_\eta(1, 0)$. This is a legacy of the “diagonal” shape of this distribution when we consider the bare TMS state (i.e. $\eta = 1$, cf. Figure 1.20a).



Proof As usual:

$$P_\eta(n_1, n_2) = \sum_{m_1=n_1}^{\infty} \sum_{m_2=n_2}^{\infty} \binom{m_1}{n_1} \binom{m_2}{n_2} \eta^{n_1+n_2} (1-\eta)^{m_1+m_2-n_1-n_2} P(m_1, m_2)$$

the symmetry of the above expression immediately gives $P_\eta(n_1, n_2) = P_\eta(n_2, n_1)$, so let us assume $n_1 \geq n_2$. Due to (1.104), we can restrict the double summation to the $m_1 = m_2 = m$ domain, and since $m \geq \max(n_1, n_2) = n_1$ we have:

$$\begin{aligned} P_\eta(n_1, n_2) &= \sum_{m=n_1}^{\infty} \binom{m}{n_1} \binom{m}{n_2} \eta^{n_1+n_2} (1-\eta)^{2m-n_1-n_2} (1-|\alpha|^2) |\alpha|^{2m} \\ &= \eta^{n_1+n_2} (1-|\alpha|^2) \sum_{m=n_1}^{\infty} \frac{(m!)^2 (1-\eta)^{2m-n_1-n_2} |\alpha|^{2m}}{n_1! n_2! (m-n_1)! (m-n_2)!} \end{aligned}$$

we can put the constant term on the left, and re-index the sum:

$$\frac{P_\eta(n_1, n_2)}{\eta^{n_1+n_2} (1-|\alpha|^2)} = \sum_{m=0}^{\infty} \frac{[(n_1+m)!]^2}{n_1! n_2! m! (m+n_1-n_2)!} (1-\eta)^{2m+n_1-n_2} |\alpha|^{2m+2n_1}$$

to keep simple notations we set:

$$\begin{cases} z = (1 - \eta)^2 |\alpha|^2 \\ \Pi = \frac{P_\eta(n_1, n_2)}{\eta^{n_1+n_2} (1 - |\alpha|^2) (1 - \eta)^{n_1-n_2} |\alpha|^{2n_1}} \end{cases}$$

leaving

$$\Pi = \sum_{m=0}^{\infty} \frac{[(n_1 + m)!]^2}{\underbrace{n_1! n_2! (m + n_1 - n_2)!}_{u_m}} \frac{z^m}{m!}$$

regarding [Definition 5](#) of hypergeometric functions we are almost done, we just need to give u_n the appropriate shape. Let us notice that

$$(n_1 + m)! = n_1! \times (n_1 + 1) \times \dots \times n_1 + m = n_1! (n_1 + 1)^{\bar{m}}$$

and therefore also

$$(m + n_1 - n_2)! = (n_1 - n_2)! (n_1 - n_2 + 1)^{\bar{m}}$$

$$\begin{aligned} u_n &= \frac{(n_1 + 1)^{\bar{m}} (n_1 + m)!}{n_2! (n_1 - n_2)! (n_1 - n_2 + 1)^{\bar{m}}} \\ &= \binom{n_1}{n_2} \frac{(n_1 + 1)^{\bar{m}} (n_1 + m)!}{(n_1 - n_2 + 1)^{\bar{m}} n_1!} \\ u_n &= \binom{n_1}{n_2} \frac{[(n_1 + 1)^{\bar{m}}]^2}{(n_1 - n_2 + 1)^{\bar{m}}} \end{aligned}$$

and putting the pieces together we have:

$$\Pi = \binom{n_1}{n_2} {}_2F_1(n_1 + 1, n_1 + 1; n_1 - n_2 + 1; z)$$

We just have to use

$$|\alpha|^2 = \frac{\nu}{1 + \nu}$$

to recover the expression [Eq. \(1.105\)](#). ■

We give a visualisation of this probability distribution in [Figure 1.17](#). Obtaining it experimentally is feasible, but requires a lot of statistical averaging. In [Chapter 5](#) we will perform the complete analysis of a dataset that we recently obtained. Unfortunately the statistics (~ 800 files) is not large enough to obtain a faithful picture of the distribution calculated above. In a near future we will be able to gather data again, and

hopefully obtain enough statistics to evaluate the measured $P_\gamma(n_1, n_2)$. However, we will see that we were able to measure experimentally the *marginal* distribution.

Now in the following paragraphs, we will study the probability distributions resulting from the interaction of the two modes of the TMS with a beam splitter. In the indistinguishable case, the two modes are mixed with each other, giving birth to interferences. In the distinguishable case each of the two modes is mixed with the vacuum, one interaction following the other. **We will always assume the beam splitter to be 50-50.**

Interferences on a beam splitter: indiscernible case

With a perfect detector If we assume the beam splitter to be symmetric (50-50), the two-mode output probability distribution can be calculated exactly:

Theorem 7 (Output probability distribution for a TMS state interfering at a 50-50 beam splitter)

Given (Q_n) the sequence defined by:

$$k \in \mathbb{N}, \quad \begin{cases} Q_{2k} = \sqrt{1 - |\alpha|^2} \left(\frac{|\alpha|}{2}\right)^{2k} \frac{(2k)!}{k!^2} \\ Q_{2k+1} = 0 \end{cases} \quad (1.106)$$

we have:

$$P_{out}(N_1, N_2) = Q_{N_1} \cdot Q_{N_2} \quad (1.107)$$

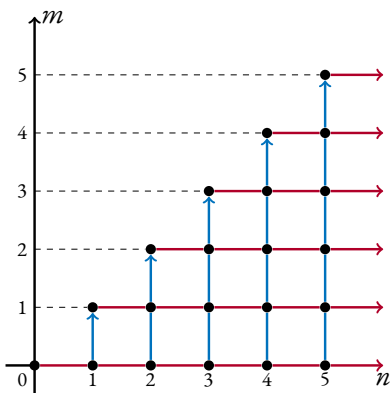


Figure 1.18: Graphical proof of the equivalence of two double summation patterns. The sum is evaluated over the black vertices, and we can choose to sum along the blue lines, or the red ones.

$$\sum_{n=0}^{\infty} \sum_{m=0}^n \bullet = \sum_{m=0}^{\infty} \sum_{n=m}^{\infty} \bullet = \sum_{m=0}^{\infty} \sum_{p=n-m=0}^{\infty} \bullet$$

Proof Following the notations introduced in Eq. (1.11) for the matrix representation of the beam splitter, we have:

$$\underline{\hat{S}}^\dagger = \frac{1}{\sqrt{2}} \begin{pmatrix} e^{-i\varphi_\tau} & -e^{i\varphi_\rho} \\ e^{-i\varphi_\rho} & e^{i\varphi_\tau} \end{pmatrix}$$

which therefore gives the fundamental coupling relations:

$$\begin{cases} \hat{a}_1 = \frac{1}{\sqrt{2}} [e^{-i\varphi_\tau} \hat{b}_1 - e^{i\varphi_\rho} \hat{b}_2] \\ \hat{a}_2 = \frac{1}{\sqrt{2}} [e^{-i\varphi_\rho} \hat{b}_1 + e^{i\varphi_\tau} \hat{b}_2] \end{cases}$$

therefore, since $[\hat{b}_1, \hat{b}_2] = 0$:

$$\begin{aligned} \hat{a}_1^\dagger \hat{a}_2^\dagger &= \frac{1}{2} \left[e^{i(\varphi_\tau + \varphi_\rho)} (\hat{b}_1^\dagger)^2 - e^{-i(\varphi_\tau + \varphi_\rho)} (\hat{b}_2^\dagger)^2 + \cancel{\hat{b}_1^\dagger \hat{b}_2^\dagger} - \cancel{\hat{b}_2^\dagger \hat{b}_1^\dagger} \right] \\ &= \frac{1}{2} \left[e^{i\phi} (\hat{b}_1^\dagger)^2 - e^{-i\phi} (\hat{b}_2^\dagger)^2 \right] \end{aligned}$$

where we have introduced

$$\phi = \varphi_\tau + \varphi_\rho$$

then we can express the *TMS* in the \hat{b} modes basis. Indeed, starting with its definition (1.103) in which we inject Eq. (1.5):

$$\begin{aligned} \frac{|TMS\rangle}{\sqrt{1-|\alpha|^2}} &= \sum_{n=0}^{\infty} \alpha^n |n, n\rangle \\ &= \sum_{n=0}^{\infty} \frac{\alpha^n}{n! 2^n} \left(e^{i\phi} (\hat{b}_1^\dagger)^2 - e^{-i\phi} (\hat{b}_2^\dagger)^2 \right)^n |vac\rangle \\ &= \sum_{n=0}^{\infty} \sum_{m=0}^n \left(\frac{\alpha}{2} \right)^n \frac{1}{n!} \binom{n}{m} \\ &\quad \times e^{im\phi} (\hat{b}_1^\dagger)^{2m} e^{i(n-m)(\pi-\phi)} (\hat{b}_2^\dagger)^{2(n-m)} \\ \frac{|TMS\rangle}{\sqrt{1-|\alpha|^2}} &= \sum_{n=0}^{\infty} \sum_{m=0}^n \left(\frac{\alpha}{2} \right)^n \frac{1}{m!(n-m)!} \\ &\quad \times e^{im\phi} (\hat{b}_1^\dagger)^{2m} e^{i(n-m)(\pi-\phi)} (\hat{b}_2^\dagger)^{2(n-m)} \end{aligned}$$

Then we transform the double summation with the little trick explained graphically in Figure 1.18:

$$|TMS\rangle = \sqrt{1-|\alpha|^2} \sum_{m,p=0}^{\infty} \left(\frac{\alpha}{2} \right)^{m+p} \frac{\left(e^{i\phi} (\hat{b}_1^\dagger)^2 \right)^m \left(e^{i(\pi-\phi)} (\hat{b}_2^\dagger)^2 \right)^p}{m! p!} |vac\rangle$$

Thus written in the output modes basis, the *TMS* has the remarkable property of being a separable state!

$$|TMS\rangle = |\psi_1^{out}\rangle \otimes |\psi_2^{out}\rangle$$

with

$$\begin{cases} |\psi_1^{out}\rangle = (1-|\alpha|^2)^{\frac{1}{4}} \sum_{n=0}^{\infty} \left(\frac{\alpha}{2} \right)^n \frac{\sqrt{(2n)!}}{n!} (e^{i\phi})^n |2n, 0\rangle \\ |\psi_2^{out}\rangle = (1-|\alpha|^2)^{\frac{1}{4}} \sum_{n=0}^{\infty} \left(\frac{\alpha}{2} \right)^n \frac{\sqrt{(2n)!}}{n!} (e^{i(\pi-\phi)})^n |0, 2n\rangle \end{cases}$$

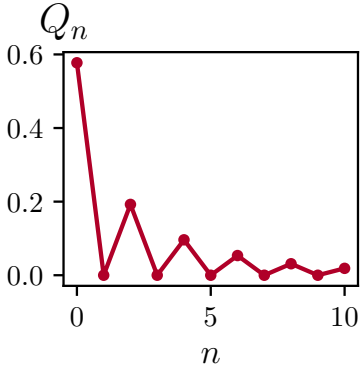


Figure 1.19: Numerical evaluation of the Q_n sequence, taken for $\nu = 2$.

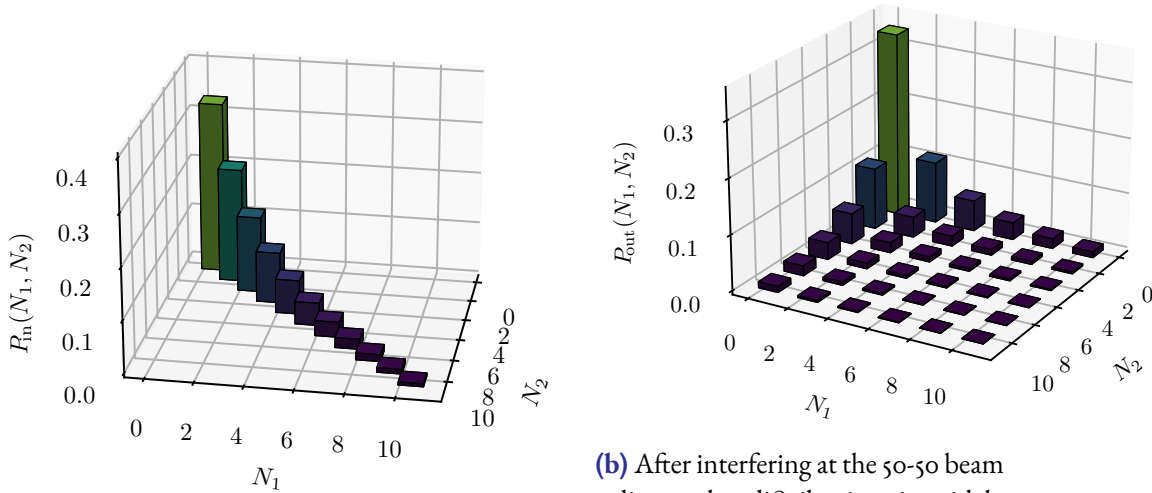
$|\psi_1^{out}\rangle$ and $|\psi_2^{out}\rangle$ only differ in the output mode and a in phase inside the sum. Since we are interested in the probabilities of detections, these phases do not play any role:

$$P_{out}(N_1, N_2) = Q_{N_1} \cdot Q_{N_2}$$

with,

$$k \in \mathbb{N}, \begin{cases} Q_{2k} = \sqrt{1 - |\alpha|^2} \left(\frac{|\alpha|}{2}\right)^{2k} \frac{(2k)!}{k!^2} \\ Q_{2k+1} = 0 \end{cases}$$

P_{out} is separable, and obviously symmetric. One can notice (for instance in Figure 1.19) that the key feature of the n -particle Hong-Ou-Mandel (nHOM) effect is preserved: no *odd* number of particles can be detected.



(a) Input TMS probability distribution. The two modes are perfectly correlated and only $P_{in}(N, N)$ takes non-zero values.

(b) After interfering at the 50-50 beam splitter, the distribution is widely spread over the (N_1, N_2) domain. However, all configurations involving an odd number of particles are forbidden.

Figure 1.20: Effect of the 50-50 beam splitter on a TMS (here $\nu = 2$).

With a finite quantum efficiency Even with finite detectivity, the distribution remains separable:

$$\begin{cases} P_{out}^\eta(N_1, N_2) = Q_{N_1}^\eta \cdot Q_{N_2}^\eta & (1.108a) \\ Q_N^\eta = \sum_{m=N}^{\infty} Q_m \eta^N (1 - \eta)^{m-N} \binom{m}{N} & (1.108b) \end{cases}$$

We can derivate an analytic solution for this sum, using again the hypergeometric functions. Let us indeed prove the following result:

Theorem 8 (Output probability distribution for a TMS interfering at a 50-50 beam splitter, with finite quantum efficiency)

Given η the quantum efficiency of the detector, and α the effective temperature of the TMS, we denote:

$$\begin{cases} z = \frac{|\alpha|}{2}(1 - \eta) \\ u_p = {}_2F_1 \left[p + \frac{1}{2}, p + \frac{1}{2}; \frac{1}{2}; 4z^2 \right] \\ v_p = {}_2F_1 \left[p + \frac{3}{2}, p + \frac{3}{2}; \frac{3}{2}; 4z^2 \right] \end{cases} \quad (I.I09)$$

we have:

$$P_{out}^\eta(N_1, N_2) = Q_{N_1}^\eta \cdot Q_{N_2}^\eta \quad (I.I10)$$

with:

$$\begin{cases} Q_{2p}^\eta = \left(\frac{\eta |\alpha|}{2} \right)^{2p} \frac{(2p)!}{(p!)^2} \sqrt{1 - |\alpha|^2} u_p \\ Q_{2p+1}^\eta = z \left(\frac{\eta |\alpha|}{2} \right)^{2p+1} (2p+2) \frac{(2p+2)!}{(p+1)!^2} \sqrt{1 - |\alpha|^2} v_p \end{cases} \quad (I.I11)$$

Proof In the view of the parity issue for the index of Q_N , it is useful to separate even and odd cases in the calculation:

if $N=2p$:

$$Q_{2p}^\eta = \eta^{2p} \sum_{m=2p}^{\infty} \binom{m}{2p} (1 - \eta)^{m-2p} Q_m$$

all the odd terms of the sum being 0, we can remove them:

$$= \eta^{2p} \sum_{m=p}^{\infty} \binom{2m}{2p} (1 - \eta)^{2m-2p} Q_{2m}$$

we inject the expression (1.106) of Q_{2m} :

$$= \eta^{2p} \sqrt{1 - |\alpha|^2} \sum_{m=p}^{\infty} \binom{2m}{2p} (1 - \eta)^{2m-2p} \left(\frac{|\alpha|}{2}\right)^{2m} \frac{(2m)!}{(m!)^2}$$

we reindex the sum, making it start from 0:

$$= \eta^{2p} \sqrt{1 - |\alpha|^2} \sum_{m=0}^{\infty} \binom{2m+2p}{2p} (1 - \eta)^{2m} \left(\frac{|\alpha|}{2}\right)^{2m+2p} \frac{(2m+2p)!}{(m+p)!^2}$$

expanding the binomial term:

$$= \left(\frac{\eta|\alpha|}{2}\right)^{2p} \frac{\sqrt{1 - |\alpha|^2}}{(2p)!} \overbrace{\sum_{m=0}^{\infty} \left[\frac{(2m+2p)!}{(m+p)!} \right]^2 \frac{1}{(2m)!} \left[\frac{|\alpha|}{2} (1 - \eta) \right]^{2m}}^T$$

The final infinite series T may seem rather uninviting, but in fact we can rearrange this to make it more orderly:

for convenience we denote

$$z = \frac{|\alpha|}{2} (1 - \eta)$$

we can force the apparition of rising factorial terms in T :

$$\begin{aligned} T &= \left(\frac{(2p)!}{p!}\right)^2 \sum_{m=0}^{\infty} \left[\frac{(2m+2p)!}{(2p)!} \right]^2 \left[\frac{p!}{(m+p)!} \right]^2 \frac{z^{2m}}{(2m)!} \\ &= \left(\frac{(2p)!}{p!}\right)^2 \sum_{m=0}^{\infty} \left[\frac{(2p+1)^{\overline{2m}}}{(p+1)^{\overline{m}}} \right]^2 \frac{z^{2m}}{(2m)!} \end{aligned}$$

in addition:

$$\begin{aligned} (2p+1)^{\overline{2m}} &= \overbrace{(2p+1)(2p+2)(2p+3)(2p+4)\cdots(2p+2m)}^{2m \text{ terms}} \\ &= 2^{2m} \left(p + \frac{1}{2}\right) (p+1) \left(p + \frac{3}{2}\right) (p+2) \cdots (p+m) \end{aligned}$$

grouping the reds together and the blues together:

$$= 2^{2m} \left(p + \frac{1}{2}\right)^{\overline{m}} (p+1)^{\overline{m}}$$

thus:

$$\frac{(2p+1)^{\overline{2m}}}{(p+1)^{\overline{m}}} = 2^{2m} \left(p + \frac{1}{2}\right)^{\overline{m}}$$

the same reasoning provides:

$$\begin{aligned} (2m)! &= 2m(2m-1)(2m-2)(2m-3)\cdots 1 \\ &= 2^{2m} m \left(m - \frac{1}{2}\right) (m-1) \left(m - \frac{3}{2}\right) \cdots \frac{1}{2} \\ (2m)! &= 2^{2m} m! \left(\frac{1}{2}\right)^{\overline{m}} \end{aligned}$$

and finally assembling up the pieces together:

$$\begin{aligned} T &= \left(\frac{(2p)!}{p!}\right)^2 \sum_{m=0}^{\infty} \frac{\left[\left(p + \frac{1}{2}\right)^{\overline{m}}\right]^2}{\left(\frac{1}{2}\right)^{\overline{m}}} 2^{2m} \frac{z^{2m}}{m!} \\ &= \left(\frac{(2p)!}{p!}\right)^2 {}_2F_1\left(p + \frac{1}{2}, p + \frac{1}{2}; \frac{1}{2}; 4z^2\right) \end{aligned}$$

we end up with an analytic formula:

$$Q_{2p}^{\eta} = \left(\frac{\eta|\alpha|}{2}\right)^{2p} \frac{(2p)!}{(p!)^2} \sqrt{1-|\alpha|^2} {}_2F_1\left[p + \frac{1}{2}, p + \frac{1}{2}; \frac{1}{2}; |\alpha|^2(1-\eta)^2\right]$$

if $N=2p+1$:

we now have to play the same little game for odd cases.

$$Q_{2p+1}^{\eta} = \eta^{2p+1} \sum_{m=2p+1}^{\infty} \binom{m}{2p+1} (1-\eta)^{m-2p-1} Q_m$$

we only keep the terms where Q_m takes a non-zero value:

$$= \eta^{2p+1} \sum_{m=p+1}^{\infty} \binom{2m}{2p+1} (1-\eta)^{2m-2p-1} Q_{2m}$$

we inject the expression (1.106) of Q_{2m} :

$$= \eta^{2p+1} \sqrt{1-|\alpha|^2} \sum_{m=p+1}^{\infty} \binom{2m}{2p+1} (1-\eta)^{2m-2p-1} \left(\frac{|\alpha|}{2}\right)^{2m} \frac{(2m)!}{(m!)^2}$$

we reindex the sum, making it start from 0:

$$\begin{aligned} &= \eta^{2p+1} \sqrt{1-|\alpha|^2} \sum_{m=0}^{\infty} \binom{2m+2p+2}{2p+1} (1-\eta)^{2m+1} \left(\frac{|\alpha|}{2}\right)^{2m+2p+2} \\ &\quad \times \frac{(2m+2p+2)!}{(m+p+1)!^2} \end{aligned}$$

expanding the binomial term:

$$= \left(\frac{\eta |\alpha|}{2} \right)^{2p+1} \frac{\sqrt{1 - |\alpha|^2}}{(2p + 1)!}$$

$$\times \overbrace{\sum_{m=0}^{\infty} \left[\frac{(2m + 2p + 2)!}{(m + p + 1)!} \right]^2 \frac{1}{(2m + 1)!} \left[\frac{|\alpha|}{2} (1 - \eta) \right]^{2m+1}}^U$$

then, with the same trick as in the previous case and using the notation z :

$$U = \left[\frac{(2p + 2)!}{(p + 1)!} \right]^2 \sum_{m=0}^{\infty} \left[\frac{(2p + 3)^{\overline{2m}}}{(p + 2)^{\overline{m}}} \right]^2 \frac{z^{2m+1}}{(2m + 1)!}$$

again:

$$(2p + 3)^{\overline{2m}} = \overbrace{(2p + 3)(2p + 4) \cdots (2p + 2m + 2)}^{2m \text{ terms}}$$

$$= 2^{2m} \times \overbrace{\left(p + \frac{3}{2} \right) \left(p + \frac{5}{2} \right) \cdots \left(p + m + \frac{1}{2} \right)}^{m \text{ terms}}$$

$$\times \underbrace{(p + 2)(p + 3) \cdots (p + m + 1)}_{m \text{ terms}}$$

$$= 2^{2m} \left(p + \frac{3}{2} \right)^{\overline{m}} (p + 1)^{\overline{m}}$$

and

$$(2m + 1)! = (1 \times) \overbrace{2 \times 3 \times \cdots \times (2m + 1)}^{2m \text{ terms}}$$

$$= 2^{2m} \left(\frac{3}{2} \right)^{\overline{m}} m!$$

and finally:

$$U = \left(\frac{(2p + 2)!}{(p + 1)!} \right)^2 \sum_{m=0}^{\infty} \frac{\left[\left(p + \frac{3}{2} \right)^{\overline{m}} \right]^2 (4z^2)^m}{\left(\frac{3}{2} \right)^{\overline{m}} m!} \times z$$

$$= z \left(\frac{(2p + 2)!}{(p + 1)!} \right)^2 {}_2F_1 \left(p + \frac{3}{2}, p + \frac{3}{2}; \frac{3}{2}; 4z^2 \right)$$

thus:

$$Q_{2p+1}^\eta = \frac{\alpha(1-\eta)}{2} \left(\frac{\eta|\alpha|}{2} \right)^{2p+1} (2p+2) \frac{(2p+2)!}{(p+1)!^2} \sqrt{1-|\alpha|^2} \\ \times {}_2F_1 \left[p + \frac{3}{2}, p + \frac{3}{2}; \frac{3}{2}; |\alpha|^2(1-\eta)^2 \right]$$

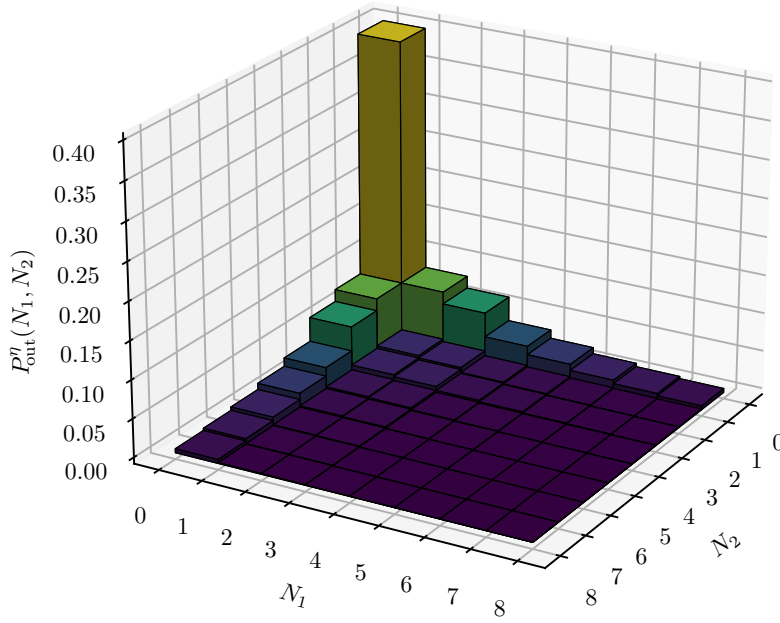


Figure 1.21: Output joint probability distribution for a TMS interfering at a 50-50 beam splitter with finite quantum efficiency. This plot has to be compared to the perfect detector case in Figure 1.20b. Here $\eta = 0.5$ and the average population per mode $\nu = 2$. We find $P_{\text{out}}^\eta(0, 0) = 0.4$ and $P_{\text{out}}^\eta(N_1 > 0, N_2 > 0) \approx 0.135$

We can check (at least numerically) that Eq. (I.III) leads to a joint probability distribution that satisfies the normalisation $\sum_{N_1, N_2} P_{\text{out}}^\eta(N_1, N_2) = 1$ and the average number of detected particles:

$$\overline{N_1 + N_2} = \sum_{N_1, N_2=0}^{\infty} (N_1 + N_2) P_{\text{out}}^\eta(N_1, N_2) = 2\eta\nu \quad (\text{I.II2})$$

We can see in Figure 1.21 that the information about the parity of the number of particles at the output channels has vanished. All the (N_1, N_2) couples are possible, but we can remark that the two “lines” $(N, 0)$ and $(0, N)$ are gathering an overwhelming majority of shots.

A satisfying feature of this distribution is that it is very different from the analogue case considering a couple of indiscernable thermal states (see Figure 1.15 on page 43). In particular, $P_{\text{out}}^\eta(N_1, N_2)$ is not a function of $N_1 + N_2$ only.

Interferences on a beam splitter: distinguishable case

With a perfect detector First, let us imagine what a distinguishable TMS interferometry experiment would be:

1. a two-mode squeezed vacuum state is generated;
2. each of the two modes are spatially separated;
3. a) one of the two modes interacts with the beam splitter...
b) ... and is then measured with the detectors placed at each output channel;
4. **the second mode waits** for a certain duration τ ;
5. the second mode interacts with the beam splitter, and is detected;

We should be careful about the fact that there are two successive measurements here, and that we are dealing with an *entangled* state. Indeed, during the first measurement the experimentalist counts the number of particles on each detector, it is a fortiori a measurement of the total number of particles in the first mode. Due to entanglement, the wave packet of the second mode collapses, and its quantum state is projected onto the ket $|N'_1 + N'_2\rangle$, (N'_1, N'_2) being the numbers of particles measured after the mixing of the first mode with the vacuum.

Theorem 9 (Output probability distribution for a distinguishable TMS interfering at a 50-50 beam splitter)

Considering a TMS with an average population per mode ν , and denoting P_{th} the thermal law of probability with the same average number of particles ν , the output probability distribution in the distinguishable case is:

$$P_{out}(N_1, N_2) = \begin{cases} 0 & \text{if } N_1 + N_2 \text{ is odd} \\ \binom{N_1 + N_2}{N_1} \frac{1}{2^{N_1 + N_2}} P_{th}\left(\frac{N_1 + N_2}{2}\right) & \text{else} \end{cases} \quad (1.113)$$

Proof Because of the wave functions collapse, we know that the same number of particles is detected for each mode (the two modes are perfectly correlated): the total number of particles must be even.

The interaction of the first mode with the beam splitter is actually the case of the mixing of a thermal state with the vacuum. The corresponding output probability distribution P_{out}^1 has already

been already in 2.2.3.

When interacting with the beam splitter, the second mode is reduced to a Fock state, whose output probability distribution has also been studied, and is given by Eq. (1.52).

Once again, we consider the combinatorial outcomes between those two distributions:

$$P_{out}(N_1, N_2) = \sum_{n_1=0}^{N_1} \sum_{n_2=0}^{N_2} P_{out}^1(n_1, n_2) \left(R_{N_1-n_1, N_2-n_2}^{(n_1+n_2, 0)} \right)^2$$

Now, we know that the exact same number of particles is measured at both detection stages:

$$\begin{aligned} n_1 + n_2 &= N_1 - n_1 + N_2 - n_2 \\ &= \frac{1}{2} (N_1 + N_2) \\ &\triangleq n \end{aligned}$$

therefore one of the two sums collapses because of the condition $n_2 = n - n_1$. The upper bound of the remaining sum is changed to n , which is the maximum number of particles detected on one channel for a mode:

$$P_{out}(N_1, N_2) = \sum_{k=0}^n \underbrace{P_{out}^1(k, n-k)}_{\binom{N_1+N_2}{k} \frac{P_{tb}(n)}{2^n}} \underbrace{\left(R_{N_1-k, N_2-n+k}^{(n, 0)} \right)^2}_{\frac{1}{2^n} \binom{n}{N_1-k}}$$

the Vandermonde's identity gives¹:

$$\sum_{k=0}^n \binom{n}{k} \binom{n}{N_1-k} = \binom{2n}{N_1}$$

and finally

$$P_{out}(N_1, N_2) = \binom{N_1 + N_2}{N_1} \frac{1}{2^{N_1+N_2}} P_{tb} \left(\frac{N_1 + N_2}{2} \right)$$

¹: the missing or extra terms (with respect to “genuine” Vandermonde's identity) in the sum are zero.

We observe the same kind of checked pattern as in the indiscernible case, but the middle of the “draughtboard” is more populated. This is no surprise: the sort of *aggregation* effect that favors the edges $(0, N)$ and $(N, 0)$ is a consequence of the interferences between indiscernible bosons.

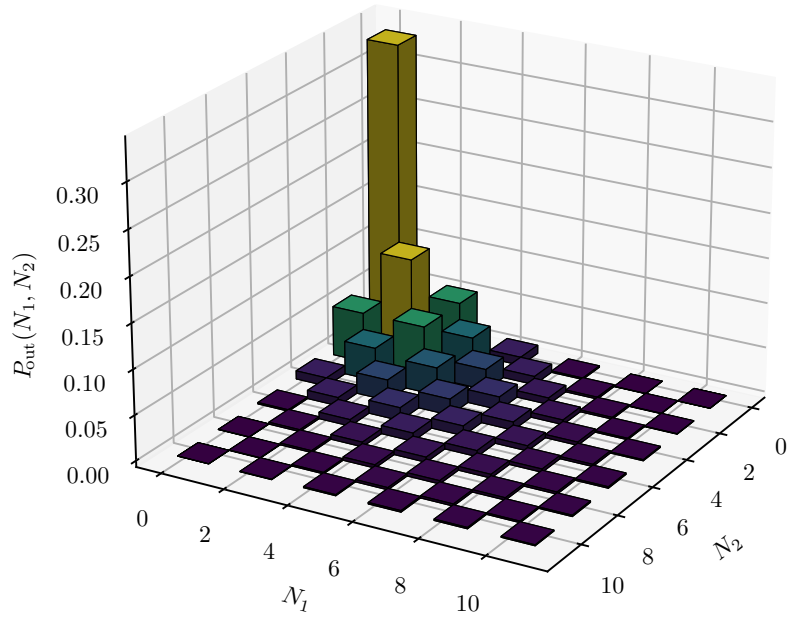


Figure 1.22: Output joint probability distribution for a “distinguishable TMS” interfering at a 50-50 beam splitter. This plot has to be compared with the indistinguishable case in Figure 1.20b.

However, the evenness of the total number of particles is an intrinsic property of the TMS: it is a consequence of the entanglement between the two modes.

The total number of particle must be even (this generates the sort of chessboard pattern), but if we look a one specific output channel, we can obviously detect an odd number of particles. The situation is less constrained than the indiscernible case.

With finite detectivity As usual, we apply the summation of all the cases involving at least N_1 and N_2 particles:

$$P_{\text{out}}^{\eta}(N_1, N_2) = \eta^{N_1+N_2} \sum_{m_1, m_2=0}^{\infty} (1-\eta)^{m_1+m_2} \binom{m_1+N_1}{N_1} \binom{m_2+N_2}{N_2} P_{\text{out}}(N_1+m_1, N_2+m_2) \quad (\text{I.II4})$$

I did not find analytical simplifications in this case, and we are left with numerical estimations, such as the one provided below in Figure 1.23. Even if the checked pattern disappeared (as always when the detectivity is finite), the resulting joint probability distribution remains very different from the indiscernible case, where the $P_{\text{out}}^{\eta}(N_1 > 1, N_2 > 1)$ terms decay extremely fast to zero.

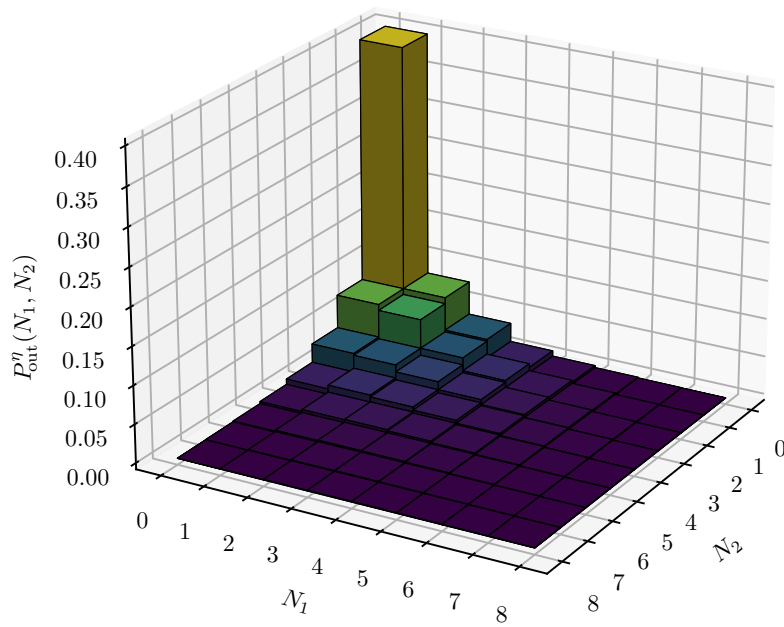


Figure 1.23: Output joint probability distribution for a “distinguishable TMS” interfering at a 50-50 beam splitter with finite quantum efficiency. This plot has to be compared to the distinguishable case in Figure 1.21.

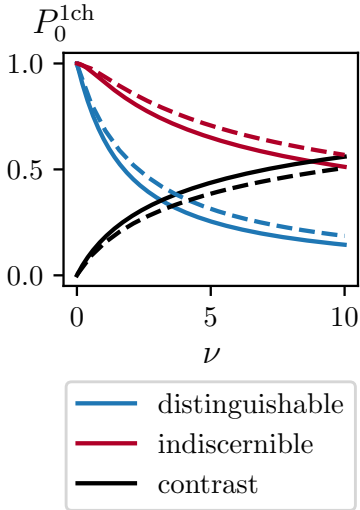


Figure 1.24: Probability to detect zero particle on an output channel, in both distinguishable and indiscernible cases, as a function of the average population per mode. The plain lines correspond to the perfect detectors cases, and the dashed lines consider a quantum efficiency $\eta = 0.5$.

Distinguishable and indiscernible comparison The shape of the joint probability distribution can be visually compared with the 3D histogram plots in Figure 1.20b/Figure 1.22 (with perfect detectors) and Figure 1.21/Figure 1.23 (with finite quantum efficiencies). However we would like to find a simple observable to distinguish both cases, even if the detectivity is not perfect.

Visually, indiscernibility seems to enhance the grouping of the particles on a same side. Let us define P_0^{1ch} : the probability to detect 0 particle on an output channel, whatever we have on the other. Concretely it corresponds to sum of the probabilities placed on “the edges” of the 3D graphs previously plotted.

P_0^{1ch} might be a good guess to witness a difference of behaviour between distinguishable and indiscernible cases:

$$P_0^{1ch} = \tilde{P}_1(0) + \tilde{P}_2(0) - P_{\text{out}}(0,0) \quad (1.115)$$

$$= 1 - P_{\text{out}}(N_1 > 0, N_2 > 0) \quad (1.116)$$

we remove $P_{\text{out}}(0,0)$, because otherwise it would be counted twice.

Luckily, we observe on the numerical calculations in Figure 1.24 that this quantity is very weakly dependent on the quantum efficiency, which is good for in the prospect of an experiment.

We show in Figure 1.24 $P_{0,\text{dis}}^{1ch}$, $P_{0,\text{ind}}^{1ch}$ (where `dis` and `ind` mean respectively distinguishable and indiscernible), as well as and the corresponding contrast C

$$C = \left| \frac{P_{0,\text{ind}}^{1ch} - P_{0,\text{dis}}^{1ch}}{P_{0,\text{ind}}^{1ch} + P_{0,\text{dis}}^{1ch}} \right|$$

The contrast between the two situations increases with ν . In our experimental setup we expect to be able to realise TMS with $\nu \sim 10$. In that case, the numerical estimation gives a contrast of roughly 50%, giving good hope of seeing a significant effect with this observable.

Conclusion

Let us conclude this chapter with a summary of the results that we have established in the second section. We will only deal with the cases where we took into account the finite quantum efficiency, since it is a constraint imposed by our experimental apparatus.

Differentiate indiscernable and distinguishable scenarios, with TMS states. We have seen in the last paragraph of the chapter that looking at the probability to measure zero particle on a given output channel could be an appropriate observable. With the states that we are able to concretely generate in the lab, we expect a relative difference of 50 % between both scenarios.

Differentiate a TMS state from a coherent state. It is rather straightforward when looking at the statistical distribution of the number of particles detected (without beam splitter): cf. [Remark 1.4](#). Although, coherent states reproduce the well known interference patterns of classical wave optics, involving a phase dependence that is not expected with TMS states. We have already observed experimentally that our source is producing a state that does not follow a semi-classical Poissonian statistics [62].

[62]: Perrier et al. (2019), “Thermal Counting Statistics in an Atomic Two-Mode Squeezed Vacuum State”

Differentiate a TMS state from a pair of thermal states. In indiscernible scenarios, the joint output probability distributions generated by those two states are very different. In particular, in the case of thermal states, it only depends on *one* parameter, which is the total number of particles. Furthermore, if we compare [Figure 1.15 on page 43](#) with [Figure 1.21 on page 59](#), it seems that the distribution corresponding to the thermal states populates the states ($N_1 \neq 0, N_2 \neq 0$) much more¹, which is another noticeable difference.

¹: “the middle of the chessboard”.

What remains to be done with this theoretical work? On a technical aspect, we still need to find a proper analytical ending to the derivations of [Equation 1.85 on page 42](#) (thermal and indiscernable), as well as an analytical form to the resulting interferences of a distinguishable TMS state, with finite quantum efficiency.

Apart from these rather formal and mathematical topics of concern, we can also look for other observables (depending only on the population

ν), clearly exhibiting the distinction between an indiscernible and a distinguishable situation. The joint probability distributions calculated in this chapter contains all the information needed to calculate the expectation values of those observable: in particular the information about the *correlations* between the detections operated at both output channels.

Contrary to the two-particle HOM effect, we did not yet found the clear signature of a quantum effect in an HOM-like experiment using TMS. Therefore, for now, such an experiment cannot provide a result as “strong” as the two-particle HOM anti-correlation. However, we exhibited a clear effect of the indiscernibility property between the distributions, which is sort of a weaker result. Let us give a possible experimental application of it.

In the following chapter, we will present a two-particle interferometer that was designed to perform Bell inequality violation experiments: it basically consists in two separated Mach-Zehnder interferometers (cf. Figure 2.8 on page 85). Both Mach-Zehnders requires to be “closed” meaning that particles interfering on the last beam splitter should be indiscernible. Since we are planning to use this setup with TMS states, the results established in this chapter could be useful to verify the correct setting of each Mach-Zehnder.

Bell inequalities **2**

Chapter's table of contents

. Introduction	68
1. General considerations	68
1.1 EPR argument	68
1.2 Bell's theorem	72
1.2.1 Main idea	72
1.2.2 CHSH inequality & violation	72
2. Rarity-Tapster interferometer	78
2.1 Introduction to the problem	78
2.2 General description	81
2.2.1 Topology	81
2.2.2 Bragg diffraction in brief	82
2.2.3 Formal effect of the deflector and beam splitters	84
2.3 Well-suited Bell inequalities	89
2.3.1 First natural approach	90
2.3.2 Second approach: projection onto two-outcome events observables	92
2.3.3 Third approach based on the CH inequality	94
. Conclusion	97

Introduction

This chapter is dedicated to the question of the Bell inequalities, and the way that we want to test them with our experimental platform. We will start in the first section by reminding the general idea of what a Bell inequality is, how it is derived, and what it means to violate it.

In a second step, we will more specifically address the issue of the concrete implementation of a Bell inequality violation with the apparatus that we have at our disposal. We will see in particular that we are planning to use the entanglement between the *momenta* of atoms to witness such a violation: this has never been done yet with massive particles. This second section will be divided in two main parts:

- ▶ first we will present the two-atom interferometer that we aspire to realise to probe nonlocal correlations. This interferometer is inspired by the Rarity-Tapster experiment [27] ;
- ▶ then we will show that the properties of the peculiar multimode quantum state that our source is producing may have a negative impact on the level of violation of the inequality. We will show that some ideas presented in a recent theoretical publication of Nemoto et al. [73] can be used to perform a cleverer treatment of the data, increasing the visibility of the violation of the Bell inequality.

[27]: Rarity et al. (1990), “Experimental violation of Bell’s inequality based on phase and momentum”

[73]: Kitzienger et al. (2021), “Bell Correlations in a Split Two-Mode-Squeezed Bose-Einstein Condensate”

1 General considerations

1.1 EPR argument

One of the most admirable successes of modern physics is general relativity: a metric theory of gravitation, that depicts the universe in a relativistic way. From the anomalous perihelion advance of Mercury (1915), the deflection of starlight by the Sun observed during an eclipse (1919) to the direct detection of gravitational waves [74] or gravitational redshift measurements [75], this elegant theory passed many experimental tests. It offers the best mathematical framework for physics at non-microscopic length scale. One of the core hypotheses of both special and general relativity theories is the *principle of locality*, that states that physical systems may only be influenced by their space-time immediate surroundings. To put it simply, *local theories* (i.e. assuming the principle of locality to be true) avoid any form of action at distance.

[74]: Abbott et al. (2016), “Observation of Gravitational Waves from a Binary Black Hole Merger”

[75]: Hafele et al. (1972), “Around-the-World Atomic Clocks: Predicted Relativistic Time Gains”

This is a very natural hypothesis, which is also at the root of a remarkably robust theory. Thus it seems legitimate to think that locality (just like causality) should be a postulate of any fundamental physics theory.

It is well known in epistemology that the famous work of Einstein et al. [13] was an attempt to exhibit a flaw in quantum theory. Indeed, essentially assuming the principle of locality to be true, it is possible to show a contradiction in the statements of quantum mechanics. Let us take a closer look at the EPR argument, in its “modern” formulation of Bohm and Aharonov [76], that we will call “EPRB” argument, or EPRB thought experiment (*gedankenexperiment* à la Einstein).

[13]: Einstein et al. (1935), “Can Quantum-Mechanical Description of Physical Reality Be Considered Complete?”

[76]: Bohm et al. (1957), “Discussion of Experimental Proof for the Paradox of Einstein, Rosen, and Podolsky”

Postulates The argument is built upon three hypotheses of capital importance, the first two being often combined into one, known as the *local realism* hypothesis¹:

Local realism hypothesis

We call *local realism* the set of the two followings hypotheses:

Hypothesis H1 (Realism) *An experimental result that can be predicted in advance may only be the consequence of a pre-existing and well-defined physical quantity. Such a quantity is called an “element of reality”.*

Hypothesis H2 (Space-time locality) *The relativistic spacetime is the correct geometrical structure to describe the physical events. The elements of reality are locally attached to spacetime, and their time evolution may only be influenced by their local surrounding.*

¹: at least, this is the definition that we will use in this manuscript. Some authors refer to local realism as the whole set of the EPR hypotheses, including H3.

The previous formulation is inspired by reference [55].

[55]: Cohen-Tannoudji et al. (2017), *Mécanique quantique - Tome 3*

Remark 2.1 An important consequence of H2 is that a physical measurement performed in a given region of spacetime cannot be influenced by an other physical transformation realised by an operator located in a separated region of spacetime. More precisely, an event E_1 may have an influence on an other event E_2 if and only if they are separated by a timelike interval². This corollary is sometimes called “*separability*”.

²: for more information about space-time intervals, we refer the interested reader towards any general relativity textbook, such as [77] or [78].

Hypothesis H3 (Quantum mechanics) *The predictions of quantum mechanics concerning the outcome probabilities of an experiment are correct.*

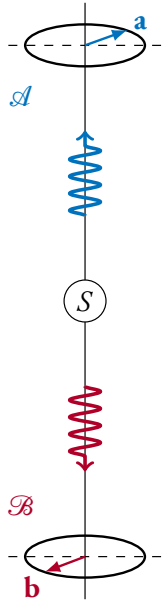


Figure 2.1: Principle of an EPRB experiment. Two particles (blue and red) are emitted from a common source S in spatially separated regions. We then look at the correlations between the *measurements* A and B , obtained by the *experimentalists* \mathcal{A} and \mathcal{B} , using detectors *oriented* by \mathbf{a} and \mathbf{b} .

Reductio ad absurdum The reasoning is essentially a proof by contradiction. An EPRB experiment – presented on Figure 2.1 – consists in a source S , emitting two physical systems (e.g. two particles or two photons) that propagate towards separate regions of space, without interaction. Two experimentalists, Alice (\mathcal{A}) and Bob (\mathcal{B}), perform measurements (respectively A and B) on the two systems, separately.

Let us consider now that the physical systems emitted by the source are *two-level systems* (like linearly polarised photons or spin- $\frac{1}{2}$ particles) emitted in a quantum *singlet state* (which is actually a particular case of what we call a *Bell state* nowadays):

$$|\psi\rangle = \frac{1}{\sqrt{2}} [|1\rangle|0\rangle - |0\rangle|1\rangle] \quad (2.1)$$

Alice and Bob’s measurements are characterised by vectors \mathbf{a} and \mathbf{b} , that they can choose freely (they correspond to a choice of basis for the quantum measurement): it would correspond to the angle of the polaroid in the case of photons, or the direction of the magnetic field in a Stern-Gerlach setup for spin- $\frac{1}{2}$ particles.

Each measurement returns a value ± 1 , and we assume that Alice and Bob choose the orientation of their detector *right before* executing their measurement, in a finite subset of the continuum of possible orientations, for example $\left\{ \frac{2p\pi}{n} / n \in \mathbb{N}^*, p \in \llbracket 1, n \rrbracket \right\}$.

Sometimes, during some pairs of measurements, \mathbf{a} and \mathbf{b} are aligned ($\mathbf{a} = \mathbf{b}$), or anti-aligned ($\mathbf{a} = -\mathbf{b}$). In those cases, whatever the distance separating Alice and Bob, quantum mechanics (hypothesis **H3**) predicts that the results are respectively anti-correlated ($A \cdot B = -1$), or correlated ($A \cdot B = 1$). Let us additionally assume that Alice performs her measurement a short time before Bob (short enough to have a spacelike interval between both measurements). It is then *certain* (according to **H3**) that if Bob chooses an orientation \mathbf{b} that is aligned (respectively anti-aligned) to Alice’s one, the correlation between the measurements will be perfectly anti-correlated (respectively correlated).

Now **H1** stipulates that if Bob’s measurement can somehow be determined with certainty, it means that an element of reality – carried by the quantum particle measured by Bob – is present and influences the detector in such a way that detection matches prediction. But Bob’s detection being separated of Alice’s one by a spacelike interval, due to hypothesis **H2**, it cannot be influenced by anything occurring in Alice’s

laboratory during her measurement¹ (in particular her measurement's outcome). It means that the results obtained by Bob and Alice² were formerly determined and since the orientation \mathbf{a} is chosen randomly, the determination is *complete* (i.e. the value of the spin/polarisation is determined in all directions). Finally, since there are no interaction during the propagation of the particles, the additional element of reality was set since the emission of the particles from the source S .

Now the problem is that quantum mechanics does not predict the existence of such a parameter: we all know that in quantum formalism, the randomness of the outcome of Alice's measurement is intrinsic. Worse, to some extent, we can even say that quantum mechanics *predicts the non-existence* of such a parameter: because the spin of particles are described by non-commuting observables, there is no quantum description where all the components of the spin are well defined, which is inconsistent with the previous statement about the completeness of the determination of the states.

Conclusion The matter of the conclusion of the EPR was at the core of decades of debates since its publishing in 1935. The authors stated that it was the proof that quantum mechanics was incomplete, and even if it provided perfectly satisfying theoretical predictions (in good accordance with experiments) it was not covering the whole physical essence of Nature. This is tacitly assuming that local realism is a valid postulate, and that the contradiction is actually sourced by hypothesis **H3**, or more correctly by the physical interpretation of quantum theory: it could indeed simply be an *incomplete* theory but providing correct statistical results (in which case in all rigour **H3** is also a valid hypothesis).

Bohr immediately proposed a very different interpretation. Even though he did not question the validity of the *concrete* constraints imposed by general relativity³, he asserted that there is an aspect of **H2** that could collapse in the quantum realm. For Bohr, an entangled system such as (2.1) may only be considered globally. Such a composite system is *not separable*, and in some cases it does not make any sense⁴ to try to give physical properties to its sub-components (here the spin or the polarisation).

1: this still would have been true even if we would not have assumed the absence of interaction.

2: by a simple symmetry argument where we exchange Alice and Bob in all the previous reasoning.

3: essentially the fact that information cannot ship at a faster speed than Einstein's speed c .

4: at least if we want to keep a maximal quantity of information in our description.

1.2 Bell's theorem

1.2.1 Main idea

The philosophical question of the correct interpretation of the EPR argument took a new perspective in 1964 with the contribution of John Bell [15], who proved the following theorem:

[15]: Bell (1964), “On the Einstein Podolsky Rosen paradox”

Theorem 10 (Bell's theorem)

Assuming the validity of the local realism hypothesis, there is no way to complete quantum mechanics such that it takes into account local elements of reality without changing some of its experimental predictions.

In particular, Bell identified a quantum system Σ , with a measurable physical quantity S , for which quantum theory predicts a value that cannot be taken in any local realistic framework. In fact, Bell showed that local realism imposes some numerical constraints to the level of correlation that can be observed between the measurements of Alice and Bob, numerical constraints that can sometimes be violated in the quantum realm. This constraint takes the form of an inequality, that must be satisfied in any local realistic (sometimes called *classical*) context. These inequality are famously known, and nowadays usually named *Bell's inequalities*.

Thanks to Bell's inequality, the existence of EPR's element of reality, or with modern wording “*local hidden-variables*”, becomes experimentally testable. In 2015, research groups in Vienna, Delft and the NIST independently measured Bell inequality violations [28–30], using *loophole free* setups: meaning that any possible classical interpretations of the results is avoided [79].

[28]: Hensen et al. (2015), “Loophole-free Bell inequality violation using electron spins separated by 1.3 kilometres”

[29]: Giustina et al. (2015), “Significant-Loophole-Free Test of Bell's Theorem with Entangled Photons”

[30]: Shalm et al. (2015), “Strong Loophole-Free Test of Local Realism”

[79]: Aspect (2015), “Closing the Door on Einstein and Bohr's Quantum Debate”

1.2.2 CHSH inequality & violation

Classical inequality It is important to understand that different quantum systems, with different correlation-based observables may be a case of application (or an illustration) of Bell's theorem: for each of them there is a specific Bell inequality, more or less conveniently testable in a laboratory.

Let us recall the most famous one, known as the CHSH inequality

ity:

Theorem 11 (Bell inequality: CHSH formulation)

Let Σ be a system of two two-level particles, spatially separated, that can be repeatedly prepared in the same quantum state. Two operators separately perform measurements of the state of the particles, with detectors characterised by their orientation, respectively \mathbf{a} and \mathbf{b} .

The experimental result of each realisation take the value $+1$ or -1 (and also possibly 0 if a detectors fails to detect a particle), they are denoted A and B , respectively for one operator and the other. For a given couple of orientations (\mathbf{a}, \mathbf{b}) , we denote $E(\mathbf{a}, \mathbf{b})$ the correlation between the measurements obtained by the operators, in extenso the average value of the product of their measurements:

$$E(\mathbf{a}, \mathbf{b}) \triangleq \langle A \cdot B \rangle \tag{2.2}$$

If we assume that a set of local hidden-variables completing the quantum mechanics in a local realistic framework exists, then given $(\mathbf{a}, \mathbf{a}')$ and $(\mathbf{b}, \mathbf{b}')$ two couples of orientations respectively used by each operator, we have:

$$|E(\mathbf{a}, \mathbf{b}) - E(\mathbf{a}, \mathbf{b}')| + |E(\mathbf{a}', \mathbf{b}') + E(\mathbf{a}', \mathbf{b})| \leq 2 \tag{2.3}$$

Remark 2.2

1. The situation described is actually the EPRB experiment proposed by Bohm and Aharonov in 1957 [76] (cf. Figure 2.1).
2. By setting

$$S(\mathbf{a}, \mathbf{a}', \mathbf{b}, \mathbf{b}') \triangleq E(\mathbf{a}, \mathbf{b}) - E(\mathbf{a}, \mathbf{b}') + E(\mathbf{a}', \mathbf{b}') + E(\mathbf{a}', \mathbf{b}) \tag{2.4}$$

the triangle inequality immediately gives the perhaps more famous (but also weaker) formulation:

$$|S(\mathbf{a}, \mathbf{a}', \mathbf{b}, \mathbf{b}')| \leq 2 \tag{2.5}$$

S is sometimes called BCHSH parameter, CHSH parameter, or simply Bell parameter.

[76]: Bohm et al. (1957), “Discussion of Experimental Proof for the Paradox of Einstein, Rosen, and Podolsky”

The inequality’s name refers to the initials of the authors who published it first in 1969: Clauser, Horne, Shimony and Holt [17], but with a

[17]: Clauser et al. (1969), “Proposed Experiment to Test Local Hidden-Variable Theories”

[18]: Bell (1971), “Introduction to the hidden-variable question”

[80]: Bell et al. (2004), “Introduction to the hidden-variable question”

quite “messy” demonstration. The proof was simplified and generalized by Bell in 1971 [18]. It is published in his reference textbook *Speakable and unspeakable* [80], and reminded in the following box:

Proof (CHSH inequality, Bell 1971) We denote λ the set of local hidden-variable, carried by the particles, making quantum mechanics local realistic. It does not matter to know the mathematical nature of λ : if it is a singleton or a set, numbers of functions, discrete or continuous. It also does not require to be “minimal”, in the sense that all the information contained in λ should be mandatory to depict the experiment in a local realistic way: it only needs to be “sufficient”.

Applying the EPR prescription, we conclude that a given λ is drawn in a large set Λ (assumed to be measurable) at each realisation, and fixed, from the emission at the source until the measurement. The results of the measurements of the two experimentalists (let us call them Alice and Bob) are functions of the orientation of their detectors (\mathbf{a} , \mathbf{b}), of λ , and also possibly of additional local hidden-variables $\lambda_{\mathbf{a}} \in \Lambda_{\mathbf{a}}$ and $\lambda_{\mathbf{b}} \in \Lambda_{\mathbf{b}}$, attached to the detectors, and that may influence the outcome of the measurements:

$$\begin{cases} A : (\mathbf{a}, \lambda, \lambda_{\mathbf{a}}) \mapsto A(\mathbf{a}, \lambda, \lambda_{\mathbf{a}}) \in \{-1, 0, 1\} \\ B : (\mathbf{b}, \lambda, \lambda_{\mathbf{b}}) \mapsto B(\mathbf{b}, \lambda, \lambda_{\mathbf{b}}) \in \{-1, 0, 1\} \end{cases}$$

0 being the outcome of a realisation where one or both detectors failed and did not return any result.

The experimental results are therefore determined at the emission of the particles, and the apparent randomness of the results registered by Alice and Bob comes from the probability density distributions $\rho(\lambda)$, $\rho_{\mathbf{a}}(\lambda_{\mathbf{a}})$, and $\rho_{\mathbf{b}}(\lambda_{\mathbf{b}})$, when the experiment is repeated.

We first introduce the measured quantities, averaged over the local variables of the detectors:

$$\begin{cases} \overline{A}(\mathbf{a}, \lambda) \triangleq \int_{\lambda_{\mathbf{a}} \in \Lambda_{\mathbf{a}}} d\lambda_{\mathbf{a}} \rho_{\mathbf{a}}(\lambda_{\mathbf{a}}) A(\mathbf{a}, \lambda, \lambda_{\mathbf{a}}) \in [-1, 1] \\ \overline{B}(\mathbf{b}, \lambda) \triangleq \int_{\lambda_{\mathbf{b}} \in \Lambda_{\mathbf{b}}} d\lambda_{\mathbf{b}} \rho_{\mathbf{b}}(\lambda_{\mathbf{b}}) B(\mathbf{b}, \lambda, \lambda_{\mathbf{b}}) \in [-1, 1] \end{cases}$$

where the inequalities

$$|\overline{A}(\mathbf{a}, \lambda)| \leq 1 \quad , \quad |\overline{B}(\mathbf{b}, \lambda)| \leq 1 \quad (\dagger)$$

are usual, reminding that ρ , $\rho_{\mathbf{a}}$ and $\rho_{\mathbf{b}}$, being probability densities, are positive, and their integral are normalised to 1.

Eq. (\dagger) also gives immediately

$$|\overline{A}(\mathbf{a}, \lambda)\overline{B}(\mathbf{b}, \lambda)| \leq 1 \quad (\ddagger)$$

With the definition Eq. (2.2), we have:

$$E(\mathbf{a}, \mathbf{b}) = \int_{\lambda \in \Lambda} d\lambda \rho(\lambda) \overline{A}(\mathbf{a}, \lambda) \overline{B}(\mathbf{b}, \lambda)$$

Then we compute

$$\begin{aligned} E(\mathbf{a}, \mathbf{b}) - E(\mathbf{a}, \mathbf{b}') &= \int_{\lambda \in \Lambda} d\lambda \rho(\lambda) (\overline{A}(\mathbf{a}, \lambda) \overline{B}(\mathbf{b}, \lambda) - \overline{A}(\mathbf{a}, \lambda) \overline{B}(\mathbf{b}', \lambda)) \\ &= \int_{\lambda \in \Lambda} d\lambda \rho(\lambda) \left[\overbrace{\overline{A}(\mathbf{a}, \lambda) \overline{B}(\mathbf{b}, \lambda)}^{\in[-1,1]} \overbrace{(1 \pm \overline{A}(\mathbf{a}', \lambda) \overline{B}(\mathbf{b}', \lambda))}^{\geq 0} \right] \\ &\quad - \int_{\lambda \in \Lambda} d\lambda \rho(\lambda) \left[\overbrace{\overline{A}(\mathbf{a}, \lambda) \overline{B}(\mathbf{b}', \lambda)}^{\in[-1,1]} \overbrace{(1 \pm \overline{A}(\mathbf{a}', \lambda) \overline{B}(\mathbf{b}, \lambda))}^{\geq 0} \right] \end{aligned}$$

where the inequalities written on the braces are given by Eq. (\ddagger).

We then use the triangle inequality, and the fact that $|\int f| \leq \int |f|$:

$$\begin{aligned} |E(\mathbf{a}, \mathbf{b}) - E(\mathbf{a}, \mathbf{b}')| &\leq \int_{\lambda \in \Lambda} d\lambda \rho(\lambda) [1 \pm \overline{A}(\mathbf{a}', \lambda) \overline{B}(\mathbf{b}', \lambda)] \\ &\quad + \int_{\lambda \in \Lambda} d\lambda \rho(\lambda) [1 \pm \overline{A}(\mathbf{a}', \lambda) \overline{B}(\mathbf{b}, \lambda)] \end{aligned}$$

which is exactly

$$|E(\mathbf{a}, \mathbf{b}) - E(\mathbf{a}, \mathbf{b}')| \leq 2 \pm [E(\mathbf{a}', \mathbf{b}') + E(\mathbf{a}', \mathbf{b})]$$

which is actually also

$$|E(\mathbf{a}, \mathbf{b}) - E(\mathbf{a}, \mathbf{b}')| + |E(\mathbf{a}', \mathbf{b}') + E(\mathbf{a}', \mathbf{b})| \leq 2$$

■

Remark 2.3 (Bell inequality with continuous variable measurements) Regarding the previous proof, one could notice that the very core of the mathematical reasoning is conducted by manipulating the quantities $\overline{A}(\mathbf{a}, \lambda)$ and $\overline{B}(\mathbf{b}, \lambda)$ (the measurements averaged over the local variables of the detectors) which are *continuous variables* contained in the interval $[-1, 1]$.

This is very interesting because it means that the CHSH inequality actually holds for continuous variable measurements.

Actually the fact that A and B should be bounded to $[-1, 1]$ is not a strong constraint. Indeed even if $A, B \in \mathbb{R}$, Alice and Bob can always apply a function mapping it into $[-1, 1]$ (tanh for instance). Less naively, if Alice and Bob have two channels of detection at their disposal (which is generally the case during an experiment) labelled “ (A_+, A_-) ” and “ (B_+, B_-) ” respectively, they can consider the normalised quantities

$$\begin{cases} \tilde{A}_+ = \frac{A_+}{|A_+| + |A_-|} & , & \tilde{A}_- = \frac{A_-}{|A_+| + |A_-|} & \in [-1, 1] & (2.6a) \end{cases}$$

$$\begin{cases} \tilde{B}_+ = \frac{B_+}{|B_+| + |B_-|} & , & \tilde{B}_- = \frac{B_-}{|B_+| + |B_-|} & \in [-1, 1] & (2.6b) \end{cases}$$

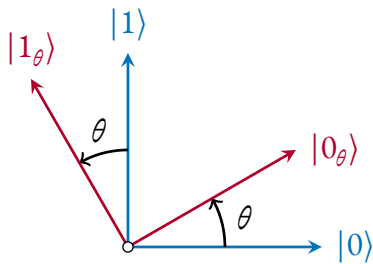


Figure 2.2: Rotation of the basis of detection of a two-level system. The two orientations are said to be aligned when $\theta \equiv 0(\pi)$. On the contrary, they are said to be anti-aligned (or *crossed* in the case of polarising beam splitters) when $\theta \equiv \frac{\pi}{2}(\pi)$: in that case, the roles of $|0\rangle$ and $|1\rangle$ are exchanged.

i: it is in fact a reference that can be chosen arbitrarily.

Quantum violation of the inequality Now it turns out that quantum mechanics make it possible to compute the correlators E directly.

Let us consider again the EPRB experiment, where the source generates a singlet state (2.1).

The orientations of the detectors $\mathbf{a}, \mathbf{a}', \mathbf{b}$ and \mathbf{b}' are coplanar unit vectors, that we will parametrise by the respective angles $\theta_a, \theta_{a'}, \theta_b, \theta_{b'}$, oriented by the Alice-Bob axis, and with $\theta = 0$ corresponding to a measurement operated in the $\{|0\rangle, |1\rangle\}$ basisⁱ. We denote $\{|0_\theta\rangle, |1_\theta\rangle\}$ the rotated basis, in which a measurement is operated by a detector with the angle θ .

Given its orientation θ , we ask the detector to return the value $+1$ when the state $|1_\theta\rangle$ is measured, and the value -1 when the state $|0_\theta\rangle$ is measured.

By definition of the correlator, we have:

$$E(\theta_a, \theta_b) \triangleq \langle A \cdot B \rangle_{(\theta_a, \theta_b)} \quad (2.7)$$

$$\begin{aligned} &= (+1) \cdot (+1) \times |\langle 1_{\theta_a}, 1_{\theta_b} | \psi \rangle|^2 \\ &\quad + (+1) \cdot (-1) \times |\langle 1_{\theta_a}, 0_{\theta_b} | \psi \rangle|^2 \\ &\quad + (-1) \cdot (+1) \times |\langle 0_{\theta_a}, 1_{\theta_b} | \psi \rangle|^2 \\ &\quad + (-1) \cdot (-1) \times |\langle 0_{\theta_a}, 0_{\theta_b} | \psi \rangle|^2 \end{aligned} \quad (2.8)$$

$$E(\theta_a, \theta_b) = P_{+,+}(\theta_a, \theta_b) - P_{+,-}(\theta_a, \theta_b) - P_{-,+}(\theta_a, \theta_b) + P_{-,-}(\theta_a, \theta_b) \quad (2.9)$$

where the last line conveniently uses the joint conditional probabilities notations, to simplify the bracket notation.

It is not a difficult exercise to check that the scalar products give

$$\begin{cases} P_{+,+}(\theta_a, \theta_b) = P_{-,-}(\theta_a, \theta_b) = \frac{1}{2} \sin^2(\theta_a - \theta_b) & (2.10a) \\ P_{+,-}(\theta_a, \theta_b) = P_{-,+}(\theta_a, \theta_b) = \frac{1}{2} \cos^2(\theta_a - \theta_b) & (2.10b) \end{cases}$$

which is in line with what we would expect with a singlet state:

- ▶ it is independent of the reference direction ;
- ▶ aligned detectors ($\theta_a = \theta_b$) lead to a perfect anti-correlation of the measures ;
- ▶ anti-aligned detectors ($\theta_a = \theta_b + \frac{\pi}{2}$) lead to a perfect correlation of the measures ;

Eq. (2.10) simplifies the expression (2.9) of the correlator:

$$E(\theta_a, \theta_b) = -\cos(2[\theta_a - \theta_b]) \quad (2.11)$$

which is an even function, which is also good since the symmetry of the problem allows us to exchange the roles of θ_a and θ_b .

Remark 2.4 The actual expression of E , is obviously dependent on the type of state that we initially choose to consider. For instance, Eq. (2.11) gives

$$\theta_a = \theta_b \Rightarrow E(\theta_a, \theta_b) = -1$$

which makes sense for a singlet state, but not for any entangled state.

For example the Bell state $|\Phi^+\rangle = \frac{1}{\sqrt{2}}(|0,0\rangle + |1,1\rangle)$ leads to the correlator:

$$E(\theta_a, \theta_b) = +\cos(2[\theta_a - \theta_b])$$

(if we take the same values returned by the detectors).

Now we just have to consider the particular quadruplet of angles

$$\theta_a = 0 \quad \theta_b = \frac{\pi}{8} \quad \theta_{a'} = \frac{\pi}{4} \quad \theta_{b'} = \frac{3\pi}{8}$$

to check that quantum mechanics predicts a BCHSH parameter:

$$S_{QM}\left(0, \frac{\pi}{4}, \frac{\pi}{8}, \frac{3\pi}{8}\right) = 2\sqrt{2} \quad (2.12)$$

Strongly violating the inequality (2.5) (by more than 40%), which is enough to prove Bell's theorem (Theorem 10).

2 Rarity-Tapster interferometer

2.1 Introduction to the problem

[20]: Freedman et al. (1972), "Experimental Test of Local Hidden-Variable Theories"

[22]: Aspect et al. (1981), "Experimental Tests of Realistic Local Theories via Bell's Theorem"

[23]: Aspect et al. (1982), "Experimental Realization of Einstein-Podolsky-Rosen-Bohm *Gedankenexperiment*"

[24]: Aspect et al. (1982), "Experimental Test of Bell's Inequalities Using Time-Varying Analyzers"

†: emitted in a radiative cascade.

The first Bell inequalities violation experiments [20, 22–24] were conducted with a source of pairs of photons[†], entangled with respect to their *polarization*, and emitted in different directions. In the followings we will call respectively *Alice* and *Bob* the fictional experimentalists performing measurements respectively on each particle of the entangled system: these names could actually indistinctly refer to the experimentalists, or their measurements.

The apparatus used for these polarisation-based experiments, only involves two polarising beamsplitting cubes (one for each side), and a coincidence counter device, that can evaluate the correlations between the measurements made upon a particle on the one hand (e.g. Alice's side), and upon the second particle on the other hand (Bob's side).

The schematic of these experiments are shown in Figure 2.3. It is worth noticing that it involves *four* detection modes: two for Alice (denoted A_+ and A_-) and two for Bob (denoted B_+ and B_-). Actually, two modes are coming from the fact that the photons are emitted in opposite directions, and then two modes are again coming from the two polarisation states of the photons: therefore we indeed have $2 \times 2 = 4$

modes.

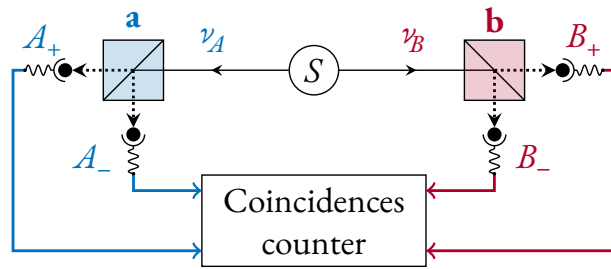


Figure 2.3: Schematic of a CHSH inequality violation experiment, with photons entangled with respect to their polarisation. The detectors’ orientations **a** and **b** are randomly chosen, right before the detection. The coincidences counter computes the correlations between the detections on the modes A_+/A_- on the one hand, and on the modes B_+/B_- on the other hand.

The key point in any Bell inequality violation experiment is that both Alice and Bob must have a “turnable button” that changes the output modes of their detector at their disposal. More concretely, these buttons control the *orientation* **a** and **b**, and in the language of quantum mechanics, this corresponds to *rotating the basis* in which the detections are performed (cf. Figure 2.2). In the case of the experiment previously mentioned, these buttons are naturally provided by the *physical* orientation of the polarising beamsplitting cubes: that is why the overall geometry of the setup remains pretty simple.

In summary, a Bell inequality violation requires three fundamental elements:

1. a source of many-particle entangled state. In this work we consider only two-particle entanglement, but the generalised many-particle Bell inequality violation is also an active research thematic [81–83];
2. single particle resolved detectors. In the case of photons it could be *photomultipliers (PM)*, or more recently *superconducting nanowire single-photon detectors (SNSPD)* (offering better performances for photon counting [84]). In the case of our experiment, the detection is carried out by a *microchannel plate (MCP)* (cf. Chapter 3 and Chapter 4): it is worth noticing that both Alice and Bob detections are performed by a same *physical* device (there is only one *MCP*) but at *different times*.
3. a technical way to change the bases of detections.

The experiments described above are designed to reveal the entanglement between the *polarisations* of photons, which is an *internal* degree of freedom (cf. Remark 2.5). In 1989, Horne, Shimony and Zeilinger proposed a different topology, that is able to probe entanglement with respect to what most closely resembles to a mechanical degree of freedom for the photon: the wave vector (or the optical path) [85]. The experiment was achieved one year later by Rarity and Tapster, who

[81]: Mermin (1990), “Extreme Quantum Entanglement in a Superposition of Macroscopically Distinct States”

[82]: Cereceda (2001), “Mermin’s n-Particle Bell Inequality and Operators’ Noncommutativity”

[83]: Laskowski et al. (2005), “Detection of N-Particle Entanglement with Generalized Bell Inequalities”

[84]: Esmaeil Zadeh et al. (2021), “Superconducting Nanowire Single-Photon Detectors”

[85]: Horne et al. (1989), “Two-Particle Interferometry”

[27]: Rarity et al. (1990), “Experimental violation of Bell’s inequality based on phase and momentum”

i: one could argue that these parameters are not *purely* quantum since both the spin and the helicity also come out of relativistic arguments. Without going deep into the details we will just say that the quantum theory plays at least a crucial role for that matter. The interested reader can refer to those references for more information: [86, 87]

were able to measure a Bell inequality violation for the momenta of photons by several standard deviations [27]. We will show in the next section that the experimental trick used to change the basis of detection, and measure a BCHSH parameter is less trivial than in the case of photon polarisation. With our experiment, we intend to reproduce the analogue of the Rarity-Tapster experiment, to probe the momentum entanglement of massive particles: helium atoms.

Remark 2.5 (Internal and external quantum parameters) For the quantum systems that we consider, we distinguish two types of degree of freedom:

- ▶ the *internal* ones: that are carried by the particle itself (without needing anything else than the particle to define it). In the case of elementary particles they usually have a purely quantum origin: for example the spin of electrons, or the helicity of photons¹. Internal parameters may also come from the composite nature of a more complex quantum system, such as atoms are. For example, the total angular momentum of an atom comes from the different contributions of its constituents (spin and angular momentum of the electrons, nuclear spin) but it is considered as an *internal* parameter because it is self-contained, in the atomic structure. In general the internal degrees of freedom can be represented with discrete quantum numbers ;
- ▶ the *external* ones: referring to the state of the particle, with respect to a wider structure to whom it is bounded. In simple words, they typically are the position or the momentum, that is why we also sometimes call them *mechanical* parameters. It is interesting to notice that these parameters have a direct classical equivalent (classical position/velocity), and anyone has a fairly natural and subjective knowledge of it. This apparent familiarity that we have with this class of parameters makes even more interesting, on the epistemological aspect, the possibility to prepare them in a highly quantum regime, such as entangled states ;

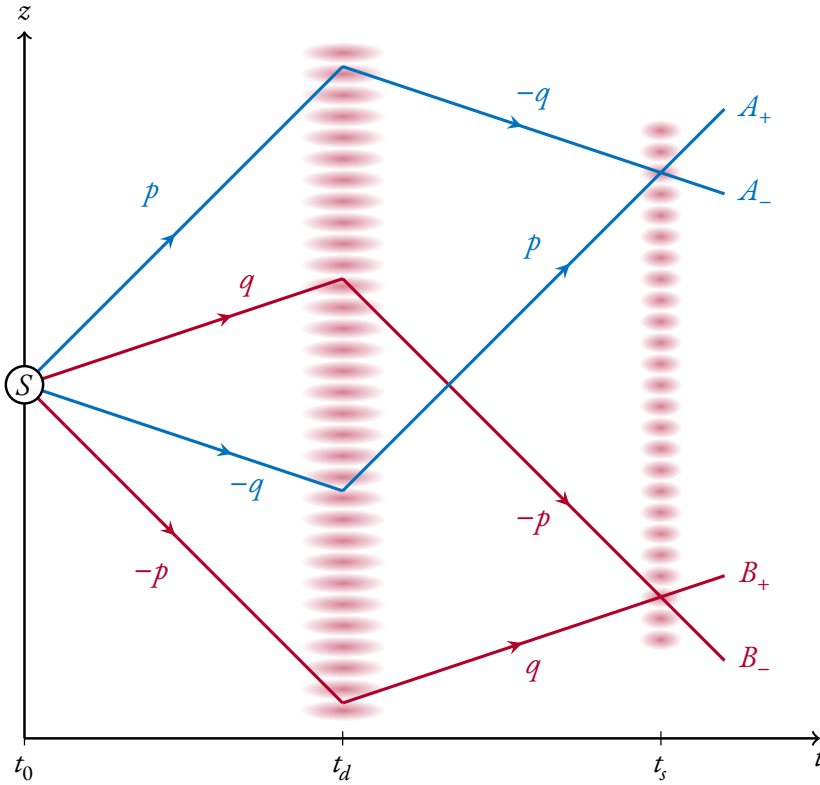


Figure 2.4: Schematic of the atomic Rarity-Tapster two-particle four modes interferometer that we want to implement so as to perform a test of Bell inequality violation. An atomic source emits two pairs of quantum correlated modes $(p, -p)$ and $(q, -q)$. A first deflection Bragg pulse is applied at $t = t_d$ so as to topologically close the interferometer. Then a second Bragg pulse is applied at $t = t_s$, realising respectively a beam splitter for Alice and for Bob.

2.2 General description

2.2.1 Topology

The figure Figure 2.4 describes the type of setup that we want to achieve¹. It is completely equivalent to the original design used by Rarity and Tapster, except that we are considering atoms (in vacuum), emitted by a source S (cf. Chapter 5) along the vertical axis, and subjected to free fall.

For now let us assume that the source is emitting a Bell state in momentum space:

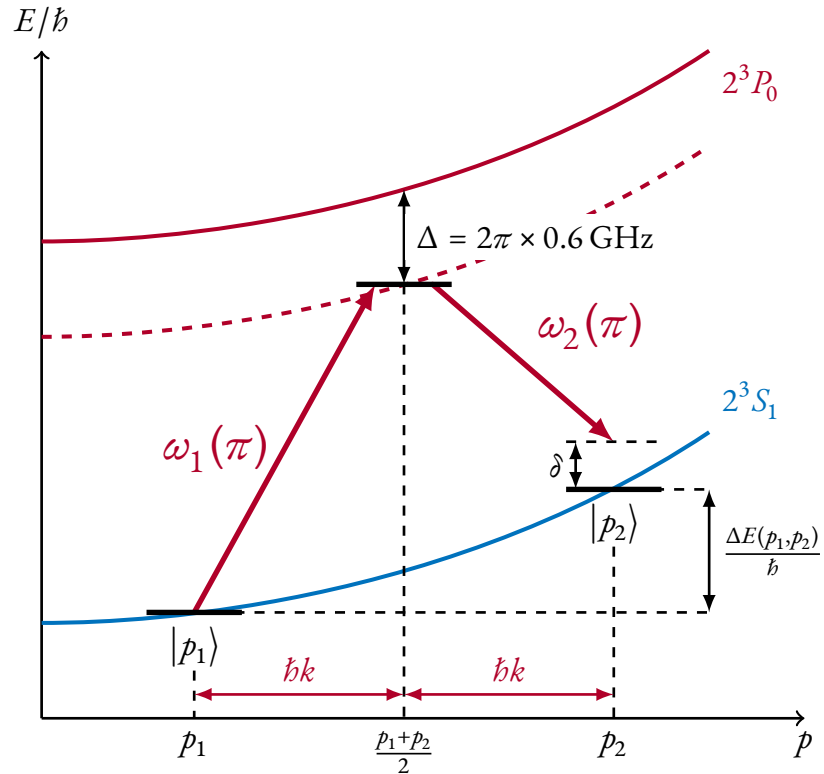
$$|\Psi\rangle = \frac{1}{\sqrt{2}} (|p, -p\rangle + |q, -q\rangle) \quad (2.13)$$

Which is an entangled two-particle state (the notation are consistent with the Figure 2.4). If we just perform the measurements after the emission from the source (corresponding to a date $t \in]t_0, t_d[$ on the Figure 2.4) we would only probe its “vanilla” correlation properties, observed with respect to a fixed given basis (the plane waves), without being able to measure a Bell parameter². Even though this work is not devoid of interest, it is not enough to claim a Bell inequality violation.

¹: pay attention to the fact the coloured lines are not trajectories, Figure 2.4 is a spacetime diagram: the emissions of the particles (helium atoms) is done along the vertical axis.

²: this is actually the current state of the experiment, and the corresponding experimental results that we have are presented in Chapter 5.

Figure 2.5: We use the 2^3P_0 excited state in order to use the same laser diode as the one used for a Raman transition that we also need on the experiment (more information are given in Remark 3.9 of Chapter 3, and in Subsection 2.1.2 of Chapter 4). The transition is operated between two $m_j = 0$ magnetic sublevels of helium, and the laser beams are therefore π polarised. The detuning Δ is very large as compared to the one-photon transition natural linewidth (1.6 MHz), so that we can approximate a coherent coupling with between two levels only ($|p_1\rangle$ and $|p_2\rangle$). The equivalent one-photon wave vector k is set by the geometrical angle between the two beams of the lattice (cf. Figure 2.6 and Eq. (2.14)). $\frac{\Delta E}{\hbar}$ is typically of the order of a few tenth of kilohertz.



To be able to change the bases used for detections, we need to mix, in a coherent manner, the natural modes $(p, -p)$ on the one hand, with the natural modes $(q, -q)$ on the other hand. Rarity and Tapster showed that such a mixing can be achieved with a two-particle four-mode interferometer, which is topologically equivalent to a double Mach-Zehnder interferometer: one for Alice (in blue) and one for Bob (in red). This requires the usage of mirrors (to “close” the interferometers) and beam splitters which (as it has been discussed in details in the Chapter 1) realise a $SU(2)$ transformation, and therefore effectively perform the desired rotation of the detection bases.

2.2.2 Bragg diffraction in brief

A fairly usual way in atom interferometry to produce mirrors and beam splitters, is to use the *Bragg diffraction* technique [88], which is nothing more than the coherent coupling between different atom velocity classes. This coupling is established with an optical lattice¹, which is resonant in a two-photon exchange process. The principle of Bragg diffraction is presented in Figure 2.5.

[88]: Cronin et al. (2009), “Optics and Interferometry with Atoms and Molecules”

¹: the beating between two laser beams, slightly detuned with each other.

The total momentum $\hbar k_{\text{bragg}}$ given to an atom when it exchanges two photons with the lattice depends on the laser wavelength, and the angle 2θ between the laser beams (Eq. (2.14)). The detuning δ to the two-photon resonance is controllable and must be set up to zero if want to be able to achieve a 100% transfer¹ (analogous to a mirror in optics).

$$\begin{cases} k = \frac{2\pi}{\lambda} \sin(\theta) & (2.14a) \\ k_{\text{bragg}} \triangleq 2k & (2.14b) \end{cases}$$

$\hbar k_{\text{bragg}}$ being fixed, given a momentum p_1 the resonance condition $\delta = 0$ is fulfilled when the angular frequency difference between both laser beams is equal to $\frac{\Delta E(p_1, p_2)}{\hbar}$:

$$\underbrace{\hbar(\omega_1 - \omega_2)}_{\triangleq \Delta\omega} = \Delta E(p_1, p_2) \quad (2.15)$$

with $p_2 = p_1 + \hbar k_{\text{bragg}}$

$$\Delta E(p_1, p_2) = \frac{p_2^2}{2m} - \frac{p_1^2}{2m} \quad (2.16a)$$

$$= \frac{\hbar k_{\text{bragg}}}{m} p_1 + \frac{\hbar^2 k_{\text{bragg}}^2}{2m} \quad (2.16b)$$

Remark 2.6 Eq. (2.16b) means that there is a linear correspondence between the angular frequency difference $\Delta\omega$ and the velocity classes (p_1, p_2) .

Since the magnitude of the Bragg kick $\hbar k_{\text{bragg}}$ is fixed by the geometry of the optical lattice, we can consider ΔE to be a function of the parameter p_1 only: Bragg diffraction always couples the velocity class $\frac{p_1}{m}$ to the velocity class $\frac{p_1 + \hbar k_{\text{bragg}}}{m} = \frac{p_1 + 2\hbar k}{m}$.

In practice, the total kick $\hbar k_{\text{bragg}}$ has been measured experimentally (with a microchannel plate (MCP): cf. Chapter 3) when the lattice was installed. We find

$$k_{\text{bragg}} = 0.550(5) k_{\text{rec}} \quad (2.17)$$

where k_{rec} is the one-photon recoil momentum with the 1083 nm laser that we use (cf. Chapter 3). We generally express our lattices' wave

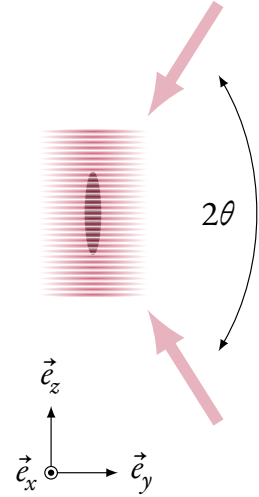


Figure 2.6: Schematic of the optical lattice used for Bragg diffraction. θ is defined as the half-angle between the beams. The coordinate system $(\vec{e}_x, \vec{e}_y, \vec{e}_z)$ is given for consistency with the Figure 3.19 (cf. Chapter 3).

¹: we can also show that when $\delta \neq 0$ there are also phases terms $e^{\pm\delta t}$ in the effective hamiltonian driving the evolution, that are preferable for us to vanish [60].

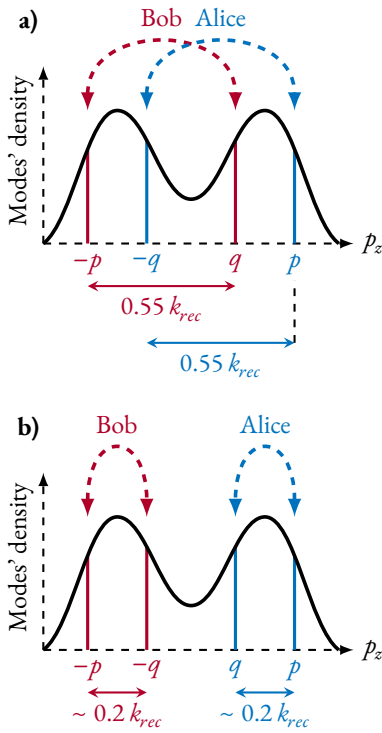


Figure 2.7: Pairing of the natural modes emitted by the source in two configurations of the Rarity-Tapster interferometer. The sub-figure **a)** on top corresponds to the geometry presented in Figure 2.4 (simpler to do experimentally), whereas the sub-figure **b)** on bottom corresponds to the Figure 2.8 (it requires a very narrow angle between both beams of the Bragg lattice).

i: these are complex numbers whose amplitude are proportional to the square-root of the intensity of the beams ($\Omega_i \propto \sqrt{I_i}$) and their argument is given by the *phase* of the lasers.

$$\left\{ \begin{array}{l} \Omega = \sqrt{\delta^2 + |\Omega_R|^2} \quad (\text{effective two-photon Rabi frequency}) \quad (2.19a) \\ \Omega_R = 2 \frac{\Omega_1 \Omega_2^*}{\Delta} \quad (\text{two-photon Rabi frequency}) \quad (2.19b) \end{array} \right.$$

We have

$$\Omega_R = |\Omega_R| e^{i\varphi} \quad (2.20)$$

where φ is the *phase difference* between both laser beam.

In the case of a *square* pulse (i.e. Ω_R and δ non-zero constants between

vectors in units of $k_{rec} \approx 5.8 \mu\text{m}^{-1}$. This corresponds to an angle

$$\theta = 32.0(6)^\circ \quad (2.18)$$

A more complete study of the Bragg diffraction, with analytical calculations about the transferred population and the resulting phase can be found in the previous PhD manuscripts of the team, in particular [8, 60, 89].

It is interesting to notice that the geometry presented on the Figure 2.8 is topologically equivalent to the one presented in Figure 2.4 (that we would like to realise first). It could even be considered to be a better configuration, as the spatial separation between Alice and Bob is larger. Indeed, we would be probing a non-local effect, spreading across larger distances, which is more interesting. However this design require much smaller values of the Bragg kick $\hbar k_{rec}$. Actually, the multi-mode source that we use emits the particles in an envelope of with two main atomic beams, in the momentum space restricted to the vertical axis (cf. Figure 2.7 and Chapter 5). While the separation between both ‘‘bumps’’ of this envelope is typically of the order of $0.6 \hbar k_{rec}$, the configuration of Figure 2.8 would require to pair modes living in a same bump, whose typical RMS width is of the order $0.1 k_{lat}$. This lead to an angle θ at least three time smaller than the current one, which may be a technical difficulty for us.

2.2.3 Formal effect of the deflector and beam splitters

Coupling matrix and degrees of freedom When a Bragg diffraction pulse is applied, the population oscillates between the coupled modes. We denote Ω_1 and Ω_2 the one-photon Rabi angular frequencies of each laser beamⁱ, and define the effective two-photon Rabi angular frequency:

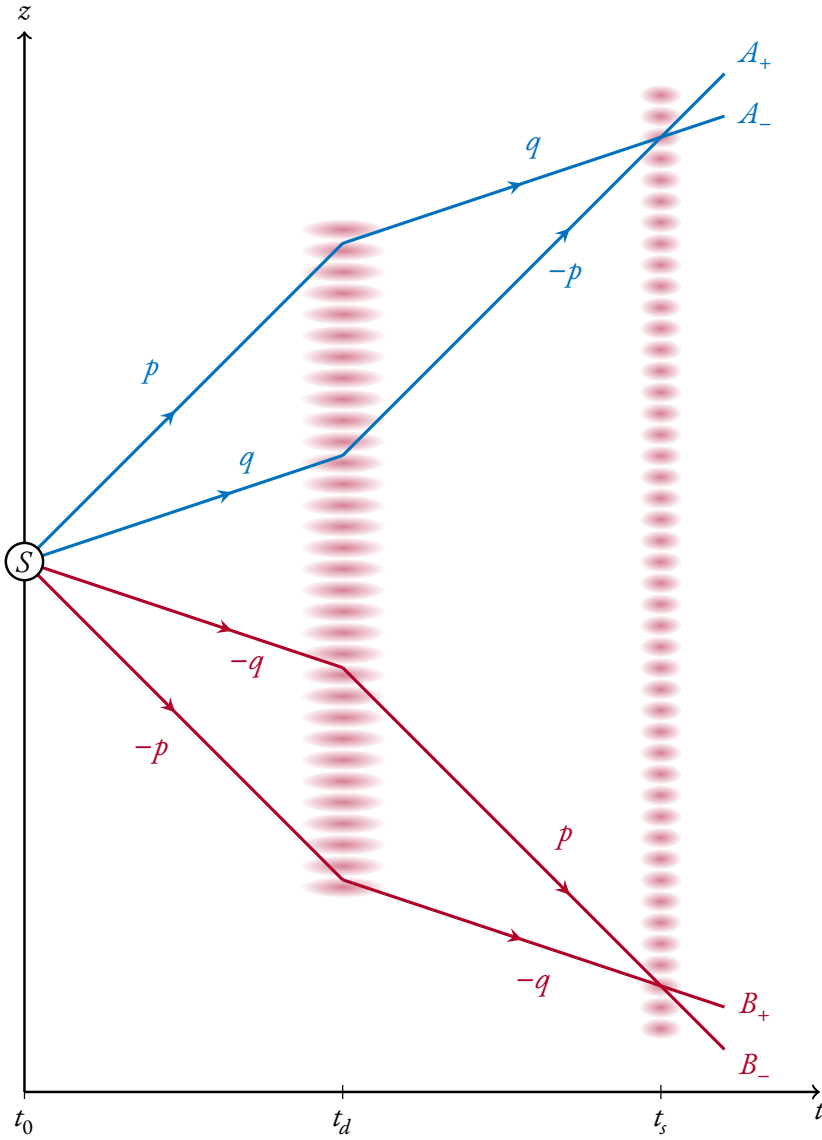


Figure 2.8: Schematic of the atomic Rarity-Tapster two-particle four modes interferometer in the large separation configuration. It is formally equivalent to the design of Figure 2.4.

$t = 0$ and $t = T$, and zero otherwise) the dynamics of the system can be solved analytically [60], and we can write the corresponding evolution operator U :

[60]: Perrier (2018), “Interférences multiples avec atomes froids”

$$U(T) = \begin{bmatrix} \left(\cos \left[\frac{\Omega T}{2} \right] - i \frac{\delta}{\Omega} \sin \left[\frac{\Omega T}{2} \right] \right) e^{i \frac{\delta T}{2}} & i \frac{|\Omega_R|}{\Omega} \sin \left[\frac{\Omega T}{2} \right] e^{i \left(\frac{\delta T}{2} + \varphi \right)} \\ i \frac{|\Omega_R|}{\Omega} \sin \left[\frac{\Omega T}{2} \right] e^{-i \left(\frac{\delta T}{2} + \varphi \right)} & \left(\cos \left[\frac{\Omega T}{2} \right] + i \frac{\delta}{\Omega} \sin \left[\frac{\Omega T}{2} \right] \right) e^{-i \frac{\delta T}{2}} \end{bmatrix} \quad (2.21)$$

This expression may seem a bit messy, but actually we recognise the general form of a $SU(2)$ operator, that we have discussed in the first chapter of this manuscript¹.

¹: in particular we can check that $\det(U) = 1$.

If we consider a couple $(|p\rangle, |q\rangle)$ of momentum states, for which the resonance condition is fulfilled ($\delta = 0$), the Bragg pulse can whether realise:

► a **mirror** (or **deflector**) when

$$\boxed{\Omega T = \pi} \Rightarrow U(T) = \begin{bmatrix} 0 & i e^{i\varphi} \\ i e^{-i\varphi} & 0 \end{bmatrix} \quad (2.22)$$

It is a π pulse: atoms are transferred from one state to the other with 100 % probability.

► a **beam splitter** when

$$\boxed{\Omega T = \pi/2} \Rightarrow U(T) = \frac{1}{\sqrt{2}} \begin{bmatrix} 1 & i e^{i\varphi} \\ i e^{-i\varphi} & 1 \end{bmatrix} \quad (2.23)$$

It is a $\pi/2$ pulse: atoms are transferred from one state to the other with 50 % probability.

In both cases the transmission and reflection phases applied are

$$\begin{cases} \varphi_\tau = 0 & (2.24a) \\ \varphi_\rho = \frac{\pi}{2} + \varphi & (2.24b) \end{cases}$$

Two important ideas must be stressed at this stage:

1. the evolution operator U also couples velocity classes that are not strictly resonant: when the small detuning δ is not zero. It means that the reflectivity profile has some width in the momenta space. This profile¹ must be studied numerically. A perturbative calculation conducted in [60] establishes that the profile of the reflectivity as a function of the small detuning δ^2 is proportional to the temporal Fourier transform of the two-photon Rabi frequency Ω_R : the shorter the pulse, the broader the reflectivity profile is. However since it comes from a perturbative approximation, this result is just a “thumb rule”, that becomes wrong when the transferred population is large (in the case of the deflector for example);
2. Ω_R being a complex number –whose argument corresponds to the phase difference φ between the laser beams– a phase may be applied to the output state. Again, due to the $\frac{i\delta}{\Omega}$ terms in the diagonal of U , this phase also depends on the velocity classes;

¹: i.e. the dependance of the reflectivity and also the *applied phase* with the detuning δ .

[60]: Perrier (2018), “Interférences multiples avec atomes froids”

²: i.e. the velocity classes that are not strictly at resonance.

Now we will see that it possible to use the *phases* applied by Alice and Bob’ respective beam splitter (obtained with the Bragg pulses (2.23)) as experimental “buttons” to compute the correlators involved in the BCHSH parameter.

This framework is different from the historical experiment of Aspect et al., where experimentalists were using the angle of polarisers (which is equivalent to the transitivity of our beam splitters) to measure the Bell parameter.

There is no formal difference between both methods, it is just simpler for us to use only 50-50 beam splitters pulses, and control the phases.

Technical implementation In practice we need to address four velocity classes (corresponding to the modes $|p\rangle, |-p\rangle, |q\rangle, |-q\rangle$ of the previous figures). We are planning to pursue a strategy keeping the optical setup as simple as possible: deflectors and beam splitters being realised with the same optical beams.

A specific numerical study must be done to find the appropriate pulses (i.e. the power and phase difference of the laser beams) performing the desired deflector and beam splitter (paying attention to the phase that is applied to the different velocity classes). This work has already been done (at least partially¹) in [60], and it is not useful to the purpose of this chapter. Therefore, we will only give the very general principle of what we want to do:

- ▶ the deflection pulse (applied at $t = t_d$ in Figure 2.4 and Figure 2.8) is “broadband”, meaning that it addresses all the velocity classes at once. This is possible using a short and intense laser pulse (therefore with a large value of Ω_R);
- ▶ the beam splitters (applied at $t = t_s$ in Figure 2.4 and Figure 2.8) are obtained with multiplexed “narrowband” pulses: meaning that one of the two beams forming the lattice contains two frequencies, creating two lattices addressing respectively Alice’s couple of modes $(p, -q)$ and Bob’s one $(-p, q)$.

Concretely, the temporal profile of the pulses ($\Omega_R[t]$) are sinc functions, multiplied by a large window function (for apodisation). The choice of sinc functions is inspired by the perturbative approach (a sinc in the time domain giving a square in the momenta space). We checked numerically that even if the regime is clearly not perturbative² the sinc shape is still giving good results.

In the following we will just consider the situation of Figure 2.4, and assume that thanks to the Bragg pulses³, it corresponds to the experiment presented in [90]. The output modes can be written in basis of

1: Charlie Leprince, PhD student and my colleague on the experiment, performed additional numerical simulations to refine this work. This was useful to have a better understanding of what we need to implement to the apparatus to realise the Bragg pulses. This complementary work can be found in his master’s degree internship report, or in his PhD manuscript (coming out next year).

2: $\sim 50\%$ of transferred population with a BS pulse, and $\sim 100\%$ with a mirror

3: with the notations of Figure 2.4 and Figure 2.8, we have a π pulse at $t = t_d$ and $\pi/2$ pulses at $t = t_s$.

[90]: Dussarrat (2017), “Expériences d’Optique Atomique Quantique, Interféromètres à 2 et 4 modes”

the natural emitted modes:

$$\left\{ \begin{array}{l} |A_+\rangle = \frac{-1}{\sqrt{2}} [e^{-i(\varphi_a - \varphi_d)} |p\rangle + ie^{-i\varphi_d} |-q\rangle] \end{array} \right. \quad (2.25a)$$

$$\left\{ \begin{array}{l} |A_-\rangle = \frac{-1}{\sqrt{2}} [ie^{i\varphi_d} |p\rangle + ie^{i(\varphi_a - \varphi_d)} |-q\rangle] \end{array} \right. \quad (2.25b)$$

$$\left\{ \begin{array}{l} |B_+\rangle = \frac{-1}{\sqrt{2}} [e^{-i(\varphi_b - \varphi_d)} |q\rangle + ie^{-i\varphi_d} |-p\rangle] \end{array} \right. \quad (2.25c)$$

$$\left\{ \begin{array}{l} |B_-\rangle = \frac{-1}{\sqrt{2}} [ie^{i\varphi_d} |q\rangle + ie^{i(\varphi_b - \varphi_d)} |-p\rangle] \end{array} \right. \quad (2.25d)$$

where φ_d is a phase applied the deflection (π) pulse, and (φ_A, φ_B) are the phases applied by Alice and Bob beam splitters. φ_A and φ_B are the “buttons” used by Alice and Bob to measure a Bell parameter.

With previous parametrisation, one can check that the emitted state $|\Psi\rangle$ of (2.13) writes:

$$\begin{aligned} |\Psi\rangle &= \frac{\sqrt{2}}{4} [-i(e^{i\varphi_a} + e^{i\varphi_b})] |A_+, B_+\rangle \\ &+ \frac{\sqrt{2}}{4} [e^{i(\varphi_a - \varphi_b)} - 1] |A_+, B_-\rangle \\ &+ \frac{\sqrt{2}}{4} [e^{-i(\varphi_a - \varphi_b)} - 1] |A_-, B_+\rangle \\ &+ \frac{\sqrt{2}}{4} [-i(e^{-i\varphi_a} + e^{-i\varphi_b})] |A_-, B_-\rangle \end{aligned} \quad (2.26)$$

leading to output probabilities very similar to Eq. (2.10):

$$\left\{ \begin{array}{l} P_{A_+, B_+}(\varphi_a, \varphi_b) = P_{A_-, B_-}(\varphi_a, \varphi_b) = \frac{1}{2} \cos^2\left(\frac{\varphi_a - \varphi_b}{2}\right) \end{array} \right. \quad (2.27a)$$

$$\left\{ \begin{array}{l} P_{A_+, B_-}(\varphi_a, \varphi_b) = P_{A_-, B_+}(\varphi_a, \varphi_b) = \frac{1}{2} \sin^2\left(\frac{\varphi_a - \varphi_b}{2}\right) \end{array} \right. \quad (2.27b)$$

Therefore, we find a correlator also similar to Eq. (2.11):

$$E(\varphi_a, \varphi_b) = \cos(\varphi_a - \varphi_b) \quad (2.28)$$

1: let us recall that both φ_a and φ_b themselves are interpreted as a phase difference between the two laser beams creating the beam splitters.

The correlator oscillates with the phase difference¹ $\Delta\phi = \varphi_a - \varphi_b$. In practice it means that it enough to control the phase difference $\Delta\phi$, and measure an oscillation of E with an amplitude larger than $\frac{\sqrt{2}}{2}$ to claim a Bell inequality violation.

Remark 2.7 (Is the Rarity-Tapster setup an interferometer?) The oscillation (2.28) of E does not have the same status as the oscillation observed in a regular one-particle interferometer (a Mach-Zehnder

for example). It is not the oscillation of an intensity (fringes), but of a correlations between two detections.

One can easily check that neither Alice nor Bob see an oscillating signal at their respective outputs:

$$P(A_+) = P(A_-) = P(B_+) = P(B_-) = \frac{1}{2} \quad (2.29)$$

One could argue that an interferometer should be (by definition) a phase correlator of a one-particle state. We do not intend to fuel a semantic debate, but we choose to call this type configuration a *two-particle interferometer*.

2.3 Well-suited Bell inequalities

Due its similarity with the correlator used CHSH inequality, Eq. (2.28) may seem satisfying. However in the previous paragraph we assumed that exactly two particles were propagating in the interferometer: this is actually the very first hypothesis that we made, by writing the input state (2.13) with a Bell state.

The “problem” is that we cannot prepare such a state. As it has been explained in Chapter 1 (and will be developed in Chapter 5), the source at our disposal produces tensor product of two-mode squeezed vacuum states. Let us recall the expression of such a state:

$$|\Psi\rangle = \left[\sqrt{1 - |\alpha|^2} \sum_{n=0}^{\infty} \alpha^n |n\rangle_p |n\rangle_{-p} \right] \otimes \left[\sqrt{1 - |\beta|^2} \sum_{n=0}^{\infty} \beta^n |n\rangle_q |n\rangle_{-q} \right] \quad (2.30)$$

Where the number of particle per mode for each TMS are given by

$$\nu_a = \frac{|\alpha|^2}{1 - |\alpha|^2} \quad \nu_b = \frac{|\beta|^2}{1 - |\beta|^2} \quad (2.31)$$

ν_a and ν_b are positive real numbers, let us assume $|\alpha| = |\beta|$ for simplicity. During an experiment, the detectors (single particle counters) placed on the channels A_+ , A_- , B_+ and B_- return positive integer values. This is a priori not a problem since the CHSH inequality is still valid in a generalised context where the measured observables are continuous variables (cf. Remark 2.3).

One can however notice that in the limit $\nu \xrightarrow{|\alpha| \rightarrow 0} 0$, the two brackets in (2.30) can be approximated to the vacuum and the first order in $|\alpha|$

contributions, in extenso:

$$|\Psi\rangle \underset{\nu \rightarrow 0}{\approx} (1 - |\alpha|^2) \left[|0\rangle + \alpha \underbrace{(|1\rangle_p |1\rangle_{-p} + e^{i\phi} |1\rangle_q |1\rangle_{-q})}_{|\Phi\rangle} \right] \quad (2.32)$$

whose non-empty part $|\Phi\rangle$ is exactly a Bell state (up to a normalisation factor and a phase $\phi = \arg[\beta/\alpha]$). That means that during an experiment, if the pair creation rate is small ($\nu \rightarrow 0$), and if we do not consider the realisations where no particle is detected (removing the vacuum), we expect to recover the same type of physics as the one presented in the previous section.

Nonetheless, in the general case, the question is to know which observable and correlator are to consider in order to construct a Bell parameter that exceed the critical value of 2. Based on the reference [73], we will show in the following different approaches, and conclude about the most suitable for us regarding the constraints imposed by our apparatus.

[73]: Kitzinger et al. (2021), “Bell Correlations in a Split Two-Mode-Squeezed Bose-Einstein Condensate”

2.3.1 First natural approach

Let us first introduce the numbers $N_{A_+}(\varphi_a)$, $N_{A_-}(\varphi_a)$, $N_{B_+}(\varphi_b)$ and $N_{B_-}(\varphi_b)$ corresponding to the number of particles counted at each channel during an experimental realisation. These are all **positive integers**. We also introduce:

$$\begin{cases} N_A = N_{A_+}(\varphi_a) + N_{A_-}(\varphi_a) & (2.33a) \\ N_B = N_{B_+}(\varphi_b) + N_{B_-}(\varphi_b) & (2.33b) \end{cases}$$

the total number of particles measured by Alice and Bob during a realisation. The conservation of the number of particles at the beam splitters implies that N_A and N_B are independent of φ_a and φ_b . We also define

$$\begin{cases} S_A(\varphi_a) = N_{A_+}(\varphi_a) - N_{A_-}(\varphi_a) & (2.34a) \\ S_B(\varphi_b) = N_{B_+}(\varphi_b) - N_{B_-}(\varphi_b) & (2.34b) \end{cases}$$

the differences of number of particles measured by Alice and Bob.

i: historically, it was the correlator used by Rarity and Tapster in their experiment.

We define the *normalised averaged* correlator[†]:

$$E_I(\varphi_a, \varphi_b) = \frac{\langle S_A(\varphi_a) S_B(\varphi_b) \rangle}{\langle N_A N_B \rangle} \quad (2.35)$$

It is possible to prove that it is subjected to the same inequality as the CHSH one (2.5), but using a slightly different derivation as the one presented in the first section¹ [19].

One can expand the terms of (2.35), and check that

$$E_I(\varphi_a, \varphi_b) = P_{+,+}(\varphi_a, \varphi_b) - P_{+,-}(\varphi_a, \varphi_b) - P_{-,+}(\varphi_a, \varphi_b) + P_{-,-}(\varphi_a, \varphi_b) \quad (2.36)$$

where

$$P_{i,j \in \{+,-\}}(\varphi_a, \varphi_b) = \frac{\langle N_{A_i}(\varphi_a) N_{B_j}(\varphi_b) \rangle}{\langle N_{A_+} N_{B_+} \rangle + \langle N_{A_+} N_{B_-} \rangle + \langle N_{A_-} N_{B_+} \rangle + \langle N_{A_-} N_{B_-} \rangle} \quad (2.37)$$

$P_{i,j}(\varphi_a, \varphi_b) \in [0, 1]$ is a crossed detection probability, thus once written in its expanded form (2.36) the correlator E_I is reminiscent of Eq. (2.9). This correlator has been proposed by Ralph et al. [91], exposing this approach to show a CHSH inequality violation from continuous variable. The appreciable point about this correlator is that it is very close to the one that we studied in the first section, when we were manipulating a genuine Bell state. It is actually quick to check that the restriction to the one particle domain ($N_A = N_B = 1$) leads to the exact same observable and correlator as in the first sections: $S_A, S_B \in \{-1, 1\}$. Eq. (2.35) is therefore sort of a generalisation of the “usual” correlator, used to perform a two-particle CHSH inequality violation.

The relations Eq. (2.25) are still valid. Knowing the state (2.30), and by injecting the quadruplet of optimal angles²

$$\varphi_a = 0 \quad \varphi_b = \frac{\pi}{8} \quad \varphi_{a'} = \frac{\pi}{4} \quad \varphi_{b'} = \frac{3\pi}{8}$$

one can compute analytically the corresponding Bell parameter S as a function of the population ν . The calculation gives:

$$S(\nu) = 2\sqrt{2} \cdot \frac{1 + \nu}{1 + 3\nu} \quad (2.38)$$

which is plotted on Figure 2.9. When $\nu \rightarrow 0$, S reaches its maximal value³ $2\sqrt{2}$. This is an expected behaviour since with this method the vacuum contribution to the correlator implicitly vanishes. Indeed, if we label with the superscript (i) the experimental realisations the correlator E_I concretely measured with n realisations writes:

$$E_I(\varphi_a, \varphi_b) = \frac{S_A^{(1)} S_B^{(1)} + S_A^{(2)} S_B^{(2)} + \dots + S_A^{(n)} S_B^{(n)}}{N_A^{(1)} N_B^{(1)} + N_A^{(2)} N_B^{(2)} + \dots + N_A^{(n)} N_B^{(n)}} \quad (2.39)$$

1: indeed, if we wanted to interpret the normalised averaged correlator Eq. (2.35) as the correlator (2.2) of the CHSH inequality proof, one should consider the observable $\frac{S_A(\varphi_a)}{\langle N_A N_B \rangle}$ and $\frac{S_B(\varphi_b)}{\langle N_A N_B \rangle}$ which are not bounded to $[-1, 1]$, and therefore do not satisfy the hypotheses of the proof.

[19]: Clauser et al. (1974), “Experimental consequences of objective local theories”

[91]: Ralph et al. (2000), “Proposal for the Measurement of Bell-Type Correlations from Continuous Variables”

2: optimal at least in the $\nu \rightarrow 0$ limit.

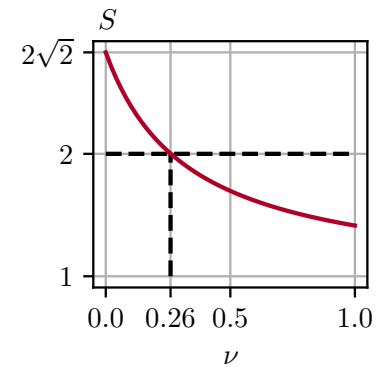


Figure 2.9: Bell parameter as a function of the population ν , using Ralph et al. correlator E_I . The black dashed line represent the CHSH critical value. Bell’s inequality is violated for $\nu \leq 0.26$.

3: the first Tsirelson’s bound.

if during a realisation (i) the vacuum turns out to be measured on a side (let us assume Alice's one), we have $N_A^{(i)} = 0$ and therefore $S_A^{(i)}$, which effectively just removes one term on both the numerator and the denominator: we have an effective postselection of the vacuum.

Therefore in the small population limits only the non-vacuum part –that can be approximated by a Bell state– contributes to the signal and we find the usual result $S = 2\sqrt{2}$.

An other remarkable property of this approach is that the measured Bell parameter $S(\nu)$ is *independent* of the quantum efficiency η of the detector! It is pretty simple to see regarding Eq. (2.37), since –by definition of the quantum efficiency– the only effect of the losses on the $P_{i,j}$ s is to add a η^2 factor on both the numerator and the denominator, that cancel out immediately.

However, it is natural to think that when the population ν increases, the level of entanglement of system increases as well. Indeed, two-mode squeezed states are completely entangled states, therefore increasing the population means increasing the number of particles involved in this entanglement. One could argue that it is a bit strange to find a Bell parameter decreasing –which is a priori the signature of *less quantum effects*– whereas the expected level of entanglement increases.

2.3.2 Second approach: projection onto two-outcomed events observables

[73]: Kitzinger et al. (2021), “Bell Correlations in a Split Two-Mode-Squeezed Bose-Einstein Condensate”

An alternative approach was proposed by Nemoto et al. [73]. The idea is to consider the observables $\text{sgn}[S_A(\varphi_a)]$ and $\text{sgn}[S_B(\varphi_b)]$ where

$$\begin{aligned} \text{sgn}: \quad \mathbb{R} &\rightarrow \mathbb{R} \\ x &\mapsto \begin{cases} -1 & \text{if } x < 0 \\ +1 & \text{if } x \geq 0 \end{cases} \end{aligned} \quad (2.40)$$

Then we can define a correlator E_{II} :

$$E_{\text{II}}(\varphi_a, \varphi_b) = \langle \text{sgn}[S_A(\varphi_a)] \text{sgn}[S_B(\varphi_b)] \rangle \quad (2.41)$$

Since both $\text{sgn}[S_A(\varphi_a)]$ and $\text{sgn}[S_B(\varphi_b)]$ are contained in $\{-1, 1\}$, E_{II} is can be used to build a CHSH inequality, based on its original derivation.

Actually in the previous case, the Bell parameter was quickly decreasing with ν due to the harmful contribution of the terms involving more than 2 particles, which effectively reduced the amplitude of the correlator E_I . In this second approach, all the measurements are projected onto the two outcomes +1 and -1. Even without giving a rigorous mathematical proof, we can have the insight that this projection has a damping effect onto the contribution of the realisation involving a large number of particles. We expect a better behaviour of the Bell parameter when the population increases.

We can have a numerical estimation of the Bell parameter, using the correlator E_{II} . However, the finite quantum efficiency of the detectors no longer cancel out, and must be taken into account in the calculations. The implementation of the losses due to the finite quantum efficiency is very similar to the one that we used in the previous chapter, the details of the derivation of the formulae can be found in the original publication [73]. We give the final result anyway:

$$G_{N_+, N_-}^\eta = 1 - 2 \sum_{\substack{0 \leq n \leq N_+ \\ 0 \leq m \leq N_- \\ n < m}} \binom{N_+}{N_+ - n} \binom{N_-}{N_- - m} \eta^{n+m} (1 - \eta)^{N_+ + N_- - n - m} \quad (2.42)$$

is the lossy $\text{sgn}[S]$ operator. Then the Born's rule gives the probability of a given outcome:

$$P_{\varphi_a, \varphi_b}(N_{A_+}, N_{A_-}; N_{B_+}, N_{B_-}) = |\langle \Psi | N_{A_+}, N_{A_-}; N_{B_+}, N_{B_-} \rangle|^2 \quad (2.43)$$

and finally

$$E_{II}(\varphi_a, \varphi_b) = \sum_{N_{A_+}, N_{A_-}, N_{B_+}, N_{B_-}=0}^{\infty} P_{\varphi_a, \varphi_b}(N_{A_+}, N_{A_-}; N_{B_+}, N_{B_-}) G_{N_{A_+}, N_{A_-}}^\eta G_{N_{B_+}, N_{B_-}}^\eta \quad (2.44)$$

A numerical calculation of the variations of the Bell parameter with the population is plotted in [Figure 2.10](#). Let us make a commentary about it:

1. whatever the quantum efficiency, when ν goes to zero, S goes to 2. This is no surprise, because the state $|\Psi\rangle$ is then approximated by the vacuum, which gives $E_{II}(\varphi_a, \varphi_b) = 1$ whatever the orientations of the detectors, and therefore $S = 1 + 1 + 1 - 1 = 2$.
2. When the quantum efficiency is large ($\geq 85\%$), the Bell parameter S increases with the population, which is very good! This

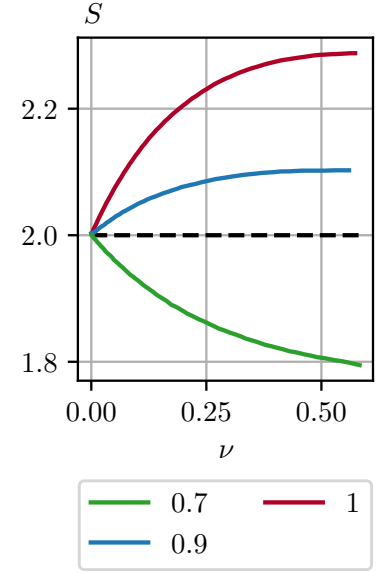


Figure 2.10: Bell parameter as a function of the population ν , using the correlator E_{II} (2.41). The black dashed line represent the CHSH critical value. The lines are labelled with the quantum efficiency of the detectors.

[73]: Kitzinger et al. (2021), “Bell Correlations in a Split Two-Mode-Squeezed Bose-Einstein Condensate”

is what we was hopping for: the Bell parameter increases when the level of correlations in the system increases. However, the strength of the violation is smaller than in the previous case ($S < 2.3$).

3. The most serious problem is that the violation collapses quickly when the quantum efficiency is not close to 1. In the case of our experiment, where the quantum efficiency is approximately 50 %, this approach is **unusable**.

2.3.3 Third approach based on the CH inequality

The main reason that explains the fact the Bell inequality violation can be strong with the first approach is that the vacuum do not contribute to the signal. Indeed, vacuum obviously do not contain any correlation, and may only have a negative effect on the measured Bell parameter. The idea of this third approach is to cumulate the advantages of both previous methods:

1. find a way to reject vacuum's contribution (inspired by the first approach), so has to keep the maximal value of the Bell parameter to a large value (if possible $2\sqrt{2}$);
2. project the results of the experimental realisations onto two-outcomes event, taking the values ± 1 , so as to have a better behaviour when the population increases;

This approach is steered by the Clauser and Holt (CH) inequality. This inequality —proved in 1974 [19]— is a constraint built from *outcomes' probabilities*¹ (joint and single-channels), it requires to consider two-outcome measurements, returning either the value +1 or -1.

[19]: Clauser et al. (1974), “Experimental consequences of objective local theories”

¹: which is slightly different from the original CHSH formulation which is only involving correlation functions. The proof of the inequality may be found in [19].

By using the notation $P_{i,j}$ (with $i, j \in \{+, -\}$) of the first section (notations introduced with Eq. (2.9)) and using the symbol “ \forall ” for the marginal probabilities:

$$\left\{ \begin{array}{l} P_{\forall, \forall} = \sum_{i,j=\pm} P_{i,j}(\varphi_a, \varphi_b) \quad (2.45a) \\ P_{i, \forall}(\varphi_a) = \sum_{j=\pm} P_{i,j}(\varphi_a, \varphi_b) \quad (2.45b) \\ P_{\forall, j}(\varphi_b) = \sum_{i=\pm} P_{i,j}(\varphi_a, \varphi_b) \quad (2.45c) \end{array} \right.$$

the CH inequality reads (long double inequality written on two lines):

$$\begin{aligned} -P_{\forall,\forall} &\leq P_{i,j}(\varphi_a, \varphi_b) + P_{i,j}(\varphi_a, \varphi'_b) + P_{i,j}(\varphi'_a, \varphi_b) \\ &\quad - P_{i,j}(\varphi'_a, \varphi'_b) - P_{i,\forall}(\varphi_a) - P_{\forall,j}(\varphi_b) \leq 0 \end{aligned} \quad (2.46)$$

It is easy to derive from (2.46) an other inequality that resemble to the CHSH one $S \leq 2$. Just by considering the quantity

$$E_{\text{III}}(\varphi_a, \varphi_b) = \frac{1}{P_{\forall,\forall}} \sum_{i,j=\pm} (i \times j) P_{i,j}(\varphi_a, \varphi_b) \quad (2.47)$$

Proof

$$\begin{aligned} (2.46) \underset{(i=j)}{\Rightarrow} & P_{i,i}(\varphi_a, \varphi_b) + P_{i,i}(\varphi_a, \varphi'_b) + P_{i,i}(\varphi'_a, \varphi_b) \\ & - P_{i,i}(\varphi'_a, \varphi'_b) \leq P_{i,\forall}(\varphi_a) + P_{\forall,i}(\varphi_b) \end{aligned} \quad (\dagger)$$

and

$$\begin{aligned} (2.46) \underset{(j=-i)}{\Rightarrow} & -P_{i,-i}(\varphi_a, \varphi_b) - P_{i,-i}(\varphi_a, \varphi'_b) - P_{i,-i}(\varphi'_a, \varphi_b) \\ & + P_{i,-i}(\varphi'_a, \varphi'_b) \leq P_{\forall,\forall} - P_{i,\forall}(\varphi_a) - P_{\forall,-i}(\varphi_b) \end{aligned} \quad (\ddagger)$$

then $(\dagger) + (\ddagger)$ gives

$$E_{\text{III}}(\varphi_a, \varphi_b) + E_{\text{III}}(\varphi'_a, \varphi_b) + E_{\text{III}}(\varphi_a, \varphi'_b) - E_{\text{III}}(\varphi'_a, \varphi'_b) \leq 2 \quad \blacksquare$$

Now we still need to define actual observables, in order to have a concrete definition of the probabilities $P_{i,j}$. The strategy is the following:

1. the vacuum is postselected, meaning that if either Alice or Bob measure zero particle on both their channels (+ and -) during an experimental realisation, this realisation is dropped.
2. if at least one particle is detected on both side ($N_A, N_B \geq 1$), then Alice and Bob consider the observables, $\text{sgn}[S_A(\varphi_a)]$ and $\text{sgn}[S_B(\varphi_b)]$, that we already introduced in the second approach.

More formally, if we denote Π the orthogonal projection operator, projecting the states onto the hyperplane orthogonal to the vacuum (i.e. the non-empty subspace), by definition of $P_{\forall,\forall}$ we have

$$P_{\forall,\forall} = \langle \Pi \rangle \quad (2.48)$$

and E_{III} can be rewritten in an expression exhibiting the fact that it is indeed a correlation function:

$$E_{\text{III}}(\varphi_a, \varphi_b) = \frac{\langle \Pi \text{sgn} [S_A(\varphi_a)] \Pi \text{sgn} [S_B(\varphi_b)] \rangle}{\langle \Pi \rangle} \quad (2.49)$$

which is (just like E_{I}) a *normalised* correlator.

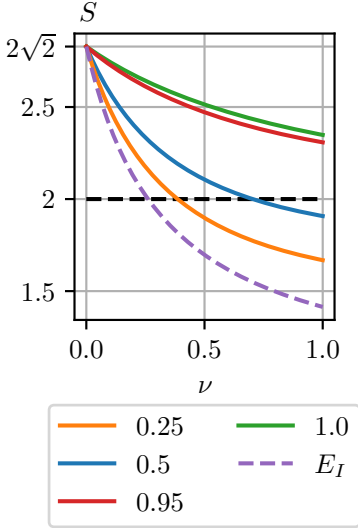


Figure 2.11: Bell parameter as a function of the population ν , using the correlator E_{III} (2.49). The black dashed line represent the CHSH critical value. The lines are labelled with the quantum efficiency of the detectors. We also plotted (mauve dashed line) the result of the first approach for comparison. With the quantum efficiency of our detector ($\eta = 0.5$) the Bell inequality is violated for $\nu \lesssim 0.7$.

[73]: Kitzinger et al. (2021), “Bell Correlations in a Split Two-Mode-Squeezed Bose-Einstein Condensate”

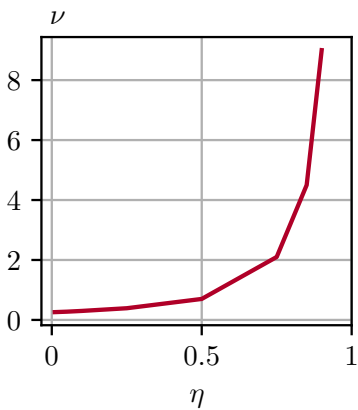


Figure 2.12: Saturation of the Bell inequality as a function of the population.

¹: as it can be the case in quantum optics.

Now we can again perform some numerical simulations, and check if there is an experimental interest with this approach. Just as in the previous case (with the correlator E_{II}) there is no simple simplification of the quantum efficiency here, and it must be taken into account during the numerical computations. Just as before, the finite quantum efficiency is treated as particle losses, similarly to the previous case (more information can be found in [73]). The results are plotted in Figure 2.11.

Even though, the Bell parameter S is decreasing with the population ν , it is significantly larger than the one resulting from the first correlator E_{I} , which is very satisfying.

An other interesting visualisation, is the profile of the population giving $S = 2$ (saturation of the Bell inequality) as a function of the quantum efficiency. This is plotted in Figure 2.12. We observe that this functions increases exponentially fast, meaning that using detectors with a quantum efficiency close to 100%¹ allows to obtain a Bell inequality violation with very large populations. In our case, with $\eta \approx 0.5$, we find $\nu_{\text{max}} \approx 0.7$, which is a gain of almost a factor 3 compared to the first approach.

Conclusion

In this chapter we have recalled what the CHSH Bell inequality is, and how it can be tested with a Rarity-Tapster interferometer. In particular, we have seen that even though the use of a two-mode squeezed state for the purpose of such an experiment is generally deteriorates the quality of the signal, the smart choice of the nonlocal correlator can improve the degree of violation, even with a finite quantum efficiency.

In a practical experiment, if we aim at obtaining a BCHSH parameter $S \approx 2.5$, with the simple approach of Ralph et al. (based on the correlator E_I) we should use an average population per mode $\nu \approx 0.07$, whereas with the third approach a population $\nu \approx 0.14$ is enough. Therefore, there is roughly a gain of a factor of 2, which is a huge improvement experimentally speaking, as it means that we can double our signal-to-noise ratio.

EXPERIMENTAL WORKS

Preparation of a Bose-Einstein condensate and single atom detection

3

Chapter's table of contents

. Introduction	102
1. Metastable helium	103
1.1 Spectroscopy	103
1.2 Collision theory	106
1.2.1 Elastic collision	107
1.2.2 Inelastic & ionising collisions	108
Two-body collisions	108
Three-body collisions	111
2. Detecting individual atoms in the momentum space	112
2.1 Microchannel plate	112
2.2 Generation of 3D data: delay lines, electronics & software	114
2.2.1 Delay lines & electronics	114
Principle	114
2.2.2 Reconstruction algorithm	120
2.2.3 From timestamps to velocities	123
2.2.4 A word about the resolution	124
2.2.5 Comparison between performances	125
3. Cooling of the metastable helium cloud: down to the BEC	127
3.1 Source of metastable helium	127
3.2 Cooling procedure	128
3.2.1 Transverse optical molasses and Zeeman slower	130
3.2.2 Magneto-optical trap & optical molasses	131
MOT loading	131
Optical molasses	132
3.2.3 Magnetic trap	133
Idea	133
Shape of the trap	134
Atoms pumping & Doppler cooling	136
Evaporation in the magnetic trap	137
3.2.4 Optical dipole trap (ODT)	139
Presentation	139
Vertical beam	139
Single beam issues	139
Crossed dipole trap	142
Final cloud	143
3.2.5 Recap	145

Introduction

The realisation of a Bose-Einstein condensate (BEC) is at the very core of our experimental procedure. As it will be discussed in the last chapter of this manuscript, the BEC acts as a cornerstone for the generation of non-classical states. Therefore, Bose-Einstein condensation is “*step zero*” in our process, and its stable generation is a mandatory condition to any experimental attempt. The successive cooling stages of the metastable helium cloud, from room temperature down to the quantum phase transition, will be an important topic of interest in this chapter.

But before giving a complete depiction of our cooling techniques, we will first discuss the crucial question of the detection of the signal. We will show in particular that our choice of atomic species is completely related to the technology we are using: a single-atom momentum resolved detector.

In this chapter, we will deal with many experimental techniques, several of those having been implemented by my predecessors, working on the experiment since its very early stages back in 1996. We will highlight with a blue background frame the recent innovations that I contributed to set up during my work in the team: namely the **compression of the MOT**, the **fluorescence imaging calibration**, the **new MCP installation**, the **new setup for the optical dipole trap (ODT)**.

1 Metastable helium

1.1 Spectroscopy

Helium –whose name is modestly derived from *Helios* (ancient Greek deity of the Sun)¹– exists under only two *stable* isotopic forms: ${}^3\text{He}$ –a fermion– with the incredibly small natural abundance on Earth of $2 \cdot 10^{-4} \%$; and the bosonic form ${}^4\text{He}$, which is much more common. As we are interested in the realisation of a BEC, we will obviously only deal with the latter in the following.

1: Helium was first detected on August 18th, 1868, by French astronomer Jules Janssen, as an unknown spectral line during a complete solar eclipse.

Helium has two electrons, but only one of them can be in an excited state. Indeed, any configuration with both electrons in an excited state would have an energy larger than the ionisation threshold, and therefore lead to the self-ionisation of the atom. Thus ${}^4\text{He}$ behaves as an effective one-electron atom². For convenience, we therefore extend the Russel-Saunders term symbols $n^{2S+1}L_J$ of the alkali metals to the noble gases, helium in particular.

2: this is fairly common for noble gases

Like most noble gases³, ${}^4\text{He}$ does not have nuclear spin, which entails the absence of hyperfine structure. That reduces the complexity of the spectroscopic structure by an appreciable amount. The specific case of helium is even simpler: since there are only two electrons (core and valence) they share the same S-state, leaving only two possible types of configurations:

3: and unlike alkali metals...

- *parahelium*, corresponding to the singlet states, with the two electrons having anti-parallel spins $|\uparrow\downarrow\rangle$. The total spin S is 0 ;
- *orthohelium*, that corresponds to the triplet states, with the two electrons having parallel spins $|\uparrow\uparrow\rangle$. The total spin S is 1 ;

any transition between these two domains is “*forbidden*” by selection rules, as it does not conserve the total spin.

This prohibition of optical transition between orthohelium and parahelium is the first reason of the apparition of a *metastable* state. One should indeed notice (c.f. Figure 3.1) that the first excited state 2^3S_1 is a triplet state, whereas the ground state 1^1S_0 is singlet. The second reason is that 2^3S_1 and the ground state share the same angular momentum quantum number ($S \leftrightarrow l = 0$), which makes the single-photon electric dipole decay impossible.

Its decay to ground state being twice-forbidden, the 2^3S_1 has an ex-

Table 3.1: Some important physical properties of metastable helium.

Physical quantity	Notation	Numerical Value
Mass	m	$6.646 \cdot 10^{-27}$ kg
Metastable state lifetime [92]	τ^*	7870(510) s
S-wave scattering length [93]	a	7.512(5) nm

[92]: Hodgman et al. (2009), “Metastable Helium”

1: with $S = J = 1$, the Landé g -factor of the state is equal to the electron spin g -factor $g_s \approx 2$. It leads to a magnetic force twice as big as for the alkali species.

2: with distributed Bragg reflector (DBR) laser diode, or distributed feedback laser (DFB) (diode or optical-fiber).

[94]: Kapitza (1938), “Viscosity of Liquid Helium below the λ -Point”

3: it is a $J \rightarrow J + 1$ transition that allows a simple magneto-optical trap (MOT) scheme.

[97]: Robert et al. (2001), “A Bose-Einstein Condensate of Metastable Atoms”

[98]: Pereira Dos Santos et al. (2001), “Bose-Einstein Condensation of Metastable Helium”

tremely long half-life time. It is actually the longest-lived neutral atomic state (τ^* is 2 h 11 !) and its characteristic decay time has been measured to be in very good agreement with QED predictions [92]. It is in particular much longer than the typical time required to prepare a BEC (~ 15 seconds with the last improvements of our apparatus). The spin-induced magnetic dipole of the state¹ 2^3S_1 allows the use of magnetic trapping techniques, which is also experimentally appealing for the purpose of the preparation of a metastable BEC. Finally, the $1.08 \mu\text{m}$ optical coupling with the $2^3P_{0,1,2}$ states is perfectly suitable to perform laser cooling with a cycling transition:

1. it is experimentally accessible² ;
2. the selection rules guarantee a return to the metastable state ;
3. the associated lifetime is short: roughly 98 ns ;

Remark 3.1 Although not formally impossible, the realisation of a BEC of helium on the genuine ground state, in a diluted phase (gas), would be quite challenging, and has not yet been achieved. The Landé g -factor of the ground state being zero, it is not possible to magnetically trap it, and the laser cooling would require intense XUV laser sources in order to perform the coupling with the far above excited states 2^1L_J , which seems rather difficult to achieve with contemporary technology.

However, in condensed matter, superfluid helium-4 (which is indeed a BEC) has been obtained in 1937 [94].

Manipulating metastable helium with the $2^3S_1 \rightarrow 2^3P$ transitions is therefore quite standard, the P_2 line ($2^3S_1 \rightarrow 2^3P_2$) being used for the first laser cooling stages³. The first BECs of helium have been observed for the first time (and almost concomitantly) in 2001 at the Institut d’Optique[97] and the École Normale Supérieure[98], thanks to laser cooling, and evaporative cooling performed by radio frequency (RF) induced spin flips, in a magnetic trap. The P_0 line ($2^3S_1 \rightarrow 2^3P_0$) is also used in our setup to implement Bragg diffraction for the atomic interferometer (cf. Chapter 2), and Raman coupling between the magnetic sublevels of the metastable state. We will come back to the

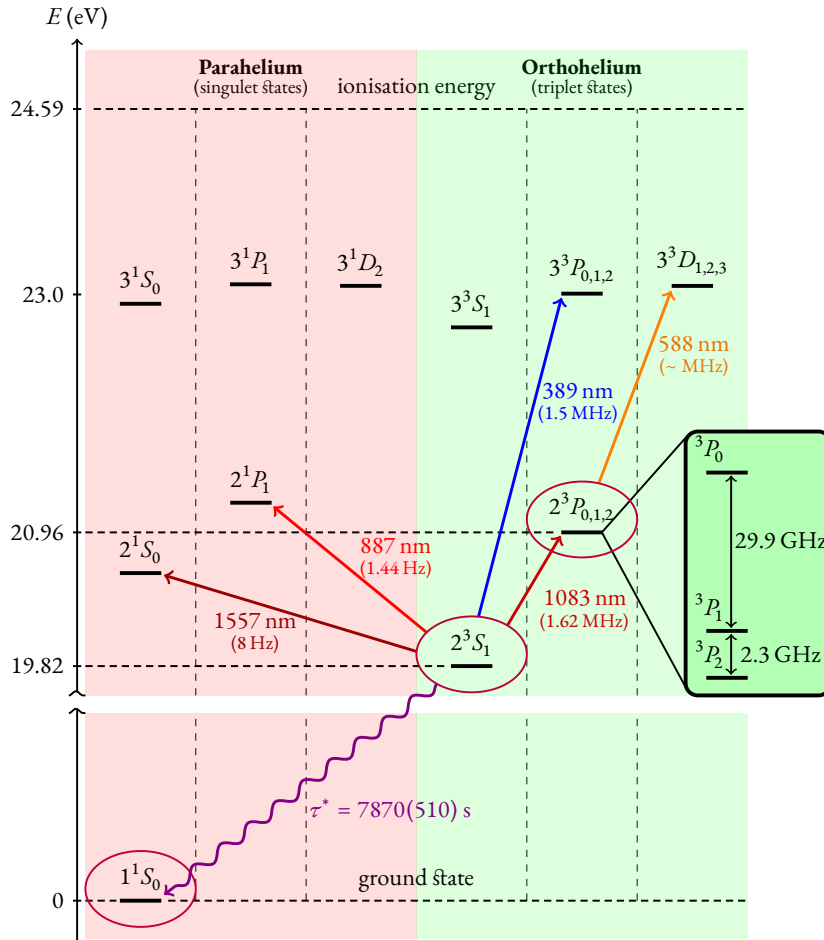


Figure 3.1: Spectroscopic structure of ${}^4\text{He}$, truncated to the states with principal quantum number $n \leq 3$. Some experimentally useful transitions are also represented, with their wavelength and natural linewidth. We also have circled in purple the states of particular interest in the current work. The relative positions of the levels are on scale. The wavy violet arrow represents the twice-forbidden transition from the metastable state to the ground state, with the measured half-life τ associated to it [92]. The numerical values of the energy levels can be calculated with quantum electrodynamics (QED), and are tabulated in [95]. The ionisation energy has been experimentally measured in [96].

latter point later in this chapter.

Concerning the other optical transitions (cf. Figure 3.1):

- the 389 nm $2^3S_1 \rightarrow 3^3P_2$ transition can also be used for laser cooling and imaging [99, 100];
- the 588 nm $2^3P \rightarrow 3^3D$ transition has been used for the preparation of a MOT [101];
- the forbidden transitions between orthohelium and parahelium have also been probed for metrological testing of the QED predictions [102, 103];

With only four nucleons, helium is a featherweight compared to other popular species of ultra-cold atoms physics. This is an advantage for us, as our experimental platform is designed to probe the velocity of individual atoms. Indeed, low mass means large recoil velocity when atoms exchange photons with a resonant laser field, which consequently increases the separation of the different velocity classes of interest in the signal, and –ultimately– the resolution of the experiment.

[99]: Koelmeij et al. (2003), “Magneto-Optical Trap for Metastable Helium at 389 nm”

[100]: Keller et al. (2014), “Bose-Einstein Condensate of Metastable Helium for Quantum Correlation Experiments”

[101]: Kumakura et al. (1992), “Visible Observation of Metastable Helium Atoms Confined in an Infrared/Visible Double Resonance Trap”

[102]: Notermans et al. (2014), “High-Precision Spectroscopy of the Forbidden $2^3S_1 \rightarrow 2^1P_1$ Transition in Quantum Degenerate Metastable Helium”

[103]: van Rooij et al. (2011), “Frequency Metrology in Quantum Degenerate Helium”

Table 3.2: Cooling transition $2^3P_2 \rightarrow 2^3S_1$ characteristics. One should keep in mind that the transition strengths Γ are the same for the three transitions $2^3P_{0,1,2} \rightarrow 2^3S_1$ (with 10^{-4} accuracy).

Physical quantity	Notation	Numerical Value
Transition wavelength [104]	λ	1083.33 nm
Transition strength [95]	Γ	$2\pi \times 1.626$ MHz
Lifetime	$\tau = 1/\Gamma$	97.89 ns
Absorption cross section	$\sigma = \frac{3\lambda^2}{2\pi}$	$5.604 \cdot 10^{-13}$ m ²
Saturation intensity	$I_s = \frac{\pi\hbar c\Gamma}{3\lambda^3}$	0.167 mW cm ⁻²
Doppler limit temperature	$T_D = \frac{\hbar\Gamma}{2k_B}$	39.01 μ K
Recoil momentum	$k_{rec} = \frac{2\pi}{\lambda}$	5.8 μ m ⁻¹
Recoil velocity	$v_{rec} = \frac{\hbar k_{rec}}{m}$	92.02 mm s ⁻¹
Recoil energy	$E_{rec} = \frac{\hbar^2 k_{rec}^2}{2m}$	2.814 $\cdot 10^{-29}$ J = 1.757 $\cdot 10^{-10}$ eV = 42.47 kHz $\times \hbar$
Recoil temperature	$T_{rec} = \frac{E_{rec}}{k_B}$	2.038 μ K

Finally, metastable helium, that we will denote He^* in the following of this manuscript, has a last remarkable feature: it is the most energetic metastable state amongst all atomic species, with the colossal value of 19.82 eV. In particular, this huge amount of energy is enough to extract an electron from a metallic surface during a collision, the associated work function being typically a few electronvolts. When amplified by an appropriate electronic chain of devices, this single electron, expelled from the metal by a single atom, can be converted into a macroscopic signal. This mechanism is at the root of the operation of our detector –microchannel plate (MCP)– that we will introduce in the next section.

1.2 Collision theory

A cold gas of helium is the seat of collisions. When it is elastic, the collision is characterised by the S-wave scattering length a . It also may be inelastic, meaning that the collision changes the internal state of the colliding atoms. In particular, due to its large internal energy, metastable helium produces ionising collisions called *Penning collisions*, that are in practice an important source of atom losses in the cloud.

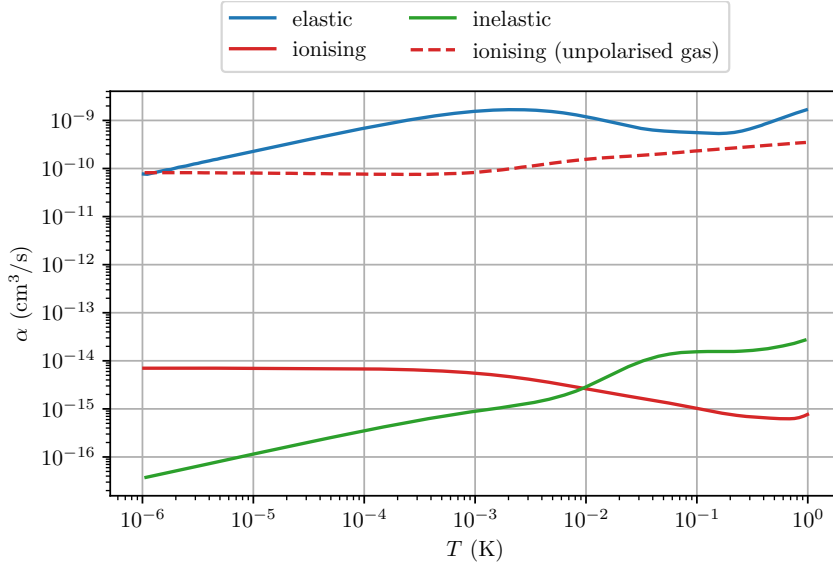


Figure 3.2: Two-body elastic, ionising and inelastic collisions constant rates as a function of the temperature (by convention ionising collisions are not included in the inelastic ones). Data are extracted from [105] and result from multichannel quantum calculations. The hamiltonian used for time evolution takes into account the kinetic part, the unperturbed hamiltonian of both atoms, the electrostatic interaction, and the magnetic spin-dipole interaction. The gas is considered to be spin-polarised, except for the dashed line.

1.2.1 Elastic collision

As in most of the ultra-cold atoms experiment, elastic collisions play a major role, as they provide the re-thermalisation mechanism during the final stage of evaporative cooling.

As always, at low temperature they only depend on the S-wave scattering length, whose value has been theoretically estimated [106] and measured [93] to be $a = 7.512(5)$ nm. The scattering cross-section at low temperature depends on the relative velocity v_r of the atoms involved in the collision, and is given by [107]:

$$\begin{cases} \sigma_0 \triangleq 8\pi a^2 \\ \sigma(k_r) = \frac{\sigma_0}{1 + a^2 k_r^2} \end{cases} \quad (3.1)$$

where k_r is the relative wave vector magnitude

$$k_r = \frac{m}{2\hbar} v_r \quad (3.2)$$

For a *classical* thermal cloud at temperature T , the relative velocity follows the Maxwell-Boltzmann velocity distribution¹, from which we can derive the average collision rate constant $\alpha(T) = \langle \sigma(k_r) v_r \rangle_T$:

$$\alpha(T) = \int_0^\infty 4\pi v_r^2 dv_r \left(\frac{m}{4\pi k_B T} \right)^{\frac{3}{2}} \exp\left(-\frac{mv_r^2}{4k_B T}\right) \sigma(k_r) v_r \quad (3.3)$$

Notation 6 $\langle \bullet \rangle_T$ represent the averaging over the velocity distribution of a thermal cloud at temperature T .

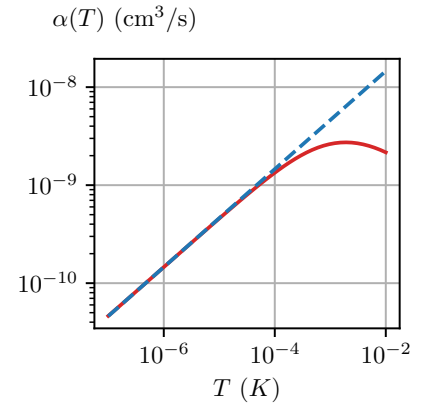


Figure 3.3: Elastic collision rate constant as a function of temperature. The red plain line is given by Eq. (3.3) and the blue dashed line is the square root approximation Eq. (3.4).

[106]: Przybytek et al. (2005), “Bounds for the Scattering Length of Spin-Polarized Helium from High-Accuracy Electronic Structure Calculations”

[93]: Moal et al. (2006), “Accurate Determination of the Scattering Length of Metastable Helium Atoms Using Dark Resonances between Atoms and Exotic Molecules”

[107]: Landau et al. (1977), *Quantum mechanics*

¹: and considering the effective reduced mass of the two-body problem $\frac{m}{2}$

When $T \lesssim 100 \mu\text{K}$, $\sigma(k) \approx \sigma_0$, and we have the good approximation

$$\alpha(T \lesssim 100 \mu\text{K}) = \sigma_0 \sqrt{\frac{16 k_B T}{\pi m}} \quad (3.4)$$

The elastic collision rate γ_{el} is then simply given by

$$\gamma_{el} \triangleq n \langle \sigma(k_r) v_r \rangle_T = n \alpha(T) \quad (3.5)$$

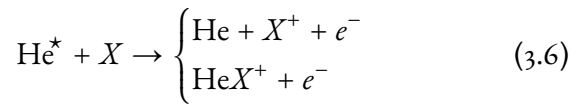
1.2.2 Inelastic & ionising collisions

Strictly speaking, ionising collisions are a particular case of inelastic collisions, but by convention and for more convenience we distinguish the two as they differ widely concerning their involved mechanism and likelihood. Due to its large internal energy, when a metastable He^* collides with other atoms or molecules, it can lead the ionisation of one of them, and the loss of the metastable state. Experimentally, with densities up to 10^{13} cm^{-3} for BECs, we are sensitive to two-body and three-body mechanisms.

Notation 7 We denote “ He^* ” the helium atoms in the 2^3S_1 metastable state, and “He” the helium atoms in the fundamental state 1^1S_0 .

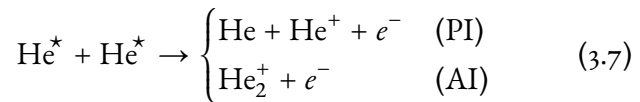
Two-body collisions...

► ...ionising with the residual gas:



the strength of the mechanism is dependent on the quality of the vacuum in the science chamber, where the metastables are trapped. It significantly contributes to the value of the lifetime of the trapped cloud ($\sim 35 \text{ s}$ in the magnetic trap). We can actually experimentally detect the flux of ions created, and use it as an insight of the number of atoms trapped in the cloud[108–110];

► ...ionising with an other metastable¹(Penning):



where PI stands for *Penning ionisation* and AI for *associative*

[108]: Sirjean et al. (2002), “Ionization Rates in a Bose-Einstein Condensate of Metastable Helium”

[109]: Seidelin et al. (2003), “Using Ion Production to Monitor the Birth and Death of a Metastable Helium Bose Einstein Condensate”

[110]: Seidelin et al. (2004), “Getting the Elastic Scattering Length by Observing Inelastic Collisions in Ultracold Metastable Helium Atoms”

1: which is sort of a particular case of the previous mechanism, but we consider it separately as in a trap it is an important source of loss of atoms

ionisation. In both cases the metastables are lost, and since the detail of the mechanism is not important in experiments, we generally call them both “two-body Penning collisions”.

In short, when two metastable atoms collide, they interact via a complex potential that has the form [111]

$${}^{2S_i+1}V(r) - \frac{1}{2} i {}^{2S_i+1}\Gamma(r)$$

where r is the internuclear separation of the atoms, ${}^{2S_i+1}V(r)$ is the molecular potential corresponding to the ${}^{2S_i+1}\Sigma_{g/u}^+$ molecular state (see [112] for more information about the notation), and ${}^{2S_i+1}\Gamma(r)$ is the ionisation width. The total spin S_i of the system can either be 0, 1 or 2, and therefore three channels corresponding to the states ${}^1\Sigma_g^+$, ${}^3\Sigma_u^+$ and ${}^5\Sigma_g^+$ must be considered.

Quantitatively, we characterise the strength of the two-body Penning losses with the collision constant $\beta(T)$ depending on the temperature, such that these losses write:

$$\boxed{\left. \frac{dn}{dt} \right|_{\text{Pinning}} = -2 \beta(T) n^2} \quad (3.8)$$

it is proportional to the squared density n^2 as it is a two-body process, and there is a factor 2 because when an interaction occurs, both atoms are lost.

We can relate $\beta(T)$ to the collisional cross sections calculated for each channel of the above model, and averaged over the different velocity classes for a cloud at temperature T :

$$\beta(T) = \beta({}^1\Sigma; T) + \beta({}^3\Sigma; T) + \beta({}^5\Sigma; T) \quad (3.9a)$$

$$\beta({}^{(2S_i+1)}\Sigma; T) \triangleq \left\langle \sigma \left[{}^{2S_i+1}\Sigma_{g/u}^+; v_r \right] v_r \right\rangle_T \quad (3.9b)$$

For temperature below ~ 1 mK, the collision is dominated by S-wave scattering, and therefore for parity conservation reasons we can neglect in good approximation the interaction led by the molecular potential ${}^3\Sigma_u^+$. In addition, in order to satisfy spin conservation¹ we have ${}^5\Gamma(r) = 0$ which means that at first order the ${}^5\Sigma_g^+$ channel does not contribute to Penning ionisations². Finally, the typical order of magnitude of $\beta(T)$ is strongly dependent on the type of gas that we are considering:

- for a spin “*unpolarised*” gas of helium, where all the spin projections quantum numbers m_s are present in equal

[111]: Leo et al. (2001), “Ultracold Collisions of Metastable Helium Atoms”

[112]: Wikipedia, The Free Encyclopedia (2021), *Molecular term symbol*

1: one should notice that the outcome of the Penning collision has a total spin that can be either 0 or 1 (but not 2).

2: there is still the (smaller) magnetic spin-dipole contribution, that plays an important role in the case of a spin polarised cloud.

quantity (a MOT for example) the Penning collision cross section is dominated by the $^1\Sigma_g^+$ term, and

$$\beta_{unpol.}(T) \sim 10^{-10} \text{ cm}^3 \text{ s}^{-1} \quad (3.10)$$

which is far too large to be able to prepare a BEC. Indeed a density n_{BEC} of typically 10^{13} cm^{-3} leads to a decay time of 1 ms!

- on the contrary for a spin-polarised gas (thanks to a magnetic field) all the atoms have the same spin projection quantum number ($m_s = +1$ in our magnetic trap), and the collisions are dominated by the $^5\Sigma_g^+$ with the magnetic spin-dipole contribution which is much smaller. We end up with

$$\beta_{polarised}(T) \sim 10^{-14} \text{ cm}^3 \text{ s}^{-1} \quad (3.11)$$

which means that the Penning losses are reduced by 4 orders of magnitude, and the realisation of a BEC is possible.

These calculations of Penning collisions cross sections have been performed taking into account the three channels in a quantum formalism for both fermionic and bosonic helium [105, 111], and are in good agreement with experimental measurements [113, 114]. We have represented the corresponding results on Figure 3.2 on page 107.

► ...inelastic with an other metastable

In addition, with the model presented in the previous paragraph, the presence of the magnetic spin-dipole interaction in the hamiltonian induces a coupling with states whose total spin and spin projection has changed. Using the space-fixed eigenstates of the noninteracting system:

$$|S_1, S_2, S_t, m_s\rangle$$

for a spin polarised gas, these inelastic collisions realise the transformations:

$$|1, 1, 2, 2\rangle \rightarrow \begin{cases} |1, 1, 2, 1\rangle & (1) \\ |1, 1, 2, 0\rangle & (2) \\ |1, 1, 0, 0\rangle & (3) \end{cases} \quad (3.12)$$

1: in cases (1) and (2) atoms are no longer trapped by the magnetic field.

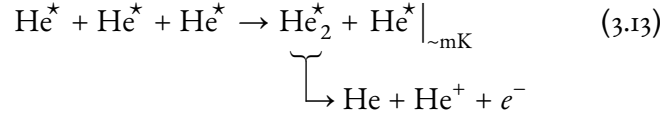
2: in case (3) the outgoing atoms feel the channel $^1\Sigma_g^+$.

leading to the loss of atoms¹ and indirect ionisation².

With the same model as before, it is again possible to have numerical evaluations of the corresponding cross section (cf. Figure 3.2 on page 107). In particular we observe that below a few millikelvins, these losses are much smaller than the Penning ion-

ising collisions.

Three-body collisions When the density of the cloud increases (i.e. close to condensation) we must also consider three-body ionisation processes:



where the helium dimer in an excited state He_2^* is a short-lived autoionising state.

Just as in the two-body case, we quantitatively characterise this three-body recombination with a collision constant ρ such that:

$$\boxed{\left. \frac{dn}{dt} \right|_{3\text{ body}} = -3\rho n^3} \quad (3.14)$$

in the low temperature limit, ρ follows a universal law [115], only dependent on the scattering length a :

$$\rho \approx 3.9 \frac{\hbar}{m} a^4 \quad (3.15)$$

Low temperature limit means that the collision energy E must be much smaller than the binding energy $\epsilon_0 = \frac{\hbar^2}{ma^2}$ between two atoms. In the case of spin-polarised He^* , we have $\epsilon_0 \approx k_B \times 2 \text{ mK}$. However, when the density becomes very large (close to condensation) quantum interference effects may cause deviations from the law Eq. (3.15) [116].

Numerically, with $a = 7.512 \text{ nm}$, Eq. (3.15) gives

$$\rho \approx 2 \cdot 10^{-28} \text{ cm}^6 \text{ s}^{-1} \quad (3.16)$$

which is in ‘‘fairly’’ good agreement with the results of an experiment previously conducted in our group [110]:

$$\rho = 8.3_{-5}^{+15} \cdot 10^{-28} \text{ cm}^6 \text{ s}^{-1} \quad (3.17)$$

Therefore, as long as the density is not much larger than 10^{13} cm^{-3} , the three-body recombination has a minor effect.

[115]: Fedichev et al. (1996), ‘‘Three-Body Recombination of Ultracold Atoms to a Weakly Bound s Level’’

[116]: Esry et al. (1999), ‘‘Recombination of Three Atoms in the Ultracold Limit’’

[110]: Seidelin et al. (2004), ‘‘Getting the Elastic Scattering Length by Observing Inelastic Collisions in Ultracold Metastable Helium Atoms’’

2 Detecting individual atoms in the momentum space

2.1 Microchannel plate

1: for probing quantum interference effects, or the emission statistics of a non-classical source.

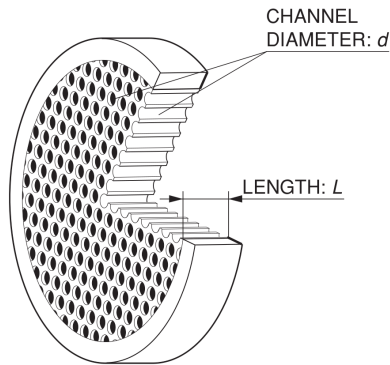


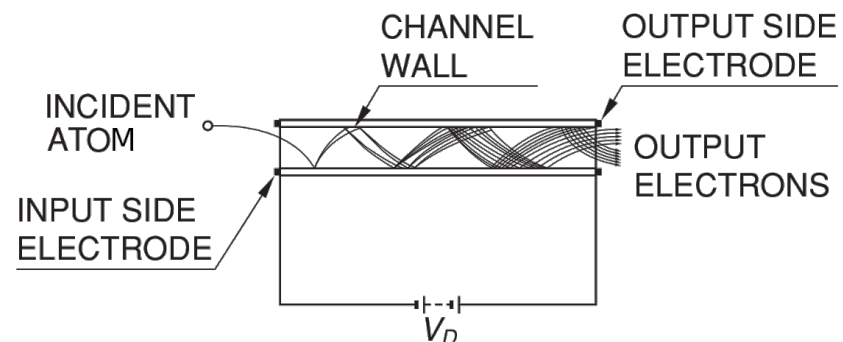
Figure 3.4: Cutaway drawing of a MCP. In our case the plate is 1 mm thick, the channels diameter is $d = 25 \mu\text{m}$, and the effective area diameter is $D = 79 \text{mm}$. The bias angle of the microchannels is $\theta = 20^\circ$. Image provided by Hamamatsu Photonics ©.

The experiments that we operate in the lab require the counting of individual atoms¹. It is therefore crucial for us to have a single-atom resolved sensor at our disposal.

The **microchannel plate (MCP)** is a device that has the ability to generate a macroscopic electric signal, out of its interaction with a single atom. It consists in a 1 mm thick ceramic slab, regularly drilled with tilted micrometric holes (cf. Figure 3.4). The ceramic is electrically resistive (our current MCP has a resistance of 30 M Ω) and can be electrically polarised thanks to a high-voltage power supply, so that a strong electric field is present inside the channels (cf. Figure 3.5).

As we will see in Subsection 2.2.3, in our usage of the MCP atoms have velocity normal to the plate during the detection, with good approximation. The bias angle between the channels and the vertical guarantees that atoms hit the channels' inner walls when they penetrate into it. As shown in Figure 3.6 this angle θ , and the diameter d of the channels define the longitudinal uncertainty when an atoms falls in a given tube. In practice, it limits the resolution of the sensor concerning the arrival times of atoms, we therefore want θ to be as close as possible to 90° .

Figure 3.5: Schematic of the electronic cascade inside a microchannel. In the lab we use a HAMAMATSU[®] MCP, with a tension $V_D = 2.34 \text{kV}$. A single metastable atom typically gives rise to 10^4 secondary electrons at the output side. The quantum efficiency of the process is estimated to be close to 50%. Image provided by HAMAMATSU Photonics ©.



When a metastable atom crashes into a microchannel, there is some probability that it will remove one or two electrons from the surface. Because of the electric field, the emitted electrons are accelerated, and collide again inside the channel, giving birth to more and more secondary electrons (cf. Figure 3.5). The amplification gain is typically 10^4 , meaning that when a single metastable falls in a channel, it may generate a cascade of 10^4 at the output. After the electronic discharge, the microchannel needs some time to recover (as it has been “emptied” of its electrons); in practice this is a source of saturation effect when the atoms flux is too large (larger than a few $10^5 \text{ s}^{-1} \text{ cm}^{-2}$ [117, 118]).

In many aspects, MCPs are similar to other electron amplifier systems (such as photomultipliers and dynodes tubes) though with the big difference that they provide *spatial information*, given that the microchannels are distributed on the whole surface of the plate.

In 2019, we changed the MCP, trading an old and deteriorated BURLE model for a new generation HAMAMATSU sensor. The latter has flared input orifices (cf. Figure 3.7). This greatly increases the open area ratio (OAR), and therefore the quantum efficiency. Numerically, the new model is expected to have 50% quantum efficiency (better than the 25% of the previous one), and a better longitudinal resolution (thanks to a bigger bias angle of the channels).

The delicate swapping operation (because the MCP is placed in a ultra-high vacuum chamber) was one of my first jobs in the team. A comparison of the raw characteristics of both MCPs is given in Table 3.3.

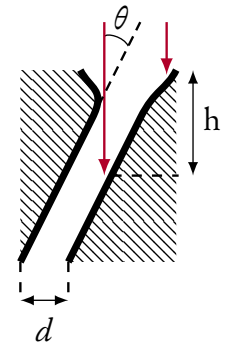


Figure 3.6: Schematic of a cross-sectional view of a microchannel. The input orifice is flared in order to increase the open area ratio (OAR) of the channels. The tilt guarantees that the atoms crash on the wall of the channel, $h = \frac{d}{\tan(\theta)}$ is the longitudinal uncertainty when an atom falls inside a given tube.

[117]: Schellekens (2007), “The Hanbury Brown and Twiss Effect for Cold Atoms”
 [118]: Cayla (2018), “Measuring the momentum distribution of a lattice gas at the single-atom level”

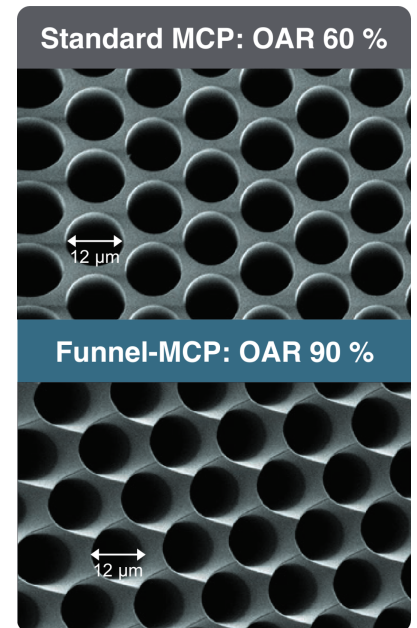
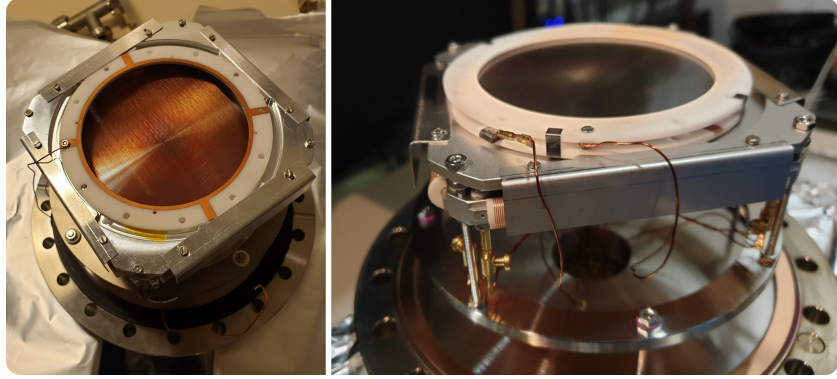


Figure 3.7: Micrometer scale photograph of the surface of standard and “funnel” MCPs. Photograph provided by HAMAMATSU Photonics ©.

Table 3.3: Raw features comparison between the old and new MCP. The longitudinal resolution h is a theoretical value, given by the geometry of the channels (cf. Figure 3.6).

Feature	Burle (old)	Hamamatsu (new)
Model reference		F1942-016F
Channel diameter	25 μm	12 μm
Bias angle	8°	20°
Longitudinal resolution	178 μm	33 μm
Open area ratio	45 %	90 %
Maximum dark current		0.5 pA cm^{-2}
Estimated quantum efficiency	25 %	50 %

Figure 3.8: Pictures taken during the MCP swapping. On the top view, on the left, the MCP is removed, and the delay lines laying beneath are visible. On the right picture, the MCP is mounted (black disc) and connected to high voltages copper wires. Everything shall be placed in high vacuum chamber (the large copper seal is visible below), and the wires are connected to the external high-voltage power supply via a vacuum feedthrough flange (hole in the middle).



2.2 Generation of 3D data: delay lines, electronics & software

2.2.1 Delay lines & electronics

Principle We are actually using two MCPs, stacked in a chevron pattern (v-shape). This increases the gain quadratically (final gain is $G = 10^8$), without damaging the plates (the 2θ angle between the channels of the two plates greatly reduces the feedback of cations).

A metastable atom therefore creates a shower of 10^8 electrons, that itself excites two copper delay lines wrapped around orthogonal axes, x and y (cf. Figure 3.9). The excitations propagate through the lines and are collected by time-tagger devices placed at the end. We name them “ X_1 ”, “ X_2 ”, “ Y_1 ” and “ Y_2 ”, depending on the line and propagation direction. Thanks to the wrapping of the lines, the effective velocity v_{\perp} of the excitations along the x and y axis is the velocity of the signal in the copper line ($\sim c/3$) divided by the number of loops N (100 in our case).

$$v_{\perp} \approx \frac{c}{3N} \quad (3.18)$$

But in practice, due to small length differences between the two lines, v_{\perp} does not have the exact same value in the x and y directions. The

Remark 3.2 Out of the delay lines, the pulses have *negative* polarity.

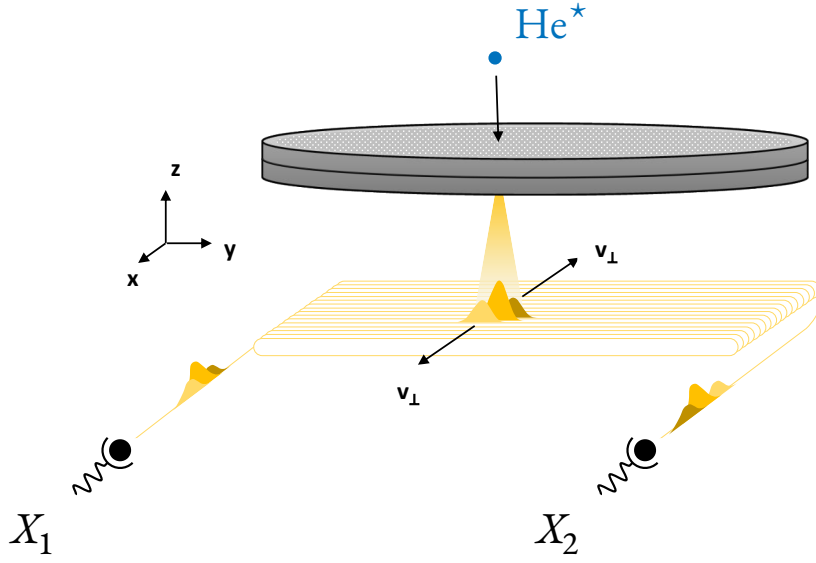


Figure 3.9: [Taken and modified from [60]]. When a metastable hits the MCP, it might create a rain of 10^8 electrons onto the delay lines standing beneath. These excitations propagate along the lines and are tagged by a time-to-digital converter (TDC).

delay lines assembly, and the electronics for the detection is provided by ROENTDEK[®], and the effective signal velocities are tabulated in the datasheet:

$$\begin{cases} v_1^x = 1.02 \text{ mm ns}^{-1} & (3.19a) \\ v_1^y = 1.13 \text{ mm ns}^{-1} & (3.19b) \end{cases}$$

Now it is possible to deduce the date and position of the impact of a metastable atom, thanks to the quadruplet of time-tags $(t_{X_1}, t_{X_2}, t_{Y_1}, t_{Y_2})$ collected at the end of the lines:

$$\begin{cases} x = \frac{v_1^x}{2} (t_{X_1} - t_{X_2}) & (3.20a) \\ y = \frac{v_1^y}{2} (t_{Y_1} - t_{Y_2}) & (3.20b) \\ t = \frac{1}{2} (t_{X_1} + t_{X_2}) & (3.20c) \\ t = \frac{1}{2} (t_{Y_1} + t_{Y_2}) & (3.20d) \end{cases}$$

Remark 3.3 In Eq. (3.20c) and (3.20d), we have neglected a propagation time $\frac{L}{c/3} \approx 80 \text{ ns}$ (the “diameter of the MCP” in time units) because it is much smaller than the time resolution induced by the bias angle of the microchannels (cf. Figure 3.6). As we will shortly see, the typical velocity of the atoms during the impact is $v \approx 3 \text{ m s}^{-1}$. The time resolution is therefore $\sigma_t = \frac{d}{v \tan(\theta)} \approx 10 \mu\text{s} \gg 80 \text{ ns}$.

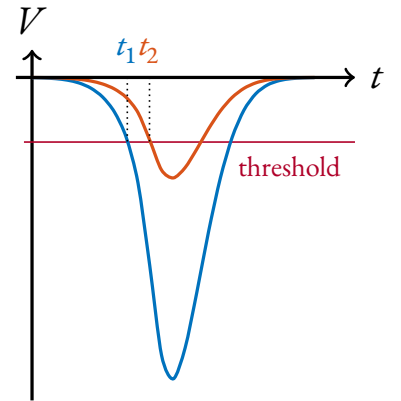


Figure 3.10: Illustration of the fact that a simple threshold triggered TDC does not work when the gain is noisy. Here the two pulses are the same, up to a multiplicative constant, but $t_1 < t_2$.

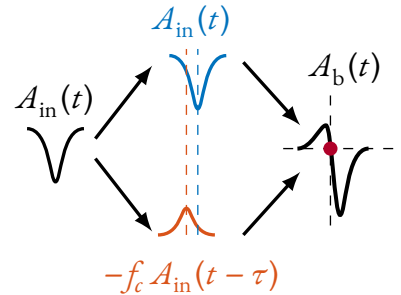
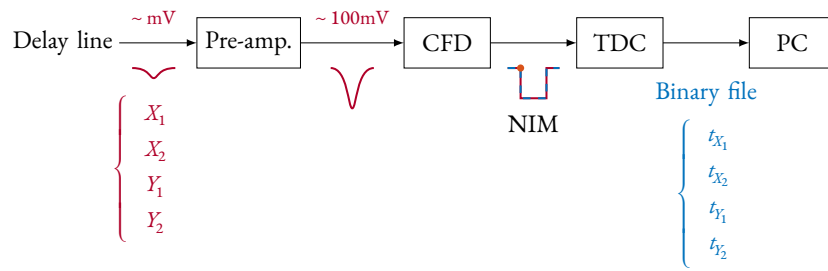


Figure 3.11: Principle of the CFD. The input signal is split in two, and one of the two partite is damped by a f_c factor, and delayed. After recombination, the resulting bipolar signal A_b has a zero (red point) whose position corresponds to a given fraction of the input signal.

Figure 3.12: Block diagram of the electronic chain used for the detection, and the conversion from analog (red) to digital (blue). Out of the delay lines, the signal only has an amplitude of a few millivolts: it is first amplified with a high-pass filter pre-amplifier ($G = 80$). It is then converted into a NIM by the CFD, before being digitised and sent to the PC by the TDC.



MCPs are very low noise detectors, but the amplification gain when an atom is detected is itself very noisy... The electronic pulses detected in the delay lines have roughly 10 ns width, but with an amplitude that can change a lot shot-to-shot (roughly up to one order of magnitude). It is however a good approximation to consider that the pulses generated by an atomic discharge always have the same *shape* (they are homothetic). Therefore, the usual way to time-tag the pulses coming out from an MCP is to use a **constant fraction discriminator (CFD)**, that will return a time independently of the amplitude of the bump. The main idea of CFDs is as follows:

Definition 6 (NIM signal) A NIM signal is a digital signal following the definition:

- ▶ when the signal voltage is between -0.8 V and -1 V , it is a logical "1".
- ▶ when the signal voltage is 0 V , it is a logical "0".

NIM is an acronym for Nuclear Instrument Modules since it has been invented for this kind of experiment.

After a first pre-amplification stage, we apply the transformation

$$A_b = A_{in}(t) - f_c A_{in}(t - \tau) \quad (3.21)$$

where A_{in} is an analog pulse (in our case an electronic pulse collected in the delay lines), $f_c \in [0, 1]$ is a number and τ a delay time of the same order of magnitude than the width of the pulse. Due to the delay, if the shape of the pulse is not "pathological", A_b has a zero whose time position is independent of the amplitude of A_{in} (cf. Figure 3.11).

This zero is used as a reference time to generate a digital NIM signal (cf. Definition 6). Afterwards, the falling edge of the NIM constitutes a convenient reference to tag and digitise the time of the incoming pulse. The functional electronic pre-treatment of the signal is summarised in Figure 3.12.

Remark 3.4 (TDC hardware) Our TDC device is the TDC-V4 developed by the Plateforme *Détection: Temps, Position, Image* (DTPI) of the Fédération *Lumière-Matière* (LUMAT) at the Université Paris-Sud. It consists in a PCI card plugged into the experiment computer, and it is connected to a 19" rackable interface (ISiBOX) that ensures the BNC connections to the MCP output channels X_1 , X_2 , Y_1 and Y_2 .

It is clocked at $\delta_t = 120$ ps, which is much smaller than the resolution limitation induced by the MCP.

The software interface is ensured by a C++ library provided by the LUMAT-DTPI (which is quite problematic as it imposes a complex C++ layer in our otherwise pythonic workflow...).

Technology changes In 2019, we effected major changes in the electronics¹, at the same time as we changed the MCP. We installed a new ROENTDEK[®] system, including:

- ▶ the high-voltage power supply (THQ by Iseg);
- ▶ a high-voltage splitter (Zener diode based circuit) that distributes the tension among the two MCPs and the delay lines;
- ▶ the pre-amplifier module;
- ▶ the CFD module;

The installation and characterisation of the new electronics was an important aspect of the beginning of my PhD. The new pre-amplifier and CFD offer the possibility to set specific settings (six parameters) to *each* of the four channels:

1. *the gain, G* – is adjustable from 10 to 90². It is set in order to have pulses whose amplitude matches the CFD recommended specifications (from -10 mV to -3 V). Experimentally we adjust it so as to have the same average value of the pulses' amplitude at each channel. These mean values are extracted from the histograms of the pulses amplitude, obtained with an oscilloscope in binning mode (cf. Figure 3.13). In practice, the four gains are set to the same value: $G = 80$. There is also a frequency dependence of the gain (see Appendix B for more details).
2. *the threshold* – even if a CFD is used, a threshold must be set to remove most of the noise fluctuations, and define from how much voltage a pulse may be considered to be due to an atom. This setting is both crucial and delicate: since there is no clear separation between the noise and the signal (cf. Figure 3.13) we want it to be slightly in the noise, so as to almost never lose the atoms. The excess pulses coming from the noise are removed in the later stage of *reconstruction*, performed by an algorithm. However, if the threshold is too close to 0 V, too much noise is sampled by the CFD and the reconstruction algorithm quickly collapses (actually the CFD itself might also saturate). The cur-

1: before, we were using an older generation of ROENTDEK[®] electronics for the detection, coupled with an home-made high-voltage power supply unit (PSU).

2: defined in amplitude, for a 10 MHz input sinusoidal signal, and measured with an oscilloscope with a 50Ω input impedance.

rent settings (date: 30/06/2022) are:

$$\begin{cases} X_1^{tb.} & = -30 \text{ mV} \\ X_2^{tb.} & = -25 \text{ mV} \\ Y_1^{tb.} & = -17 \text{ mV} \\ Y_2^{tb.} & = -15 \text{ mV} \end{cases}$$

3. the fraction f_c – affects the shape of the bipolar pulse A_b . The technology allows the values $[0.14, 0.35, 0.57, 0.8, 1]$. This setting is rather empirical and we let it to the default value 0.35, which is well adapted for near-gaussian input signals ;
4. the delay τ – also has an effect on A_b (which is obviously not independent of the fraction f_c). It is experimentally set with an extra propagation in a short additional LEMO cable. In order to have a fine shape for the bipolar signal (zero-crossing with a big slope), we have a “thumb rule”:

$$\tau \approx T_{\text{rising}}(1 - f_c) \quad (3.22)$$

where T_{rising} is the typical 10 % to 90 % rising time. In our case:

$$\begin{cases} T_{\text{rising}} & \approx 10 \text{ ns} \\ \tau & = 4 \text{ ns} \end{cases}$$

5. the walk level Z – actually the output **NIM** is generated when the logical product **.AND.** between two logical signals L_1 and L_2 is true:
 - ▶ L_1 is true when the (pre-amplified) input signal A_{in} overtakes the threshold. It is false otherwise ;
 - ▶ L_2 is true when the bipolar signal A_b is above the walk level Z , and false otherwise ;

with this trick, we ensure that a **NIM** is generated only when the pulse’s amplitude is large enough to potentially be due to an atom, **AND** (logical) when the bipolar pulse crosses the zero (independent of the amplitude). In practice, Z must be set to the baseline of A_b (which presents no difficulty to do) ;

6. the width w – of the output **NIM** signal. It acts as a deadtime for the electronics. If it is too large some events might be lost. In order to avoid any false-positive event (e.g. very short-time electronic ripples) we set it to 20 ns, which is roughly the duration of an input pulse ;

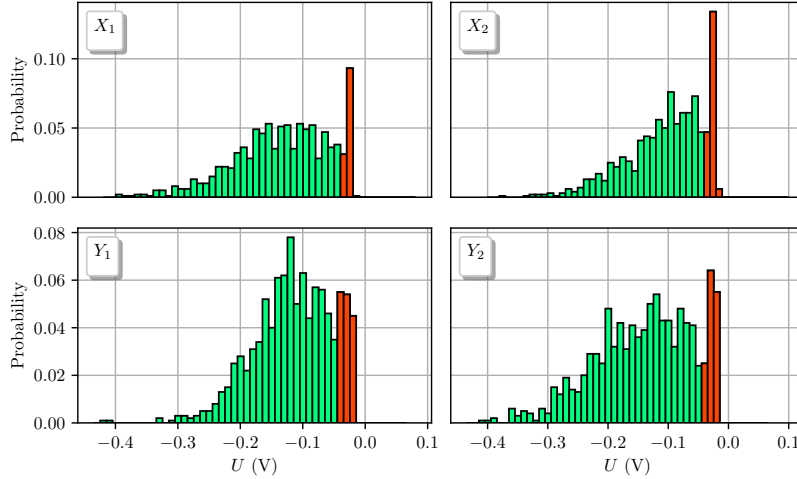


Figure 3.13: Pulses amplitude histograms (after pre-amplification). Side by side plots share a same grid axis. G is the pre-amplification gain of the channel. A sample of 1000 pulses is used for each plot: acquired with an oscilloscope binning the minimum voltage read in a 50 ns large window, triggered in normal mode, with a threshold of a few millivolts. We identify a contribution of the noise (in red) with small amplitude pulses, and a contribution of the signal (in green) with amplitudes ranging up to approximately 0.6 V. There is no sharp separation between the noise and the signal.

It is interesting to have an individual control of these parameters for each of the four channels because of their behaviour is not symmetric. The coupling between the delay lines and the MCP is not linear, and very sensitive to the inhomogeneities encountered along the lines: that is why the pulses' amplitude distribution (Figure 3.13) exhibits differences between the channels.

As we mentioned previously, these histograms are useful to have a first insight of where to put the threshold: slightly in the noise, with the purpose of keeping all the atoms in the digitised signal. In fact, it appears that the performances of our detection system are strongly dependent on the values of the thresholds. Aiming to maximise the homogeneity of the detectivity, and the overall quality of the reconstructed signal, we experimented new techniques to have a fine adjustment of the thresholds.

Number of events per channel When the experiment is running, we have the possibility to print the number of events $N_{\text{ev}}(Z_i)$ for each channel $Z_i \in \{X_1, X_2, Y_1, Y_2\}$ and the number of reconstructed atom N_{at} (more details about the reconstruction are given in the next subsection) in live, at each run.

We can define the reconstruction rate for each channel:

$$\rho(Z_i) = \frac{N_{\text{at}}}{N_{\text{ev}}(Z_i)} \in [0, 1] \quad (3.23)$$

If we increase the threshold, the number of events decreases, and the reconstruction rate increases, because the events are more likely to be due to atoms. Assuming that the number of events should be approximately the same for each channel, we adjust the threshold so as to have

Definition 7 (TDC event) We call "event" a digitised NIM pulse, collected and time-tagged by the TDC. It is not necessarily due to an atom, as it could also have been induced by an above-threshold noise fluctuation.

the same reconstruction rate everywhere. We chose the value $\rho = 90\%$, because we empirically know that in this regime the reconstruction algorithm removes the noise efficiently, and produces faithful data.

Events self-correlation in time A common issue that we face when working with MCPs and delay lines is the so-called “*pulse rebounds*” problem. Indeed, because of impedance mismatching, when a pulse reaches the edge of a delay line, some fraction of its energy is reflected backwards. It is then reflected again on the other side of the line, and eventually detected a second time on the initial side. It is also possible to generate pulse rebounds in the middle of the line, induced by impedance inhomogeneities.

As a result, when a pulse is observed at the end of a line, we often see short-time “aftershocks” with smaller amplitudes. When the rebounds occur on the edges of the lines, we expect them to be separated by twice the time-length of the lines: $2 \times 80 \text{ ns} = 160 \text{ ns}$. It is also the role of the thresholds to remove most of those rebounds.

2.2.2 Reconstruction algorithm

The passage from digitised event timestamps to atoms momenta coordinates obviously involves an important software processing. This *reconstruction* stage is performed in real time by a C++ code run at the end of each experimental cycle. It is also the program that interfaces the TDC with the computer, loading its driver and parametrising the acquisition options. We shall describe the outlines of how this process works in the current subsection.

Generation of raw data First, the driver of the TDC is loaded, such that it will wait the trigger signals to start and stop the time-tagging of the NIM pulses it receives. These triggers are TTLs generated by the experiment’s sequencer (connected to the IsiBox rack via two LEMO cables), they define an adjustable time range of typically 600 ms, during which we expect the metastable atoms to fall onto the MCP.

The data produced by the TDC are directly loaded into the computer’s memory¹, they take the form of 32 bits words, eventually stored in a C++ `<vector>` structure (cf. blue column in Figure 3.14). There are two types of words: *encoding words* that carry an event time, and *service words* that are used to fulfill communication operations between

¹: the flow of data is ensured by an on-chip buffer memory with a size of 509 32 bits words.

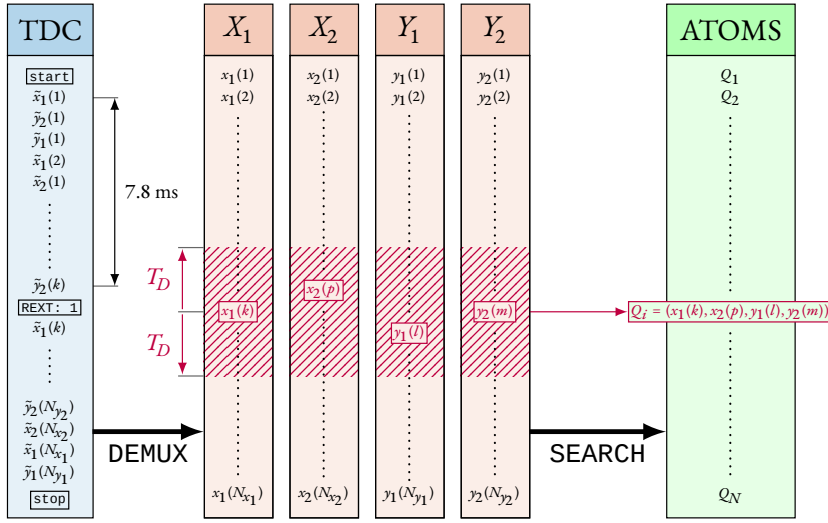


Figure 3.14: Diagrammatic representation of the reconstruction algorithm. The computer receives a large vector (in blue) of 32 bits words from the TDC. Most of them are *encoding words* ($\tilde{z}_i(j)$ words on the diagram), but there also are *service words* (framed words) used to stabilise the interfacing between the hardware and the software, and extend the limited range of encoding words with 26 bits (thanks to the REXT word). The first step is the DEMUXING, where the different encoding words are sorted by channel label (in orange), in separate vectors. Their timestamps $z_i(j)$ are also corrected, taking into account the REXT words. Finally we proceed to the SEARCHING stage, in bulbs where the maximal distance between two events is given by the MCP diameter T_D .

hardware and software. The bitset of each word is divided into two parts:

- ▶ the first 6 bits are a LABEL field. It indicates the channel number (if the word is an encoding word) or the nature of the function realised by a service word ;
- ▶ the last 26 bits are the DATA field. For encoding words, it contains the *timestamp*, expressed in discrete time step units¹. In the case of a service word, it may give some additional information, useful for its function ;

¹: in our case a time step is $\delta_t = 120$ ps.

Demuxing One may notice that the time range accessible with a 26 bits long word (T_{\max}) is finite. Its value is simply given by:

$$T_{\max} = 2^{26} \times \underbrace{\delta_t}_{120 \text{ ps}} \approx 8 \text{ ms} \quad (3.24)$$

T_{\max} is in particular much smaller than the typical acquisition time of an experiment (few hundreds of milliseconds). To overcome this problem, the *range extension* (REXT) service word is used: when a time overflow is about to occur² the TDC generates a REXT word, and resets the clock to zero. When the reconstruction algorithm reads the TDC raw data vector, it keeps track of the generated REXT words so as to add the correct amount of missing time to the timestamps. This trick allows to extend the accessible time range indefinitely. We perform this time correction, as well as the encoding words sorting by channel numbers, in a first main stage that we call “*demuxing*”. For security and long

²: after 7.8 ms, so as to keep a 0.2 ms margin and prevent any overflow.

term reproducibility, we also save at this moment the TDC raw data vector, and the four demuxed channels vectors (cf. Figure 3.14).

Atoms searching and filtering The last step is the very core of the algorithm, the aim is to find “*time correlated*” events quadruplets. That means that we are looking for four events –each one on a separate channel– whose time differences are compatible with the hypothesis that a metastable atom created them via the relations Eq. (3.20). To do this, we apply successive filtering criteria:

- ▶ we know that the diameter of the MCP is $T_D = 80$ ns, therefore two events cannot be separated by more than T_D . The search is performed by looping over X_1 events, and looking for the other three in a bulb with T_D time radius (purple diagonal lines in Figure 3.14);
- ▶ an atom must fall inside the disc defined by the MCP shape:

$$|t_{X_1} - t_{X_2}|^2 + |t_{Y_1} - t_{Y_2}|^2 \leq T_D^2 \quad (3.25)$$

if a quadruplet candidate is found at the previous step, we check the condition Eq. (3.25), if it is not fulfilled we reject it ;

- ▶ by construction, (3.20c) – (3.20d) gives:

$$S \triangleq (t_{X_1} + t_{X_2}) - (t_{Y_1} + t_{Y_2}) = 0 \quad (3.26)$$

actually Eq. (3.26) is not true: geometrical constraints imply that the S quantity –that we call *offset*– is not zero everywhere. It has small spatial variation, depending on the location of the impact, but these variations are bounded and stable (they only depend on the winding of the delay lines and the electronics). We use an upper bound of the S values as an additional filtering criterion:

$$|S| \leq S_{\max} = 10 \text{ ns} \quad (3.27)$$

it is a coarse sieve, and the value of 10 ns has been chosen after a specific study of the offset map.

- ▶ we use as a last filtering step a finer version of the previous filtering, where we compare the offset value of a candidate quadruplet to a reference value of the offset for this specific location. With (x, y) the impact coordinate associated with a quadruplet, we check the condition:

$$|S(x, y) - S_{\text{ref}}| \leq \Delta S_{\max} = 5 \delta_t = 0.6 \text{ ns} \quad (3.28)$$

This final sieve is much more selective, and guarantees the keeping of faithful data, but it also requires a reference offset map, previously acquired, averaging a large amount of data (and without this final filtering stage). The threshold value of 5 time steps has been chosen after a specific study I made in 2019, more details are given in Appendix B.

2.2.3 From timestamps to velocities

At this stage, Equation 3.20 on page 115, allows to calculate an impact time t , and (x, y) in-MCP plane coordinates. However, it has already been said several times since the introduction of this manuscript that the observable that we need to probe is the *momentum* of the atoms. We need a last set of relations, that transcript the (x, y, t) “MCP coordinates” into $(\vec{p}_x, \vec{p}_y, \vec{p}_z)$ momentum coordinates. With that in mind, it is interesting to notice that the distance L separating the trapped cloud from the detector (~ 45 cm) is very large compared to the typical size of the cloud ($\sim 100 \mu\text{m}$): we often say that the MCP is performing a detection in the *far field regime*. When the trap is released, atoms realise a free fall¹, whose final impact point is known thanks to the MCP measurement, and we can take (with very good approximation) the centre of the trap cloud as the emission point. Knowing these two points, simple classical mechanics gives the unique initial velocity that link them via a free fall whose duration Δt is known (cf. Figure 3.15 on the side). In practice we take the trap shutdown as the time reference such that $\Delta t = t$. Setting the origin in the middle of the MCP plane, we have:

$$\begin{cases} p_x = m \frac{x}{t} \end{cases} \quad (3.29a)$$

$$\begin{cases} p_y = m \frac{y}{t} \end{cases} \quad (3.29b)$$

$$\begin{cases} p_z = m \left(\frac{1}{2} g t - \frac{L}{t} \right) \end{cases} \quad (3.29c)$$

Regarding Eq. (3.29), it is important to notice that x and y give the information about momenta in the horizontal (or *transverse*) plane, whilst the arrival time t provides a measurement of the vertical (or *longitudinal*) velocity. This point is crucial, because it means that the resolution of the detection in the horizontal and vertical directions are not necessarily the same.

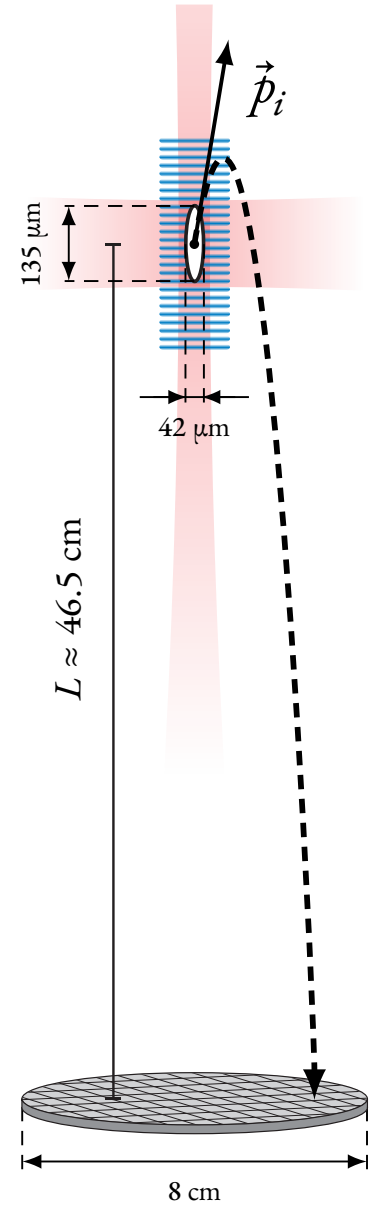


Figure 3.15: Schematic of the far field regime detection with an MCP. The typical size of the cloud is given by the waists of the laser beams trapping it (cf. Subsection 3.2.4). When the trap is released, atoms are transferred in $m_J = 0$ with a Raman transition and then perform a free fall whose trajectory is dependent on their initial velocity $\vec{v}_i = \vec{p}_i/m$.

¹: to be perfectly rigorous, as it will be explained in details in Subsection 2.1.2 of Chapter 4, they also receive a kick during a Raman transfer from the magnetic sublevel $m_J = 1$ to $m_J = 0$. By the way, this transfer is very much required as it guarantees that the atoms do not feel the residual magnetic field, and indeed perform a “genuine” free fall.

2.2.4 A word about the resolution

We already discussed in [Subsection 2.1](#) the question of the longitudinal resolution: [Figure 3.6](#) shows in particular that it is constrained by the geometry of the microchannels. As we will see in [Chapter 5](#), our source expels pairs of correlated atoms with momenta (mainly) along the long axis of the BEC: it means that in the current configuration of the experiment where the BEC is elongated along the vertical, the longitudinal resolution is the most important element for probing quantum correlations.

It is also obviously important to have the knowledge of the transverse resolution. In space units, we denote them σ_x and σ_y , with respect to the delay lines directions. With [Eq. \(3.20\)](#), with a statistical definition of the resolution, and denoting σ_t the time resolution we have:

$$\left\{ \begin{array}{l} \sigma_x = \frac{v_{\perp}^x}{2} \sqrt{\sigma_{t_{x_1}}^2 + \sigma_{t_{x_2}}^2} = \frac{v_{\perp}^x}{\sqrt{2}} \sigma_t \\ \sigma_y = \frac{v_{\perp}^y}{2} \sqrt{\sigma_{t_{y_1}}^2 + \sigma_{t_{y_2}}^2} = \frac{v_{\perp}^y}{\sqrt{2}} \sigma_t \end{array} \right. \quad (3.30a)$$

$$\left\{ \begin{array}{l} \sigma_x = \frac{v_{\perp}^x}{2} \sqrt{\sigma_{t_{x_1}}^2 + \sigma_{t_{x_2}}^2} = \frac{v_{\perp}^x}{\sqrt{2}} \sigma_t \\ \sigma_y = \frac{v_{\perp}^y}{2} \sqrt{\sigma_{t_{y_1}}^2 + \sigma_{t_{y_2}}^2} = \frac{v_{\perp}^y}{\sqrt{2}} \sigma_t \end{array} \right. \quad (3.30b)$$

where we assume the time resolution to be independent of the channel (it is a simple model that ignores subtle electronic effects that may differentiate between the various behaviours of the channels). Then, the definition (red box) [Eq. \(3.26\)](#) gives:

$$\sigma_S = \sqrt{\sigma_{t_{x_1}}^2 + \sigma_{t_{x_2}}^2 + \sigma_{t_{y_1}}^2 + \sigma_{t_{y_2}}^2} = 2\sigma_t \quad (3.31)$$

we therefore have a relation between the transverse resolution, and the standard deviation of the offset values:

$$\left\{ \begin{array}{l} \sigma_x = \frac{v_{\perp}^x}{2\sqrt{2}} \sigma_S \\ \sigma_y = \frac{v_{\perp}^y}{2\sqrt{2}} \sigma_S \end{array} \right. \quad (3.32a)$$

$$\left\{ \begin{array}{l} \sigma_x = \frac{v_{\perp}^x}{2\sqrt{2}} \sigma_S \\ \sigma_y = \frac{v_{\perp}^y}{2\sqrt{2}} \sigma_S \end{array} \right. \quad (3.32b)$$

these relations are very useful, as it means that the standard deviation of the offset map, is a picture of the transverse resolution: we obviously call it “*resolution map*”.

2.2.5 Comparison between performances

The resolution map is one of the two major features that provide quantitative information about the performances of the detection system. The other one is the so-called *detectivity* map that characterises the homogeneity of the detection. It is the normalised number of atoms detected on a given location of the MCP, when we “shine” it with an homogeneous flux of atoms¹. Since it is not possible in practice to have a precise value of the total number of atoms incoming onto the MCP², it is only a *relative* quantity, and not a map of the quantum efficiency.

I acquired these data in 2019, before and after changing the system, in identical experimental situations, and the results are plotted in Figure 3.16. We can be satisfied by the gain of homogeneity of the detectivity, and a resolution roughly 3 times better.

If we compare the transverse resolution $\sigma_{x/y}$ with the theoretical longitudinal resolution h (cf. Figure 3.6 and Table 3.3), with the approximation $v_{\perp}^x \approx v_{\perp}^y \approx 1 \mu\text{m}/\text{ps}$, we get:

$$\begin{cases} \sigma_{x/y} \approx 50 \mu\text{m} & (3.33a) \\ h = \sigma_z \approx 33 \mu\text{m} & (3.33b) \end{cases}$$

These numbers come out from modelling approaches, and are not direct measurements of the resolution. This can also be done, thanks to an Hanbury Brown and Twiss (HBT) experiment, when probing correlation lengths smaller than the resolution [119, 120].

Remark 3.5 (Orientation of the optical setup) Regarding the values given in Eq. (3.33), there is no wide difference between the transverse resolution and the longitudinal resolution. This was however not always the case: Figure 3.16 and Table 3.3 show that in the old setup the longitudinal resolution was about $180 \mu\text{m}$, and the transverse one was in the range of $300 \mu\text{m}$. At the time, there was a significant advantage into having the BEC elongated along the z axis, and therefore emitting the atomic pairs along the direction towards which the resolution is the best.

The major drawback of the configuration (that has been kept for legacy reasons) is the presence of an intense vertical laser beam, hitting right in the middle of the detector: this can be a problem (cf. Chapter 4). Now, with our new electronic setup, the resolution should not

1: usually a hot cloud coming from a magneto-optical trap (MOT).

2: even if we have an additional fluorescence imaging detector, it does not evaluate precisely the number of atoms in the MOT cloud, and moreover due to the high temperature many atoms of the cloud do not fall onto the MCP...

[119]: Gomes et al. (2006), “Theory for a Hanbury Brown Twiss Experiment with a Ballistically Expanding Cloud of Cold Atoms”

[120]: Schellekens et al. (2005), “Hanbury Brown Twiss Effect for Ultracold Quantum Gases”

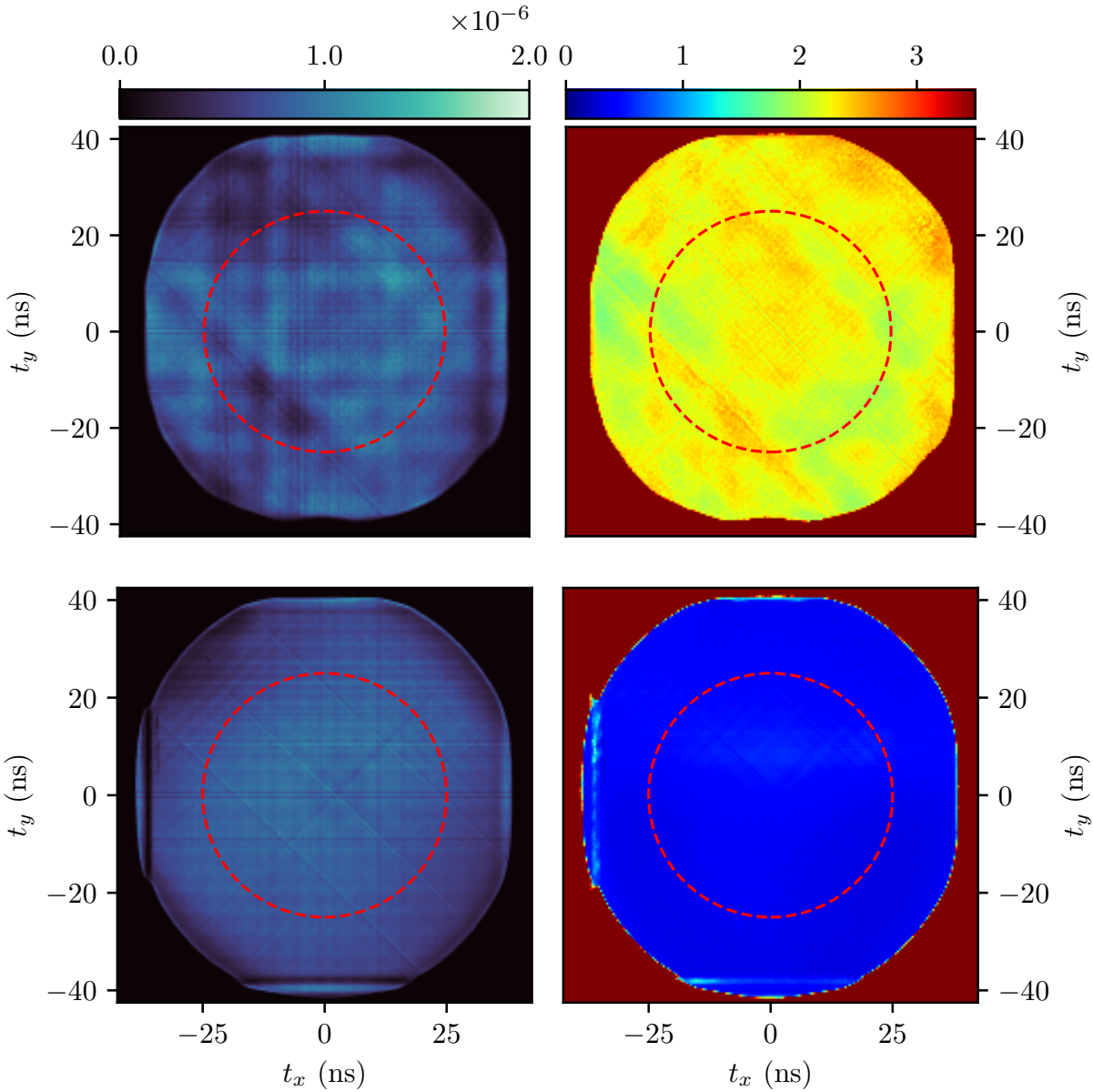


Figure 3.16: Comparison of the gain (on the left) and resolution $\frac{\sigma_s}{2\sqrt{2}}$ (on the right) maps between the old (on top) and new (on the bottom) detection system. Data have been collected in may 2019, by making hot MOT fall onto the MCP. The total number of atoms at each run is kept small in order to avoid any saturation (in practice the collimation of the atomic beam with the transverse molasses has been switched off). The averaging is made over 14 000 files, and the statistics per pixel is roughly 200 shots. The detectivity is normalised with the total number of atoms detected. The resolution is given in time steps units $\delta_t = 120$ ps. Qualitatively, we observe that the detectivity is much more homogeneous, and the resolution is finer with the new electronics (the colour maps have the same scaling). Quantitatively, we can compute means and standard deviation inside a central disc (red dotted line) with 50 ns of diameter, which is the main region of interest in our experiments:

	Detectivity fluctuations	Resolution (mean and standard deviation)
Old	33 %	2.22 δ_t (16 %)
New	16 %	0.41 δ_t (17 %)

be a topic of concern anymore, and we could consider to redesign the apparatus, such that the atomic pairs would be emitted in the horizontal plane, and no laser beam would touch the MCP's surface (cf. Remark 4.3).

3 Cooling of the metastable helium cloud: down to the BEC

3.1 Source of metastable helium

The 2^3S_1 state of helium cannot be prepared with a laser excitation (due to its very large energy). Instead, we produce it chaotically, during an electronic discharge that generates a plasma containing all kinds of excited and ionised states [121]. This procedure is extremely inefficient (less than one atom out of ten thousand is excited in the metastable state) yet effectively very bright considering the typical number of atoms loaded in a cold cloud ($\sim 10^9$). A schematic description of the source is given in Figure 3.18. The plasma is ejected at a discharge cap placed at the end of a narrow capillary tube (250 μm of diameter and 1 cm long). This reduces the width Δv_s of the velocity distribution of the plasma of atoms. Indeed, the mean free path λ_0 of an atom is related to the helium collisional cross section σ and the density n [122, 123]:

$$\left\{ \begin{array}{l} \sigma \approx 37 \text{ \AA}^2 \\ \lambda_0 = \frac{1}{\sqrt{2}n\sigma} \end{array} \right. \quad (3.34a)$$

$$(3.34b)$$

and the supersonic jet theory gives the mean \bar{v}_s and RMS width Δv_s of the velocity distribution:

$$\left\{ \begin{array}{l} \bar{v}_s = \sqrt{\frac{2\gamma}{\gamma-1} \frac{k_B T}{M}} \\ \Delta v_s = \sqrt{\frac{4}{\gamma-1} \frac{k_B T}{M} K_n} \end{array} \right. \quad (3.35a)$$

$$(3.35b)$$

where γ is the heat capacity ratio, which is $\frac{5}{3}$ for a monoatomic gas such as helium, and K_n is the Knudsen number which depends on the diameter D of the capillary:

$$K_n = \frac{\lambda_0}{D} \quad (3.36)$$

[121]: Lu et al. (2001), "A Bright Metastable Atom Source at 80 K"

[122]: Kaiser (1990), "Manipulation par laser d'hélium méta stable: effet Hanle mécanique, refroidissement sous le recul d'un photon"

[123]: Labeyrie (1998), "Deux outils pour l'optique atomique : jet intense d'hélium méta stable et miroir à onde évanescente exaltée"

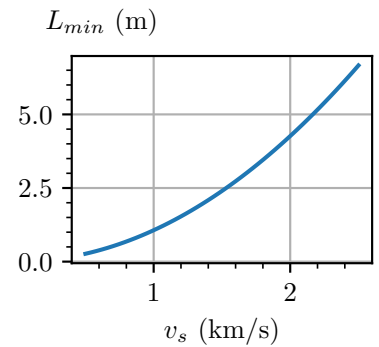
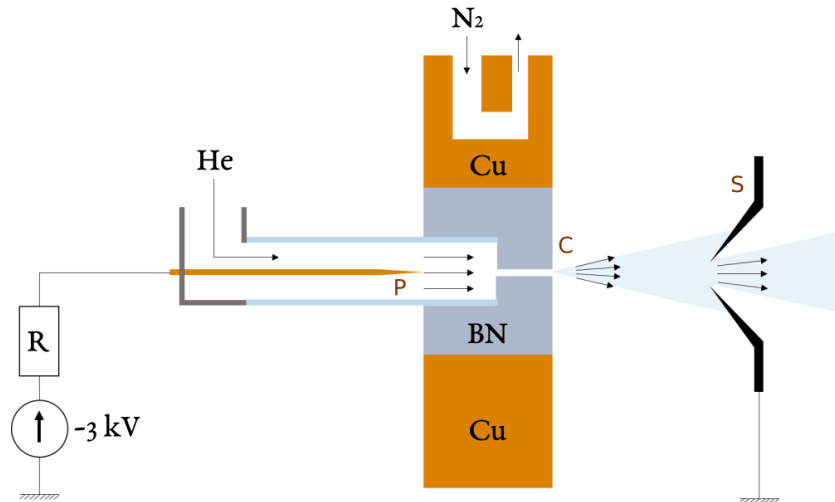


Figure 3.17: Minimal Zeeman slower length for helium, as a function of atoms velocity

Figure 3.18: Representation of the helium plasma source. Figure extracted from [60]. Helium is injected from an insulating glass tube into a boron nitride nozzle (good thermal conductor and electric insulator). The plasma is produced in the nozzle thanks to a metallic needle (P) that plays the role of a cathode. $R = 150 \text{ k}\Omega$, and the plasma resistance is estimated at $37 \text{ k}\Omega$. The plasma is ejected from the nozzle at a discharge cap (C), and crosses a skimmer (S) that acts as an anode. Discharge heat is dissipated with a copper bloc cooled down with liquid nitrogen.



Without liquid nitrogen cooling, the typical discharge temperature of 650 K would lead to an average velocity of 2600 m s^{-1} . Thanks to cooling, the typical speed is reduced to $\bar{v} \approx 1200 \text{ m s}^{-1}$ out of the discharge cap. This allows for a Zeeman slower with a reasonable length (cf. Table 5.1 and Figure 3.17).

After the skimmer, the atomic jet flux is estimated to $10^{12} \text{ s}^{-1} \text{ mm}^{-2}$ with a divergence of 40 mrad [124].

[124]: Browaeys (2000), “Piégeage magnétique d’un gaz d’hélium métastable : vers la condensation de Bose-Einstein”

3.2 Cooling procedure

Once the metastable atoms are generated, the cooling of the gas is operated through many stages. A general description of the apparatus is provided in Figure 3.19. The cloud is successively loaded and transferred into three types of traps in the science chamber:

- ▶ a magneto-optical trap (MOT) ;
- ▶ a biased magnetic trap (MT) ;
- ▶ an optical dipole trap (ODT) ;

In the following, we will briefly run through these processes. We also recall some numbers in Table 5.1.

Physical quantity	Notation	Numerical Value
Absorption cross section	$\sigma = \frac{3\lambda^2}{2\pi}$	$5.604 \cdot 10^{-13} \text{ m}^2$
Saturation intensity	$I_s = \frac{\pi\hbar c\Gamma}{3\lambda^3}$	0.167 mW cm^{-2}
Maximum deceleration	$a_{max} = \frac{\Gamma \hbar k_{rec}}{2m}$	$4.69 \cdot 10^5 \text{ m s}^{-2}$
Effective plasma temperature	$T_{\text{discharge}}$	$\approx 140 \text{ K}$
Atomic jet velocity	$v_{\text{discharge}}$	$\approx 1200 \text{ m s}^{-1}$
Minimum stopping length	$L_{min} = \frac{v_{\text{discharge}}^2}{2a_{max}}$	1.5 m

Table 3.4: Slowing and trapping characteristics of metastable helium, with the $2^3P_2 \rightarrow 2^3S_1$ transition.

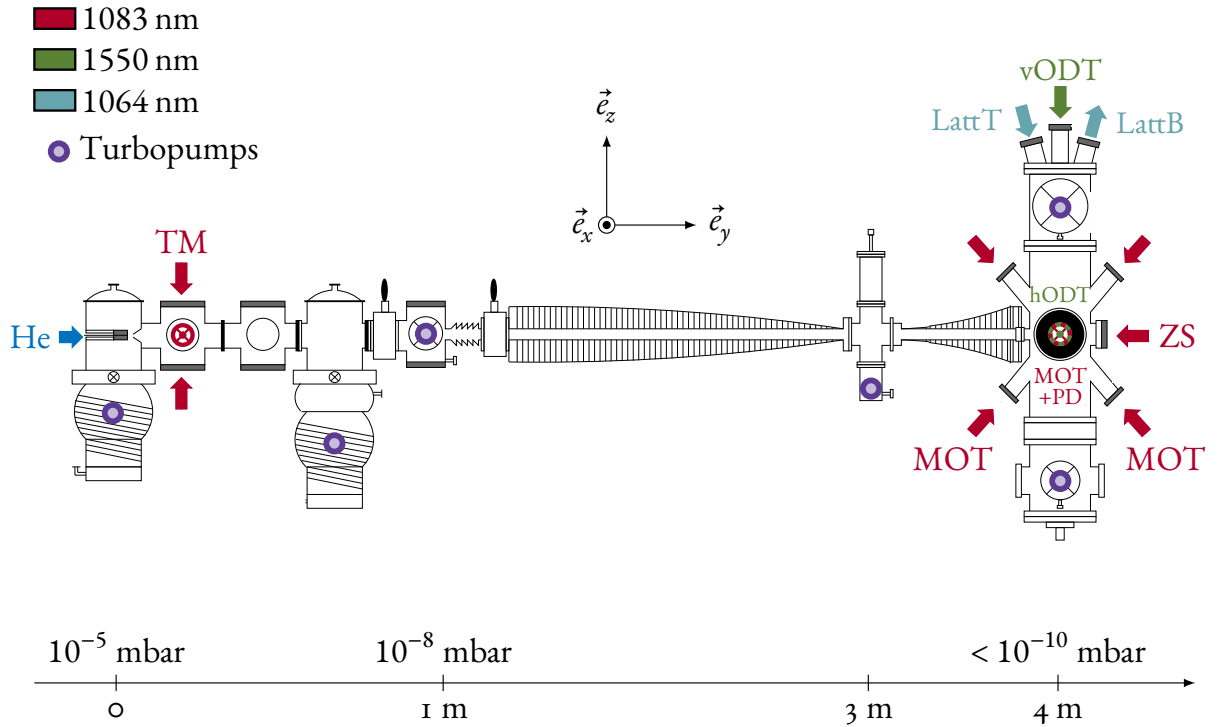


Figure 3.19: Schematic of the experiment apparatus (extracted and modified from [125]). The atomic source is on the very left, and the science chamber is the thick black ring on the very right. The MCP chamber lays below the science chamber (both chambers can be insulated from each other with a manual vacuum valve placed between the two). The different laser beams are also represented, with a given colour for each wavelength. Helium is injected on the left, in a first chamber cooled with liquid nitrogen, and where the plasma is formed. The resulting atomic beam is collimated with a transverse optical molasses (TM) of resonant light, before being slowed down across the Zeeman slower (ZS). A 3D MOT cloud is then loaded in the science chamber, thanks to three retro-reflected MOT beams. We also have an additional resonant laser beam along the y axis in the science chamber to perform atom pumping and a 1D doppler cooling (PD). Finally the cloud can be loaded in a crossed optical dipole trap (vertical: vODT, and horizontal along the x axis: hODT) in which we can perform evaporative cooling. The two laser beams LattT (lattice top) and LattB (lattice bottom) are used for generating pairs of atoms with correlated momenta. The source part (before the Zeeman slower) can be insulated from the “high-vacuum” part (after the Zeeman slower) thanks to two manual vacuum valves placed before the Zeeman slower (black handles on the drawing). A Faraday cup is also installed between the large and the small Zeeman slower, to measure the atomic flux out of the source.

3.2.1 Transverse optical molasses and Zeeman slower

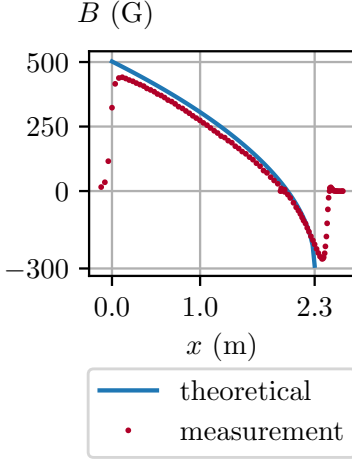


Figure 3.20: Measurement of the magnetic field along the Zeeman solenoid [124]. The theoretical is given in Eq. (3.37), without fitting adjustment.

Table 3.5: Characteristics of the Zeeman and transverse molasses beams

Transverse molasses	
Horizontal waist	59 mm
Vertical waist	11 mm
Aspect ratio	5.4
Power per beam	100 mW
Peak intensity	$59 I_3$
Detuning	-2.94 MHz
Zeeman beam	
Power	62 mW
Detuning	-394 MHz

¹: let us recall for comparison that the human g -LOC occurs at about $5g$...

[123]: Labeyrie (1998), “Deux outils pour l’optique atomique : jet intense d’hélium métastable et miroir à onde évanescente exaltée”

²: 40 cm long

Without collimation, the clipping of the atomic jet across the 4 m long Zeeman solenoid (cf. Figure 3.19) would reduce the flux in the science chamber down to $10^7 \text{ s}^{-1} \text{ mm}^{-2}$. The transverse molasses consists in two pairs of retro-reflected elliptical beams, red-detuned by 1.8Γ with respect to the $2^3S_1 \rightarrow 2^3P_2$ transition. The major axis of the ellipses is along the atomic jet, so as to have a long interaction time. This reduces the transverse (ie. in the xz -plane) velocity of the atoms a lot, and increases the flux in the science chamber. The number of atoms incoming in the science chamber per time unit has been measured in [124] to be around 10^{11} s^{-1} .

In order to be able to trap the atoms, longitudinal velocity also needs to be reduced. This is the role of the Zeeman slower, where the atoms interact with a counter-propagating beam, and the Doppler effect induced by the slowing is compensated by a spatially varying magnetic field, so as to keep the interaction resonance all the way along the tube. The maximum deceleration a_{max} is an intrinsic property of the transition and is roughly equal to $50\,000g^1$ (cf. Table 5.1). This Zeeman slower has been designed to apply a deceleration of 66 % of a_{max} [123], and is therefore slightly longer than L_{min} the minimal stopping length (cf. Table 5.1). The laser light is red-detuned by $\Delta\nu_z \approx 400 \text{ MHz}$ so as not to interact with the atoms trapped in the science chamber: this is possible with the *small* Zeeman slower² that generates a magnetic field of opposite direction such that the atoms reach the science chamber with smaller speed ($\sim 70 \text{ m s}^{-1}$) while being resonant with the far red-detuned Zeeman laser beam. The small Zeeman solenoid is shut down during the following *MOT* loading step, in order to avoid its parasitic magnetic field. The theoretical spacial profile of the field –required to perform the Zeeman slowing– takes the form:

$$B(y) = \frac{-\Delta\nu_z}{\bar{\mu}_B} + \frac{v_s}{\lambda \bar{\mu}_B} \sqrt{1 - \frac{y}{L}} \quad (3.37)$$

where $L \approx 2.3 \text{ m}$ is the solenoid length and

$$\bar{\mu}_B \triangleq \frac{\mu_B}{h} \approx 1.4 \text{ MHz G}^{-1} \quad (3.38)$$

is the Bohr magneton in Planck constant units. Measurements of this magnetic field has been made in the past, an example is given in Figure 3.20.

3.2.2 Magneto-optical trap & optical molasses

First realised 35 years ago [126], the theory of the magneto-optical trap (MOT) with a $J \rightarrow J + 1$ transition is very well known, and described in many lectures and textbooks[127, 128]. We will therefore not explore the MOT theory further, and just provide some important numbers for the current state of the experiment.

MOT loading We prepare a 3D MOT with 3 retro-reflected near resonance laser beams (cf. Figure 3.19). The magnetic field is generated by a pair of anti-Helmholtz coils, producing a gradient along their axis of 40 G cm^{-1} at the centre of the trap (cf. Figure C.2). In practice, the power supply delivers the maximum current possible (225 A) and the number of atoms is optimised by adjusting the detuning of the laser beams with an acousto-optic modulator (AOM). Light is red-detuned by 34.6Γ , with a power of approximately 30 mW per axis.

The detuning must be large compared to Γ , because the number of atoms in a MOT of metastable helium is quickly limited by the Penning collision assisted by resonant light. Indeed, in the MOT cloud is not spin-polarised, which means that the bare Penning collision rate is already very high ($\sim 10^{-10} \text{ cm}^3 \text{ s}^{-1}$ cf. Subsection 1.2.2 on page 108), but it is in addition greatly enhanced by a light-assisted mechanism[129–132]. The idea is that an atom in the excited state 2^3P_2 can interact with a metastable via a very favorable dipole-dipole interaction. When light is close to resonance, this increases the collision rate constant by two orders of magnitude! The solution to counteract this is to keep the population in the excited state very small, with far detuned MOT beams. Since with helium the cooling in MOT is only carried out by Doppler mechanisms¹, this large detuning implies large temperatures.

We use light beams as large as the viewports allow, in order to maximise the capture volume. A cloud of approximately $2.5 \cdot 10^9$ atoms is loaded in 1.5 s, with a temperature estimated² between 0.5 mK and 1 mK.

Remark 3.6 The measures of the number of atoms in the MOT are not precise, and probably underestimated: when the cloud is hot, atoms with large velocities can be out of resonance due to the

[126]: Raab et al. (1987), “Trapping of Neutral Sodium Atoms with Radiation Pressure”

[127]: Dalibard (2015), “Une brève histoire des atomes froids - Chapitre 2”

[128]: Metcalf et al. (1999), *Laser Cooling and Trapping*

Table 3.6: Characteristics of the MOT beams, and the pulses performed with it.

Waist	20 mm
MOT	
Power per beam	26 mW
Peak intensity	$25 I_s$
Detuning	-56.3 MHz
Duration	1.5 s
cMOT	
Power per beam	$190 \mu\text{W}$
Final peak intensity	$1 I_s$
Final detuning	-14.3 MHz
Ramp duration	20 ms
Optical molasses	
Power per beam	$30 \mu\text{W}$
Peak intensity	$0.18 I_s$
Detuning	-1.8 MHz
Duration	3 ms

[129]: Kumakura et al. (1999), “Laser Trapping of Metastable H^3e Atoms”

[130]: Tol et al. (1999), “Large Numbers of Cold Metastable Helium Atoms in a Magneto-Optical Trap”

[131]: Browaeys et al. (2000), “Two Body Loss Rate in a Magneto-Optical Trap of Metastable He”

[132]: Pereira Dos Santos et al. (2001), “Penning Collisions of Laser-Cooled Metastable Helium Atoms”

¹: in fact, since with helium the Doppler limit and the recoil limit for temperature are “relatively” close (cf. Table 3.2 on page 106), sub-Doppler mechanisms for cooling are never used in a MOT.

²: with the ballistic expansion of the cloud in time of flight, observed with fluorescence imaging.

Doppler effect. In practice, we measure the number of atoms in the cMOT (next cooling step, see next paragraph) to be larger than the one in the MOT, which does not make sense. In the same way, the temperature estimation is not very precise with hot gases, and should be considered as an order of magnitude.

MOT compression At the end of the loading we perform a dynamical compression of the MOT by ramping the detuning (closer to resonance), and lowering the optical power in 20 ms. The compression cools the cloud even further, and increases the phase-space density (PSD)[133]. Theoretically it might be a good idea to also ramp the current in the coils so as to adapt the magnetic field gradient accordingly during the compression (that is what is done in an analogous experiment installed in Camberra [134]), it is however difficult for us to do, as the response time of our power supply does not allow to have control at times shorter than a few tens of milliseconds. We therefore keep the same magnetic gradient during the compression.

The power per beam is lowered down to $190 \mu\text{W}$, and the detuning at the end of the compression is -8.8Γ . We end up with a compressed magneto-optical trap (cMOT) with $3 \cdot 10^9$ atoms at approximately $150 - 200 \mu\text{K}$.

The very point of this new feature is that it allows to increase a lot the PSD, by reducing both the temperature and the volume of the cloud. There is a balance to find between temperature and number of atoms: generally using laser beams closer to resonance gives cooler clouds, but with fewer atoms. Empirically, we optimise the parameters of the beams (frequency and power) by maximising:

1. the number of atoms during the MOT ;
2. the phase space density during the MOT compression ;

Optical molasses The MOT beams are used a last time for cooling, with a three-dimensional optical molasses (OM) stage, occurring right after the compression. The laser cooling mechanism of a 3D OM on helium can lead to steady-state temperature very close to the Doppler cooling limit $T_D \approx 40 \mu\text{K}$ for a laser detuning $\delta = -\frac{\Gamma}{2}$ [135].

In practice, some technical imperfection of our apparatus make the OM quite unstable, and we regularly need to control and adjust its setting. First the magnetic environment is not under control: so as

[133]: Petrich et al. (1994), “Behavior of Atoms in a Compressed Magneto-Optical Trap”

[134]: Abbas et al. (2021), “Rapid Generation of Metastable Helium Bose-Einstein Condensates”

[135]: Chang et al. (2014), “Three-Dimensional Laser Cooling at the Doppler Limit”

to keep a maximum of atoms, the quadrupole magnetic field of the MOT is shut down right before the OM¹, but because of the eddy currents induced inside the metallic frame of the science chamber, the magnetic field takes a few milliseconds to vanish. This has an effect on the detuning that we must set, but may also give a velocity to the cloud [136]². In addition, the OM is realised with the same beams as the ones used for the cMOT (we just ramp their frequency and power); these being retro-reflected laser beams, it means that the optical intensity on the way back is smaller than the one on the way forth... This power imbalance can have a negative impact on the time required to reach a steady-state, as well as the stability [135].

The molasses is applied during 3 ms with near resonance light and we can reach a final temperature of 60 μK . The measurement of the final size of the cloud is technically challenging for us, as we use the same beams to perform the cMOT, the OM and the imaging. Indeed, one of the beams is placed along the axis of the imaging camera, and we have to wait the closing of a mechanical shutter (hiding this beam) before taking the picture. This deadtime is of the order of a few hundreds of microseconds. The cloud is in the ballistic expansion regime during the 3D OM phase, we can have a coarse estimation of the typical size by considering a linear time evolution of the temperature (from $\sim 200 \mu\text{K}$ to $\sim 60 \mu\text{K}$) and a typical initial size of 1.5 mm (cMOT size). We find sizes from 2 to 3 mm, quite compatible with the time of flight (TOF) images we are able to take, a few milliseconds after the OM.

3.2.3 Magnetic trap

The second set of cooling stages is performed inside a purely magnetic trap.

Idea By definition, the metastable state 2^3S_1 has a total angular momentum quantum number $J = S = 1$, and therefore an angular momentum \mathbf{J} and a magnetic moment $\boldsymbol{\mu}$ such that

$$\boldsymbol{\mu} = -g \frac{\mu_B}{\hbar} \mathbf{J} \quad (3.39)$$

where $g = 2g_s \approx 2$ is the Landé g -factor of the metastable state³. In the presence of a magnetic field, the atoms with the total angular momentum projection quantum number $m_J \in \{-1, 0, 1\}$ acquire a potential

1: there is only 10 μs of delay between the end of the MOT compression and the beginning of the OM.

[136]: Walhout et al. (1992), " $\sigma_+ - \sigma_-$ Optical Molasses in a Longitudinal Magnetic Field"

2: and indeed, when the parameters are set such that the OM has a positive effect on the temperature, we can see a global motion of the cloud in the $-\vec{e}_x$ direction.

3: g_s being the electron spin g -factor [137].

1: if we consider semi-classically that the magnetic moment is a vector always aligned with the field, which is legitimate in our case as the Larmor precession pulsation $\Omega_L = \frac{\mu_B}{\hbar}$ is large compared to the trapping frequency.

energy $E_p(\mathbf{r})$ depending on the magnitude $B(\mathbf{r})$ of the field¹:

$$E_p(\mathbf{r}) = g m_J \mu_B B(\mathbf{r}) \quad (3.40)$$

By creating a local minimum of magnetic field, the force resulting from the vector gradient of the potential energy traps the atoms polarised in the $m_J = 1$ state.

[124]: Browaeys (2000), “Piegeage magnetique d’un gaz d’hélium métastable : vers la condensation de Bose-Einstein”
 [138]: Mewes et al. (1996), “Bose-Einstein Condensation in a Tightly Confining DC Magnetic Trap”

Shape of the trap We realise a Ioffe-Pritchard trap with two symmetric clusters of coils in a cloverleaf configuration [124], similar to those used for the preparation of the first condensates [138] (cf. Figure C.3).

Remark 3.7 We are using the same coils as the one installed by Antoine Browaeys et al. in 2000. It is a homemade design, and we are planning to change it very soon because we recently faced some problems with it (cf. Subsection 2.3 of Chapter 4).

It consists in the superposition of a dipole field along the x direction and a quadrupole field in the transverse yz -plane. Its reduction to second-order terms writes:

$$\mathbf{B} \left(\begin{bmatrix} x \\ y \\ z \end{bmatrix} \right) = \begin{bmatrix} B_0 \\ 0 \\ 0 \end{bmatrix} + B' \begin{bmatrix} 0 \\ y \\ -z \end{bmatrix} + B'' \begin{bmatrix} x^2 - \frac{1}{2}(y^2 + z^2) \\ -xy \\ -xz \end{bmatrix} \quad (3.41)$$

from which we deduce the 3D repartition of the magnitude of the field:

$$B(x, \rho = \sqrt{y^2 + z^2}) = B_0 + B' x^2 + \underbrace{\left(\frac{B'^2}{2B_0} - \frac{B''}{2} \right)}_{B''_\rho} \rho^2 \quad (3.42)$$

The trap is therefore quasi-harmonic at the centre, we denote ω_{\parallel} and ω_{\perp} the trapping frequencies along the coils' axis, and the transverse plane respectively.

B_0 is the *bias* field, it prevents having a field zero at the centre of the trap, that would induce nonadiabatic spin-flip losses, known as *Majorana losses* [139]. At the end of the OM the cloud is isotropic, with a size σ_0 and temperature T . Ideally, in order to conserve the **phase-space density (PSD)**, the harmonic trap should be set up to be also isotropic

[139]: Bergeman et al. (1989), “Quantized Motion of Atoms in a Quadrupole Magnetostatic Trap”

during the loading ($B'_\rho = B''$) and should match the condition:

$$2\mu_B B'' \sigma_0^2 = \frac{1}{2} k_B T \quad (3.43)$$

where σ_0 is the $1/\sqrt{e}$ size of the cloud, before the loading in the MT (after the optical molasses), and T the temperature of the cloud during the loading. With a cloud of 2 mm, at 60 μK (cf. 3rd paragraph of Subsection 3.2.2), this corresponds to a curvature of 5 G cm^{-2} .

The maximum curvature that we are able to generate with our coils (with the PSU at full power) is $B'' \approx 20 \text{ G cm}^{-2}$, greater than the value calculated above. It *should* therefore be optimal to proceed to the loading with a smaller current (for the adaption of the trap), and then adiabatically ramp up the current to compress the cloud.

However in practice, this kind of study has been tested in the early 2000s, without seeing much of a difference: we therefore make it as simple as possible, and load the cloud in the MT with the maximum curvature. Notice that this study was made at a time where there was no imaging system, and the size of the cloud was unknown. We will very soon change the coils of the magnetic trap (cf. Subsection 2.3 of Chapter 4). It would be interesting at this time to redo this type of testing, and see if we can find a small gain there.

Remark 3.8 One should also notice in Eq. (3.42) that the bias may control the transverse stiffness of the trap, if we want to compress it. The compression increases the collision rate (which is required to reach the evaporative cooling regime).

The trap is semi-linear (asymptotically linear in the transverse plane and harmonic in the longitudinal axis), but the bottom of the trap can always be approximated with a 3D harmonic potential.

When the trap is compressed, the region where it can be approximated with a transverse harmonic potential becomes smaller. The increase of collision rate can be computed [124] as well as the resulting heating in such a case.

When we perform the compression of the trap by reducing the bias, we have

$$\begin{cases} B' \sim 75 \text{ G cm}^{-1} \\ B'' \sim 20 \text{ G cm}^{-2} \\ B_0 < 25 \text{ G} \end{cases}$$

B'^2/B_0 is typically much larger than B'' , and

$$\omega_{\perp} \approx \sqrt{\frac{\mu_B B'^2}{m B_0}} = 2\pi \sqrt{\frac{\Lambda}{B_0}} \quad (3.44)$$

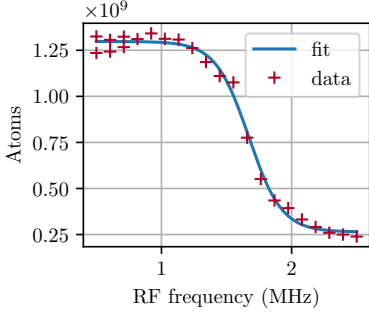


Figure 3.21: Bias measurement in the magnetic trap (explanation in the text). The data points are fitted with a tanh function, from which we extract the center, that we empirically define as the measured bias. In this example, the fit returns a measured bias of 1.67 MHz.

i: thanks to an antenna in the science chamber

To perform a bias measurement, we use the RF coupling between the magnetic sublevel $m_J = 1$ (trapped) and the magnetic sublevel $m_J = 0$ (not trapped): cf Figure 3.23 on the next page. Indeed, after the compression of the magnetic trap, we apply a RF fieldⁱ, whose frequency is constant. This frequency is scanned (from one experimental realisation to the next), starting to “small” values (smaller) towards higher values. When the RF frequencies reaches the threshold $2 \bar{\mu}_B B_0$, atoms in the $m_J = 1$ state are coupled to the $m_J = 0$ state and therefore lost from the trap: we can witness these losses by taking picture of the cloud with fluorescence imaging. An example of such a measurement is given in Figure 3.21.

Oscillation frequencies of the atoms in the trap are directly measured with fluorescence imaging, for different values of the bias current in the coils.

In practice we measured

$$\Lambda = 0.40(1) \text{ G kHz}^2 \quad (3.45)$$

Table 3.7: Characteristics of the pumping and Doppler pulses. The detunings are selected by optimising the number of trapped atoms (for the optical pumping) and the temperature (for the Doppler cooling). Because of the presence of the magnetic field, they appear to be blue-detuned.

Waist	$\sim 20 \text{ mm}$
Optical pump	
Power per beam	12 mW
Peak intensity	$\sim 11 I_s$
Detuning	23.8 MHz
Duration	50 μs
1D Doppler	
Power	15 μW
Peak intensity	$\sim 0.015 I_s$
Detuning	26.4 MHz
Duration	1 s

The longitudinal trapping frequency is however independent of the bias, and only depends on the curvature:

$$\omega_{\parallel} \approx 2 \sqrt{\frac{\mu_B B''}{m}} \approx 2\pi \times 45 \text{ Hz} \quad (3.46)$$

Atoms pumping & Doppler cooling We do not have the control on the polarisation (meaning the m_J value) of the atoms in MOT. We therefore apply a short and intense laser pulse at the beginning of the MT, with the σ^+ polarisation to transfer most of the atoms in the trapped magnetic sub-level $m_J = 1$.

We then apply a phase of 1D Doppler cooling with a dim retro-reflected beam along the x axis, very close to the resonance (about $\Gamma/2$ red detuned). The theory of the 1D Doppler cooling in a magnetic trap is not

trivial[140]. The main idea is that with a large density and therefore a big optical density, the atoms are cooled transversely by absorbing the photons spontaneously emitted by the atoms excited by the laser beam. This mechanism is slow, and might also be in competition with the optical molasses along the x axis, which is unfavourable when the density is high, and eventually leads to the heating of the cloud. This competition can be visualised in Figure 3.22, where we can see the “transverse temperature” of the cloud decreasing with the density (doppler cooling), while the “longitudinal temperature” is increasing. Even though the Doppler cooling mechanism is more efficient with dimmer light, interacting for longer times, in our case the fact that the beam also has a small π polarisation component (because of its constrained orientation) limits the maximal duration we can achieve without depolarising the gas.

Prior to Doppler cooling, we apply a first compression of the MT. This compression is done by ramping the bias down to $\bar{B}_0 = 74$ MHz in 20 ms, where

$$\bar{B}_0 = 2 \bar{\mu}_B B_0 \quad (3.47)$$

is the bias in frequency units. The resulting harmonic trap has a longitudinal frequency $\omega_{\parallel}/2\pi = 45(5)$ Hz, and a transverse frequency $\omega_{\perp}/2\pi = 122(2)$ Hz. After the Doppler cooling, we end up with a cloud of $N \sim 2.5 \cdot 10^9$ atoms at 100 μ K. Thanks to the compression and the Doppler cooling, the density has increased to (peak values) $n \sim 2.8 \cdot 10^{11} \text{ cm}^{-3}$, and the PSD to $n \lambda_{dB}^3 \sim 1.8 \cdot 10^{-4}$. Where λ_{dB} is the de Broglie thermal length given by

$$\lambda_{dB} = \frac{h}{\sqrt{2\pi m k_B T}} \quad (3.48)$$

and n is evaluated with the RMS volume of the harmonic trap:

$$\begin{cases} n = \frac{N}{(2\pi)^{3/2} \sigma_{\parallel} \sigma_{\perp}^2} & (3.49a) \\ \sigma_{i \in \{\parallel, \perp\}} = \frac{1}{\omega_i} \sqrt{\frac{k_B T}{m}} & (3.49b) \end{cases}$$

Evaporation in the magnetic trap A last compression of the magnetic trap is operated after the Doppler cooling. The bias \bar{B}_0 is lowered to 1.3 MHz, which increases the transverse trapping frequency to $\omega_{\perp} = 2\pi \times 930$ Hz, and therefore also increases the elastic collision rate.

[140]: Schmidt et al. (2003), “Doppler Cooling of an Optically Dense Cloud of Magnetically Trapped Atoms”

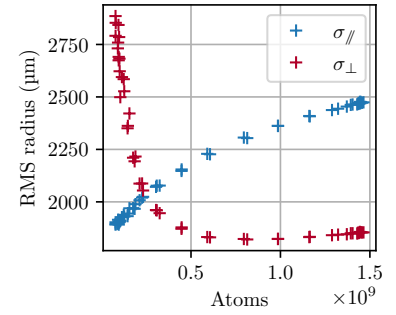


Figure 3.22: Competition between the doppler cooling in the magnetic trap, and the heating due to the longitudinal optical molasses. The data are acquired with fluorescence imaging, after a time of flight of the cloud of 3 ms: the RMS size of the cloud is therefore a picture of the temperature. When the density increases, the longitudinal length of cloud σ_{\parallel} increases as well, while transversely the cloud is smaller.

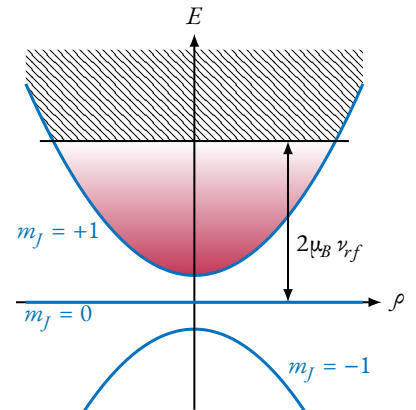


Figure 3.23: Schematic of the RF coupling used to perform evaporative cooling in the MT. Only atoms in the $m_j = 1$ magnetic sublevel are trapped (red shaded area). They oscillate in the trap, in a domain depending on their kinetic energy (which follows a Maxwell-Boltzmann distribution, driven by the temperature T of the cloud). The “hottest” atoms, with an energy above $2\mu_B \nu_f$ (hatched pattern), are coupled with the untrapped sublevel $m_j = 0$, and are therefore lost.

We then perform an evaporative cooling stage, with an RF antenna that couples the trapped $m_J = 1$ magnetic sublevel to the not trapped $m_J = 0$ magnetic sublevel. Starting at large frequency, and slowly lowering it, the RF evacuates the most energetic atoms and the cloud has the time to re-thermalise thanks to the elastic collisions [141]. The goal is to prepare a cloud cold enough to be trapped in the optical dipole trap (ODT), in which we apply the last steps of the experimental cycle. The RF frequency ν_{rf} has a temporal profile of decaying exponential with the typical following parameters:

[141]: Luiten et al. (1996), “Kinetic Theory of the Evaporative Cooling of a Trapped Gas”

Ramp duration	1.5 s
Time constant	0.9 s
Initial RF frequency	35 MHz
Final RF frequency	8 MHz

At the end of the RF evaporation, the cloud contains $N \sim 5 \cdot 10^8$ atoms, with a temperature $T \sim 45 \mu\text{K}$.

We also have the possibility to push the evaporation further, in order to obtain a BEC in the MT. Historically, the group prepared the first BEC of metastable helium this way [142]. With a bias $\bar{B}_0 = 1.3 \text{ MHz}$, the evaporation parameters are typically:

[142]: Robert et al. (2001), “A Bose-Einstein Condensate of Metastable Atoms”

Ramp duration	2.5 s
Time constant	0.9 s
Initial RF frequency	35 MHz
Condensation frequency	2.3 MHz
Typical final RF frequency	1.8 MHz

However, current and vibrational instabilities in the coils induce painful bias fluctuations (especially since an episode of overheating of the coils that occurred in October 2020... see Chapter 4). These fluctuations make the number of atoms, probability of condensation and even the position of the cloud not very reliable when the evaporation in MT is pushed very far. This was one of the motivations for installing an optical trap in which we perform the final cooling stage.

3.2.4 Optical dipole trap (ODT)

Presentation After the evaporation in the MT, we shine two intense laser light beams at 1550 nm (i.e. very far red-detuned) focused on the cloud, in order to load the atoms in a crossed ODT. The first beam is oriented along the vertical axis (going from the top to the bottom), and the second one is horizontal (oriented along \vec{e}_x). The overlap between the MT and the ODT lasts 500 ms, letting some time to the trap to capture atoms. We keep a magnetic field of a few gauss¹, along \vec{e}_x during the trapping, such that the atoms remain in the $m_j = 1$ sublevel, and the Penning collisions are strongly reduced.

Once loaded in the ODT, we induce evaporative cooling of the cloud again, by lowering the optical power. At some point, the PSD crosses the critical value, and BEC is obtained.

The ODT laser source has been changed in 2017. However no BEC was obtained at the time until 2022, because of different issues that will be explained in details in Chapter 4. I contributed to the fixing of these problems, and the setting of a new evaporation protocol, generating BECs in a stable and reliable way.

The vertical beam (vODT) is the most powerful (5 W during the loading) and has the smallest waist (42.5 μm). It drives the evaporation and compensates the gravity potential, during most of the cooling stage². The temporal profile of its power is represented in Figure 3.24, and the power-related quantities are given in Table 3.8 and Table 4.1.

Power rising duration	150 ms
Full power duration	500 ms
Evap. ramp duration	2.5 s
Evap. ramp time constant	500 ms
Final power holding	400 ms

Single beam issues At the end of the evaporation, the longitudinal trapping frequency of the vertical beam is very small (~ 10 Hz cf. Table 4.1) and as a consequence the trapping area is very elongated: the centre

Table 3.8: Characteristics of the ODT during the loading. Gravity is taken into account in the evaluation of the depth.

vODT	
Waist	42.5 μm
Power	5 W
Depth	160 μK
Transverse trap. freq.	5.23 kHz
Longitudinal trap. freq.	43 Hz
hODT	
Waist	135 μm
Power	1 W
Depth	3.7 μK
Transverse trap. freq.	231 Hz
Longitudinal trap. freq.	0.6 Hz

¹: it is generated by a pair of coils, in an approximate Helmholtz configuration, with a current of 0.8 A.

Table 3.9: Characteristics of the ODT at the end of the evaporation. With such low powers, neither of the two beams can compensate the gravity. We give the total trapping depth of the trap, which is strongly dependent on the relative position of the waists of the beams: we just have an order of magnitude.

vODT	
Power	0.4 W
Transverse trap. freq.	1.48 kHz
Longitudinal trap. freq.	12.1 Hz
hODT	
Power	0.1 W
Transverse trap. freq.	73.3 Hz
Longitudinal trap. freq.	189 mHz

²: when its power is lowered below 0.55 W it no longer compensates the gravity, and the vertical trapping is carried out by the horizontal beam.

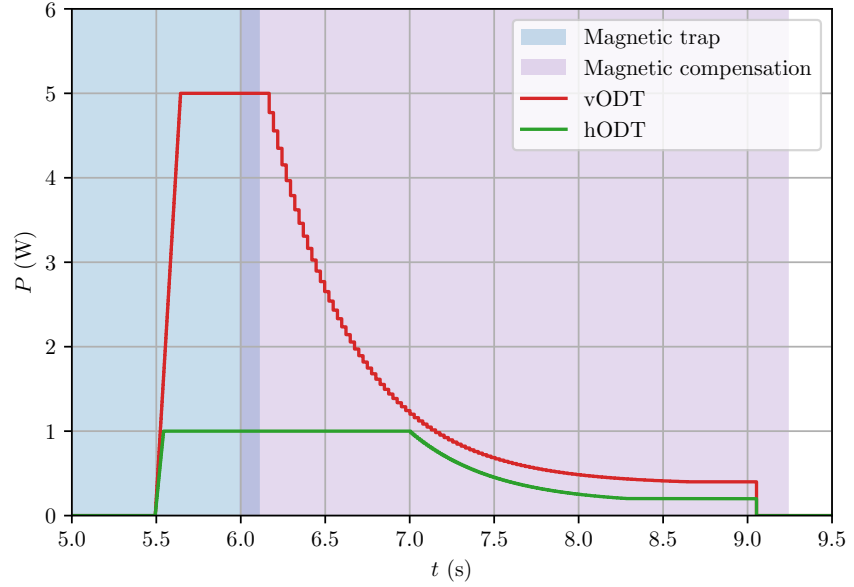
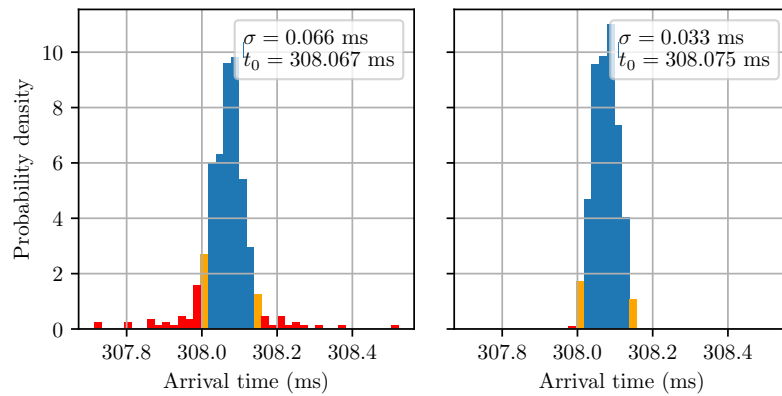


Figure 3.24: Temporal profile of the power of the ODT beams. There is a roughly 115 ms long overlap between the MT and the magnetic compensation. $t = 0$ corresponds to the beginning of an experimental realisation.

Figure 3.25: Histograms of BECs arrival times without horizontal ODT (on the left: 438 BEC realisations), and with the horizontal beam (on the right: 516 BEC realisations). The orange bins are at the same time values on both graphs, their colour is different in order to guide the eye. Due to a bigger jitter (red bins) the standard deviation σ without the hODT is twice as large as in the crossed ODT. A similar study has been carried out in 2015 with the previous laser, and can be visualised (with more data statistics) in [8]. However, at the time a much less powerful laser were used, and this effect was even stronger.



of the cloud may slightly oscillate along this axis. This very strong anisotropy of the trapping frequency ($\omega_{\perp}/\omega_{\parallel} \approx 120$) causes two main issues, that motivate the realisation of a crossed ODT by installing an horizontal beam:

1. By looking at the arrival times of BECs on the MCP, we observe that it effectively broadens the shot-to-shot fluctuations of the initial velocity of the cloud when the trap is shut down (cf. Figure 3.25 histogram on the left).

This is problematic because, as we will see in Chapter 5, the momentum of the BEC has an important effect on the mechanism of emission of correlated atoms that we use. Such a jitter also blurs the signal of second-order correlation functions that we measure for the momenta of pairs of atoms (with large statistical averaging). Increasing the trapping frequency along the vertical axis reduces these shot-to-shot fluctuations.

2. When the transverse confinement is much larger than the longitudinal one, the transverse motion becomes *frozen* for the atoms, and the physics of the BEC enters the 1D regime. By denoting a_{bo} the characteristic length of the quantum harmonic oscillator

$$\boxed{a_{bo}^\perp = \sqrt{\frac{\hbar}{m\omega_\perp}}} \quad \boxed{a_{bo}^\parallel = \sqrt{\frac{\hbar}{m\omega_\parallel}}} \quad (3.50)$$

the transverse size of such 1D quasi-BEC is gaussian with width $\sigma_\rho \propto a_{bo}^\perp$, and its length depends on the chemical potential. We can estimate in which regime the cloud lays with an adimensional number χ [143] that roughly quantifies the ratio of the mean-field interaction energy to the radial confinement energy:

$$\boxed{\chi = N \frac{\omega_\parallel a}{\omega_\perp a_{bo}^\perp}} \quad (3.51)$$

When $\chi \gg 1$, the interactions dominate and we recover in the 3D Thomas-Fermi (TF) case. On the contrary, when $\chi \ll 1$ the transverse degrees of freedom are frozen, and the condensate is effectively one-dimensional. With the vertical beam alone, and the parameters in Table 4.1, we have $\chi \approx 1.41$ which is an intermediate regime described in [144].

In particular, it is known for those elongated ultra-cold clouds that there is a regime of temperatures, below the critical temperature T_c , where the density fluctuations vanished but there is still low-energy excitations that cause *phase* fluctuations[†] [145, 146]

$$\left\{ \begin{array}{l} \bar{\omega} \triangleq \sqrt[3]{\omega_\parallel \omega_\perp^2} \\ k_B T_c \approx \sqrt[3]{N \hbar \bar{\omega}} \end{array} \right. \quad (3.52a)$$

$$\left\{ \begin{array}{l} \bar{\omega} \triangleq \sqrt[3]{\omega_\parallel \omega_\perp^2} \\ k_B T_c \approx \sqrt[3]{N \hbar \bar{\omega}} \end{array} \right. \quad (3.52b)$$

we denote T_ϕ the temperature to reach so as to remove these phase fluctuations:

$$\boxed{T_\phi = 15 (\hbar\omega_\parallel)^2 \frac{N}{32 \mu k_B}} \quad (3.53)$$

where μ is the chemical potential.

Without horizontal beam, with $N \sim 3 \cdot 10^4$ and the parameters in Table 4.1 for the vertical beam, we estimate:

$$\left\{ \begin{array}{l} T_c \sim 450 \text{ nK} \\ T_\phi \sim 100 \text{ nK} \end{array} \right. \quad (3.54a)$$

$$\left\{ \begin{array}{l} T_c \sim 450 \text{ nK} \\ T_\phi \sim 100 \text{ nK} \end{array} \right. \quad (3.54b)$$

[143]: Menotti et al. (2002), “Collective Oscillations of a One-Dimensional Trapped Bose-Einstein Gas”

[144]: Gerbier (2004), “Quasi-1D Bose-Einstein Condensates in the Dimensional Crossover Regime”

†: the phase coherence of the cloud is not strictly satisfied and that is why we talk about *quasi*-BEC.

[145]: Petrov et al. (2001), “Phase-Fluctuating 3D Bose-Einstein Condensates in Elongated Traps”

[146]: Gallucci et al. (2012), “Phase Coherence in Quasicondensate Experiments”

This defines a problematic range of temperatures where the phase fluctuations are not negligible and induce velocity fluctuations (which is the observable that we probe after time of flight). It would also affect the coherence of the atomic pair production. We do want to avoid this regime.

Crossed dipole trap We therefore installed another beam in the horizontal plane, forming an angle of 7° with respect to the x axis, and with a waist of $135 \mu\text{m}$. It increases the trapping frequency along the vertical direction up to $\sim 75 \text{ Hz}$ at the end of the evaporation (cf. Table 3.8 and Table 4.1). The temporal profile of the power is represented in Figure 3.24, and the power-related quantities are given in Table 3.8 and Table 4.1. Concerning the horizontal beam, we set up:

Power rising duration	50 ms
Full power duration	1.5 s
Evap. ramp duration	1.3 s
Evap. ramp decay rate	500 ms
Minimal power holding	760 ms

Two 40 MHz AOMs create a 80 MHz frequency difference, such that there is no slow modulation of the intensity due to the beating between the two axis.

In the cylindrical basis defined by their axis of propagation and centred on their waists (ρ, φ, ζ) , each beam creates a dipole potential V_{dip} :

$$\left\{ \begin{array}{l} V_{dip}(\rho, \varphi, \zeta) = \frac{V_0}{1 + \left(\frac{\zeta}{z_R}\right)^2} \exp\left(-\frac{2\rho^2}{w^2 \left[1 + \left(\frac{\zeta}{z_R}\right)^2\right]}\right) \quad (3.55a) \\ V_0 = -\frac{3\pi c^2}{2\omega_0^3} \frac{2P}{\pi w^2} \left(\frac{\Gamma}{\omega_0 - \omega} + \frac{\Gamma}{\omega_0 + \omega}\right) \quad (3.55b) \\ z_R = \frac{\pi w^2}{\lambda} \quad (3.55c) \end{array} \right.$$

where $\lambda = 1550 \text{ nm}$ is the laser wavelength, $\omega = 2\pi\frac{c}{\lambda}$ is the associated angular frequency, ω_0 is the angular frequency of the $2^3S_1 \rightarrow 2^3P_2$ cooling transition, $\Gamma = 2\pi \times 1.6 \text{ MHz}$ is the corresponding natural linewidth, w is the waist of the beam and z_R its Rayleigh length.

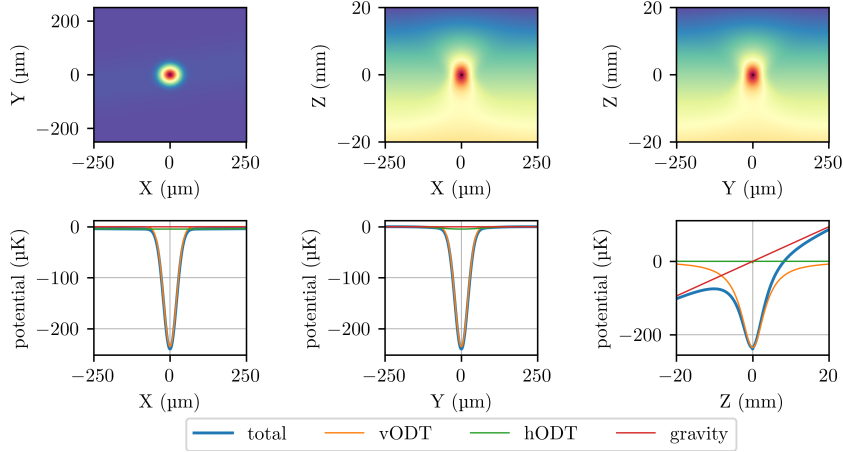


Figure 3.26: Potential seen by the atoms during the loading. Even though the trapping frequency of the hODT along the vertical axis z is higher than the vODT one, it effectively has no effect because it is far too shallow. Due to this huge difference of intensity, the horizontal beam is also almost invisible in the xy plane, on the top left heatmap.

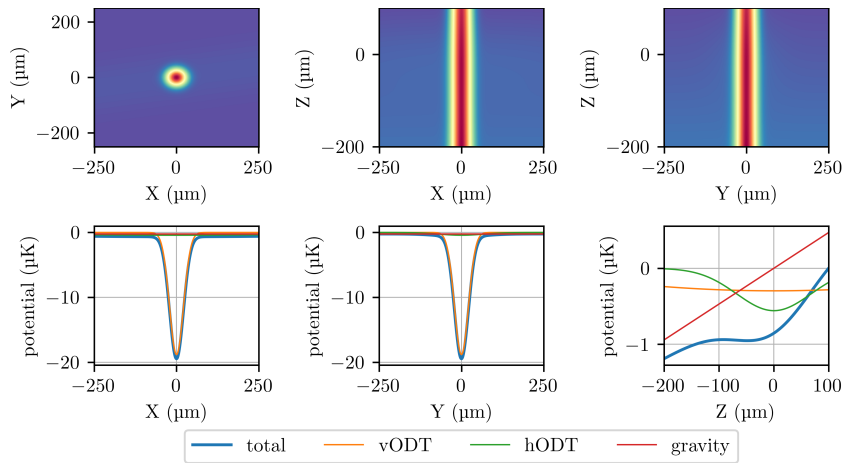


Figure 3.27: Potential seen by the atoms at the end of the evaporation. Now the horizontal beam has a dominant effect on the depth and trapping frequency along the vertical z direction. The depth in the Z direction is difficult to evaluate, because it is very sensitive to the geometry of the beams. It is however probably of the order of $1 \mu\text{K}$. We added an unimportant offset to the vODT potential to make it visible on the same 1D bottom right graph.

The gravitation generates the well known potential V_{grav} :

$$V_{grav}(z) = -mgz \quad (3.56)$$

We can take all the pieces together and simulate the total potential V_{tot} seen by the atoms in a Python code to generate the visualisation in Figure 3.26 and Figure 3.27.

Final cloud The counting of the number of atoms in the BEC is not trivial in our experiment. Indeed, the velocity distribution of the atoms in a BEC is very narrow, which means that after releasing the trap, many atoms are detected on a small area of the MCP ($\sim 1 \text{ cm}^2$) in a very short time range ($\sim 100 \mu\text{s}$). This flux of atoms is in particular larger than $10^5 \text{ s}^{-1} \text{ cm}^{-2}$, the typical flux saturation of the MCP, and the number of atoms is strongly underestimated...

We can slightly enlarge the velocity distribution by heating the cloud with the optical lattice used for the atomic pair generation (cf. Chapter

5). More atoms are detected but we still see saturation of the detector at the BEC arrival time. We measured $N \sim 2.8 \cdot 10^4$ atoms with this technique, which is therefore a lower bound. An improvement of this technique would be to realise Bragg diffraction of the cloud to many orders, so as to spread the falling of the atoms over a very long time, but this part of the apparatus is not perfectly operational at the time when this manuscript is being written. This technique was used a few years ago (however with a different ODT configuration) and a value of $N \sim 5 \cdot 10^4$ was found [8], with 20% uncertainty because of the inaccurate knowledge of the MCP quantum efficiency.

[8]: Lopes (2015), “An Atomic Hong-Ou-Mandel Experiment”

If we compare the current state of the ODT with the configuration that was used before 2018, we use beams with roughly the same waist as before, but with much more power (we went from ~ 1.5 W available on atoms to ~ 11 W available on atoms). Due to the small optical power, in the previous configuration people were forced to load a cloud already very cold in the ODT, meaning that it required to be cooled in the MT down to a temperature very close to the bias of the MT (which is known to be very prone to fluctuations). Therefore the relative fluctuations of the initial number of atoms in the ODT was large. In addition, the ratio $U/k_B T$ between the depth of the ODT and the thermal energy of the cloud was not very favourable to an efficient evaporative cooling (~ 3).

With the new laser, we improved the initial loading by two orders of magnitude, and the loaded cloud is warmer. We are no longer sensitive to the fluctuations of the MT’s bias. The evaporative cooling is also more efficient.

	2015	2022
Atoms loaded	$\sim 2 \cdot 10^5$	$\sim 2 \cdot 10^7$
Loaded cloud temperature	3 μ K	22 μ K
BEC atoms number	$5 \cdot 10^4$	$N > 2.8 \cdot 10^4$
Thermal fraction temperature	200 nK	~ 200 nK

Even though we estimate that the final number of atoms in the BEC did not change much, and lays between $3 \cdot 10^4$ and 10^5 , we improved the stability and the reliability of condensation a lot.

Remark 3.9 (Raman transfer) Until the end of the ODT, atoms are polarised in the $m_j = 1$ magnetic sublevel. This is not good during the free fall following the release of the trap, because stray

magnetic fields could deviate the cloud during falling or induce phase fluctuations.

We therefore need to perform a transition between the sublevels $m_J = 1$ and $m_J = 0$ right after the releasing of the trap. We perform a two-photon Raman transition, with the 2^3P_0 state. This way we can achieve more than 90 % of transfer efficiency.

3.2.5 Recap

The entire cooling procedure takes less than 10 seconds (cf. Figure 3.28), which is a significant improvement in comparison with the previous states of the experiment (roughly speaking, before 2019) where a similar cycle used to take more than 30 seconds. In addition, the setup currently being neither fully complete nor perfectly stable, we did not yet proceed to the ultimate time optimisation of all the cooling stages. Thus we have good reasons to hope that this final optimisation could save one second or more (especially during the evaporative processes).

This enhancement of the duty cycle of the experiment is particularly appreciable. Indeed, the quantum effect that we aim at requires the use of an atomic-pair source¹ that usually has a very low pair production rate². When the experiment is running, and considering a TMS with an average number of particle per mode ν , the average number of pair detected per second is

$$\gamma_{pair} = \nu \frac{\eta^2}{T_{exp}} \quad (3.57)$$

where T_{exp} is the duty cycle of a run, η is the quantum efficiency of the MCP (squared because we want to detect two atoms) ν is the average number of atoms per mode. With the changing of the MCP, and the cooling speedup, we increased this rate by a factor 12.

1: this source is described in Chapter 5, where we will see that the BEC is an important component of it.

2: we have seen in Chapter 2 that a Bell inequality violation based on a TMS is easier to see when the average number of particle per mode ν is small: in practice typically of the order of 0.1

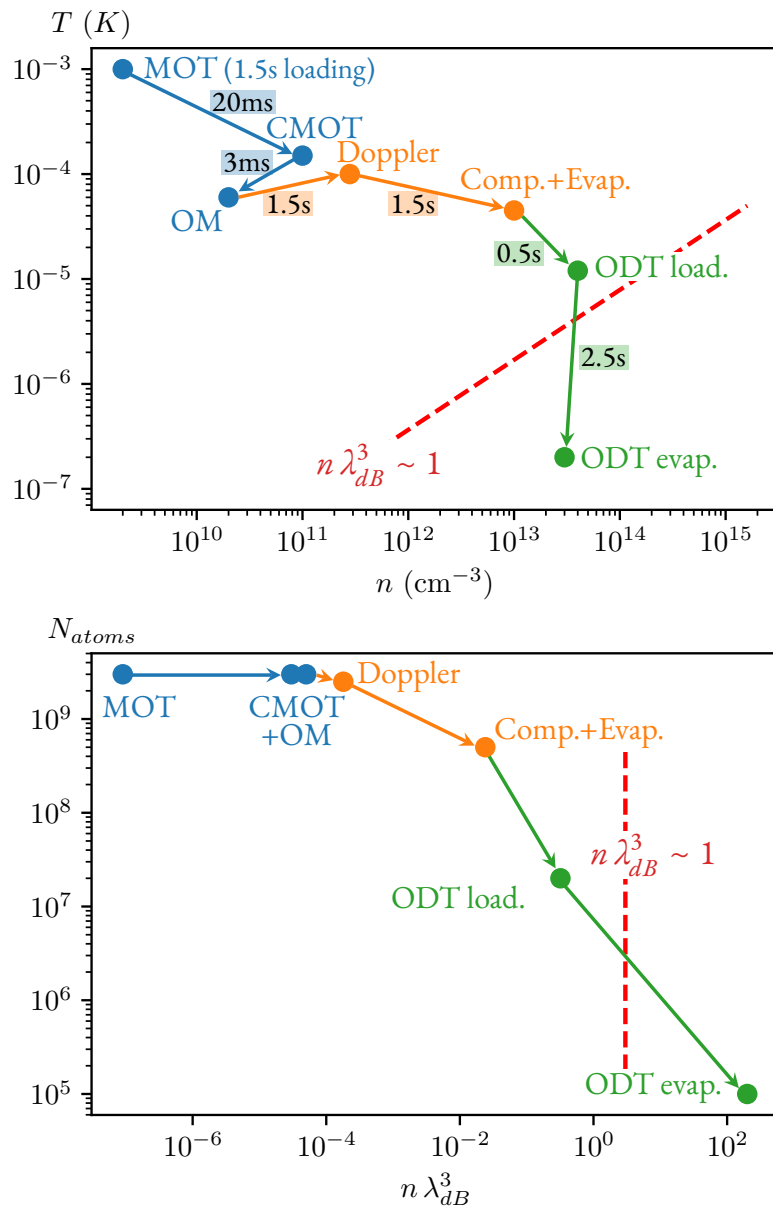


Figure 3.28: Overview of the different cooling steps of the procedure: from a MOT cloud to a BEC. The numerical values are order of magnitudes (especially for the MOT clouds in blue where the measurements are not easy). The red dashed line represents the condensation threshold.

Technology changes | 4

Chapter's table of contents

. Introduction	148
1. Status of the experiment in 2019	149
2. Problems and workarounds during my PhD	150
2.1 Holes in the MCP	151
2.1.1 Genesis of the breakdown	151
2.1.2 Pushing the cloud with a Raman kick	152
2.1.3 Protecting the MCP with a copper plate	154
2.2 A new cooling laser	159
2.2.1 Why do it?	159
2.2.2 The new laser	160
2.2.3 Obtained effects	161
2.3 Instabilities of the magnetic trap	163
2.4 A next-gen sequencer and software control	164
2.4.1 GUS and the old hardware	164
2.4.2 ADwin sequencer and the QControl3 project	166
2.4.3 QControl3 structure	166
2.4.4 A word about HAL	169

Introduction

[59]: Lopes et al. (2015), “Atomic Hong–Ou–Mandel Experiment”

[9]: Dussarrat et al. (2017), “Two-Particle Four-Mode Interferometer for Atoms”

I joined the team of professors Boiron & Westbrook (as a Master’s student) in April 2019. At the time, people of the team had already been facing technical difficulties for more than 2 years, which prohibited the realisation of new scientific measurements. The last milestones of the team were the atomic HOM effect [59] and the two-particle four-mode atomic interferometer [9], respectively published in 2015 and 2017.

Several repairs and apparatus upgrades had already been made when I arrived, but unfortunately I cannot say that we quickly saw the light at the end of the tunnel... My PhD too was marked by serious technical difficulties, that checked our initial ambition to observe an atomic Bell inequalities violation.

In February 2021, it was collectively decided that we would operate heavy modifications on the apparatus, in order to (hopefully) fix the various stability problems that we encountered. This considerable investment in both time and money seemed to be worth it, and we will detail what has been done concretely in this chapter.

1 Status of the experiment in 2019

In April 2019 the experiment was just recovering from a first wave of issues [60], including two major ones amongst the rest:

1. **Vacuum (June 2016):** A science chamber's turbopump broke down → **6 months** of maintenance (long delivery times and the changing operation required the dismantling of many optomechanical components).
2. **ODT (2017):** The laser used for experiments [59] and [9] was not powerful enough to guarantee a stable condensation of the cloud (1.5 W usable on the atoms). The breadboard for the optomechanics (placed vertically) was not perfectly stable. The laser was therefore changed, and the optomechanics completely remade, but the new laser (designed by Keopsys[®]) died twice in less than two months¹. After two consecutive repairs, the laser was finally restrained to a 20 W nominal power. In total, an other **6 months** of work was spent on this operation. Actually, we continued to have problems with this laser, even very recently²

In order to complete the detection system, a *short-wave infrared* (SWIR) InGaAs camera³ was also installed in 2017 to perform fluorescence imaging. Indeed, even though the MCP is very well-suited for the detection of low density clouds in the far field (atomic pairs in our case), it is not very convenient for the daily monitoring of the clouds: it easily saturates when the density or the number of atoms is large ; it only provides information in the momentum space (we cannot see the cloud spatially in the trap) ; if the atoms are polarised, residual magnetic fields may perturb the “free fall”. The camera solves these issues by observing the fluorescence of the cloud, along the axis of one of the three MOT beams, while the two other beams briefly excite the atoms with resonant light. It also simplifies the alignment of the ODT, since the loaded atoms can be seen directly. The setup is a bit complicated, because it requires a motorised flip-mirror to toggle between the 3D MOT configuration and the imaging configuration, but it is the best compromise since the experiment was not initially thought to host such a camera, and optical access to the vacuum chamber is very limited.

To provide a correct estimation of the number of atoms, the fluorescence imaging pulse requires to saturate the $2^3S_1 \rightarrow 2^3P$ transition. The problem was that at the time not enough power was available in the MOT beams' cluster⁴. Eventually, almost the entire optical setup for the cooling had to be redone. The total time cost of the installation

[60]: Perrier (2018), “Interférences multiples avec atomes froids”

1: we have good reasons to believe that the company sold a technology (30 W 1550 nm fibered laser) that they did not master

2: the most recent breakdown having taken place on July 2022. We therefore ordered a new 30 W IPG Photonics[®] fibered laser that we will soon install on the experiment.

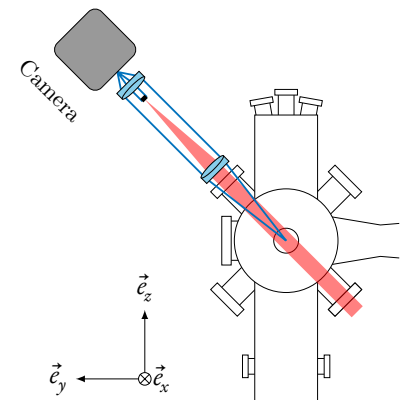


Figure 4.1: Schematic of the camera set-up, used for the fluorescence imaging. The figure is modified from [60]. Axis orientations are consistent with Figure 3.19. The telescope forms the image of the cloud on the CCD during the imaging (blue rays), and a motorised flip-mirror is used for the retro-reflection of the MOT beam.

3: Xeva 320 Series designed by Xenics[®], with 80 % of quantum efficiency and 30 μm large pixels.

4: for legacy reasons many components (AOMs, lenses, RF amplifiers...) were not fitting the needs, and the beams had many defects (bad waists, bad power balance, bad optical isolator (OI) coupling...)

of the camera was therefore also amounted to several months.

The final software integration of the imaging system was done during my PhD (cf. Appenfix B for technical details).

When I joined the team, the ODT was not yet focused on the atoms, and the condensation was not successfully observed with the new Keopsys[®] laser. A Hamamatsu[®] new generation MCP (with better quantum efficiency) was available in the lab, but not installed on the experiment. The main short-term objectives therefore were:

1. aligning the ODT and finding power temporal profiles for the evaporation to condensation ;
2. testing the performances of the new MCP on a benchmarking bench, before installing it on the MCP ;
3. putting the pair creation and Bragg optical lattices back into service.

2 Problems and workarounds during my PhD

Since 2016 and the apparition of the previously mentioned problems, the apparatus suffered from many technical issues. Our hope that the fixing operations, briefly explained in the first section of this chapter, would lead to a quick healing of the experiment, and new scientific investigation vanished rapidly. Instead, we had to deal with other difficulties: hardware/software malfunction, equipment breakdown (sometimes due to human mistake and sometimes not), cloud instabilities... After struggling a long time, without durable progress, we finally collegially decided –in February 2021– to proceed to massive apparatus changes. It was not an easy decision to make, as it also meant that the scientific part of the project would also be in standby for several months more.

As I write this manuscript, even if the setup is not fully upgraded yet, we already have very promising experimental results, that convinced us that this laborious work was worth it. In this section, I will detail the nature of the issues that we encountered, and what solutions we decided to implement to cure them.

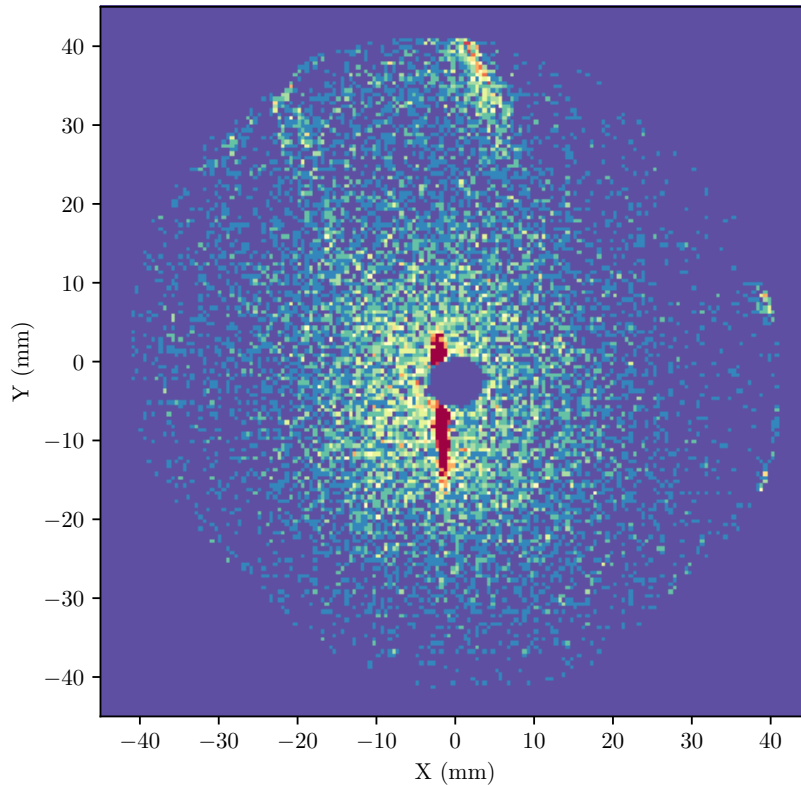


Figure 4.2: Image of the hole in the old Burle MCP. Axis orientations are consistent with Figure 3.19. Colours encode the number of atoms detected. The red line corresponds to BEC obtained with RF evaporative cooling in the magnetic trap: after time of flight the cigar-shaped BEC along the x -axis becomes a pancake in the transverse yz -plane, due to the famous anisotropic expansion of BECs. A zero-detectivity disc at the centre is visible. The diameter of this hole roughly matches the $1/e^2$ size of the vODT on the MCP... Data come from a single run (which is why the heatmap is quite “sparse”).

2.1 Holes in the MCP

2.1.1 Genesis of the breakdown

A few months after the beginning of my PhD, we obtained a BEC in the ODT and we started to optimise the atomic pair creation process. For the following it is worth noticing that the vODT hits right in the middle of the MCP¹. In August 2019, we tried to keep the vODT beam at full power during the MOT phase (8 W at the time) in order to keep the AOM and the fiber coupler warm, and minimise the thermal fluctuations during the loading of the ODT². It turned out to be quite a bad idea. The MCP could not dissipate that much power for such a long time (a few seconds per run cycle) and a “hole” (i.e. zero detectivity) in the detectivity map quickly appeared (cf. Figure 4.2).

This experimental mishap motivated the installation of the brand new Hamamatsu[®] MCP, that I had finished testing on a separate minimal apparatus a few weeks before that. This was a rather heavy operation:

- ▶ it required to brake the ultra-high vacuum in the MCP chamber, and therefore a one-week baking was needed afterwards ;
- ▶ the vacuum high-voltage electrical connections are delicate ;
- ▶ once the change of the MCP and the chamber baking had been

¹: which is not an optimal design, but we do not have that much flexibility with our science chamber, if we want the BEC to be cigar-shaped along the vertical direction. It never was an issue with the previous IPG Photonics[®] laser (with 1.5 W on the atoms) and the MCP that was used at that time.

²: in many aspects, the coupling of the high power optical fibers has always been a technical issue for us. In particular it appeared that when the laser is switched on, the coupling efficiency fluctuates for a few seconds because of the heating of optical components.

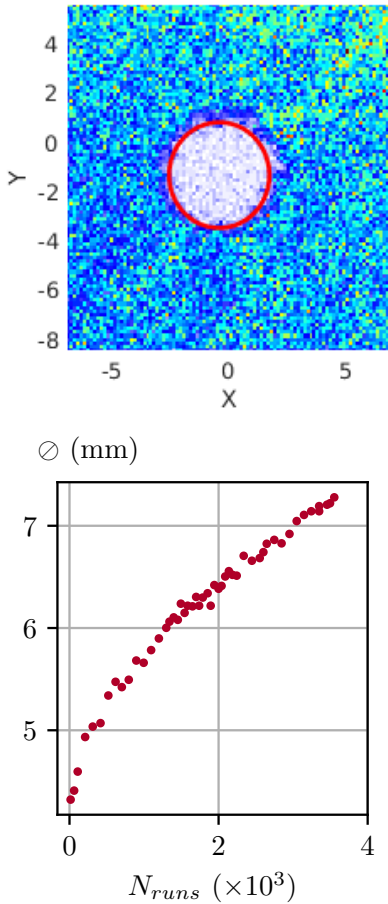


Figure 4.3: Evolution of the diameter of the hole, as a function of the number of experimental realisations. During each run, the vODT makes a $1.8 \text{ W} \rightarrow 0.5 \text{ W}$ exponential decay in 4 s, and the hole diameter is then evaluated with a bidimensional fitting (top graph). We then plot the evolution of the diameter (bottom graph), where every red point is the statistical average of the measured diameters for ~ 30 consecutive runs.

successfully achieved, the MCP needed to degas all the residual impurities present in the microchannels. This process was stimulated by the activation of the microchannels with metastable atoms (in practice we repeat the falling of hot MOT clouds on the MCP), but it was still very long (several weeks).

We finally got back to the evaporation in the ODT in January 2019 (5 months later). We reduced the maximum power of the vODT to 5 W, and dropped the idea of keeping it on at full power for a long time. Yet, another hole, similar to the previous one (Figure 4.2), appeared in the middle of the plate... It turns out (phenomenologically) that the new Hammamatsu[®] MCPs are far less resilient to heating than the ones previously used in the experiment. It is a major issue for us, because the atomic pair creation process generates atoms whose velocities are along the BEC axis. Thus, the hole, the BEC and the atomic pairs are aligned along the vertical axis, and the signal of interest is undetectable (the pairs fall right in the middle of the hole)!

In order to check if once the hole is made it continues to grow, we tried to repeat fake exponential evaporation with the vertical beam (without atoms) lowering again its maximum power down to 1.8 W (which is roughly the minimum power we need to reliably prepare a BEC). The result is presented on Figure 4.3, where we can see that the hole’s diameter does not converge quickly towards an “acceptable value” (which would be less than 10 mm, as it will be explained in the following subsection). We therefore stopped doing this and looked for more sustainable workarounds, to overcome the two following problems:

1. *How to detect the signal of interest with a zero-detectivity disc in the middle of the MCP?*
2. *How to stop the hole from growing?*

2.1.2 Pushing the cloud with a Raman kick

As it has been briefly mentioned in Remark 3.9, we need to perform a Raman transfer, right after the release of the trap, to have only atoms in the $m_j = 0$ magnetic sublevel falling onto the MCP. Depending on the orientation of the two laser beams creating the Raman lattice, some momentum is passed on to the atoms due to the two-photon exchange: it is not difficult to prove with momentum conservation that the direction of this kick is given by the external bisector of the two beams.

In the previous configuration of the experiment, the Raman beams were contained in the yz -plane, in such a way that the kick given to the atoms was directed upwards. Atoms were falling in the middle of the MCP, at a slightly delayed time because of this additional initial velocity.

We changed that configuration such that the kick is given along the x axis (cf. Figure 4.5), and the cloud (as well as the atomic pairs) is pushed away from the hole standing beneath.

Remark 4.1 The Raman transition is realised with the 2^3P_0 excited state so has to keep the atoms in the $m_J = 0$ state after the (σ^-, π) transitions. Indeed, if we were using the P_1 or P_2 transitions, an additional (σ^-, π) couple of transitions would be possible (relying on the $2^3P_{1,2}, m_J = -1$ excited state) leading to the $2^3S_1, m_J = -1$ state.

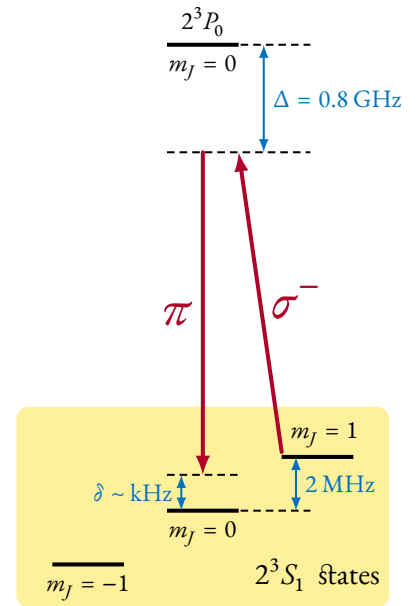


Figure 4.4: Raman transfer towards the $m_J = 0$ magnetic sublevel. The 2 MHz frequency gap corresponds to an approximately 1 G magnetic bias. σ^- and π are the photons' polarisations, with respect to the magnetic bias. The single photon transition is red-detuned of $\Delta = 800$ MHz, which simplifies the situation to an effective two level coherent coupling, with a two-photon angular Rabi frequency $\Omega_{2pb} = \Omega_{\sigma^-} \Omega_{\pi} / 2\Delta$.

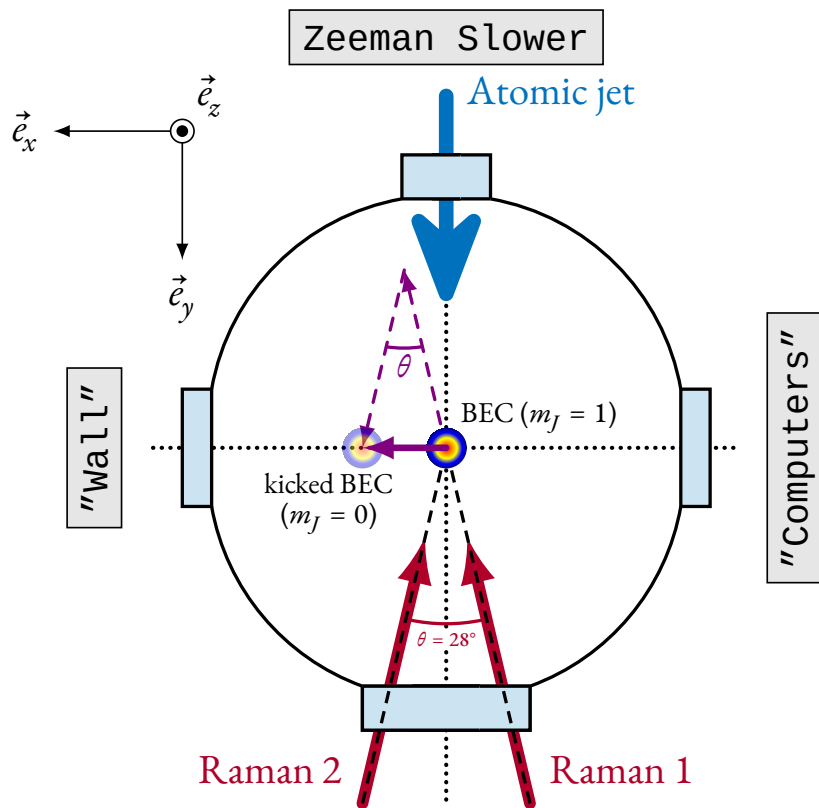


Figure 4.5: Top view of the Raman beams, and of the kick given to the BEC. Axis orientations are consistent with Figure 3.19. The labels "Wall" and "Computers", are just experimentalists' naming conventions, referring to the orientation of the room. The θ angle is limited by the diameter of the viewport. In reality, for historical reasons, the "Raman 1" is not perfectly in the xy plane (by a few degrees), and there is therefore also a small vertical contribution to the kick. Violet dashed lines correspond to the virtual one-photon kicks, and the plain violet line is the actual two-photon kick. A magnetic bias of a few gauss is kept along the x axis.

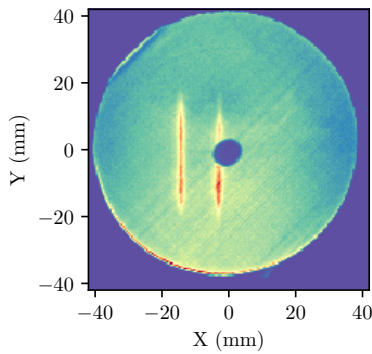


Figure 4.6: Raman kick applied to a BEC trapped in the MT. Data are averaged over 91 experimental realisations, in each file an average of $3.2 \cdot 10^5$ atoms are reconstructed.

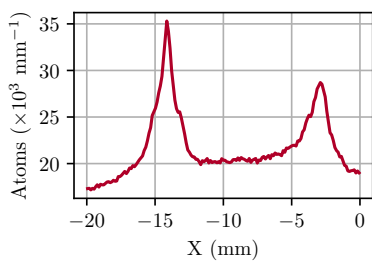


Figure 4.7: Integration over the Y axis of Figure 4.6. We measure a shift of 11.5 mm.

The one photon recoil velocity is 92 mm s^{-1} , which after 308 ms of free fall corresponds to approximately a 28 mm shift on the MCP. Considering the angle of 28° between the two Raman beams, we expect a 13.5 mm total shift, in the \vec{e}_x direction. We are geometrically limited by the diameter of the viewport, and this is therefore the largest kick we can give (at least by using this optical access): this sets an upper bound to the diameter of the holes that we are able to “dodge” (the diameter on the MCP of the BEC obtained with the ODT typically being 10 mm itself).

In practice we measure a slightly smaller kick (11.3(2) mm shift on the MCP); the small vertical contribution to the kick or an overestimated angle between the two beams could explain this discrepancy. Whatever, the cloud is pushed far enough so that we can consider the first of the two *hole-related* problems as solved.

Additional details about the technical realisation of the Raman pulse, and its quality control are given in appendix A.

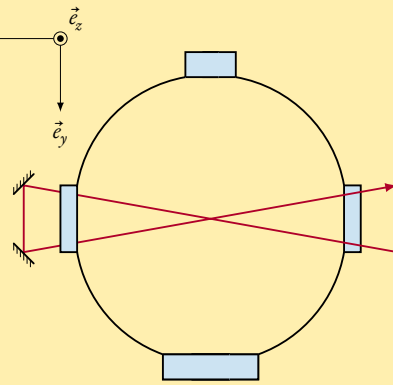
2.1.3 Protecting the MCP with a copper plate

Based on our experience of 2019, we understood that it was no longer possible to have an intense optical beam hitting the MCP surface directly.

Our first workaround attempt was to drive the evaporation with the horizontal beam, allowing us to reduce the power of the vertical beam below 1 W. This solution required to change the optical setup, realising a “butterfly” configuration, presented in Remark 4.2.

Remark 4.2 (“Butterfly configuration”) Because of the large waist of the hODT ($135 \mu\text{m}$), it was necessary to change the configuration of the horizontal beam, in order to increase the trapping frequencies by a few hundreds of hertz.

The idea was to recycle a first passing of the hODT with two mirror (and two lenses) and send it back towards the atoms. The “butterfly” self-crossing of the beam increases the trapping frequency during the loading up to 40 Hz along \vec{e}_x and 500 Hz in the transverse plane.



This configuration is much more delicate to realise, as it requires to overlap the waists of three beams (instead of two), and the second passing of the hODT is obviously not independent of the first one...

I will not go deep into the details of this technique, because even though we succeeded in loading a cloud in this trap, the evaporative cooling was inefficient and we never obtained a BEC this way. It was mostly a waste of time.

We therefore went back to the initial configuration (two beams only and the evaporation driven by the vertical one), but adding a protective copper plate, hanging above the middle of the MCP thanks to a stainless steel arm (Figure 4.8 and Figure 4.9). The blueprint of the assembly is available in the Appendix (Figure D.1).

Copper has been chosen for its good thermal conductivity properties, the piece is 6 mm thick (for having a heat capacity large enough). It has a rough surface finish in order to diffuse the laser light in a wide solid angle. We also added a tilt angle of 7° so as not to reflect most of the light backward towards the atoms. We also cut the plate, to only hide the part of the MCP exposed to laser light.

We performed a bunch of benchmarks (on the experiment but also on a testing apparatus) and we made sure that less than 5 % of the laser power reaches the MCP. We never observed again a localised loss of detectivity on the MCP, even using large optical powers, which makes this change a success.

Table 4.1: Characteristics of the copper plate

Thickness	6 mm
Diameter	2.54 mm
Cutting distance from centre	5 mm
Tilt angle	7°

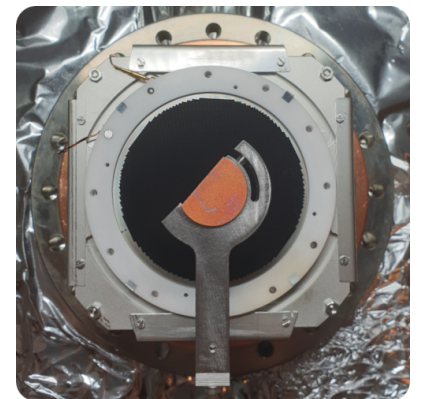


Figure 4.8: Top view of the protective copper plate. Picture taken on the day of the installation (30/09/2021).

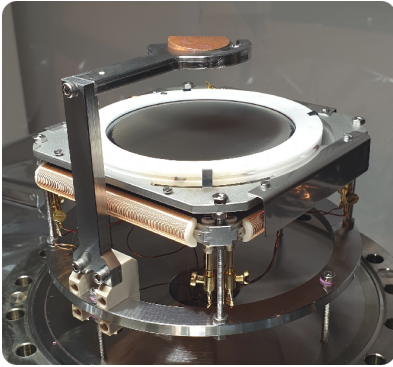
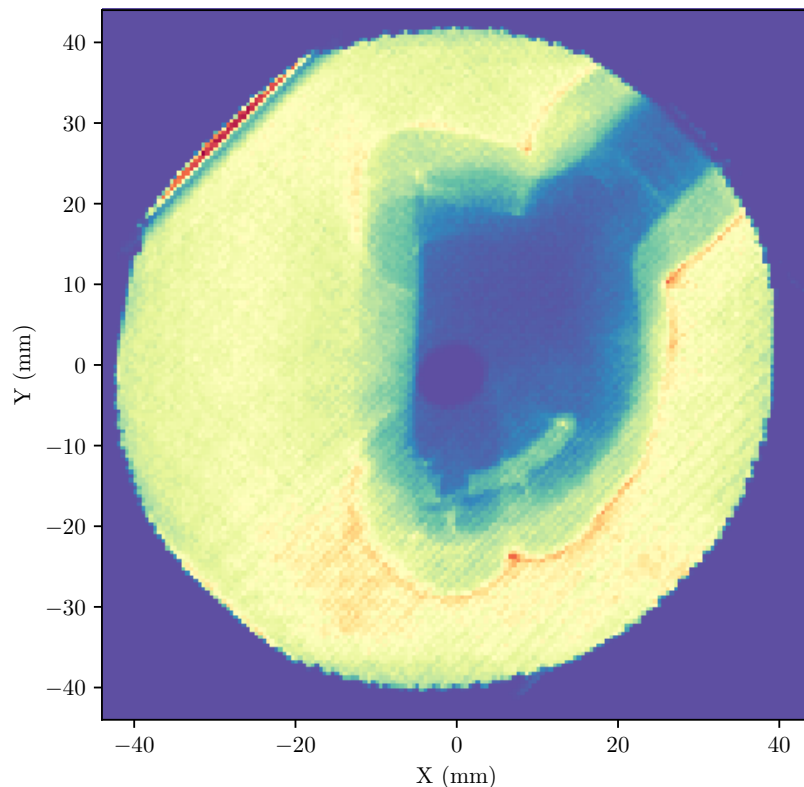


Figure 4.9: Side view of the protective copper plate. The copper plate, the MCP and the delay lines are visible. The picture was taken during a second changing operation (13/01/2022) where we insulated the stainless steel arm and the plate from the high voltage with a polyether ether ketone (PEEK) piece (here the white piece connected to the ring). Then, the arm and the plate were connected to the ground with a wire.

Figure 4.10: Detectivity map of the MCP protected with the copper plate. The map is obtained by accumulating data from MOT clouds without the transverse molasses stage (to reduce the number of atoms per run and avoid any saturation of the electronics). A strange structure with more atoms than average is visible around the metallic arm, within a range of a few millimeters.

However, when paying attention to the resulting detectivity map, the metallic structure is obviously visible, and the copper plate's shadow is just brushing against the hole (which is good), but we can also see a strange and unclear structure all around the sharp shadow (cf. Figure 4.10).



We first imagined that this disturbance could be due to uncontrolled electric fields (the arm first being at the same high voltage potential than the delay lines: ~ 2.6 kV). That is why we tried to electrically insulate this protective structure from the high voltage part with a PEEK support piece (Figure 4.9). This modification did not change a thing in the detectivity map.

The map in Figure 4.10 was obtained with MOT clouds, where a mix of atoms in all magnetic sublevels. However, when we do the same kind of map, with atoms coming out of an optical dipole trap and then transferred in $m_J = 0^1$, detectivity is much cleaner near the arm and plate's shadow (cf. Figure 4.11).

The stainless steel stand arm was crafted by a subcontractor, and it has been made of “SAE 304” stainless steel. It is less magnetic than

¹: we can easily separate the $m_J = 0$ atoms from the few remaining $m_J = 1$ ones with post-selection over the time of arrival on the MCP: the atoms polarise in the $m_J = 1$ arriving roughly 30 ms before the $m_J = 0$ because of the residual magnetic field gradients.

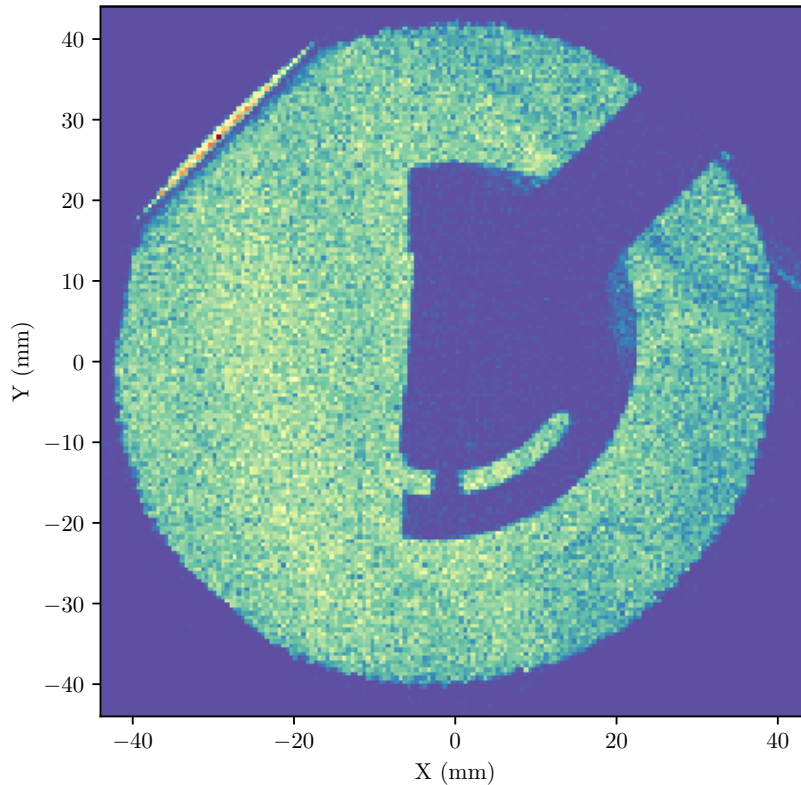


Figure 4.11: Detectivity map obtained with $m_j = 0$ atoms coming out of an ODT. At each run we load the ODT at full power (5 W) and we do not evaporate (the cloud has a temperature $T \sim 22 \mu\text{K}$ large enough to cover the MCP homogeneously). We then post-select and keep only the atoms in the [308, 309]ms arrival time range (centred on the arrival time of the $m_j = 0$). Data come from the averaging of 536 experimental realisations, with $1.6 \cdot 10^3$ atoms on average per file ($8.7 \cdot 10^5$ atoms in total). The ungracious structures around the shadow almost vanished.

conventional steel, but still more than the “SAE 316”: an interesting upgrade could therefore be to remanufacture the pieces in 316 stainless steel. Regarding the size of the shadow, it might also be tempting to design smaller pieces, but actually the signal of interest falls whatever on the left side of the MCP; the correlations that we want to observe are carried out by the vertical component of the atoms’ velocities, thus their arrival time: velocities in the transverse plane are no crucial information in our design¹, we essentially use them to post-select velocity boxes matching the size of the atomic pairs modes. It is therefore probably safer (in this configuration) to keep a piece of metal massive enough to endure the laser-induced heating.

With these replacement solutions, we solved the problems related to the formation of a hole at the centre of the detector. A stable BEC in the vertical ODT alone was then obtained on the 02/02/2022; it was the first time since 2017. That milestone was quickly followed by a BEC in the crossed ODT on the 15/03/2022, and finally a signal of atomic pairs on the 30/03/2022.

¹: contrary to other experiments such as the one managed by David Clement’s team, also at the Institut d’Optique.

Remark 4.3 (Another configuration) Even if we worked around the hole issue, it is still frustrating to have this piece of metal casting a large shadow over the detector. As it has been shown above with the unfortunate magnetic effects we encountered, it is obviously also not a good thing to add a massive handmade metallic structure in an environment which has been precisely calibrated by a constructor to have suitable detection conditions with MCPs.

A rather radical idea would be to rotate the whole optical setup (the ODT and the three optical lattices) by 90° around the y axis. The BEC would be cigar-shaped along the x axis. We would not have laser hitting/heating the surface of the MCP, and we could get rid of this additional protective part.

This would however be quite a colossal change in the optical setup, mostly consisting in a game of musical chairs:

1: the atomic pairs would be created along the x axis.

2: as the Bragg diffraction should also kick the atoms along \vec{e}_x .

3: in a dynamical Casimir effect (DCE) experiment, the pairs are created on either sides of the BEC, close to it (no kick is needed); however the pairs generated by the dynamical instability of the lattice are created on the same side, and then the two Bragg deflections push the atoms of 2×3 cm on the MCP level which is out of the 4 cm radius of the plate: we would need to compensate it with an opposite Raman kick.

4: we could actually get it out of the chamber, which is much cleaner!

- ▶ the pair creation lattice would be obtained with a pair of counter-propagating beams along the x axis¹;
- ▶ the Raman beams could keep their current location, but they should also be able to perform the Bragg pulses²: an electro-optic modulator (EOM) shall be used to quickly change one of the beams from the σ^- polarisation (for Raman pulses) to π polarisation (for Bragg pulses);
- ▶ depending on the type of experiment we perform to generate atomic pairs³ the atoms might get out of the MCP area: a Raman kick towards the centre of the plate could sometimes be needed and sometimes not. We should therefore find a way of having the possibility the mix two frequencies and polarisations (π and σ^-) inside the same Raman beam; we would have therefore have the possibility to choose whether we want to perform a Raman transfer with a kick along \vec{e}_x , or with zero momentum exchange;
- ▶ we would need to change the current hODT beam's waist (from $135 \mu\text{m}$ down to a value close to $40 \mu\text{m}$) making it the most confining axis, and install another beam, with $\sim 135 \mu\text{m}$ waist, along one of the 7° tilted vertical axis available (currently used for the pair creation lattice, cf. turquoise arrows in Figure 3.19): it would not touch the MCP⁴, and would create a weak confinement along the x axis;

2.2 A new cooling laser

2.2.1 Why do it?

Since the early stages of the experiment, and until June 2021, the laser source used for the cooling system was a DFB diode¹, amplified with a 2 W Keopsys[®] Ytterbium doped fiber amplifier.

Even though it was possible to work with this type of laser source for quite a long time, it was however not an ideal solution. Indeed, the linewidth of the diode is 2 MHz²: since the natural linewidth of the cooling transition is 1.6 MHz this is pretty bad, especially when we need to use light very close to resonance (as it was the case during the optical molasses or the Doppler cooling).

Historically, the typical shot-to-shot fluctuation level of the number of atoms in the MOT was of the order of 30 %, and we roughly kept this level of fluctuation all along the cooling procedure. Gradually, since 2019, we also witnessed the apparition of *drifts* of the cloud's properties (especially the number of atoms). These drifts are added to the already existing fluctuations, and can involve different timescales (from minutes to hours or even a few days). An example of drift of the number of atoms in a Doppler cooled cloud is given in Figure 4.12. In particular, we noticed that the amplitude of this drift of the number of atoms over time can reach 100 % (the number of atoms drops down to zero).

The origin of these instabilities is probably multifactorial, and even if we investigated almost all the aspects of the apparatus for a long time (frequency servo loops, optomechanical components, strong currents electronic circuit, laser diode feedback...) we never found *one* single element that could explain their growth unequivocally³. However we are quite sure that the cooling laser diode was involved in these problems: in winter 2020, the experiment became extremely sensitive to any external mechanical stress. Touching the optical table or even speaking too loud could annihilate the MOT loading! This level of sensitivity could have been considered to be the signature of a laser feedback on the diode's cavity, but changing the diode and rearranging to the first optical elements did not solve the problem.

1: Toptica - Eagle Yard[®] 1083 nm single frequency laser diode.

2: in fact, by studying the beat note frequency between two laser diodes, or between one laser diode and another narrowband fibered laser, we sometimes measured linewidth of the order of 1.7 MHz.

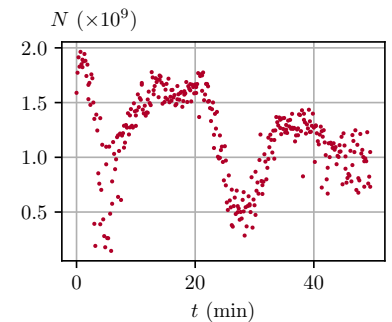


Figure 4.12: Example of drift of the number of atoms in a Doppler cloud. The number of atoms is measured with fluorescence imaging. Each point is an experimental run.

3: that is why we decided to change globally what we estimated to be various weak points of our system, roughly at the same.



Figure 4.13

Table 4.2: New fibered laser reference

Brand	NKT Photonics®
Range	Koheras ADJUSTIK
Model	Y10
Serial number	K0043893
Vac. ref. wavelength	1083.33 nm

1: these characteristics correspond to the *narrow* frequency tuning, controlled with *single-ended input signal*. There is also a *wide* frequency range (10 GHz) and other voltage control modes, but they are not suitable/useful for our frequency locking servo loop. See [documentation](#) for more information.

2: before, the separation was made in free space inside the frequency locking setup.

2.2.2 The new laser

We decided to install a new narrowband fibered laser source for the cooling. We ordered the same device (cf. Table 4.2) as the one used by our colleagues from the *Helium lattice* team (conducted by David Clément). It is a single DFB fiber laser, with passive vibration reduction. The output power is factory set to 33 mW and cannot be changed, we can monitor it with a dedicated low power output (returning 0.4 % of the effective power).

The output power is remarkably stable: we measured it of the order of 0.01 %. After amplification (and after the optical isolator) power fluctuations are smaller than 1 % for the usable beam, and only generated by the laser amplifier.

The emission wavelength can be tuned with two independent features:

- ▶ *thermal tuning*: the laser's fiber is mounted under tension on a substrate that tightens or expands when the temperature changes. Due to the thermal contraction or dilation of the substrate, the laser's cavity length (and therefore the modes) also changes. In addition, the temperature of the cavity itself has a thermo-optic effect, modifying its refractive index. These two effects contribute to the dependence of the optical path length –and therefore the emission wavelength– with temperature ;
- ▶ *fast wavelength modulation*: the emission wavelength can also be modulated with a piezoelectric crystal acting on the cavity. We can control the wavelength over a range of 1 GHz, with a ± 2.5 V tension, and a modulation bandwidth of 30 MHz¹.

We remade the frequency locking servo loop: it is a rather usual design (cf. Figure 4.14) based on the saturated absorption spectroscopy principle. Yet, in comparison with the previous version of the setup (with the laser diode) we have a few enhancements:

- ▶ a much more compact design, without external optical isolator (OI), as an OI is already included inside the laser box ;
- ▶ we have a strong separation between the frequency locking optical setup and the cooling optical setup, obtained with a fiber splitter² ;
- ▶ the small frequency modulation used for the lock-in amplification is performed with RF onto the AOM: it is not present in the optically-amplified beam used for the cooling. In the previous

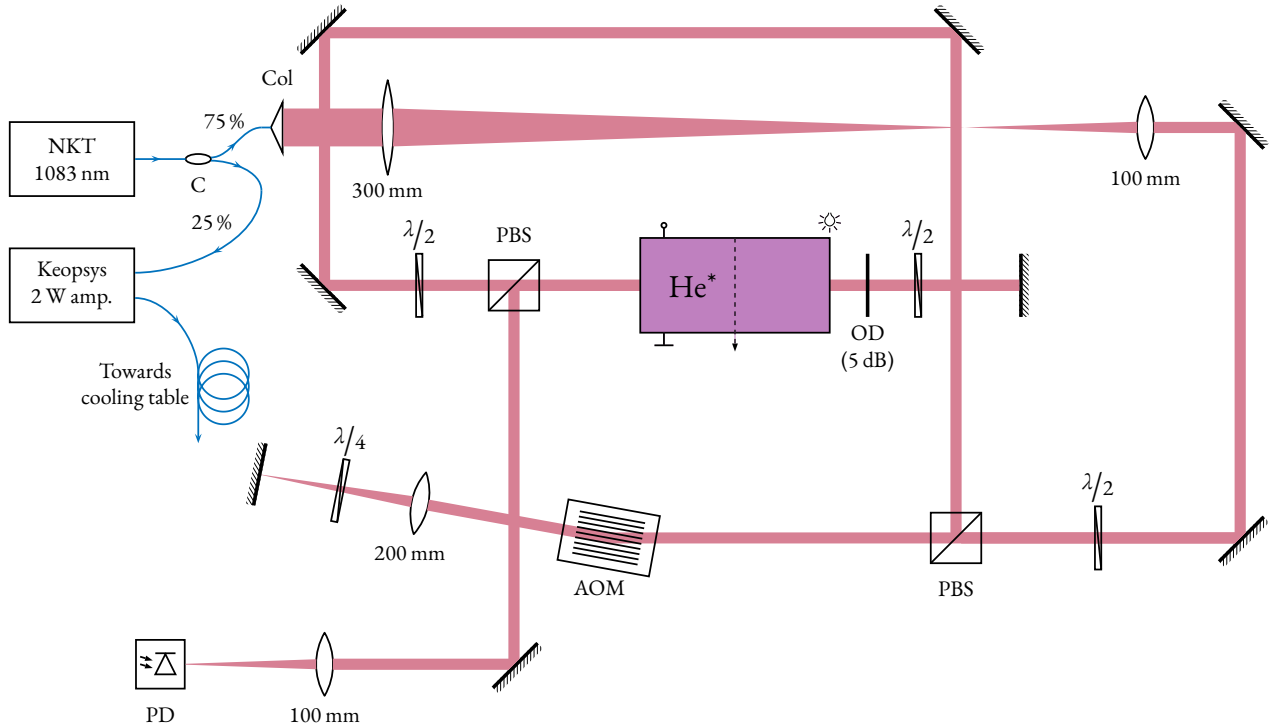


Figure 4.14: Laser frequency locking: optical schematic. This is a standard setup using saturated absorption spectroscopy, with a helium discharge cell. Blue wires are fiber optics. We use a 1×2 fiber optic coupler (C) to split the output fiber of the NKT[®] laser source: 75% of the power (≈ 27.3 mW) is used for the saturated absorption spectroscopy, and the remaining 25% is amplified and used for the actual cooling. The waist of the beam out of the fiber collimator (Col) is ~ 1.6 mm, we reduce it to $325 \mu\text{m}$ with a first telescope in order to match the usage recommendation of the AOM (the AOM is placed at the minimal waist position, 1 m away from the fiber collimator). The AOM is used in double-pass (70% of double-pass efficiency): a 200 mm plano-convex lens is making the image of the waist (centred on the AOM) onto the retro-reflecting mirror (in a $1f - 1f$ gaussian optics configuration). The AOM is fed with 110 MHz RF, and the laser is therefore locked 220 MHz away from the atomic resonance (red-detuned). The signal of the photodiode (PD) is treated with a lock-in amplifier, and then used in a servo loop that generates the feedback on the laser. A 5 dB optical density is used to reduce the intensity of the probing beam: its value has been chosen to optimise the relative amplitude of the saturated absorption peak.

setup, the AOM was poorly resilient to RF frequency changes, and this modulation was performed onto the laser diode's current, and therefore affected the whole cooling procedure...

We checked the spectral width of the emitted laser beam after frequency locking: we studied the beat note with the laser of the Helium lattice team with a spectrum analyser and found a value of a few tens of kilohertz, which is the expected order of magnitude.

2.2.3 Obtained effects

We did not observe a significant gain in terms of cooling performances with the new laser: the temperatures are roughly the same as before at each cooling stage, and we did not increase the number of atoms a lot. However, we obtained a huge gain of stability: mechanical sensitivity

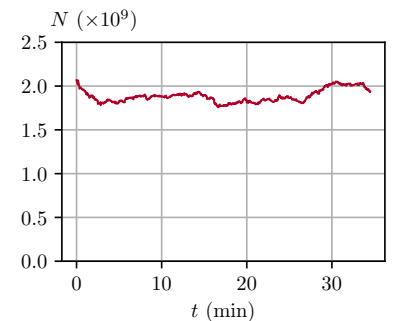


Figure 4.15: Example of Stability of number of atoms in a Doppler cloud with the new NKT[®] laser. The number of atoms is measured with fluorescence imaging. The fluctuations are dominated by slow drifts, with an amplitude of 2% RMS (5% peak-peak). The short term fluctuations are even much smaller than that ($< 0.5\%$ RMS), and are not relevant anymore for us.

of the apparatus (acoustic noise, vibrations...) vanished, and we usually have less than 5 % of fluctuations of the number of atoms in the cMOT and Doppler clouds.

In summary:

- before:** 30 % of short time fluctuations of the number of atoms, and long-term drifts with an amplitude a few tens of percent → Figure 4.12 ;
- now:** almost zero short time fluctuations of the number of atoms, and a long-term drift with an amplitude smaller than 5 % → Figure 4.15 ;

Needless to say, we consider this change a victory.

Remark 4.4 (Average number of atoms) One could argue that –on average– the number of atoms in Figure 4.15 is also higher than in Figure 4.12, and it would be appealing to conclude that the new narrowband laser also leads to a gain in the mean number of atoms loaded in the cloud: this is erroneous.

It is delicate to compare these numbers between situations separated by several months or years¹ as we know it also depends on external factors that we do not always master: air conditioning temperature, watercooling temperature, plasma source temperature and pressure, etc. Secondly, many parameters of these “*prototype*” apparatus drift a bit with time, and we regularly have to adjust it: quality of the optical fibers’ coupling, RF noise, strong current stability, etc. Finally, we know that the number of atoms is strongly related to the intensity of the helium plasma source. In particular the metallic needle (cf. Figure 3.18) ages through the years, and should be changed every two to five years, which has never been done in over a decade...

However the gain of stability mentioned above is:

1. resilient over time ;
2. unprecedented in the history of the experiment ;
3. completely correlated in time to the change of the laser source ;

we can therefore legitimately claim that it is induced by the new fibered DFB laser.

¹: data in Figure 4.12 were taken on 17/12/2020, whereas data in Figure 4.15 were taken on 21/02/2022.

2.3 Instabilities of the magnetic trap

The magnetic trap is realised with two clusters of coils in a cloverleaf design (each cluster is symmetrically disposed on both side of the science chamber, along the x axis: cf. Subsection 3.2.3). On 7 October 2020, due to a human mistake¹, one of two quadrupole coils overheated (our logging system suggests that the temperature of the cluster exceeded 100 °C). Since this episode, we observe positional instabilities of the cloud in the magnetic trap (cf. Figure 4.16). These are both shot-to-shot instabilities ($\sigma_x \sim 300 \mu\text{m}$, $\sigma_y \sim 100 \mu\text{m}$), and day-to-day drift of the mean value (same order of magnitude).

¹: an experimentalist forgot to open one of the watercooling valve of the coils.

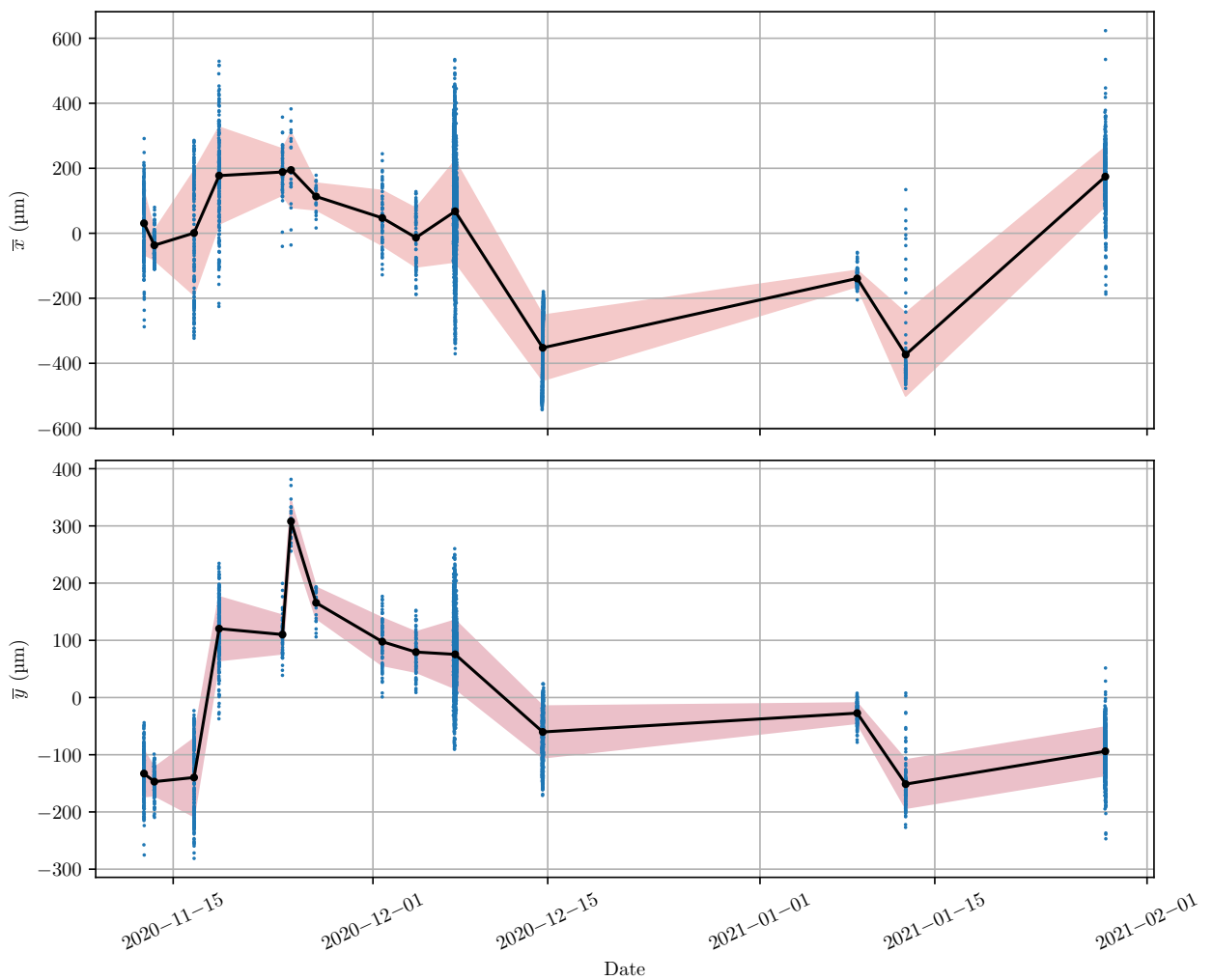


Figure 4.16: Position of the centre of a cloud trapped in the magnetic trap, and evaporated down to $\sim 15 \mu\text{K}$ (corresponding to a final RF frequency of 4 MHz). These data are acquired through *in situ* fluorescence imaging, meaning that the picture of the cloud is taken *in* the trap, before the release of the cloud. Each blue point is an experimental realisation. The black points are obtained by averaging the data acquired on a given day, and the red area is the corresponding $\pm 1\sigma$ standard deviation. The plotted data spread over a 77 days time range.

1: it not stable shot-to-shot and day-to-day

In practice this is quite harmful as the position of the cloud is not well defined at the end of the evaporation in the MT¹, which causes serious issues during the loading of the cloud in the ODT (the position of the ODT beams' waists obviously being fixed).

In addition, it prevents us from performing direct measurements of the trapping frequencies in the MT. These measurements are sometimes required, because we know that for a given current, the bias field B_0 , and therefore the transverse trapping frequency, may shift a bit with time. Indeed, generally we do not see changes of the bias on the one day timescale, but sometimes (typically once in a few months) an unmastered event may shift it of a few hundreds of kilohertz. This is not particularly surprising as the bias is a small field (a few gauss) resulting from the annihilation of strong fields (several hundreds of gauss): it is extremely sensitive to the geometry of the coils (at the micrometer length scale), and the trapping frequency (scaling in $\frac{1}{\sqrt{B_0}}$) is also sensitive to the variations of the bias...

2: in the past, even when the bias and therefore the transverse trapping frequency changed for some reason (at fixed current i_{BOT} , cf. Section 2 in Chapter 1), the product $\omega_{\parallel}^2 \times \overline{B_0}$ remains the same.

Fortunately, the gradient B' is resilient, meaning that the Λ constant in the relation Eq. (3.44) is also robust². Therefore our knowledge of the transverse trapping frequency can rely on our measurements of the Λ constant Eq. (3.45).

3: in the current system, the coils are cast in epoxy, but in some places the layer of epoxy is quite thin, and we already had to reinforce the insulation with protective Kapton tape.

We ordered to Oswald Elektromotoren[©] the fabrication of professional grade clusters of coils (received in September 2022). Contrary to the previous coils that were homemade (winded by hand), these coils will have precise sizing and tolerances (typically of the order of the tenth of millimeter). The electrical insulation should also be of better quality³. In addition to the fact that the current coils are getting old⁴, we know –regarding the electrical resistance– that a loop in one of the cloverleaves is short-circuited: the changing of the magnetic trap will also correct the induced symmetry issue.

4: we recently noticed that the cooling water flow inside the coils has been reduced by a factor of almost 2 since 2000 (probably due to limestone deposit).

The blueprint of the Oswald's clusters of coils is given in the Appendix: see Figure D.2.

2.4 A next-gen sequencer and software control

2.4.1 GUS and the old hardware

Until the end of May 2021, the sequencer of the experiment was an old frame in which we had plugged various cards (TTL output, analog

output, RF output...) that were made at the electronics workshop of the IOGS¹. The system was software controlled by a heavy Matlab script. This piece of technology was set up roughly 20 years ago, and we had several problems with it:

1: by André Villing

- ▶ on the hardware side, the electronics engineer who had designed the sequencer's cards left the institute many years ago, and we did not have hardware maintenance anymore. In particular –due to aging– we often had output channels (or even sometimes a whole card) breaking down, without the possibility of repairing or replacing it. We were basically under the clock, waiting for the time where we would be running out of spare output channels and cards ;
- ▶ on the software side, the Matlab script² consisted in a heavy stacking of patches (getting bigger and bigger as the successive generations of PhD students joined and leaved the team). Even if we proceeded to a “trimming of the fat” back in 2020, the code was not perfectly stable, and very prone to bugs. When something went wrong during the experiments, it was also quite frustrating to always suspect the sequence code rather than some physical issue to explain it ;
- ▶ the last point that was not very satisfying was the very hacky way to control the two PSUs used for the MOT and the MT. Communication was established with an old-fashion GPIB bus. In order to keep the time synchronisation of the events occurring during an experimental cycle, the changing of output state of the PSUs had to be triggered by the sequencer: we used three TTL output channels (that could therefore encode $2^3 = 8$ states), that were connected to a serial port of our experiment computer's motherboard³. The state of the serial port was then read every 50 ms by the Matlab's script, and an according GPIB signal was sent when a change of state was detected... With this solution, we were limited to 8 current configurations for the PSUs, and, during an experiment, changing from one configuration to another was done abruptly. The USB to GPIB (or LAN to GPIB) adapter was not very faithful as well, and regularly caused experiment to crash. Finally, we could not beat the 50 ms jitter on the time control of the PSUs, corresponding to the reading frequency of the serial port ;

2: that was named “gus”

3: serial port that was initially supposed to serve a completely different purpose...

We therefore took the decision to terminate the use of this dying setup, and install a brand new system, based on a recent factory-made sequencer, and a Pythonic 🐍 framework to carry out the software interface.



Figure 4.17: Picture of the ADwin-Pro II-light sequencer frame. More details can be found in the [official documentation](#).

1: useful information can be found in the [french official documentation](#)

2: postdoc at the time in the [Quantum Many Body Systems](#) team.

3: group leader, [Quantum Many Body Systems](#), strontium experiment.

4: group leader, [Rydberg Dressed Quantum Many-Body Systems](#).

5: who was introduced to [QControl3](#) during his postdoc position at the [MPQ](#).

2.4.2 ADwin sequencer and the QControl3 project

The new hardware is a flexible and modular Jäger ADwin © system, model ADwin-Pro II-light (7 slots frame). We can plug different types of input/output electronic cards in it, the first one being a CPU and LAN interface card: Pro-CPU-T12. This CPU is used to compile the sequences' script (containing all the events that occur during an experimental realisation), and sets the time resolution of the clock up to the nanosecond scale, which is much better than what we need (the shortest timescale we need to address being in the microsecond range). We must however notice that even if the hardware is able to work at the nanosecond timescale, we have a software issue (coming from QControl3: our interfacing layer, see next paragraph) that causes a crash in the compilation of the sequences when we want to perform pulses shorter than 5 μ s. This is an annoyance, and when this manuscript is being written this bug has not yet been fixed.

This sequencer is programmed with a dedicated native compiled language called *ADbasic*¹ (the language and the binary compiler share the same name). In practice we rarely have to work with it, because we use a Python framework designed for cold atoms experiments, that behaves as a software wrapper of the low-level ADbasic control of the sequencer: QControl3. This software project has started in February 2016 at the [Max-Planck-Institute for Quantum Optics \(MPQ\)](#), with the initial contribution of Dr. Christoph Gohle², Dr. Sebastian Blatt³ and Dr. Christian Groß⁴. In our group it was imported by Dr. Marc Cheneau⁵, who set it up now for his own strontium experiment at the [IOGS](#), and is now a regular contributor and maintainer of the project.

It would be quite cumbersome to go deep into the details about the way QControl3 is coded; I will restrict my explanations to its general structure, what problems it is meant to solve, how we implemented it in our experiment and finally give some pros and cons about it.

2.4.3 QControl3 structure

QControl3 has a server/client structure, that allows for the synchronisation of events carried out by the ADwin sequencer (TTL pulses, analog output ramps...) with operations realised by other devices (PSUs, RF synthesisers...). The synchronisation is managed at the software level by the "Timing system" (cf. [Figure 4.18](#)) that sets a namespace where all these events are declared, and keeps tracks of their triggering. Using external devices in sync with sequencer's channels events was a

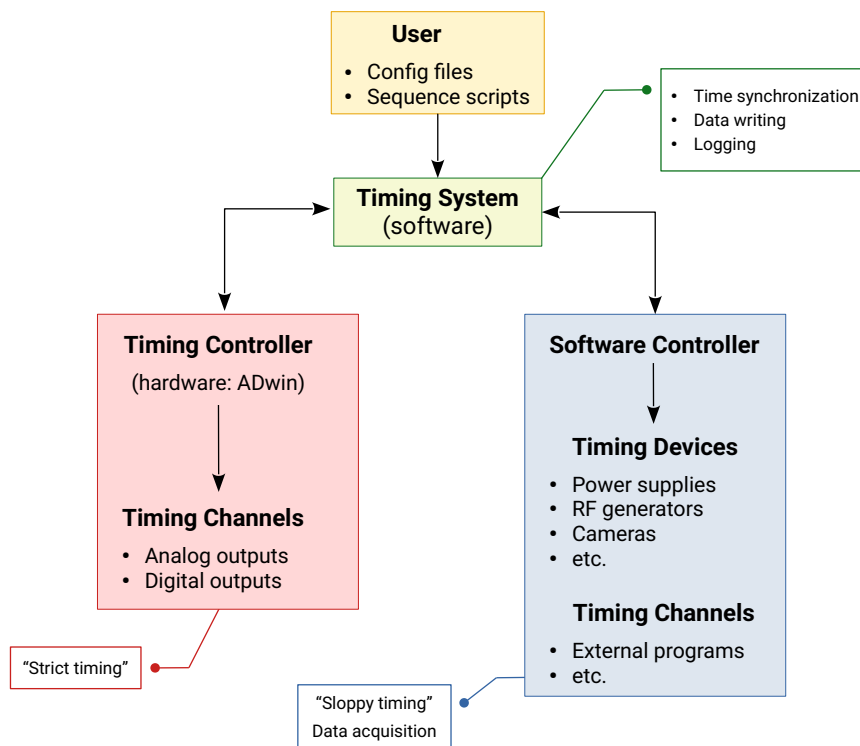


Figure 4.18: Chartflow diagram of the coarse architecture of the QControl3 program. The core of the code is the “*Timing System*”, that is mainly a server launched on the experiment’s computer once and for all (linux based system). This server receives a queue of requests from “clients”, that consist in sequence script files, and configuration files. With a bare installation of QControl3 the interaction between the client and the server is carried out by a command line interface (CLI), but we also added a simple graphical user interface (GUI) as a plugin, to have a rather user-friendly control over the various parameters. The Timing System is responsible for the synchronisation between the sequencer’s part (in red: the *Timing Controller* Adwin and its various *Timing Channels*) and the software / external devices part (in blue: the *Software Controller*). It also writes the output files (HDF5...) at the end of the run. All these terms are just naming conventions chosen by the first developers of the QControl3 project.

real issue with our previous system.

In the experimental sequence’s script (provided by the users) there is only one time variable t involved. After compilation and execution of the sequence, depending on the device that we call upon, events are triggered with respect to a timing that is managed either by the computer’s internal clock¹ (“*sloppy timing*”) or the very precise ADwin’s clock² (“*strict timing*” for all the events involving a card slotted in the ADwin’s sequencer).

Concerning data saving and logging, each experimental realisation returns an HDF5 archive file, containing the complete sequence scripts, all the parameters used during the run, and can also contain the “output” data of interest (PNG image coming from the fluorescence imaging, or MCP data): this big file therefore contains all the depth of an experimental realisation, from the users’ request to raw data measurements. In practice, even though the writing of this HDF5 file is a very good habit (regarding the reproducibility crisis in science), it is quite heavy and slow to manipulate (especially in our data analysis programs). To overcome this, we save the relevant parameters and the data separately, in appropriate lighter files, devised for a fast digital treatment³, in addition to the HDF5 archive.

1: e.g. the time at which an external device receives a set of SCPI instructions, or we request the execution of a side program...

2: e.g. the time of triggering of an external device, the toggling of a sequencer’s TTL signal, the voltage ramping of an analog output...

3: json or toml for the experiment parameters (frequency/power of AOMs, laser pulses durations...), PNG for the images coming out of the InGaAs camera, and binary files (with 64 bits integers) for the MCP raw data and the reconstructed atoms files.

The couple ADwin/QControl3 also provided an unexpected advantage: the reduction of duty cycle, by approximately 4 s! Indeed, in the previous system based on Matlab, the experimental scripts were executed without compiling, with the *interpreted languages paradigm*. In particular the initialisation of each run, and the final resetting of the apparatus was time consuming, and caused a painful dead time between each experimental realisation. QControl3 proceeds differently: the “Timing System” sends a compiled version of the sequence to the ADwin sequencer (or “Timing Controller”), and compiles the next realisation while the current one is running. With this strategy, there is no dead time between the runs, and the duty cycle is strongly reduced (cf. Table 4.3).

Table 4.3: Typical duty cycles of different types of clouds. These numbers come from “stability test” sequences, acquired between February and April 2022 (by taking the average run time rounded up to the first decimal). It may vary downside in the upcoming months, as we did not yet proceed to a final optimisation of the duty cycle.

cMOT	2.3 s
Doppler	4.7 s
Evaporated MT	6.2 s
BEC in ODT	11.4 s

1: typically: one TTL gate to turn on the AOM’s RF, two analog outputs to control its power and frequency and one TTL gate to open the mechanical shutter.

2: in summer 2021, I spent some time implementing a multi-channel calibration class, where the input and output quantities can have arbitrary dimensions: e.g. the power of a beam diffracted in an AOM (1 quantity) may depend on the RF power and frequency (2 quantities).

[147]: Keshet et al. (2013), “A distributed, graphical user interface based, computer control system for atomic physics experiments”

3: i.e. drivers for electronic cards.

Finally, QControl3 was imagined to be object-oriented, which simplifies the readability of the sequences’ script a lot. There is no longer any need to constantly have the “micro” control of the apparatus (at the single channel scale), because we can now define `mixin` and complex objects, that will implement useful methods to control it. For example, if we want to switch on a laser at a given time, and ramp its frequency with an AOM, instead of individually addressing all the sequencer channels involved in the state of this beam¹, we can rather define a `Laser` python class taking into account all parameters and calibrations (mechanical shutters delays, 2D frequency/power AOM calibrations²...) and only having in the script an instruction of the type:

```
myLaser.turn_on(detuning=20MHz, power=10mW)
```

which is much easier to read and debug.

Pros and cons The relative low visibility of QControl3 in the community of ultra-cold atoms experiments can be considered to be a disadvantage of this solution. Indeed it could have been possible to choose a more “mature” system on software level, with a larger community of users, such as the Cicero Word Generator [147] developed at the MIT, and based on National Instruments commercial hardware. This heavy community support of Cicero translates into an appreciable gain of time: we can expect the code to be essentially bug-free, and most of the hardware implementation is already done³. Apart from the fact that Cicero is widely known and has to be a reliable system, it is also a natively graphical user interface (GUI) program, making it fairly user-friendly. On the contrary, the workflow after the default installation of QControl3 is fully scripted.

However `QControl3` offers a very easy way of accessing to a deep control of the hardware, and the sequence that we want to run. Python is currently the most popular programming language, it is well-established in academic teaching programs, and very fast to learn. `QControl3` provides a clean and readable framework to quickly write sequences in a Python file. The drawback of fully `GUI` programs such as Cicero occurs when it is once needed to do something that is not covered by the `GUI`. In such a case, the only solution is to go back to the core source code of the software¹, which in the case of Cicero turns out to be written in `C#`²... I would therefore claim that `QControl3` is probably more versatile. We also integrated a `GUI` module to our implementation of `QControl3`.

With only a few days of learning, Python scripts allow for an almost complete control on the way data are generated and saved. We have integrated to our framework a live data analysis program, also written in Python, that can manage both 3D `MCP` data, and 2D imaging data. We shall briefly describe this new interface in the next subsection.

2.4.4 A word about HAL

We deployed `Helium Atom Locator` (`HAL`) a few months before moving to `QControl3`, under the initial impulse of Alexandre Dareau³, who started the project before he left the team. The motivation for the development and maintenance of this new software was twofold:

1. we first meant to modernise and unify the previous Matlab based `GUI` programs. Before `HAL`, `MCP` data, and imaging data were treated in separate softwares, with an important amount of old “legacy” code that was difficult to maintain⁴. Without going too deep into the details, in the case of `MCP` data the workflow was particularly bad, as it required the use of a chain of interdependent softwares, ultimately relying on `gus` (the previous sequencer interface)... It was no longer reasonable to continue living with this ;
2. we also wanted to develop a moduable software, that could be reused (and co-maintained) by other teams of our group, and (why not?) other groups.

As of today, `HAL` is perfectly functional⁵, although (in my opinion at least) not mature and complete enough to start promoting it out of our group. As one of the current main developers, I contributed to many aspects of this project⁶. I will quickly explain what `HAL` can

1: which is generally not much known by regular users.

2: which is a complex *compiled* programming language, derived from the `C++`.



Figure 4.19: `HAL`'s logo

3: who worked as a postdoc for the team between 2019 and 2020.

4: actually, most of the code of these programs was inherited from even older programs developed by the successive generation of PhD students of the team.

5: actually some figures of this manuscript, exposing visualisations of experimental data were generated thanks to a data exportation module of `HAL`.

6: to cite a few: the data and metadata loading modules (in particular for the `MCP`), enhancements of the visualisations, fitting and interpolation modules (in particular in 2D), several scripts and libraries for data analysis (e.g. the momenta correlation of atoms extracted from `MCP` data) etc.

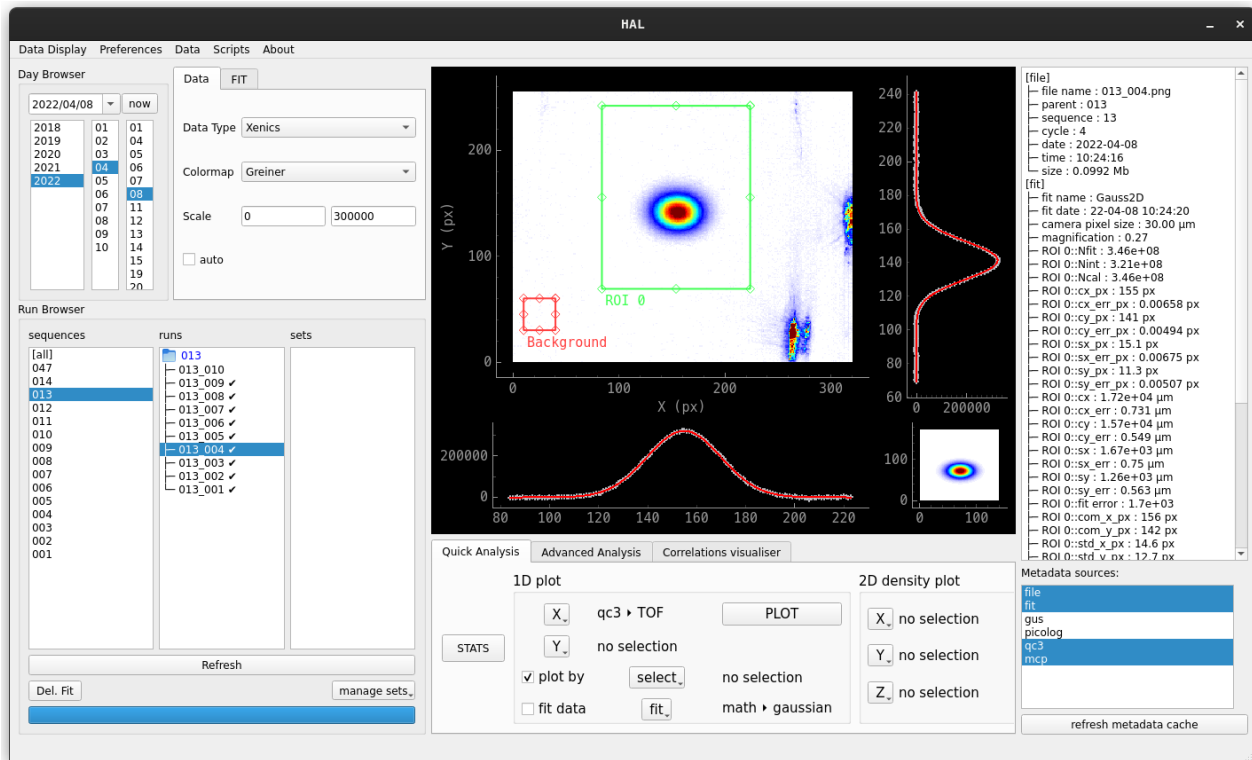


Figure 4.20: User interface of HAL. In the centre we have a *display* panel where the main visualisation of data is placed (here it is the fluorescence imaging of a cloud in the MT, but it could also be an image similar to Figure 4.11 for MCP data). On the left, we find a customisable data explorer and selector, and a quick fit panel. The panels are dedicated to metadata, with a selector of sources, and the text printing of selected files' metadata. At the bottom we have quick access to common plotting methods. The custom analysis scripts (generally more complex) can be accessed via a dedicated menu placed at the top of the window.

currently do, coarsely how it is build and thought, and finally how I would like it to evolve in a near future.

HAL is able to load and process different raw data types —in our case PNG files (coming out of the fluorescence imaging), and custom binary files (containing raw MCP) data— but also different *metadata* types. Metadata refer to anything giving information about rawdata:

- ▶ file timestamp, file size, file path... ;
- ▶ sequence parameters ;
- ▶ fit results ;
- ▶ external data (e.g. room temperature at the time of the run)
- ▶ etc.

HAL's interface then offers simple plotting and fitting routines: it basically allows us to visualise data as functions of metadata (e.g. how the number of atoms in the cloud evolves when we change an experimental parameter), or data as functions of other data (i.e. correlations).

HAL's power lies in its modular architecture. Indeed, in order to load

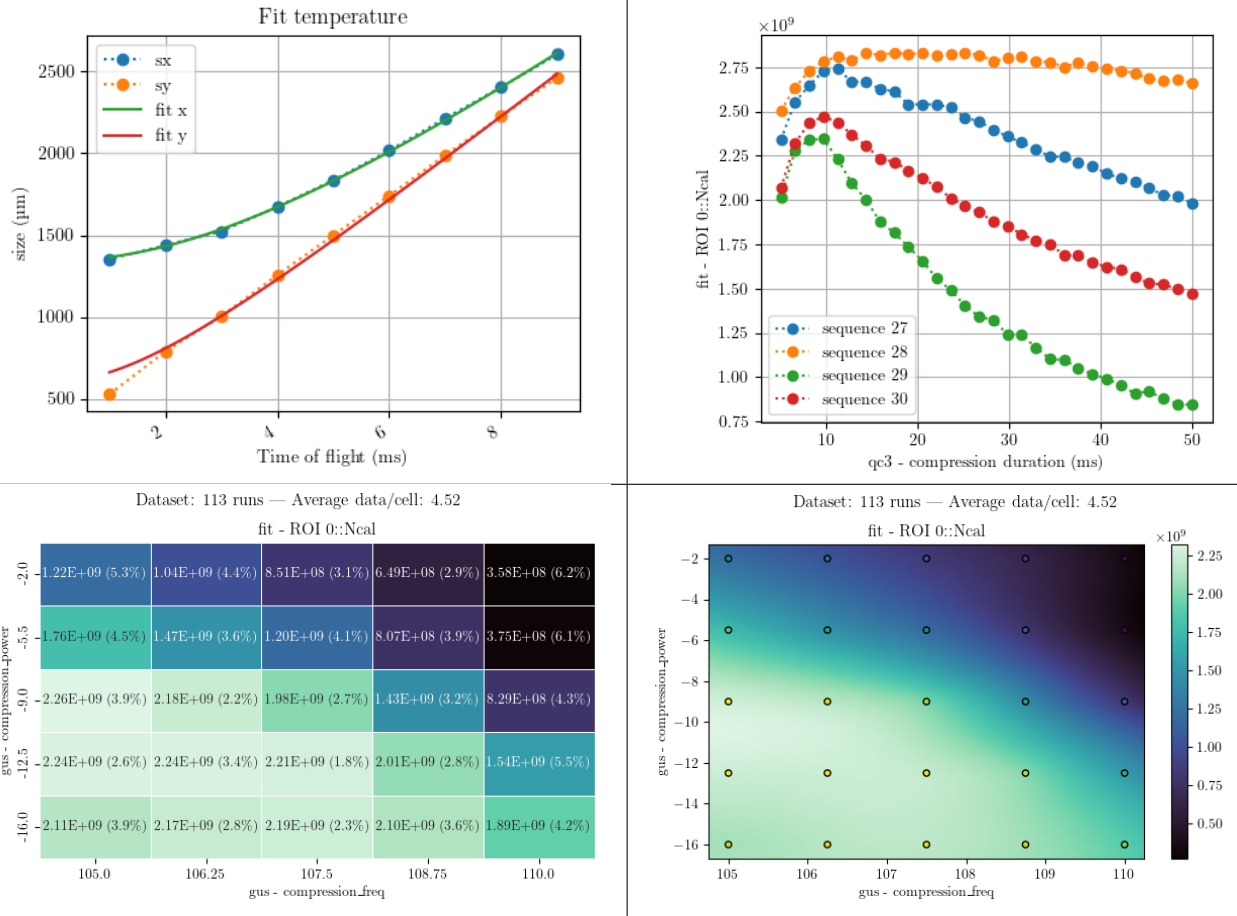


Figure 4.21: Examples of visualisations generated with HAL. The top left 1D plot results from an automated script returning the temperature of a cloud, out of fluorescence images taken after different times of flight. At the bottom I plotted examples of 2D visualisations, that can be very handy when we want to probe the effect of two interdependent experimental parameters at the same time. The bottom right plot is actually performing an interpolation of the data points, which can be useful when we want to have a 2D density plot as a function of parameters that are not regularly positioned in a “square” array.


data and/or metadata, HAL makes use of “user-modules”¹ that are in charge of explaining to HAL how a given file is formatted/serialised. Data and metadata are then loaded in a universal manner, and can be processed with any other data or metadata. The particular data class of 2D pictures is for the most part already implemented in the core code of HAL (since it is by far the most common data file type used in experiments)².

In addition to the user-modules, HAL loads “user-scripts” at startup, which are also custom extensions that a research team can quickly incorporate to HAL’s GUI to perform specific treatments onto the data. For example, visualisations of the momenta correlations between atoms that I will show in Chapter 5 are generated with custom user-scripts that I wrote for the team.

HAL core code is maintained in a git repository that is currently

¹: that are placed in a configuration folder in user’s home directory.

²: the corresponding loading module incorporates basic default parameters, and can be easily extended (thanks to Python class inheritance) to include additional custom features: e.g. pixel size, magnification factor etc.

hosted on A. Dareau's Github[®]  page: <https://github.com/adareau/HAL>. Members of other teams of our group would like to integrate HAL to their workflow. After discussions, the next major features that we would like to implement are:

- ▶ the caching of loaded data for better performances ;
- ▶ an asynchronous and multiprocessing behaviour of the software (meaning that the whole software is not frozen when we ask it to run a long task) ;

The user -modules that we use in our team are available on my own Github[®]  page <https://github.com/quentinmarolleau/HAL-modules> ; and our user -scripts are hosted on Charlie Lep-rince's page <https://github.com/charlieleprince/HAL-scripts>.

Pair production and experimental results **5**

Chapter's table of contents

• Introduction	174
1. Source of momenta-correlated atoms	175
1.1 Generalities	175
1.1.1 Parametric down conversion	175
1.1.2 Four-wave mixing	176
1.1.3 Extension to the atomic case	176
1.2 A bit of formalism	177
1.2.1 Four-wave mixing in a BEC	177
1.2.2 Phase-matching condition in a periodic potential	179
1.2.3 Dynamics, density and correlations	181
1.2.4 Turning on and off the optical lattice	185
2. Experimental results	187
2.1 Optical setup	187
2.2 Generation of pairs	188
2.2.1 First characterisation of the pair creation's behaviour	188
2.2.2 Density of pairs	193
2.3 Probing the correlation	195
2.3.1 Short definition reminder	196
2.3.2 Second-order correlations: 2D map	197
2.3.3 1D analysis: correlation amplitude and modes' width	199
2.4 Emission statistics	203
• Conclusion	206

Introduction

[148]: Lücke et al. (2014), “Detecting Multiparticle Entanglement of Dicke States”

[149]: Strobel et al. (2014), “Fisher Information and Entanglement of Non-Gaussian Spin States”

[150]: Lange et al. (2018), “Entanglement between Two Spatially Separated Atomic Modes”

[151]: Shin et al. (2019), “Bell Correlations between Spatially Separated Pairs of Atoms”

[152]: Greiner et al. (2005), “Probing Pair-Correlated Fermionic Atoms through Correlations in Atom Shot Noise”

[6]: Jaskula et al. (2012), “Acoustic Analog to the Dynamical Casimir Effect in a Bose-Einstein Condensate”

[153]: Clark et al. (2017), “Collective Emission of Matter-Wave Jets from Driven Bose-Einstein Condensates”

[154]: Bücke et al. (2011), “Twin-Atom Beams”

[155]: Borselli et al. (2021), “Two-Particle Interference with Double Twin-Atom Beams”

[5]: Perrin et al. (2007), “Observation of Atom Pairs in Spontaneous Four-Wave Mixing of Two Colliding Bose-Einstein Condensates”

[156]: Kheruntsyan et al. (2012), “Violation of the Cauchy-Schwarz Inequality with Matter Waves”

[157]: Hodgman et al. (2017), “Solving the Quantum Many-Body Problem via Correlations Measured with a Momentum Microscope”

[163]: Hilligsøe et al. (2005), “Phase-Matched Four Wave Mixing and Quantum Beam Splitting of Matter Waves in a Periodic Potential”

[164]: Campbell et al. (2006), “Parametric Amplification of Scattered Atom Pairs”

[7]: Bonneau et al. (2013), “Tunable Source of Correlated Atom Beams”

Atomic pair production exhibiting quantum correlations is a research thematic that has been actively explored in the last fifteen years, and is at the very core of our experiment. In this topic, one may be interested in the correlations considered with respect to *internal* degrees of freedom, which can be achieved through a wide variety of ways, including spin-squeezing [148], nonlinear coupling and non-gaussian states generation [149], magnetic separation of spin states [150], BEC collisions [151]... All these works have revealed strong quantum properties of the prepared states. The other approach – which is the one considered by our team – consists in focusing on *external* (or *mechanical*) degrees of freedom, such as momentum. Different generation protocols have also been explored, like the pair-wise dissociation of molecules [152], the parametric excitation of a BEC [6, 153] (which is currently still under study in our team), collisional deexcitation [154, 155] or the collision between BECs [5, 156, 157] that was developed and used in our team from 2006 to 2012.

Actually, some techniques developed since the 1980’s in quantum optics (in particular the *spontaneous parametric down-conversion* (SPDC) [158, 159] and the *four-wave mixing* (FWM) [160–162]) may serve as an inspiring guideline to reproduce this type of nonclassical sources in the realm of ultra-cold atoms. In 2005, the theoretical contribution of Mølmer et al. [163] initiated the setting of a new generation of experiments where the production of atomic pairs is induced by the presence of an optical lattice, generating a dynamic instability. The first experiments making use of this technique were achieved in the group of Wolfgang Ketterle [164], and since 2012 our team also implemented it [7]. This technique offers a better flexibility and control over the generated pairs than the one based on the collisions between BECs.

This aspect of our experiment has been studied in depth, and is well documented in the thesis manuscripts of my predecessors. In particular, the interested reader can find a depiction of the FWM process in the BEC in Marie Bonneau’s thesis [165], simulations in Josselin Ruaudel’s thesis [166], and a perturbative study in Pierre Dussarrat’s thesis [90]. We will only give in this manuscript some general reminders about the theoretical that we usually use to describe our source.

After roughly 5 years of inactivity, and thanks to the recent upgrades that we described in the previous chapter, our source is finally able to produce atomic pairs again. In the second part of this chapter, we will present the most recent experimental results that we obtained in the last few months.

1 Source of momenta-correlated atoms

1.1 Generalities

1.1.1 Parametric down conversion

Nowadays, SPDC is one of the most common techniques used in quantum optics to generate highly correlated pairs of photons [167], it has proven to be able to generate highly quantum correlation [168] and the hamiltonian describing the process –in the classical and non-depleted¹ pump approximation– is well-known, and studied since the 1960's [169]:

$$\hat{H}_{\text{SPDC}} = \int_{p,s,i} \hbar \kappa_p^{(s,i)} \sqrt{N_p} (\hat{a}_s^\dagger \hat{a}_i^\dagger + \hat{a}_s \hat{a}_i) \quad (5.1)$$

Where $\kappa_p^{(s,i)}$ is a function characterising the efficiency of conversion, N_p is the average number of particles of the pump in the mode p , and \hat{a}_s / \hat{a}_i are the annihilation operators of the correlated particles, canonically named *signal* and *idler*.

Naturally, the SPDC is maximally efficient when energy and momentum (or wave vector) are conserved, which (with obvious notations) reads:

$$\begin{cases} E_p = E_s + E_i & (5.2a) \\ \mathbf{k}_p = \mathbf{k}_s + \mathbf{k}_i & (5.2b) \end{cases}$$

These relations are usually called *phase-matching condition*.

However, SPDC is a second-order nonlinear process (involving the second-order susceptibility $\chi^{(2)}$ of a nonlinear medium). In second quantisation, it corresponds to a “one in, two out” situation, where a single photon from the pump may give birth to two correlated photons: this is clearly not something that can be considered in a monoatomic gas (but it is possible with molecules [152]). We unfortunately can not get helium atoms to come out of nowhere for free...

We have to look for the next order nonlinear effect to find a situation where the total number of particles is conserved.

[167]: Mandel et al. (1995), *Optical Coherence and Quantum Optics*

[168]: Walborn et al. (2010), “Spatial Correlations in Parametric Down-Conversion”

¹: the non-depleted approximation is valid as SPDC is generally an inefficient process. For the matter, this poor brightness is its weakest point for modern applications to quantum technologies.

[169]: Louisell et al. (1961), “Quantum Fluctuations and Noise in Parametric Processes. I.”

[152]: Greiner et al. (2005), “Probing Pair-Correlated Fermionic Atoms through Correlations in Atom Shot Noise”

1.1.2 Four-wave mixing

While it is less common in quantum optics, the **FWM** involves the third order susceptibility $\chi^{(3)}$ of a nonlinear medium. It can be interpreted with a “two in, two out” picture, where two particles in different modes interact and generate two particles in the correlated modes signal and idler. Since the number of particles is conserved it may have a non-zero effect in a monoatomic gas.

Assuming again that the pumps are classical and not depleted, it is easy to check that the **FWM** leads to the same type of quadratic hamiltonian as for **SPDC** [52, 166, 167]:

$$\hat{H}_{\text{FWM}} = \int_{p_1, p_2, s, i} \hbar \kappa_{p_1, p_2}^{(s, i)} \sqrt{N_{p_1}} \sqrt{N_{p_2}} (\hat{a}_s^\dagger \hat{a}_i^\dagger + \hat{a}_s \hat{a}_i) \quad (5.3)$$

The conservation of energy and momentum now involves four particles:

$$\begin{cases} E_{p_1} + E_{p_2} = E_s + E_i & (5.4a) \\ \mathbf{k}_{p_1} + \mathbf{k}_{p_2} = \mathbf{k}_s + \mathbf{k}_i & (5.4b) \end{cases}$$

1.1.3 Extension to the atomic case

These conversion processes require the intervention of a non-linear medium, which is naturally provided in a **BEC** thanks to the inter-atomic interactions. That being said, a simple and natural approach to turn on the generation of correlated atomic pairs consists in colliding two **BECs**: a lot of collisions take place and the mechanism of **FWM** is strongly activated. This technique has been pioneered at the **NIST**, in the team of William D. Phillips [170] and then improved in the team of Wolfgang Ketterle [171, 172]. It was also used in our team between 2006 and 2012 [5]: in particular, the observation of a Cauchy-Schwarz inequality violation, and sub-shot-noise statistics [156] was achieved with this technique. The main problem with this method is its lack of control. Momentum conservation imposes that the scattered atoms are on a sphere¹ (in the momentum space), the remaining condensates after collision, pancake-shaped after expansion, lying on the edge of the sphere. This source of correlated pairs with opposite momenta is not very convenient for performing atom interferometry with Bragg diffraction.

[52]: Gerry et al. (2005), *Introductory Quantum Optics*

[166]: Ruauudel (2013), “Création et caractérisation d’une source ajustable de paires d’atomes corrélés”

[167]: Mandel et al. (1995), *Optical Coherence and Quantum Optics*

[170]: Deng et al. (1999), “Four-Wave Mixing with Matter Waves”

[171]: Vogels et al. (2002), “Generation of Macroscopic Pair-Correlated Atomic Beams by Four-Wave Mixing in Bose-Einstein Condensates”

[172]: Vogels et al. (2003), “Coherent Collisions between Bose-Einstein Condensates”

[5]: Perrin et al. (2007), “Observation of Atom Pairs in Spontaneous Four-Wave Mixing of Two Colliding Bose-Einstein Condensates”

[156]: Kheruntsyan et al. (2012), “Violation of the Cauchy-Schwarz Inequality with Matter Waves”

¹: in the reference frame of the collision, the sphere is centred on zero, and the **BECs** momenta give its radius.

Since 2012, our team took better control of the phase-matching of the pair creation process condition by adding an optical lattice [7], following Mølmer et al.'s proposal [163]. The strength of this solution lies in its versatility: the control on the phase and amplitude of the lattice is transposed into the control over the dispersion relation to which the atoms are subjected, and –ultimately– over the two main parameters of interest for such a source: the emission momenta and the average number of particles per correlated mode [62]. Even if the source remains multimode, the pairs are no longer scattered on a whole sphere, but rather inside a cone of vertical principal axis: this is more convenient for the realisation of Mach-Zehnder like interferometers with Bragg diffraction.

[7]: Bonneau et al. (2013), “Tunable Source of Correlated Atom Beams”

[163]: Hilligsøe et al. (2005), “Phase-Matched Four Wave Mixing and Quantum Beam Splitting of Matter Waves in a Periodic Potential”

[62]: Perrier et al. (2019), “Thermal Counting Statistics in an Atomic Two-Mode Squeezed Vacuum State”

1.2 A bit of formalism

1.2.1 Four-wave mixing in a BEC

In the Heisenberg picture, the field operator $\hat{\Psi}$ describing the BEC satisfies the evolution equation:

$$i\hbar \partial_t \hat{\Psi}(\mathbf{r}, t) = [\hat{\Psi}(\mathbf{r}, t), \hat{H}] \quad (5.5)$$

\hat{H} being the hamiltonian containing the relevant physics, in particular the interatomic forces.

A rather simple depiction of \hat{H} is obtained with the dilute gas hypothesis¹ at temperature close to zero [173]. It allows to replace the microscopic interatomic potential by the regularised contact interaction (only depending on the s -wave scattering length), and to apply the Bogoliubov prescription².

1: meaning

$$n r_0^3 \ll 1 \quad (5.6)$$

with n being the cloud's density and r_0 the range of the interatomic force.

[173]: Pitaevskii et al. (2016), *Bose-Einstein Condensation and Superfluidity*

2: replacing the zero-momentum annihilation operator \hat{a}_0 by the number \sqrt{N} .

The hamiltonian \hat{H} then reads:

$$\hat{H} = \int d^3\mathbf{r} \hat{\Psi}^\dagger \left(-\frac{\hbar^2}{2m} \Delta + V(\mathbf{r}, t) + \frac{g}{2} \hat{\Psi}^\dagger \hat{\Psi} \right) \hat{\Psi} \quad (5.7)$$

V corresponding to an external potential (typically the trap used in experiments) and g the coupling constant, which fulfills:

$$g = \frac{4\pi\hbar^2 a}{m} \quad (5.8)$$

Now we can *a priori* force the apparition of the FWM terms by decomposing the field operator over the four modes that it involves, written with the appropriate annihilation operators:

$$\hat{\Psi}(\mathbf{r}, t) = \underbrace{\Phi_{p_1}(\mathbf{r}, t)\hat{a}_{p_1} + \Phi_{p_2}(\mathbf{r}, t)\hat{a}_{p_2}}_{\text{pump modes}} + \underbrace{\Phi_s(\mathbf{r}, t)\hat{a}_s + \Phi_i(\mathbf{r}, t)\hat{a}_i}_{\text{scattered modes}} \quad (5.9)$$

Actually, in our case the depletion induced by the FWM is very small when compared with the number of atoms in the gas, and the dynamics of the wave function above is expected to be very slow compared to the typical duration of the pair creation process during our experiments¹: we can drop time dependence in Eq. (5.9). In addition, by considering the low temperature limit, the BEC reduces to the zero-momentum mode contribution: both atoms of the pump have zero momentum, and the decomposition (5.9) may be restricted to three terms only²:

$$\hat{\Psi}(\mathbf{r}) = \underbrace{\Phi_0(\mathbf{r})\hat{a}_0}_{\text{BEC (pump)}} + \underbrace{\Phi_s(\mathbf{r})\hat{a}_s + \Phi_i(\mathbf{r})\hat{a}_i}_{\text{scattered modes}} \quad (5.10)$$

1: in fact, the evolution equation Eq. (5.5) leads to $\hat{\Psi}(\mathbf{r}, t) \propto e^{-\frac{i}{\hbar}(E_s+E_i-E_{p_1}-E_{p_2})t}$, where $E_s, E_i, E_{p_1}, E_{p_2}$ are the energies associated to each mode, and the FWM is effective only when the energy is conserved. On the timescale of the pair creation process ($\sim 400 \mu\text{s}$) this phase term does not have the time to evolve.

2: in nonlinear optics, this situation with a single pump mode is sometimes called *partially degenerated* four-wave mixing.

the facts that there are exactly four field operators in the interaction term of the hamiltonian (5.7) guarantees that four-wave mixing is the only nonlinear conversion process that may appear.

The injection of (5.10) inside the interaction part $\frac{g}{2} \int d^3\mathbf{r} \hat{\Psi}^\dagger \hat{\Psi}^\dagger \hat{\Psi} \hat{\Psi}$ of (5.7) generates many terms among which only two kinds fulfill the momentum conservation (and therefore significantly contribute to the dynamics of the system):

1. mean-field interaction terms:

$$\begin{aligned} \hat{H}_{MF} &= 2g \sum_{i \neq j} \int d^3\mathbf{r} |\Phi_i(\mathbf{r})|^2 \hat{a}_i^\dagger \hat{a}_i |\Phi_j(\mathbf{r})|^2 \hat{a}_j^\dagger \hat{a}_j \\ &\quad + \frac{g}{2} \sum_{i \in \{0, s, i\}} \int d^3\mathbf{r} |\Psi_i(\mathbf{r})|^4 \hat{a}_i^\dagger \hat{a}_i^\dagger \hat{a}_i \hat{a}_i \end{aligned} \quad (5.11)$$

2. two four-wave mixing terms:

$$\hat{H}_{FWM} = g \int d^3\mathbf{r} (\Phi_0^2(\mathbf{r})\Phi_s^*(\mathbf{r})\Phi_i^*(\mathbf{r})\hat{a}_s^\dagger \hat{a}_i^\dagger \hat{a}_0 \hat{a}_0 + \text{h.c.}) \quad (5.12)$$

Indeed, using the Bogoliubov prescription $\hat{a}_0 \approx \sqrt{N} \cdot \mathbf{1}$, with the classical and non-depleted pump approximation, and by denoting

$$I_{s,i} \triangleq \int d^3\mathbf{r} \Phi_0^2(\mathbf{r})\Phi_s^*(\mathbf{r})\Phi_i^*(\mathbf{r}) \quad (5.13)$$

we have

$$\hat{H}_{FWM} = Ng \left(I_{s,i} \hat{a}_s^\dagger \hat{a}_i^\dagger + I_{s,i}^* \hat{a}_s \hat{a}_i \right) \quad (5.14)$$

which has the same form as Eq. (5.1) and Eq. (5.3), with a complex rate

$$\kappa \triangleq \frac{Ng}{\hbar} I_{s,i} \quad (5.15)$$

$I_{s,i}$ is an overlap integral term, with the dimension of a density, that is obviously dependent on the spatial shape of the wave functions Φ . This integral term corresponds to momentum conservation.

1.2.2 Phase-matching condition in a periodic potential

If we neglect the mean-field interaction energy for a moment, and rewrite Eq. (5.4a) only with the kinetic energy contribution of the modes,

$$\frac{\hbar^2 k_{p_1}^2}{2m} + \frac{\hbar^2 k_{p_2}^2}{2m} = \frac{\hbar^2 k_s^2}{2m} + \frac{\hbar^2 k_i^2}{2m} \quad (5.16)$$

with a single BEC, both atoms of the pump are in the same mode k_0 , giving

$$\frac{\hbar^2 k_0^2}{m} = \frac{\hbar^2 k_s^2}{2m} + \frac{\hbar^2 k_i^2}{2m} \quad (5.17)$$

it is not difficult to see that, in free space, without additional external potential, it is not possible to fulfill the phase-matching condition with partially degenerated four-wave mixing (i.e. when the two pump modes are equal). This is why the former generation of experiments carried out in our team required the *collision* between two BECs.

With a single condensate ($p_1 = p_2$) the dispersion relation seen by the atoms must be modified, so that the phase-matching condition can be satisfied. It has been proven [163] that it can be achieved with a periodic potential, that is in practice obtained with an optical lattice. The first experiment of this kind has been conducted by Ketterle et al. [164] in 2006.

Remark 5.1 (Band structure and quasi-momentum) With a spatially periodic potential, Bloch's theorem guarantees that there is a basis of wave functions, each being an energy eigenstate, that can be written:

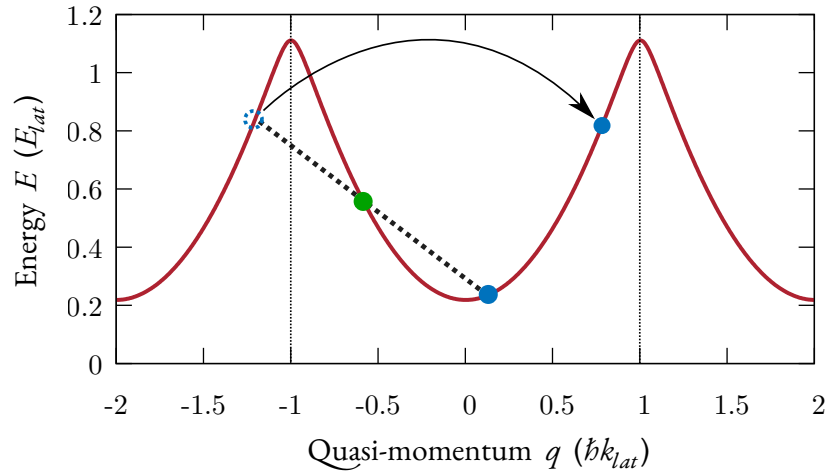
$$\Psi(\mathbf{r}) = e^{i \frac{\mathbf{q}\mathbf{r}}{\hbar}} u_{\mathbf{q}}(\mathbf{r}) \quad (5.18)$$

where u has the same periodicity as the potential.

[163]: Hilligsøe et al. (2005), "Phase-Matched Four Wave Mixing and Quantum Beam Splitting of Matter Waves in a Periodic Potential"

[164]: Campbell et al. (2006), "Parametric Amplification of Scattered Atom Pairs"

Figure 5.1: Pair creation process in the lowest energy band of the optical lattice (with $0.45E_{lat}$ depth). In the reference frame of the lattice, the BEC (green point) has a quasi-momentum $-0.6k_{lat}$. The periodicity of the dispersion relation makes it possible to find a solution to the phase-matching condition (edges of the dotted black line). When the lattice is switched off, Bloch's wave functions with quasi-momentum q (eigenstates of the hamiltonian with the lattice) are projected onto the plane waves with momentum p_z . If it is switched off adiabatically, the momenta p_z are just the restriction to the first Brillouin zone of the quasi-momenta. Picture adapted from [90].



[174]: Kittel (2018), *Introduction to Solid State Physics*
 [175]: Ashcroft et al. (1976), *Solid State Physics*

Then the resolution of the eigenvalues equation (the time-independent Schrödinger equation) gives the band structure of the atoms in the periodic potential (details of the calculations may be found in any solid state physics textbook, such as [174, 175]). We therefore find out that the dispersion relation is no longer quadratic (as in free space) but periodic, with a period $k_{lat} = \frac{\pi}{a}$ (a being the spatial period of the potential).

In our case the potential is periodic along the vertical direction, which is also the elongated axis of the BEC, that is why we often restrict the problem to 1D physics:

$$\Psi(z) = e^{i \frac{q_z z}{\hbar}} u_{q_z}(z) \tag{5.19}$$

q_z is very much alike a momentum, except that it is restricted to the first Brillouin zone $q_z \in [-\hbar k_{lat}, \hbar k_{lat}]$; it is called *quasi-momentum*. For simplicity, we will drop the z index in the following, and only denote q the quasi-momentum along the vertical axis.

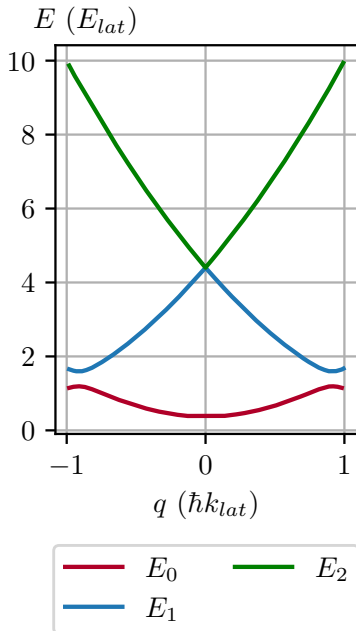


Figure 5.2: First three bands of the modified dispersion relation, for $\mathbf{V}_0 = 0.8 \mathbf{E}_{lat}$ (harmonic potential). In the case of the adiabatic turning on of the lattice, the pairs are only generated on the lowest energy band E_0 .

In the pair creation lattice, without the interactions, Bloch's wave functions are the right modes to consider, and the phase-matching corresponds to the conservation of the *quasi-momentum* and energy, similar to Eq. (5.4). In practice due to the high density of the gas, the interactions are not negligible and modify the energy conservation equation. We model it with a mean-field term, that we add to the bare equation involving Bloch's wave function in the non-interacting problem:

$$\begin{cases} 2E(q_0) = E(q_s) + E(q_i) + 2g n_0 & (5.20a) \\ 2q_0 = q_s + q_i \pmod{2\hbar k_{lat}} & (5.20b) \end{cases}$$

where $2g n_0$ is the mean field interaction term (n_0 is the peak density of the BEC). Solutions can be found thanks to periodicity (cf. Figure 5.1).

Remark 5.2 (Critical BEC's quasi-momentum) With a periodic potential, it is the change in concavity in the modified dispersion relation (cf. Figure 5.1) that provides a solution to Eq. (5.20). However it does not mean that such a solution exists whatever the value of the quasi-momentum q_0 is. Without trying to prove a very general mathematical theorem with all its rigorous assumptions, we will just remember the following result, that is a key element for experiments:

$$\begin{aligned} \text{a solution to the phase-} & \Leftrightarrow \text{the solution is unique} \\ \text{matching equations exists} & \\ \Rightarrow |q_0| \geq q_c(V_0) & > 0.5 \hbar k_{lat} \end{aligned}$$

where q_c is a critical value of the BEC's quasi-momentum, which depends on the lattice depth V_0 .

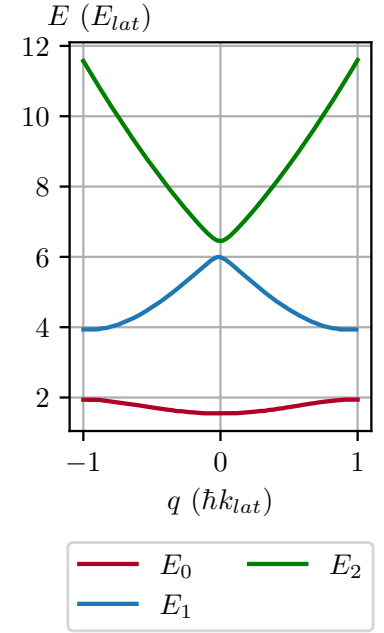


Figure 5.3: First three bands of the modified dispersion relation, for $V_0 = 4 E_{lat}$ (harmonic potential). Compared to Figure 5.2, the gap between the bands has increased.

1.2.3 Dynamics, density and correlations

We will not give a detailed description of the dynamics of the pair creation in this manuscript. This work has already been done in the references [90, 166]. We will just recall that the two-mode emission with a FWM term in the hamiltonian (such as (5.14)) is well-known. In particular, it is not difficult to check (using the Heisenberg picture) that the creation operators associated to the pairs have the form:

$$\begin{cases} \hat{a}_s(t) = \hat{a}_s(0) \cosh(|\kappa| t) - i e^{i\varphi_\kappa} \hat{a}_i^\dagger(0) \sinh(|\kappa| t) & (5.21a) \\ \hat{a}_i(t) = \hat{a}_i(0) \cosh(|\kappa| t) - i e^{i\varphi_\kappa} \hat{a}_s^\dagger(0) \sinh(|\kappa| t) & (5.21b) \end{cases}$$

where $\kappa = |\kappa| e^{i\varphi_\kappa}$ is defined in Eq. (5.15).

It is then possible to calculate expectation values and second-order correlation functions for the modes s and i , after the application of the

[90]: Dussarrat (2017), “Expériences d’Optique Atomique Quantique, Interféromètres à 2 et 4 modes”
 [166]: Ruaudel (2013), “Création et caractérisation d’une source ajustable de paires d’atomes corrélés”

pair creation lattice for a duration T :

$$N_{s|i}(T) = N_{\bar{s}|\bar{i}}(T) = \langle \hat{a}_{s|i}^\dagger \hat{a}_{s|i} \rangle = \sinh^2(\kappa T) \triangleq \nu \quad (5.22a)$$

$$g_{loc}^{(2)}(T) = \frac{\langle \hat{a}_{s|i}^\dagger \hat{a}_{s|i}^\dagger \hat{a}_{s|i} \hat{a}_{s|i} \rangle}{N_{s|i}^2(T)} = 2 \quad (5.22b)$$

$$g_{crossed}^{(2)}(T) = \frac{\langle \hat{a}_s^\dagger \hat{a}_i^\dagger \hat{a}_s \hat{a}_i \rangle}{N_s(T)N_i(T)} = 2 + \frac{1}{\nu} \quad (5.22c)$$

where the notation $s|i$ means that the quantity is the same whatever the mode we consider (actually this model is completely symmetric between the two modes).

g_{loc} is the normalised local second-order correlation function for each mode, which is equal to 2 due to bosonic bunching. $g_{crossed}^{(2)}$ is the normalised crossed second-order correlation function between the two modes, that we usually want to be as large as possible to witness quantum effects.

It is even possible to solve the Schrödinger equation (in the Schrödinger picture) to extract the form of the quantum state generated by the amplification process:

$$|\psi(T)\rangle = \frac{1}{\cosh(|\kappa|T)} \sum_{n=0}^{\infty} e^{in\varphi_\kappa} \tanh^n(|\kappa|T) |n, n\rangle_{s,i} \quad (5.23)$$

which is exactly the TMS that has been discussed in Subsection 2.2.4 of Chapter 1.

The results above are obtained by considering that the conservation of quasi-momentum and energy are strict, which leads to a simple two-mode emission. In fact, we empirically know that our source of pairs is *multi*-mode. This is not a big surprise since the duration of application of the lattice is short (less than a millisecond) which relaxes the energy conservation condition, and due to the trapping potential, the BEC has a finite size, which also relaxes the momentum conservation condition.

We do not have an exact analytical treatment of the multi-mode emission of source. Pierre Dussarat proposed in his PhD a **1D perturbative approach**, assuming the gas to be **homogeneous**, and the pair creation lattice to be **shallow**: the general procedure is similar to the one used for the two-mode emission, but in order to find the expression of the annihilation operators (similarly as Eq. (5.21)) the coupling between

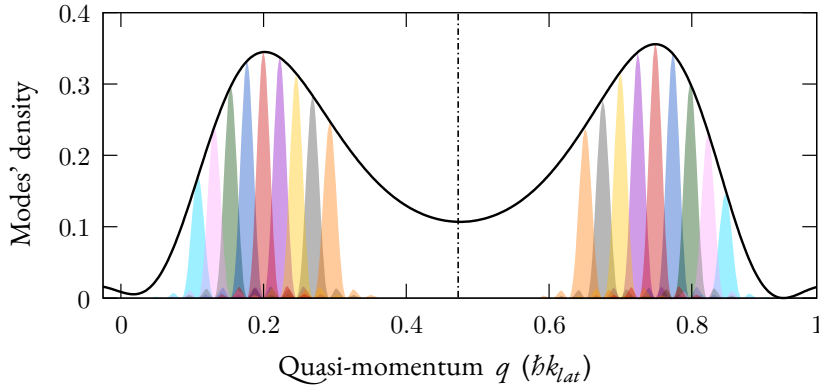


Figure 5.4: Profile of the density for the multi-mode emission. The black line is obtained with the perturbative model (5.27). Its shape depends on the time of application of the lattice (the larger the duration, the stricter the conservation of energy is, and the tighter the bumps are) and on the BEC's quasi-momentum. If we consider now the strict conservation of quasi-momentum, only pairs of modes, symmetrically distributed, are correlated: we represented them with the same colour.

the modes is truncated to the first order. With a shallow lattice, the wave functions of the atoms are approximated by plane waves truncated to the box delimiting the BEC, and the overlap integrals are computable:

$$\overbrace{I_{s,i}}^{\text{two modes}} \longrightarrow \overbrace{I(q, q')}^{\text{multi-mode}} = \frac{1}{V} \text{sinc} \left(\Delta q(q, q') \frac{L}{2} \right) \quad (5.24)$$

where V is the volume of the BEC and L its length, and

$$\Delta q(q, q') = 2q_0 - q - q' \pmod{2\hbar k_{lat}} \quad (5.25)$$

is the deviation from quasi-momentum conservation.

The pair creation rate is therefore also computable:

$$\begin{aligned} \overbrace{\kappa = \frac{Ng}{\hbar} I_{s,i}}^{\text{two modes}} &\longrightarrow \overbrace{\kappa(q, q')}^{\text{multi-mode}} = \frac{Ng}{\hbar} I(q, q') \\ &= \frac{gn_0}{\hbar} \text{sinc} \left(\Delta q(q, q') \frac{L}{2} \right) \end{aligned} \quad (5.26)$$

where n_0 is the atomic density of the gas.

This leads to an approximated expression of the number of particles $\nu(q)$ emitted in each mode, as a function of their quasi-momenta:

$$\nu(q) = \int \frac{dq'}{\Delta q_m} |\kappa(q, q')|^2 |\varepsilon(q, q')|^2 \quad (5.27)$$

where

$$\varepsilon(q, q') \triangleq T \text{sinc} \left(\frac{\Delta E(q, q') T}{\hbar} \frac{L}{2} \right) \quad (5.28)$$

$$\Delta E(q, q') = 2E(q_0) - E(q) - E(q') - 2gn_0 \quad (5.29)$$

is the deviation from energy conservation, and $\Delta q_m = \frac{2\pi}{L}$ is the size of the modes (depending on the length L of the BEC).

An example of such density distribution is given in Figure 5.4 (black line). The scaling $\nu \propto T^2$ is consistent with the simple two-mode emission model Eq. (5.22a), in the perturbative regime where $\kappa T \ll 1$. n_0 is the peak atomic density of the BEC.

Now, in the same way, this perturbative model allows for the evaluation of the second-order correlation function¹ between the modes². One finds:

$$G^{(2)}(q_1, q_2) = \nu(q_1) \cdot \nu(q_2) \quad (5.30a)$$

$$+ \left| \int \frac{dq}{\Delta q_m} \kappa^*(q_1, q) \kappa(q_2, q) \varepsilon^*(q_1, q) \varepsilon(q_2, q) \right|^2 \quad (5.30b)$$

$$+ |\kappa(q_1, q_2)|^2 |\varepsilon(q_1, q_2)|^2 \quad (5.30c)$$

where three different terms are present: (5.30a) is the uncorrelated background, (5.30b) is the local correlation term (similar to (5.22b)), and (5.30c) is the crossed correlations term (similar to (5.22c)).

Numerically, with parameters chosen to match our experimental regime, we can check that the correlation vanishes extremely fast when the quasi-momentum is not conserved. We therefore simplify the model even further, by imposing the *strict* conservation of quasi-momentum³. The local and crossed –normalised– second-order correlation functions take the simple form⁴:

$$\left\{ \begin{aligned} g_{loc}^{(2)}(q_1, q_2 = q_1 + \delta q) &= 1 + \text{sinc}^2\left(\delta q \frac{L}{2}\right) \end{aligned} \right. \quad (5.31a)$$

$$\left\{ \begin{aligned} g_{crossed}^{(2)}(q_1, q_2 = 2q_0 - q_1 + \delta q) &= 1 + \frac{1}{\nu(q_1)} \text{sinc}^2\left(\delta q \frac{L}{2}\right) \end{aligned} \right. \quad (5.31b)$$

We will obviously *never* observe correlations that fit such sinc^2 profiles experimentally: many approximations have been made to obtain this analytical result, and we also have to keep in mind that this study is perturbative, and should be wrong when the average number of particles per mode becomes “large”⁵.

The interesting point of this work is that it provides a consistent scaling between the width of the correlations (local and crossed) and the typical Δq_m size of the modes: both scale in $\frac{1}{L}$, the inverse size of the condensate. The physical interpretation of this is satisfying: correlations are present if we overlap an atomic mode with itself, or with its

1: a reminder about the correlation is given in Subsection 2.3

2: the perturbative model actually provides the dynamics of the creation/annihilation operators, and thus the correlation functions, as expressed as the expectation value of a product of these operators.

3: which basically means (regarding Eq. (5.26)) that we set $\kappa(q_1, q_2) = \frac{g^{n_0}}{\hbar} \delta[\Delta q(q_1, q_2)]$

4: Eq. (5.31b) looks like Eq. (5.22c), but with $g_{crossed}^{(2)} \xrightarrow{\nu \rightarrow \infty} 1$, instead of 2... This comes from the fact that it is a perturbative calculation, only valid in the limit $\frac{g^{n_0}}{\hbar} T \ll 1$, thus $1, 2 \ll \frac{1}{\nu}$.

5: even if we do not precisely know where the perturbative approach collapses

correlated partner. It also shows the experimental advantage we have by preparing elongated condensates: the number of correlated modes fitting in the emission envelope is larger, making the design of many particles interference experiments possible.

Three ideas are worth remembering:

1. the *relaxed* energy conservation relation sets the width of the envelope for the density of emitted pairs (cf. Figure 5.4). It is experimentally controlled by the duration of the pair emission process (cf. Eq. (5.27) and Eq. (5.28));
2. the width of the modes is proportional to $\frac{1}{L}$, which is also the typical size of the correlations between q_1 and q_2 ;
3. the conservation of quasi-momentum can be considered to be strict in very good approximation, which guarantees that the nonlocal correlation only occurs for *pairs* of modes;

With all of this in mind, we can propose the following quantum state to describe what our source is emitting:

$$|\psi\rangle = \bigotimes_{q \in Q} \left\{ \sqrt{1 - |\alpha_q|^2} \sum_{N=0}^{\infty} \alpha_q^N |N, N\rangle_{q, 2q_0 - q} \right\} \quad (5.32)$$

where Q is the set of modes of width Δq_m fitting in the envelope $n(q, T)$, and α_q is the two-mode squeezed state parameter, relatively to the couple of modes $(q, 2q_0 - q)$, which satisfies:

$$\sum_{N=0}^{\infty} N |\alpha_q^N|^2 = \nu(q) \quad (5.33)$$

1.2.4 Turning on and off the optical lattice

The pairs production is carried out by the collisions, and therefore requires high density to be efficient. That is why the pair creation lattice is applied while the ODT is still operating.

However, the pair creation lattice is not switched on and off abruptly. We actually proceed to a linear ramping of the optical power, in approximately $T_r \approx 100 \mu\text{s}$.

- the lattice is switched on adiabatically so that the BEC is loaded in the lowest energy band of the modified dispersion relation¹ (cf. Figure 5.1). The general case would require to take into

¹: thereafter the pairs are created in this lowest energy band.

[176]: Denschlag et al. (2002), “A Bose-Einstein Condensate in an Optical Lattice”

[177]: Messiah (1961), *Quantum Mechanics*

[8]: Lopes (2015), “An Atomic Hong-Ou-Mandel Experiment”

account the complete band structure while describing the pair creation process, and has been explored experimentally in [176]. The condition of adiabaticity can be written [177]

$$\frac{dV_0}{dt} \ll \frac{\Delta E(q_0)^2}{\hbar} \quad (5.34)$$

where V_0 is the amplitude of the periodic potential, and $\Delta E(q_0)$ is the energy difference between a Bloch state with quasi-momentum q_0 in the lowest energy band E_0 , and a Bloch state with quasi-momentum q_0 in the first excited band E_1 (cf. Figure 5.2 and Figure 5.3). Indeed, the BEC must be loaded adiabatically in the lattice, with a relative quasi-momentum $q_0 > 0.5 \hbar k_{lat}$ (cf. Remark 5.2). In practice, it means that there is no Bragg diffraction of the BEC by the lattice (see [8] for more details), which is a criterion that can be checked experimentally.

This condition is more complicated than it seems, because the band structure (and therefore $\Delta E(q)$) depends on V_0 . In general, the required ramping time (T_r) of the lattice’s potential increases with V_0 and $|q_0|$ (cf. Figure 5.2 and Figure 5.3: when $|q_0|$ increases, ΔE decreases and therefore $T_r \propto \frac{1}{\Delta E}$ increases). Some numerical simulations have been performed in reference [8] with different parameters. We generally find that

$$T_r \gg [1 - 10] \mu\text{s}$$

but with a very deep lattice ($V_0 \gtrsim 4 E_{lat}$) and with a BEC having a large quasi-momentum ($|q_0| \approx 0.9 \hbar k_{lat}$) we can find

$$T_r \gg 100 \mu\text{s}$$

- when the lattice is switched off, Bloch’s states are projected on the free space eigenstates, which are the plane waves. If the switching off is done abruptly, we are basically measuring the Bloch’s states components in the plane waves’ basis. It turns out that when the lattice is shallow, the decomposition of the Bloch’s states is very close to the trivial decomposition (only one component in the plane waves’ basis is populated) [90, 176]. It is indeed quite natural to think that in the limit of the very shallow periodic potential, the physics is almost the same as in free space, and the Bloch’s states match the plane waves perfectly. We therefore also perform an adiabatic turning off of the pair creation lattice in order to map the Bloch’s states of the generated pairs onto plane waves lying inside the first Brillouin zone.

[90]: Dussarrat (2017), “Expériences d’Optique Atomique Quantique, Interféromètres à 2 et 4 modes”

[176]: Denschlag et al. (2002), “A Bose-Einstein Condensate in an Optical Lattice”

2 Experimental results

We will present in this section the latest experimental results that we have obtained. At the time this manuscript is being written, this work can still be considered to be a *work in progress*. Indeed, we succeeded in making our first atomic pairs on 30 March 2022, and we got a new apparatus break down approximately two months later: the ODT fibered laser died and we also faced electrical[†] and vacuum issues. We still have to figure out the cause of the electrical problems, but we already have ordered and received a new IPG Photonics[®] laser that we should install soon.

[†]: one the two PSUs used for the MT stops randomly during the experiments, and the IGBT watercooling system began to malfunction.

The main goal (which has not achieved been yet) is to find two sets of parameters:

- ▶ a first one generating correlated pairs with a large average number of particles per mode (useful for n -particles HOM-like experiments);
- ▶ a second one with a very small number of particles per mode, that should be used to perform Bell inequalities violation experiments;

When the apparatus issues forced the experiment to stop producing pairs (in May 2022) we were mostly exploring the first type of regime.

In the first sub-section we will describe our optical setup, and then we will give an example of analysis for a specific dataset. We cannot claim that this dataset is *optimal*, because we did not have time to properly test the effect of the different parameters. We can only say that we observed promising correlation with it.

2.1 Optical setup

As it has already been discussed, the periodic potential is realised with an optical lattice, resulting from the crossing of two laser beams. We use an ultra-stable Nd:YAG 1064 nm laser (Mephisto by Coherent[®]). It is very far (in blue) from the atomic transition ($2^3S_1 \rightarrow 2^3P_2$ at $\lambda_{lat} = 1083$ nm), making the one-beam induced spontaneous emission negligible during our $\lesssim 1$ ms long pulses (in reference [8] a rate of $2 \cdot 10^{-5} \text{ ms}^{-1}$ is calculated with our typical parameters).

The atoms feel a repulsive potential proportional to the optical inten-

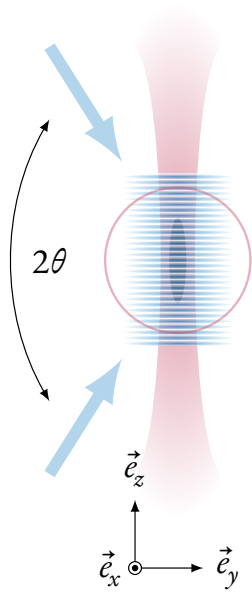


Figure 5.5: Schematic representation of the pair creation lattice. The red vertical narrow and the large red circles represent the two beams of the ODT. The lattice, is represented in blue, with its two beams forming a 2θ angle. Axes orientations are set in compliance with Figure 3.19 on page 129.

Table 5.1: Parameters of the lattice

λ_{lat}	1064 nm
θ	83°
a_{lat}	536 nm
k_{lat}	$5.86 \mu\text{m}^{-1} \approx 1.01 k_{rec}$
v_{lat}	93 mm s^{-1}
typical $\delta\omega$	$2\pi \times 105 \text{ kHz}$
typical v_0	56 mm s^{-1}

sity:

$$I(z, t) = 4I_0 \sin^2 \left[k_{lat}z + \delta\omega \frac{t}{2} \right] \quad (5.35)$$

with

$$k_{lat} \triangleq \frac{\pi}{a_{lat}} \quad (5.36a)$$

$$a_{lat} = \frac{\lambda_{lat}}{2 \sin(\theta)} \quad (5.36b)$$

$$v_{lat} = \frac{\hbar k_{lat}}{m} \quad (5.36c)$$

a_{lat} being the lattice periodicity, and $\delta\omega$ being the angular frequency difference between the two beams. It is often convenient to give the atoms' velocities/momenta in the lattice's units of velocity/momentum (respectively v_{lat} and $\hbar k_{lat}$).

If we then work in the lattice's frame of reference, the potential writes:

$$V_{lat}(z) = V_0 \sin^2(k_{lat}z) \quad (5.37a)$$

$$V_0 = \frac{\hbar\Gamma^2 I_0}{2 I_s \Delta_{lat}} \quad (5.37b)$$

$$\Delta_{lat} = 2\pi c \left(\frac{1}{\lambda_{lat}} - \frac{1}{\lambda} \right) \quad (5.37c)$$

I_0 being the single gaussian beam peak intensity.

The intensities of the beams are controlled with the RF frequency of the two AOMs used to tune them. This RF power is modulated with Mini-Circuit[®] RF attenuators. However this control is not yet satisfying due to the nonlinear time response of the attenuators (which could be an issue for the adiabatic loading of the BEC in a very deep lattice). We should improve this part of the setup in the near future.

2.2 Generation of pairs

2.2.1 First characterisation of the pair creation's behaviour

When we performed our first pair generation experiments, we initially tried to maximise the pair density signal (for convenience). That is why we explored a regime where the average number of particles per mode is large. Since we had to stop the experiments at a time when we were still setting it up, we currently do not have many datasets with a

Date	13/05/2022
Sequence number	022
Lattice detuning	$\delta\omega = 2\pi \times 105$ kHz
Power per beam	85 mW
Lattice ramping up/down duration	100 μ s
Lattice max. power duration	800 μ s
Lattice depth	$V_0 = 0.54(1) E_{rec}$
BEC's quasi-momentum	$q_0 = 0.6 \hbar k_{lat}$
vODT power	0.4 W
hODT power	0.1 W
Number of files	802

reasonable number of experimental realisations (to perform statistical averaging). We give in Table 5.2 the reference and some information about the dataset that we will use in the following for the computation of second-order correlations.

As it has been discussed in the first section, the two important variable parameters characterising the pair creation regime are the *BEC quasi-momentum* (controlled by the lattice's beams relative frequency), and the *lattice depth* (controlled by the beams power). Even though the lattice depth could be evaluated with Eq. (5.37b), it does not give a faithful value, because of our poor knowledge of the waists of the lattice's beams¹. The safest way to evaluate the lattice's depth is to perform Rabi oscillations of the BEC, using the lattice.

The idea (as always for Rabi oscillations) is to perform the *coherent coupling* between the state of zero-momentum in the trap $|\hbar k = 0\rangle$ and the state with a momentum resulting from the exchange of two photons with the lattice $|2\hbar k_{lat}\rangle$. To this end, we just have to apply a lattice detuning corresponding to the kinetic energy of an atom in the $|2\hbar k_{lat}\rangle$ state:

$$\delta\omega = \frac{2\hbar k_{lat}^2}{m} \quad (5.38)$$

The Rabi oscillation can then be visualised by counting the number N_0 of atoms falling on the MCP inside a temporal box centred on a time corresponding to the zero-initial velocity (308 ms), and the number N_2 of atoms falling in a temporal box centred on a time corresponding to an initial vertical velocity $\frac{2\hbar k_{lat}}{m}$ (327 ms). Both boxes have the same “size” – a few milliseconds – which is larger than the typical time arrival spread of a BEC on the MCP (cf. Figure 3.25). An exemple of such a

Table 5.2: Sequence reference and informations about the dataset chosen to measure densities and correlation

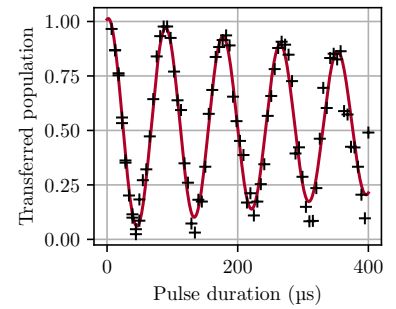
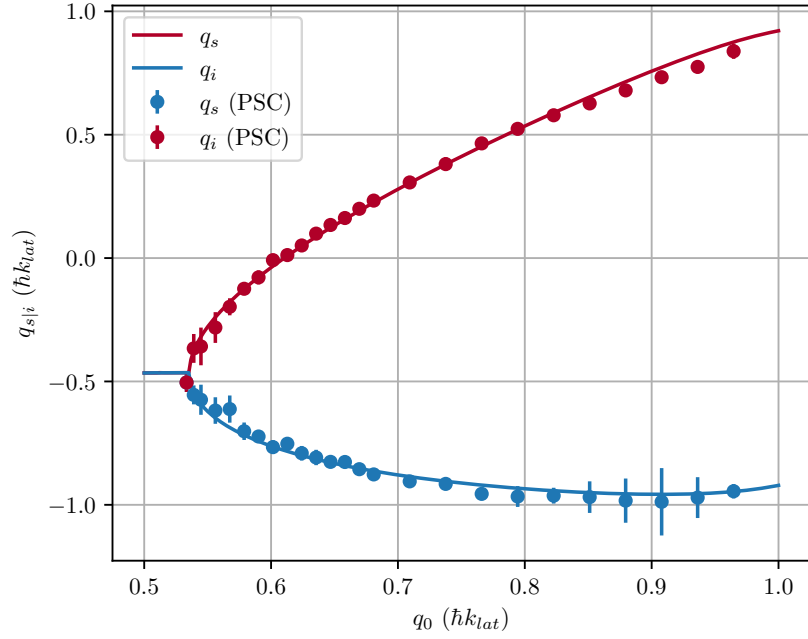


Figure 5.6: Example of Rabi oscillations with the pair creation lattice, with 85 mW (value used for the dataset Table 5.2). Here we plot the normalised transferred population: $\overline{N}_t = \frac{|N_1 - N_0|}{N_1 + N_0}$. The fit returns a Rabi angular frequency $\Omega = 2\pi \times 11.4$ kHz. In order not to saturate the MCP, the experimental realisations are performed with slightly off-detuned Raman transfers, so that only a small fraction of the total number of atoms is detected.

¹: their waists are large, and we do not have a convenient access to measure them. Additionally we found numerical discrepancies in the previous PhD manuscripts/lab notebooks concerning these waists.

Figure 5.7: Quasi-momenta of the pairs as a function of the BEC’s quasi-momentum. The lattice’s depth is fixed to $V_0 = 0.54 E_{rec}$. The plain lines correspond to the numerical solving of the phase-matching conditions Eq. (5.20), adjusted with the free parameter n_0 . We observed that the pair generation starts for $q_0 > q_c \approx 0.53 \cdot \hbar k_{lat} > 0.5$, which is expected (cf. Remark 5.2). We find a BEC’s density $n_0 \approx 1.3(2) \cdot 10^{13} \text{ cm}^{-3}$.



measurement is given in Figure 5.6.

Then the lattice’s depth is simply given by (Ω being the Rabi angular frequency of the lattice):

$$V_0 = 2\hbar\Omega \quad (5.39)$$

that we usually express in recoil energy units E_{rec} (cf. Table 3.2).

The BEC’s quasi-momentum in the lattice’s frame of reference is even simpler to evaluate. It is the exact opposite of the running speed of the lattice in the laboratory reference frame, therefore:

$$q_0 = mv_0 = m \frac{\delta\omega}{2k_{lat}} \quad (5.40)$$

In order to test the behavior of the source, we measured the quasi-momenta of the generated pairs, as a function of the BEC’s quasi-momentum, with a lattice’s depth fixed to $V_0 = 0.54 E_{rec}$. This experiment actually consists in the verification of the phase-matching conditions Eq. (5.20), that can be solved numerically. This type of experiment has been conducted in our team back in 2013 [7], our recent results are presented in Figure 5.7. Since the mean field correction, proportional to the BEC’s density, plays an important role in the energy conservation equation (5.20a), and is the only fitting parameter to have a good matching between our experimental data and the numerical

[7]: Bonneau et al. (2013), “Tunable Source of Correlated Atom Beams”

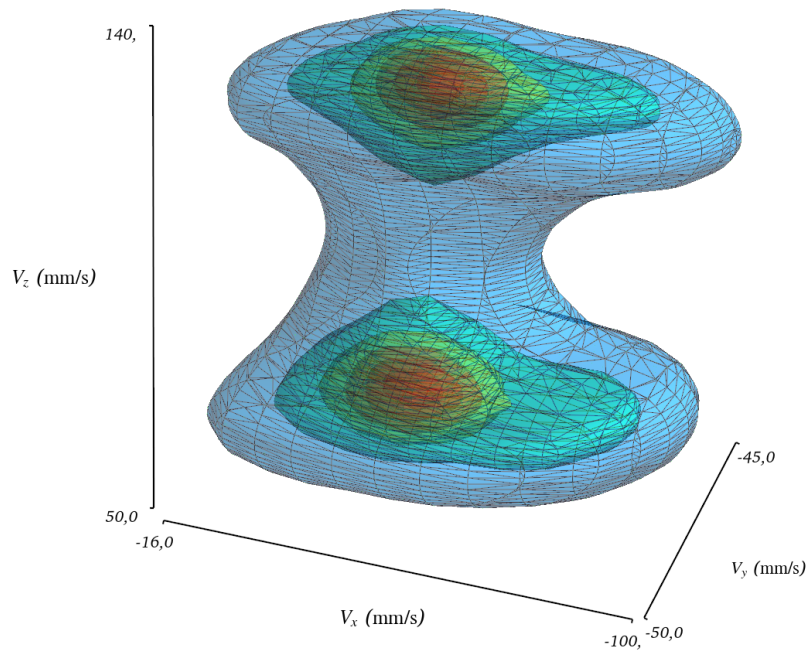


Figure 5.8: 3D pairs' density iso-surfaces. The visualisation in the momentum space is computed with kernel density estimation based on the experimental dataset Table 5.2. The iso-surfaces are linearly spaced, from low densities (blue outer sheet) to high densities (red inner sheet). The correlations are maximal in the region where the density is the largest. This 3D graph is mostly a first qualitative visualisation of the shape of the data.

estimation, this experiment is effectively a measure of the BEC's density in the optical trap. We found a value

$$n_0 = 1.3(2) \cdot 10^{13} \text{ cm}^{-3}$$

which is the expected order of magnitude. However we do not have an alternative measurement method to compare this value yet. Indeed, as it has been discussed in Chapter 3¹, the saturation of the MCP prevents us from performing a direct measurement, and fluorescence imaging cannot resolve the BECs obtained in the ODT (due to the small number of atoms). As I write this manuscript, we are testing an imaging technique based on the absorption of the photons by the cloud². This technique is used by our colleagues in the *Helium lattice* team, and provided them very good result to estimate the number of atoms in the BEC, and also calibrate the quantum efficiency of their MCP. However we only have preliminary data: a more complete depiction of this approach will probably be discussed in the manuscript of Charlie Leprince (currently PhD student on the experiment).

¹: last paragraph of Subsection 3.2.4

²: with the same camera as the one used for the fluence

Figure 5.9: 2D histograms of the pairs' density in the momentum space. The numerical values are normalised by the number of files (averaging) and the size of the pixels (40 bins for the q_x/q_y axes and 100 bins for the q_z axis): these values are therefore expressed in atoms/ $(\hbar k_{lat})^2$. The coloured dashed lines mark out coarse domains used in Figure 5.10 to compute 1D histograms for both modes separately. We can clearly see a sharp cut in the (q_x, q_z) domain on the left graph (close to $q_x = 0$): this is due to the copper plate (cf. Chapter 4) that hides most of the MCP's area corresponding to $q_x > 0$.

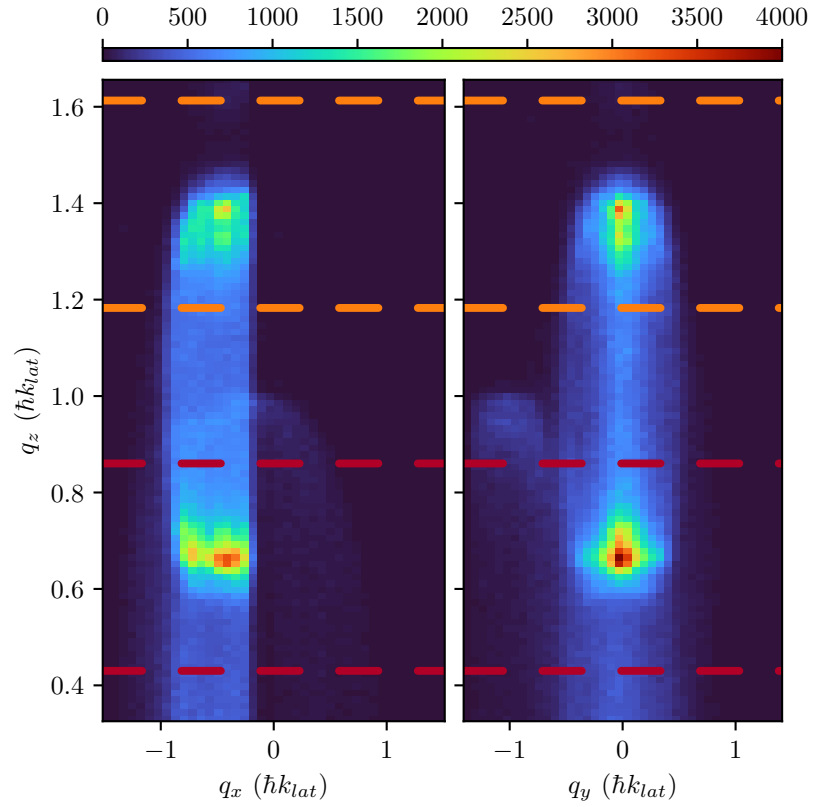
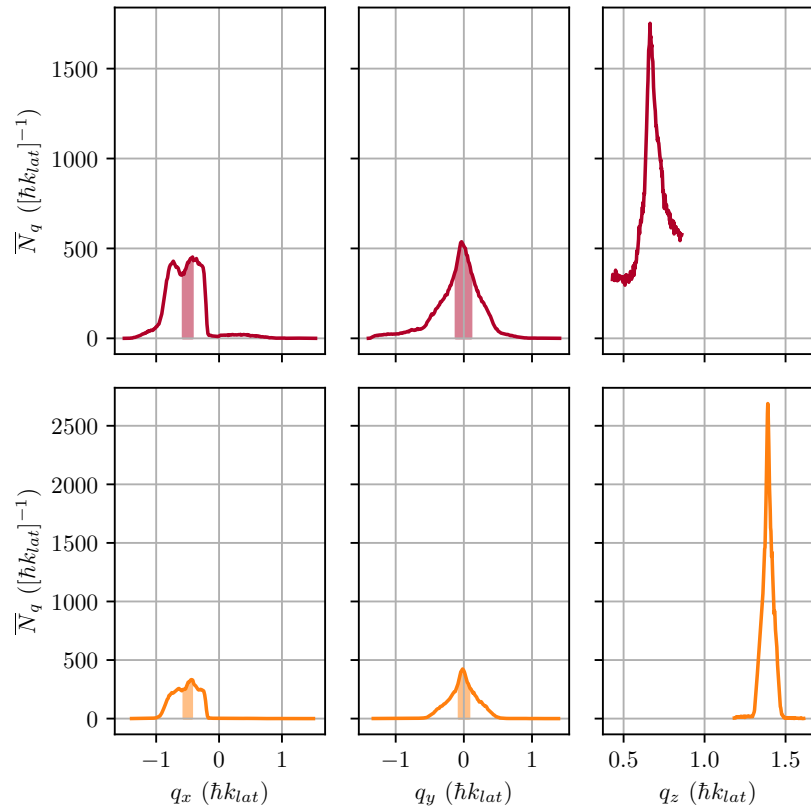


Figure 5.10: 1D pairs' density histogram in the momentum space. Both regions of emission are treated separately and the domains chosen to perform the binning are represented in Figure 5.9 (with the corresponding colours). The values are normalised by the number of files (averaging) and the size of the bins (200 bins for each axis). The integral under each curve of the same colour is the same (equal to the average number of atoms in the domain). The shaded area under the plain lines correspond to the modes' size, estimated by studying the second-order local correlation functions along each axis (cf. Figure 5.14). We can check that in the transverse plane the emission is almost mono-mode. However along the longitudinal axis the modes are too small to even be visible: the emission is multi-mode.



2.2.2 Density of pairs

We can then visualise the density of atoms in the momentum space, restricted to the region where the pairs are emitted (Figure 5.8, Figure 5.9, Figure 5.10). Once we have estimated the size of the modes (by computing the local second-order correlations, cf. Subsection 2.3) we can check the multimode nature of the emission along the different axes, and also compute the average number of atoms per mode ν .

Concerning the number of modes emitted, a simple way of proceeding consists in computing the number of modes fitting in the density envelope, by calculating the ratio

$$\begin{cases} n_m \triangleq \frac{\sigma_d^i}{\sigma_c^i/\sqrt{2}} & d \equiv \text{density} \\ & c \equiv \text{correlations} \\ i \in \{x, y, z\} \end{cases} \quad (5.41)$$

where σ_d^i is the RMS width of the 1D density along the q_i axis (cf. Figure 5.10) and σ_c^i is the RMS width of the second-order correlations along the same axis: it is a direct picture of the RMS width of the mode, up to a $\sqrt{2}$ factor coming out of the fact that the $g^{(2)}$ function is essentially a *product* of densities, and not a density itself (cf. Figure 5.14 in the Subsection 2.3.3). We find

Atomic beam	n_x	n_y	n_z
$\mathbf{q}_z \approx 0.7 \mathbf{hk}_{\text{lat}}$	3.6	2.4	15.2
$\mathbf{q}_z \approx 1.4 \mathbf{hk}_{\text{lat}}$	3.2	2.6	12.4

Table 5.3: Estimation of the number of atomic modes emitted along each direction, estimated with the ratio (5.41) between the RMS size of the modes, and the RMS width of the pairs' density profile.

These numbers are slightly larger than the old estimations of the number of emitted modes performed in 2015 and 2017. In particular, in the transverse directions the emission is not perfectly monomode: we must therefore perform postselection in the transverse plane (to consider only a single transverse mode) before computing the correlations along the vertical direction.

Along the vertical axis, the emission is multimode, which is good to set up a multi-particles interferometer (such as the Rarity-Tapster interferometer [27]) to probe the entanglement between the modes (cf. Chapter 2).

[27]: Rarity et al. (1990), "Experimental violation of Bell's inequality based on phase and momentum"

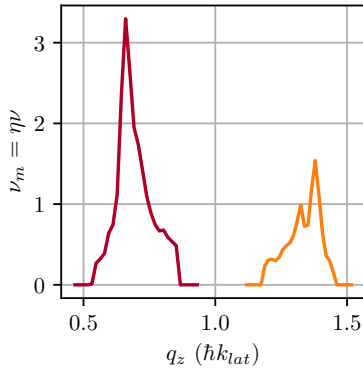


Figure 5.11: Average number of particle per mode ν as a function of the centre q_z of the mode. The protocol used to compute these values is explained in the main text. The red line corresponds to the first atomic beam ($q_z \approx 0.7 \hbar k_{lat}$), and the orange line corresponds to the second one ($q_z \approx 1.4 \hbar k_{lat}$). Here ν_m is the *measured* population, meaning that it reduced by the quantum efficiency of the MCP: the actual population are therefore approximately twice as large. The boxes inside which the atoms are counted are rectangular, with sizes chosen in compliance with the measured local correlations lengths (plotted in Figure 5.14): $\Delta q_i = 2 \times \sigma_c^i / \sqrt{2}$. We give here these sizes in units of $\hbar k_{lat}$:

red line:	Δq_x	0.18
	Δq_y	0.24
	Δq_z	0.013
blue line:	Δq_x	0.14
	Δq_y	0.17
	Δq_z	0.011

1: the transverse sizes of the boxes are visible with the shaded area of Figure 5.10. The longitudinal size is too small to be visible on this figure.

2: in order not to wash away the correlations by mixing up uncorrelated modes in a same box.

Knowing the size of the modes, we can also compute the average number of particles per mode ν . For the matter, we will distinguish the two regions of emissions 1 and 2 (respectively in red and orange in Figure 5.9 and Figure 5.10), and also denote $\nu_m \triangleq \eta\nu$, the *measured* number of particles per mode, that is dependent on the quantum efficiency η of the detector. By computing the average number of atoms in boxes

- ▶ centred on the zones where the density is maximal (cf. Figure 5.9);
- ▶ with sizes given by $\sigma_c^{x,y,z} / \sqrt{2}$, the estimated natural size of the modes¹;

we find:

$$\begin{cases} \nu_{m,1} = 3.2 \\ \nu_{m,2} = 1.5 \end{cases} \quad (5.42)$$

These values corresponds to the average number of particles per mode in the region where the atomic beams are the brightest. We can also do the same thing, changing the centre of the mode: the resulting graph is plotted in Figure 5.11.

There is a strong asymmetry between average populations of the two modes. However, one should notice that there is also a significant difference between the size of the boxes that were used to obtain the graph of the Figure 5.11. Indeed, as we will see in Subsection 2.3.3, the measurements of the local correlation lengths give slightly different values between the two atomic beams. But in practice, the measurements of these lengths are not extremely precise (with the data that we currently have), and anyway the natural modes are obviously not square shaped. During an interferometry experiment, we will only need to select boxes that are slightly smaller than the natural modes² and having the same size. We can therefore redo the same graph as in the Figure 5.11 but using this time boxes having the same volume and shape. The result is plotted in Figure 5.12. The values corresponding to the first atomic beam are strongly reduced, reducing a lot the asymmetry between the two beams. The maximum values are now

$$\begin{cases} \nu_{m,1} = 1.6 \\ \nu_{m,2} = 1.5 \end{cases} \quad (5.43)$$

It remains a small difference between $\nu_{m,1}$ and $\nu_{m,2}$: this is not something new for us (this sort of unbalance has always been observed), and it has

also been reported by Ketterle et al., in similar experiments [164]. Two hypotheses may be considered to explain this phenomenon:

1. it is always the mode with the largest momentum which is the less populated. In the schematic Figure 5.1, it corresponds to the Bloch state with the highest energy (that is remapped inside the first Brillouin zone). Since its energy is larger, the probability for an atom in this Bloch state to tunnel in the upper band is also higher. If that happens, when the lattice is switched off, the atom is recast at a different momentum, and does not contribute to the density distribution that we measure.
2. the concavity of the dispersion relation also makes it possible for two atoms in the high energy Bloch state to realise a secondary collision and generate higher order pairs, which obviously depletes the population of this Bloch state.

However, we never proceeded to numerical simulation or experimental tests to check the plausibility of these hypotheses, for now they are just “food for thought”.

Setting aside the question of the profile’s asymmetry, in absolute terms, the values (5.43) are large as compared to those used during the last experiments conducted in the team [9, 59], where ν was intentionally set to a value smaller than 1, such that the non-vacuum part of the emitted state could be approximated by a $|1, 1\rangle$ state. The difference is approximately one order of magnitude.

This regime with a “large” number of particles per mode is not very well known in our group, and has only been observed previously back in 2013 [7]. The study of the correlations of the source in this regime is a new investigation for us. With these measured values, and assuming that the MCP has a detectivity of 50 %, the *actual* number ν of particles per mode should be ranging between approximately 3 and 4, which is promising to perform HOM-like experiments with TMS states, that we have discussed in Chapter 1.

2.3 Probing the correlation

Let us now focus on the correlations that can be measured with the sample.

[164]: Campbell et al. (2006), “Parametric Amplification of Scattered Atom Pairs”

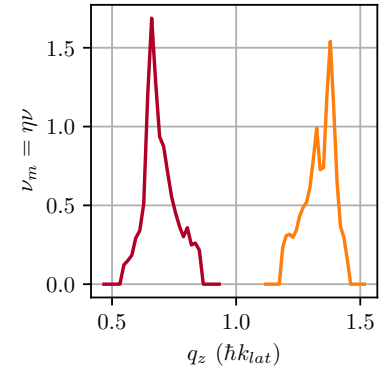


Figure 5.12: Same graph as Figure 5.11 but using the same boxes, whose size is given by:

Δq_x	0.14
Δq_y	0.17
Δq_z	0.011

[9]: Dussarrat et al. (2017), “Two-Particle Four-Mode Interferometer for Atoms”

[59]: Lopes et al. (2015), “Atomic Hong–Ou–Mandel Experiment”

[7]: Bonneau et al. (2013), “Tunable Source of Correlated Atom Beams”

2.3.1 Short definition reminder

We first need to recall some definitions for the correlations functions.

[69]: Glauber (1963), “The Quantum Theory of Optical Coherence”

[70]: Glauber (1963), “Coherent and Incoherent States of the Radiation Field”

Definition 8 (second-order correlation function) n^{th} -order correlation functions were introduced by Glauber in 1963 [69, 70].

The second-order correlation function –probing density (or intensity) correlations– is usually written:

$$G^{(2)}(\mathbf{q}_1, \mathbf{q}'_1; \mathbf{q}_2, \mathbf{q}'_2) = \langle \hat{a}_{\mathbf{q}_1}^\dagger \hat{a}_{\mathbf{q}'_1}^\dagger \hat{a}_{\mathbf{q}_2} \hat{a}_{\mathbf{q}'_2} \rangle \quad (5.44)$$

Where $\mathbf{q}_1, \mathbf{q}'_1, \mathbf{q}_2, \mathbf{q}'_2$ are general parameters: in our case velocities, or momenta. This mathematical object is however not hermitian, and therefore not a physical observable. In experiments we usually restrict to the case where $\mathbf{q}_1 = \mathbf{q}'_1$ and $\mathbf{q}_2 = \mathbf{q}'_2$, and write:

$$G^{(2)}(\mathbf{q}_1; \mathbf{q}_2) \triangleq \langle \hat{a}_{\mathbf{q}_1}^\dagger \hat{a}_{\mathbf{q}_1}^\dagger \hat{a}_{\mathbf{q}_2} \hat{a}_{\mathbf{q}_2} \rangle = \langle : n_{\mathbf{q}_1} n_{\mathbf{q}_2} : \rangle \quad (5.45)$$

where $n_{\mathbf{q}_i}$ is the density of particles in the mode \mathbf{q}_i , and the columns indicate the normal ordering of the annihilation/creation operators. Given the commutation relations $[\hat{a}_{\mathbf{q}_i}, \hat{a}_{\mathbf{q}_j}^\dagger]$, this quantity can be related to the number of particles collected with a detector.

In our case, we will see that the typical correlation length is not negligible compared to the size of the pair’s density profile in the momentum space. This means that the “background” of the $G^{(2)}$ correlations is also dependent on the momenta $\mathbf{q}_1, \mathbf{q}_2$. Thus we prefer to work with *normalised* second-order correlation functions:

Definition 9 (Normalised second-order correlation function) We define the normalised second-order correlation function by:

$$g^{(2)}(\mathbf{q}_1, \mathbf{q}_2) \triangleq \frac{G^{(2)}(\mathbf{q}_1; \mathbf{q}_2)}{\langle \hat{a}_{\mathbf{q}_1}^\dagger \hat{a}_{\mathbf{q}_1} \rangle \langle \hat{a}_{\mathbf{q}_2}^\dagger \hat{a}_{\mathbf{q}_2} \rangle} = \frac{\langle : n_{\mathbf{q}_1} n_{\mathbf{q}_2} : \rangle}{\langle n_{\mathbf{q}_1} \rangle \langle n_{\mathbf{q}_2} \rangle} \quad (5.46)$$

That takes the value of 1 when the two modes are not correlated.

In this manuscript when we refer to second-order correlation function, we will always mean normalised second-order correlation function.

In the previous section, we already discussed the fact that we can observe two types of correlations with our source:

- ▶ *local correlation*: when a mode is correlated with itself. These are the correlations that are probed during an HBT-like experiment [120, 178], where the correlation length is directly related to the inverse size of the BEC $\frac{1}{L}$. In our model, where our source produces a TMS state, each single mode taken alone should behave like a thermal state, and therefore thermal bosonic bunching: we expect the local correlations to reach the value $2! = 2$ (cf. Eq. (5.31a) and [71]).
- ▶ *nonlocal (or crossed) correlation*: when the two modes of a same pair are correlated. Eq. (5.31b) suggest that these correlations may be larger than 2, especially when the population is small.

[120]: Schellekens et al. (2005), “Hanbury Brown Twiss Effect for Ultracold Quantum Gases”

[178]: Mølmer et al. (2008), “Hanbury Brown and Twiss Correlations in Atoms Scattered from Colliding Condensates”

[71]: Liu et al. (2009), “Nth-Order Coherence of Thermal Light”

2.3.2 Second-order correlations: 2D map

The first analysis that we perform is the calculation and plotting of the complete $g^{(2)}(q_1, q_2)$, relative to the velocities along the vertical¹. This map exhibits both local and nonlocal correlations: its visualisation is given in Figure 5.13.

¹: for the simplicity of the notations we will for now drop the z index of the momenta, and write $q_1 \equiv q_z^1$ and $q_2 \equiv q_z^2$

The calculation of these correlations requires to set boxes (in the 3D momentum space) inside which we can count the number of atoms detected. The shape (and size) of these boxes play a crucial role: they have an averaging effect on the signal that we will quantify in a few paragraphs. For now, let us just remember that ideally we want boxes that are:

- ▶ narrow as compared to the modes’ size, along the direction in which we want to probe the correlations. We indeed want to be sensitive to the width of the correlations which is actually given by the size of the mode ;
- ▶ roughly fitting the size of the modes’ in the other two directions: so as to increase the signal to noise ratio (more atoms are detected), without reducing the amplitude of the signal too much because of the averaging effect of large boxes ;

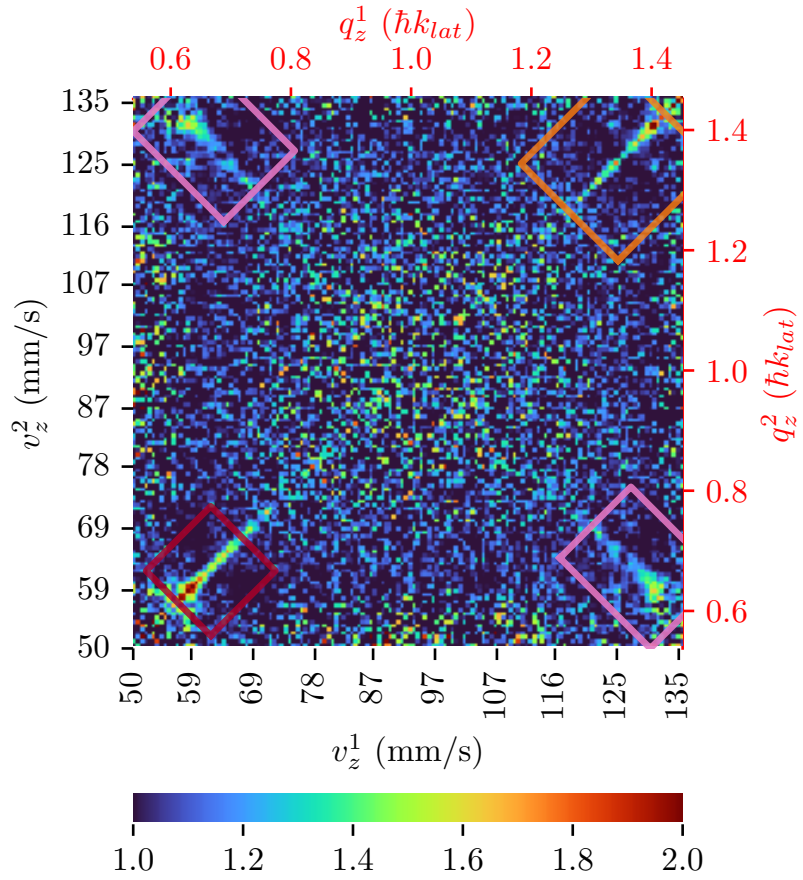
For each experimental realisation, we compute the following quantities

$$q_1, q_2 \in [0.54, 1.45] \hbar k_{lat} \quad \begin{cases} N(q_1) \times N(q_2) & \rightarrow 2D \text{ array} \\ N(q_1) & \rightarrow 1D \text{ list} \end{cases}$$

Figure 5.13: 2D map of the second-order correlation function, with regards to the v_z velocities. Each pixel corresponds to the $g^{(2)}(v_z^1; v_z^2)$ term, computed by counting the atoms falling in momenta boxes (with cylindrical shape) parametrised as such:

Centers:	\bar{v}_x	-40.5 mm s^{-1}
	\bar{v}_y	1.5 mm s^{-1}
	\bar{v}_z	v_z^i
Diameter:	$D_{x y}$	16.0 mm s^{-1}
Height:	Δv_z	0.6 mm s^{-1}

In this case, the centres of the boxes in the transverse direction are the same (this is not mandatory): that is why the line $v_z^1 = v_z^2$ is a symmetry axis of the graph. The local correlations are visible on the $v_z^1 = v_z^2$ diagonal line, while the crossed correlations are present on the $v_z^1 + v_z^2 = \text{cte} \approx 190 \text{ mm s}^{-1}$ anti-diagonal line. The red and orange boxes (containing local correlations) and the pink boxes (containing nonlocal correlations) delimit the domains used to compute the 1D graphs of Figure 5.14 and Figure 5.15.



where $N(q)$ is the number of atoms counted in a box centred on q_z . We can then calculate the average and the standard deviation of those quantities (over the files of the dataset), and compute the average values of the second-order correlation functions:

$$g^{(2)}(q_1, q_2 \neq q_1) = \frac{\langle N(q_1) N(q_2) \rangle}{\langle N(q_1) \rangle \langle N(q_2) \rangle} \quad (5.47a)$$

$$g_{loc}^{(2)}(q, q) = \frac{\langle N^2(q) \rangle - \langle N(q) \rangle}{\langle N(q) \rangle^2} \quad (5.47b)$$

i: with a usual quadratic propagation of the standard deviations of the different terms of the formula.

as well as the corresponding standard deviations¹.

The extra-term $\frac{-1}{\langle N(q) \rangle}$ in the local correlation case comes from the normal ordering in the definition of the second-order correlation function (cf. Eq. (5.45)): the commutation relations $[\hat{a}_q, \hat{a}_q^\dagger] = \mathbb{1}$ generates a shot noise term that must be subtracted.

Figure 5.13 displays the average values of $g^{(2)}$, but we are also able to give an error bar on each pixel of the map. We tested many choices of parametrisation for the boxes (sizes and centres on the transverse

plane), in order to reveal the correlations as clearly as possible. The dataset is not very big (802 files only) and the signal turns out to be very noisy when we try to use boxes that are “too small”: there is a balance that needs to be found between the signal to noise ratio, and the amplitude/resolution of the signal.

We will discuss the matter of the size of the modes in the next paragraph, but we can already say that the map plotted in Figure 5.13 uses cylindrical boxes, with a diameter approximately fitting the measured transverse modes’ size, and a height 2 times *smaller* than the longitudinal length of the modes, along the q_z direction. With this parametrisation, the statistics is good enough to see the local correlations (in the red and orange boxes), and also distinguish the crossed correlations (in the pink boxes).

2.3.3 1D analysis: correlation amplitude and modes’ width

To extract “more quantitative” information, we plot 1D data: the aim is to find the amplitude of the correlation, and the width of the modes.

Local correlations Concerning local correlations, the procedure is the same for each axis¹: we will detail it as an example for the q_z direction.

Both atomic beams are treated separately: we keep the same colour code (red for the first region, and orange for the second one), adopted since the beginning of this section, in particular in Fig. 5.9, Fig. 5.10 and more importantly Fig. 5.13. The data are restricted to a domain where preliminary visualisations revealed that the correlations are significantly out of the noise: in our example, the orange and red squares in Figure 5.13.

We know that the local correlations are maximised (and a priori equal to 2) when $\partial q = q_1 - q_2 = 0$: we therefore plot the data as a function of ∂q , which means that the data are averaged “along the diagonal direction”². The error bars on each pixel of Figure 5.13 are used to compute the error bars of the 1D plot.

Since more data are stacked in such a 1D projection, we can select smaller boxes, mitigating the averaging effect, and guaranteeing a sufficiently fine resolution to measure the correlation lengths³.

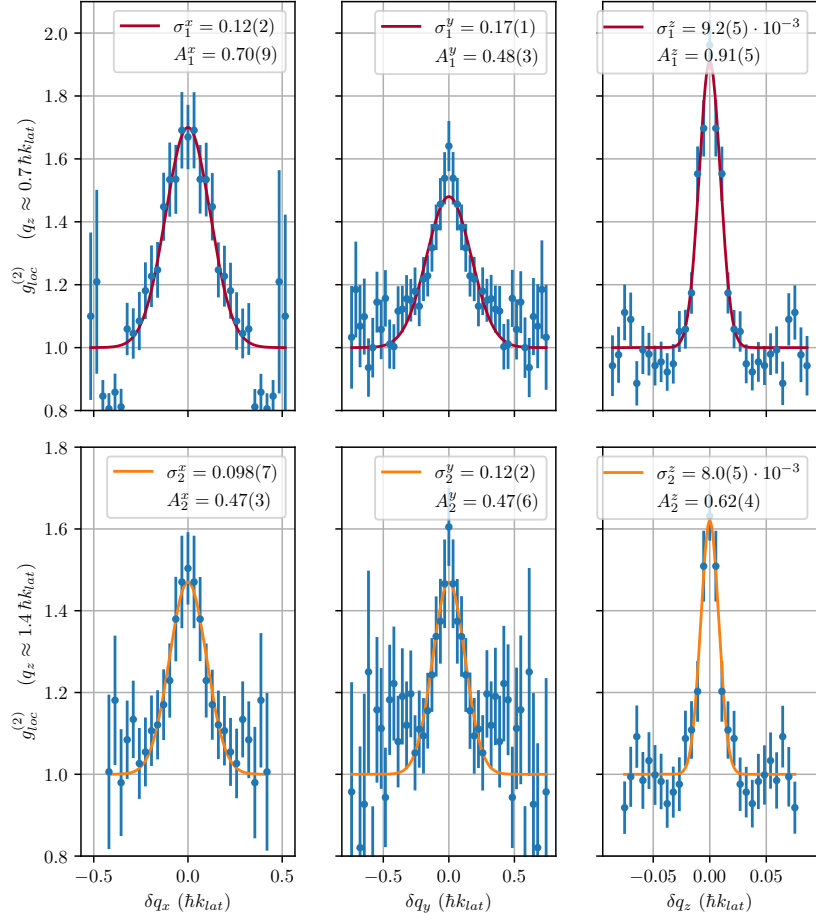
1: it just requires to adapt the shape of the boxes to keep a good resolution along the axis that we want to probe.

2: more formally the averaging is performed along lines of equation $q_1 - q_2 = k$, where k is a constant indexing the line.

3: in practice we tested different values of the box’s height Δv_z , to find the value starting from which the measured correlation length does not change, and we finally set Δv_z smaller than this, to have a security margin.

Figure 5.14: 1D local correlations as a function of the difference of quasi-momenta $\delta q = q_1 - q_2$. Boxes (used to compute the correlations) are rectangular shaped, with widths Δv_i chosen such that they are smaller than the natural width of the modes in the probed direction, and roughly fitting the natural width of the modes in the transverse directions:

$\mathbf{g}^{(2)}(\delta \mathbf{q}_z)$	Δv_z	0.5 mm s^{-1}
	Δv_\perp	8.0 mm s^{-1}
$\mathbf{g}^{(2)}(\delta \mathbf{q}_{x y})$	$\Delta v_{x y}$	3.0 mm s^{-1}
	Δv_z	4.0 mm s^{-1}
	$\Delta v_{y x}$	15.0 mm s^{-1}



The results are presented in Figure 5.14. The width σ_i^j and amplitude A_i^j are evaluated with gaussian fits:

$$i \in [1, 2], j \in [x, y, z] \quad / \quad g_{loc}^{(2)} \approx 1 + A_i^j e^{-\frac{(\delta q)^2}{2(\sigma_i^j)^2}} \quad (5.48)$$

are a direct measurement of the modes' size, up to a $\sqrt{2}$ factor.

These measurements are useful to evaluate the typical number of modes emitted, and the average number of atoms per mode, that we have already presented in Table 5.3 and Eq. (5.43) of the previous subsection.

The strength of the correlations can be evaluated with the amplitude parameter A of the fits. However, depending on the shape of the modes, the gaussian function may not always be perfectly adapted to fit the data: in particular one would notice that along the q_y direction, the fit is always smaller than the data around $\delta q_y = 0$, which is also the point where the correlations are the largest...

The fact that we do not always reach the value of 2 may be an averaging

effect, coming out of the size of the integration box. Indeed, let us consider a gaussian shape for the density of pairs (centred on $\mathbf{q} = 0$ for simplicity):

$$n(\mathbf{q}) = n_0 e^{-\frac{\sum_i q_i^2}{2\sigma_{n,i}^2}} \quad (5.49)$$

During the digital treatment of the data, the momentum space is discretised into boxes of volume $V_\Omega = \Delta q_x \Delta q_y \Delta q_z$, that we can index with $m_x, m_y, m_z \in \mathbb{Z}$ (let us say $m_x = m_y = m_z = 0$ corresponds to the box centred on $\mathbf{q} = 0$). The average number of atoms in the box (m_x, m_y, m_z) corresponds to the integration of the density of atoms in that box:

$$\langle N(m_x, m_y, m_z) \rangle = n_0 \prod_{i \in \{x,y,z\}} \int_{(m_i - \frac{1}{2})\Delta q_i}^{(m_i + \frac{1}{2})\Delta q_i} dq_i e^{-\frac{q_i^2}{2\sigma_{n,i}^2}} \quad (5.50)$$

Then, the definition of the second order correlation function is

$$g^{(2)}(\mathbf{q}, \delta\mathbf{q}) = \frac{\langle N_{\mathbf{q}} N_{\mathbf{q}+\delta\mathbf{q}} \rangle}{\langle N_{\mathbf{q}} \rangle \langle N_{\mathbf{q}+\delta\mathbf{q}} \rangle} \quad (5.51)$$

now if we work with our discretised quantities (let us consider $m_x = m_y = 0$ for simplicity), and if we add the expected profile of correlations (using the correlation width $\sigma_{cor,z}^z$ that we measured experimentally) we end up with:

$$g^{(2)}(m_z, m'_z) = \frac{\prod_{i \in \{x,y\}} \int_{-\frac{\Delta q_i}{2}}^{\frac{\Delta q_i}{2}} dq_i dq'_i \int_{(m_z - \frac{1}{2})\Delta q_z}^{(m_z + \frac{1}{2})\Delta q_z} dq_z \int_{(m'_z - \frac{1}{2})\Delta q_z}^{(m'_z + \frac{1}{2})\Delta q_z} dq'_z e^{-\frac{q_i^2 + q_i'^2}{2\sigma_{n,i}^2}} e^{-\frac{q_z + q_z'}{2\sigma_{n,z}^2}} e^{-\frac{q_z^2 - q_z'^2}{2\sigma_{cor,z}^2}}}{\text{same thing without the red term}} \quad (5.52)$$

We finally perform a final averaging (to consider 1D data):

$$g^{(2)}(\Delta m_z) = \langle g^{(2)}(m_z, m_z + \Delta m_z) \rangle_{m_z \in \mathbb{Z}} \quad (5.53)$$

We can do this type of calculation for each axis. Knowing the box sizes Δq_i that we used, the measured correlation width σ_i , and the width of the density of atoms, we can perform a numerical estimation of the “expected” amplitudes A_i^j that we should measure with this model, and compare it to the ones that we indeed measured: the results are gathered in Table 5.4.

Even if the matching is not perfect, the computed values are closer to the measured ones. An improvement of this treatment would consist in considering the raw experimental data for the density profile rather

Table 5.4: Comparison between the expected amplitude of the local correlations, and the ones measured and plotted in Figure 5.14. Notice that even the “expected” values make use of measured ones, due to the σ_i^j correlation width, that we assume to be independent of their amplitude.

A_i^j	Expected “averaged” value	Measured value
A_1^x	0.41	0.70(9)
A_1^y	0.39	0.48(3)
A_1^z	0.91	0.91(5)
A_2^x	0.34	0.47(3)
A_2^y	0.32	0.47(6)
A_2^z	0.86	0.62(4)

than a gaussian shape (resulting from its RMS size measurement).

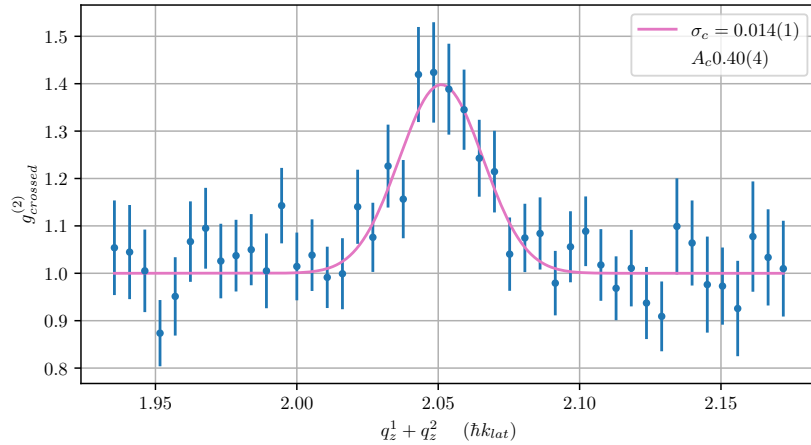
This study, at least, confirms our belief that the rather small amplitude that we measured may come from the size of the correlations boxes that we had to use, and that with a larger dataset we could compute the correlations with smaller boxes, and find a higher signal.

Crossed correlations We apply the same type of procedure to generate a 1D visualisation of the crossed correlations: experimental data are plotted in Figure 5.15.

Figure 5.15: 1D crossed correlations as a function of the sum of quasi-momenta $q_z^1 + q_z^2$. Rectangular boxes are used to compute the correlations, parametrised as such:

$\mathbf{g}^{(2)}(\delta\mathbf{q}_z)$	Δv_z	0.5 mm s^{-1}
	Δv_\perp	8.0 mm s^{-1}

The correlations are computed in the pink rectangular subset of Figure 5.13 (which one of the two pink rectangles does not matter since due to symmetry they contain the same data).



Regarding the data, there is no doubt that there is a nonlocal correlation. Its amplitude is however smaller than the local one. At first glance this is no good, because if we were dealing with a genuine TMS, we would expect to find the nonlocal correlation larger than the local ones (cf. Eq. (5.22c)).

However, we have already seen that the pair emission was operating in a regime where the average number of particles per mode ν is large (between 3 and 4). Therefore, the additional $\frac{1}{\nu}$ contribution to the correlation may be lost in the noise.

In addition to the fact that there is strong dependence of the amplitude of the crossed correlation with the shape, centres, and sizes of the boxes (which again could be improved with smaller boxes and better statistics), we could argue that even if the perturbative study (and previous experiments [62]) showed that it may be well described by a TMS, we do not know if it is still the case when the number of particles per mode is large. It is actually quite natural to think that when the number of particles increases, it is more and more difficult to prepare an entangled state (such as the TMS), and the level of nonlocal correlations could decrease.

Nevertheless, if we compare these values to similar measurements performed in the past on the experiment and documented in the thesis manuscripts of R. Lopes [8] and P. Dussarrat [90], they found crossed correlations with a peak amplitude of 1.2 to 1.3¹, which is even smaller than the correlations that we registered (1.4 ± 0.1).

It should also be noticed that the nonlocal correlation that we measured is larger than the local one: $\sigma_c \approx 1.8 \sigma_{local}$. This has a favourable effect for a potential Cauchy-Schwarz inequality violation. Indeed, even though a simple calculation shows that violating the Cauchy-Schwarz inequality *implies* that the local correlation is smaller than the nonlocal one, it is possible to consider another version of the inequality taking into account the “volume” of the correlations (i.e. the width of above graphs) [2]. We have not yet completed this study with our recent data.

2.4 Emission statistics

We can finally study the statistics of the number of atoms collected in boxes, who should be slightly smaller than the natural modes. This is a similar study as the one published in [62].

If the state emitted by the source –and restricted to regions where the boxes are placed– is indeed a two-mode squeezed state, then the statistics of each mode should follow a thermal law (cf. Chapter 1):

$$P(N) = \frac{1}{1+\nu} \left(\frac{\nu}{1+\nu} \right)^N \quad (5.54)$$

In logarithmic scale, it gives a straight line, whose slope is related to the population.

In the graphs of figure Figure 5.16 and Figure 5.17 we have plotted these

[62]: Perrier et al. (2019), “Thermal Counting Statistics in an Atomic Two-Mode Squeezed Vacuum State”

[8]: Lopes (2015), “An Atomic Hong-Ou-Mandel Experiment”

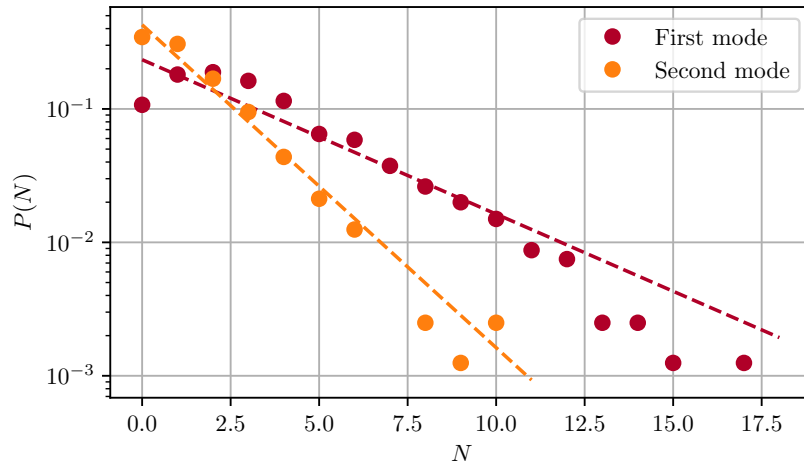
[90]: Dussarrat (2017), “Expériences d’Optique Atomique Quantique, Interféromètres à 2 et 4 modes”

¹: with also larger correlation boxes in the case of the results presented by P. Dussarrat.

[2]: Kheruntsyan et al. (2012), “Violation of the Cauchy-Schwarz Inequality with Matter Waves”

[62]: Perrier et al. (2019), “Thermal Counting Statistics in an Atomic Two-Mode Squeezed Vacuum State”

Figure 5.16: Counting statistics of the two modes emitted by the source. Here the boxes are the same as in Figure 5.11, meaning that the box used to compute the statistics of the first mode is larger than the one used for the second mode. The dashed lines represent the thermal probability law $P_{th}(N) = \frac{1}{1+\nu_m} \left(\frac{\nu_m}{1+\nu_m}\right)^N$, where ν_m is computed by counting the total number of atoms in the box: there is no fitting parameter. Even though the data of the second mode fit pretty well the theoretical thermal law, it not the case for the first mode. In particular, there is a discrepancy when N is either very large or very small: the shape of the red data points is reminiscent of a Poissonian distribution, that is expected to occur when several modes are mixed in the same box.



date, and we compare it with the thermal power law with a parameter ν_m that is the measured averaged number of particles in the box: it is not a fitting parameter.

In Figure 5.16 we used the same boxes as in Figure 5.11: their sizes are given by the correlation lengths¹ that we measured in Subsection 2.3.3. In the case of the “first mode” (which is the brightest: located in $q_z \approx 0.66$) we can see a non-thermal behaviour when $N \lesssim 4$. This profile is studied in [62], and it is the signature of the fact that the box that is used to compute counting statistics is too large, as compared to the natural size of the mode. Just like what we did for Figure 5.12, we replot the same graph but this time using boxes of the same size (the smaller one). We find a much better agreement with the theoretical thermal law for of probabilities. Since there is no fitting, this fairly good match between the data and the expected thermal profile is a solid argument for stating that our state is indeed a TMS.

Remark 5.3 Let us highlight the fact that the study of the emission statistics is a useful tool to check that the boxes chosen for the numerical analysis of the data are small enough.

If a the box is too large, the statistics exhibits a profile that looks like a Poissonian distribution².

1: up to a $\sqrt{2}$ factor.

2: the reference [62] shows that it actually intermediate between a thermal and a Poisson distribution.

With a larger data set, we could extend this type of analysis, by computing the joint counting statistics, and compare it to the expected model, for which I derived an analytical formula (cf. Equation 1.105 on

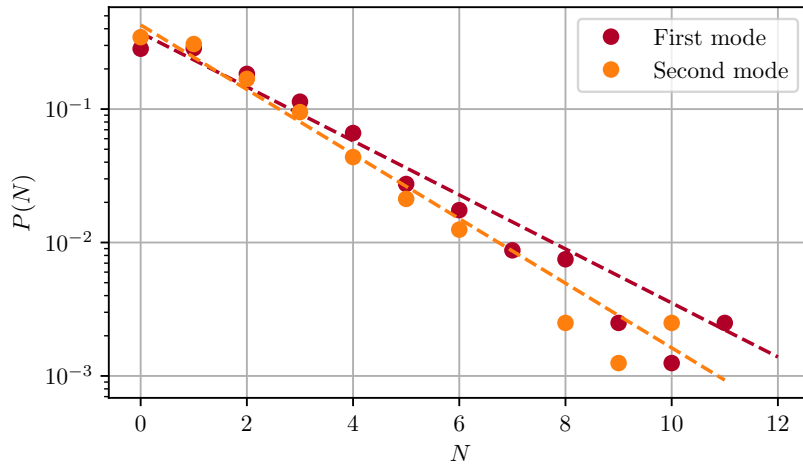


Figure 5.17: Same graph as in Figure 5.16, except that now the boxes in which the statistics is computed have the same size for both modes. We used the same box as in Figure 5.12, whose size in $\hbar k_{lat}$ units is:

Δq_x	0.14
Δq_y	0.17
Δq_z	0.011

The power laws fits the data pretty well.

page 49).

Conclusion

In this chapter we have exposed the most important results that we obtained during my PhD. These data were acquired between april and june 2022: the only three month during which it was possible to generate correlated pairs. Indeed, our progresses were stopped by the death of the laser used for the optical dipole trap (at the beginning of july), and also by the breakdown of a part of the high current electrical system, that we use during the MOT and the magnetic trap¹ (since august).

¹: the watercooling system used for the IGBT became deficient, and several IGBT modules died due to overheating. In addition one of our high power PSU (used during the magnetic trap) now switches off randomly, in middle of the experimental realisations. Finally we faced in october vacuum issues (at the very start of the apparatus: where the room temperature helium is injected).

Nonetheless, with these data we showed that our atomic source presents interesting correlations properties, that could be use advantageously in upcoming experiments. Let us do a very short summary of what is known about our source:

What was already known before my PhD?

- ▶ the statistics of emission for the two modes of a pair was studied in 2019 (but using a dataset acquired in 2016), in a regime where the average population per mode were small: $\eta\nu \approx 0.158$ [62]. A thermal statistics was found, which is indeed expected with a TMS state ;
- ▶ again in this regime where ν is small, nonlocal correlations were witnessed during the PhDs of R. Lopes and P. Dussarrat [59, 90]. A violation of the Cauchy-Schwarz inequality was even observed in [59], which is the signature of strong correlations.
- ▶ a preliminary experiment of two particle interferometry [9] exhibited a two-particle correlator² $E \neq 0$. This result is extremely promising: indeed, let us recall the state that we want to use in the Bell inequality violation experiment reads:

$$\left[\sqrt{1 - |\alpha|^2} \sum_{n=0}^{\infty} \alpha^n |n\rangle_p |n\rangle_{-p} \right] \otimes \left[\sqrt{1 - |\beta|^2} \sum_{n=0}^{\infty} \beta^n |n\rangle_q |n\rangle_{-q} \right]$$

$|\alpha|$ and $|\beta|$ are related to density of pairs that are generated, that are known to be stable during an experiment. However, we have a priori no clue about the relative phase $\arg\left[\frac{\alpha}{\beta}\right]$ between these two TMS. If this phase was shot-to-shot fluctuating, in a Rarity-Tapster experiment the correlator E would always be 0, killing any hope of witnessing a Bell inequality violation. In [9] a correlator $E \approx 0.6$ was measured, indicating that the variations of $\arg\left[\frac{\alpha}{\beta}\right]$ are not too problematic.

[62]: Perrier et al. (2019), “Thermal Counting Statistics in an Atomic Two-Mode Squeezed Vacuum State”

[59]: Lopes et al. (2015), “Atomic Hong–Ou–Mandel Experiment”

[90]: Dussarrat (2017), “Expériences d’Optique Atomique Quantique, Interféromètres à 2 et 4 modes”

[9]: Dussarrat et al. (2017), “Two-Particle Four-Mode Interferometer for Atoms”

²: we refer here to the correlator that is used in a Rarity-Tapster experiment.

What is new?

We explored a regime where the populations are approximately 10 times larger than before. In particular we checked that:

- ▶ each of the two modes have the expected properties of a thermal state, in particular:
 - the bosonic bunching ($g^{(2)}(0) = 2$) when we probe the local correlations ;
 - a thermal counting statistics ;
- ▶ we find non-zero crossed correlation between both mode, even if we did not yet find a quantum signature of this correlation (such as the violation of the Cauchy-Schwarz inequality).

What do we want to do next?

Concerning the study of the source, when the experiment will be running again, we would like to acquire dataset so as to:

- ▶ obtain the full joint counting statistics: i.e. $P(N_1, N_2)$ and compare it to the model that has been derived in [Chapter 1](#) ;
- ▶ use smaller boxes for the computation of the correlations, and try to find a situation where the nonlocal correlations are larger than the local ones. This could lead to the violation of the Cauchy-Schwarz inequality, and therefore reveal some quantumness in the state that we generate.

General conclusion

Even if during my PhD several evolutions of our apparatus and software platform have led to the obtention of promising results (cf. [Chapter 5](#)), the scientific goals that were set seven years ago have not yet been achieved. Indeed, after the successful obtention of the atomic HOM effect [[59](#)], it was decided that a Bell inequality test would be the next natural field to explore with our experimental platform. Indeed, the microchannel plate offers the remarkable opportunity to extract information on the mechanical state of single massive particles. This could pave the way towards the study of the interplay between gravitation and entanglement. Such a study would obviously be extremely interesting, given the well-known difficulties that modern physics encounters to integrate gravitation in a quantum framework. A violation of Bell inequalities would also constitute a first milestone before trying to prepare quantum entangled states with more particles, which a microchannel plate should also be able to probe *a priori*.

In this quest, a preliminary result was obtained in 2017 [[9](#)]; at this time it was however not possible to measure a Bell parameter, because there was no active control of the phase difference between *Alice*'s interferometer and *Bob*'s one¹ (cf. [Chapter 2](#) for more explanation about the interferometric setup). Implementing two independent Bragg pulses, and obtaining the control on this phase difference is the next step. Unfortunately —as it has been explained in [Chapter 4](#)— in the last five years, technical issues have considerably slowed down our progress, and forced us to work on aspects of the experiments that were achieved for the most part more than ten years ago.

Lacking scientifically new experimental material to present, this manuscript therefore aims at meeting different objectives. One of those is setting a reference point concerning the current status of the experiment. Indeed, in the last few years, many experimental procedures have evolved, or have been replaced: I provided in [Chapter 3](#) and [Chapter 4](#) as much technical detail about it as possible.

Another objective was to offer some food for thought on other possible experiments that we could conduct when the platform is ready (cf. [Chapter 1](#)). I cannot claim that the theoretical work about the n -particle HOM physics is over, as I have not yet found the striking signature of a many-body quantum effect with it. To this end, an interesting field to explore (and that I did not consider in this manuscript) could be

[59]: Lopes et al. (2015), “Atomic Hong–Ou–Mandel Experiment”

[9]: Dussarrat et al. (2017), “Two-Particle Four-Mode Interferometer for Atoms”

¹: actually, the final beam splitters of both “Mach-Zehnder” interferometers were realised by *the same* Bragg pulse.

the study of n^{th} -order correlation functions $G^{(n)}$: after all, if the $G^{(2)}$ function contains the trace of the quantum two-particle HOM effect, is it not natural to imagine that $G^{(n)}$ could contain a similar trace, for a situation in which the number of particles is larger?

The last element that I have attempted to clarify in this manuscript is the description of the Bell inequality test experiment that we still aspire to achieve, and to provide a methodology for data processing (cf. [Chapter 2](#)). However, information on this work is not exhaustive here: the numerical study of the effect of Bragg deflectors and beam splitters, as well as their concrete implementation with our hardware, are indeed of primary importance. This work should be presented in the upcoming manuscript of Charlie Leprince.

Regarding the recent progress that we have made in the last six months, one can venture to be optimistic about what will happen in the upcoming few months. Indeed, apart from recent breakdowns, we have reached a state that is close to that of the experiment back in 2017. Essentially, the last part that we still need to set up is the Bragg diffraction lattice: we are currently working on it. At last, once this final aspect of the experiment will be sorted out, we should be able to go on, and realise the experiments that have been put on hold for so long.

APPENDIX

Appendices' table of contents

A. Raman lattice	215
B. Imaging camera settings	217
C. Magnetic trap	219
1 Coils and IGBT setup	219
2 Bias measurements and calibration	220
D. Blueprints	223
• Bibliography	227
• List of Terms	243

A

Raman lattice

Quality control of the Raman transfer can be made by looking at the Rabi oscillations between the two magnetic sublevels, by scanning the duration of application of the Raman lattice. Previously in the experiment, it was only possible to look at the $m_J = 0$ atoms with the MCP (cf. Figure A.2). We recently found out that it is now also possible to observe the oscillations with the fluorescence, with a cold thermal cloud, intensifying the spatial separations between the two clouds by pushing the $m_J = 1$ atoms with a small magnetic gradient (cf. Figure A.1).

The expected effective two-photon Rabi frequency Ω_R^{eff} is easy to estimate, knowing the powers $P_{1/2}$ of the beams and the small detuning δ defined in Figure 4.5. The peak intensity of the gaussian beam is given by

$$I_0 = \frac{2P}{\pi \bar{w}^2} \quad (\text{A.1})$$

where \bar{w} is the geometric mean of the waist (considering a slightly elliptical beam). Then, Ω_R^{eff} can be expressed with Ω_R^{1pb} and Ω_R^{2pb} , respectively the one-photon and two-photon angular Rabi frequencies:

$$\left\{ \begin{array}{l} \Omega_R^{1pb} = \Gamma \sqrt{\frac{I_0}{2I_s}} \times \frac{1}{\sqrt{3}} \end{array} \right. \quad (\text{A.2a})$$

$$\left\{ \begin{array}{l} \Omega_R^{2pb} = \frac{\Omega_R^{1pb}(\sigma^-) \Omega_R^{1pb}(\pi)}{2\pi \times \Delta} \end{array} \right. \quad (\text{A.2b})$$

$$\left\{ \begin{array}{l} \Omega_R^{\text{eff}} = \sqrt{(2\pi \times \delta)^2 + (\Omega_R^{2pb})^2} \end{array} \right. \quad (\text{A.2c})$$

where $\frac{1}{\sqrt{3}}$ is a Clebsch–Gordan coefficient, and we considered detunings defined in hertz, as in Figure 4.5.

When conducting the experiment, we find out that we need to take into account a power loss coefficient to fit the theoretical law (cf. Figure A.3). This is probably due to a small imperfection of the polarisation of the beams (implied by their geometrical orientations) and the absence of anti-reflective coating, but this is not really an issue for us, as we can

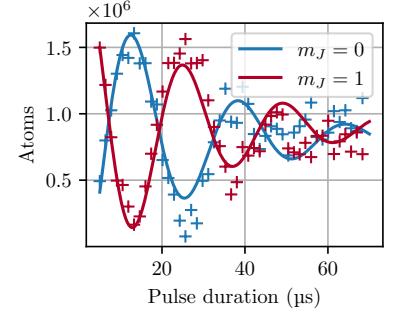


Figure A.1: Rabi oscillations of the Raman coupling, observed with fluorescence imaging.

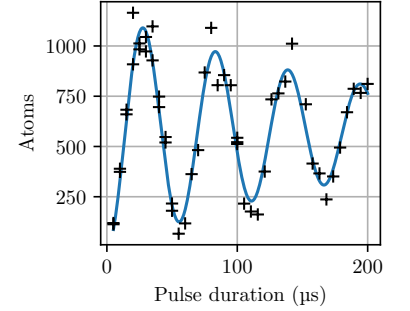
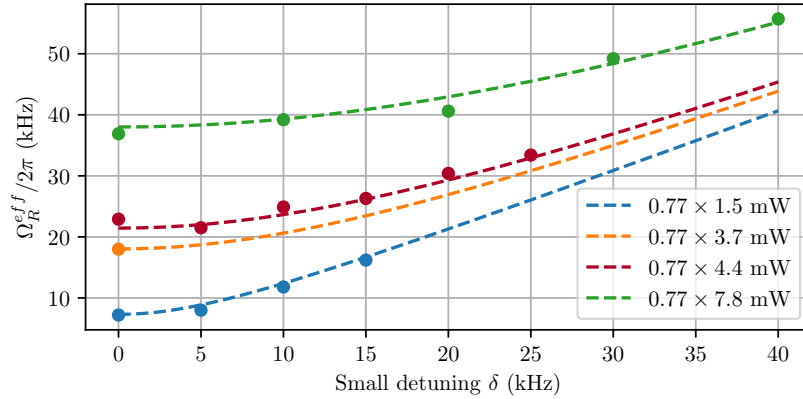


Figure A.2: Rabi oscillations of the Raman coupling, observed with the MCP.

Figure A.3: Two-photon Rabi frequencies, for different powers and detuning of the Raman beams. The coloured dots are experimental measurements, and the dashed lines are given by Eq. (A.2), considering that only 77% of the beams' power is available for the atoms: the absence of anti-reflective coating on this viewport, and polarisation imperfections because of the angle of the beams with respect to the direction of the magnetic bias may explain this loss.



easily compensate this by increasing the overall power.

However we are still a bit puzzled with the damping of the Rabi oscillations over time (cf. Figure A.1, Figure A.2). I performed numerical simulations, taking into account the gaussian repartition of the intensity of the beams¹, the light shift with the Stark effect, and the spatial repartition of the cloud's density (with a Thomas-Fermi profile for example): I could not reproduce a damping of the oscillations on the observed timescale ($\sim 100 \mu\text{s}$). The damping is reproducible by adding a magnetic gradient, which is a reasonable hypothesis.

¹: that induces a spatial dependence of the Rabi frequency.

B

Imaging camera settings

We use a Xenics[®] Xeva 320 series short-wave infrared camera for fluorescence imaging. This camera generates a PNG file (in greyscales) out of the number of photons received during a given integration time. The complete chain of conversion for fluorescence imaging is given in Figure B.1.

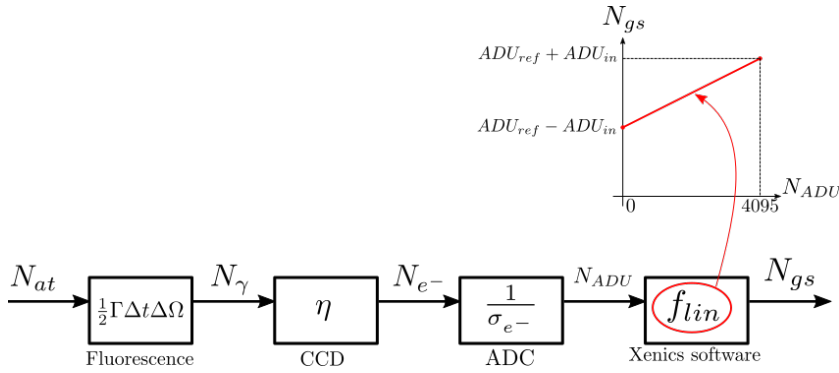


Figure B.1: Chain of conversions for fluorescence imaging: from a number of atoms to the greyscales of a PNG file

Where

- N_{at} : initial number of atoms
- N_γ : number of scattered photons collected by the lens
- N_{e^-} : number of electrons induced in the sensor
- N_{ADU} : output value of the analog to digital converter
- N_{gs} : grayscale value on a pixel of the image.
- Γ : linewidth = $2\pi \times 1.62$ MHz
- Δt : exposure time = 200 μs
- $\Delta\Omega$: solid angle = $2.5 \cdot 10^{-3}$ str²
- η : quantum efficiency ~ 0.7
- σ_{e^-} : electron sensitivity of the ADC = $45.7e^- / ADU$ ³
- f_{lin} : linear rescaling function applied by the Xenics software.

²: for the 2" lens 250 mm away from the atoms.

³: in low gain mode ($915e^- / ADU$ otherwise).

The final data is a 16bits PNG file: a matrix of grayscale (N_{gs}) numbers. Beware: a PNG cannot contain negative values (it will be written as a 0) and while writing the PNG file, we can choose either of the two endianness convention \rightarrow right-writting must be chosen for backward compatibility with our data analysis softwares.

ADU_{ref} and ADU_{in} parameters can be manually chosen in the Xenics controller: $ADU_{ref} = ADU_{in} = 2048$ is a wise choice...

Numerically, the usual constant of conversion from greyscales to atoms (with above values) is $K \approx 93$ atoms/gs

C

Magnetic trap

1 Coils and IGBT setup

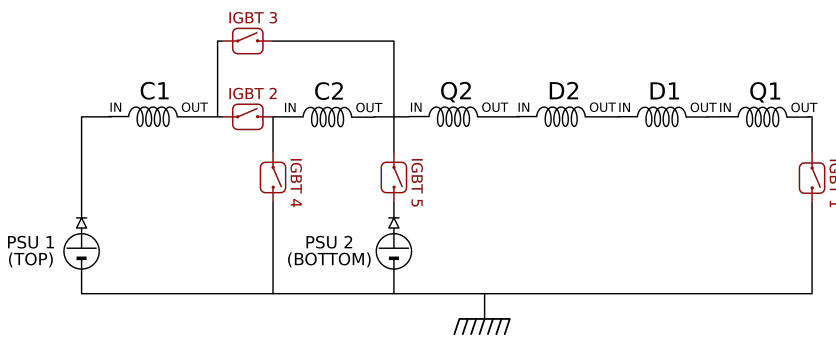


Figure C.1: General electrical network of the Ioffe-Pritchard magnetic trap. We have the individual control of the five IGBTs. We use Semikron[®] IGBTs: SKM 500GA124D (IGBT 1 and 2) and SKM 500GA124D (IGBT 3, 4 and 5). When an IGBT is closed, the typical voltage between the collector and the emitter is 1 to 2 V, for a current of 200 A. Both PSUs are 5 kW Hewlett-Packard[®] model 6682A (21 V 240 A), with a relative current ripple measured to be in the order of a few 10^{-5} .

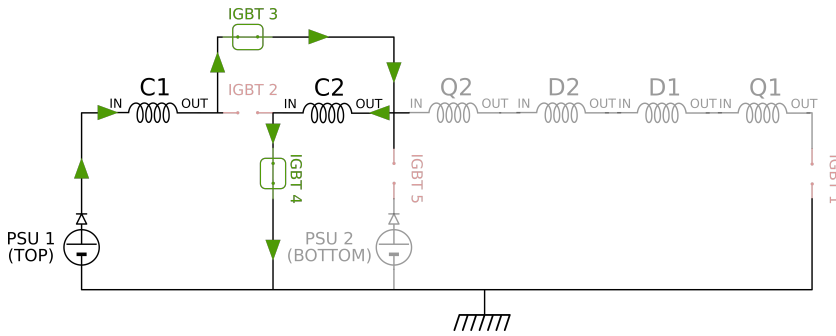


Figure C.2: MOT configuration of the IGBTs circuit. Only the “compensation” coils (C1, C2) are used, in anti-Helmholtz configuration, with a current of 225 A.

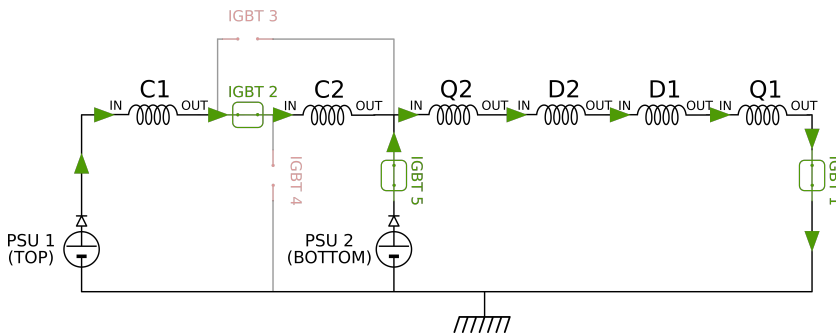


Figure C.3: MT configuration of the IGBTs circuit. The current in PSU1 is set to 198 A, and the current of PSU2 depends on the level of compression we want to achieve: 210 A for the uncompressed gas, 48 A during the Doppler cooling phase, and ~ 18 A for the final compression during the RF evaporative cooling phase.

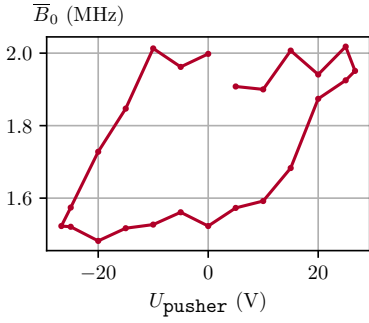


Figure C.4: We noticed the field generated by the “pusher” coil (used to remove the atoms in the $m_j = 1$ magnetic sublevel after the Raman transfer) can change magnetisation of the science chamber’s surroundings. This coil is in voltage control (legacy reason), and we tried to apply a 400 ms magnetic pulse between successive bias measurement experiments. It revealed a characteristic hysteresis cycle, exhibiting the presence of a residual magnetisation field. Expressed in the frequency domain, we typically find $\bar{B}_{\text{offset}} \sim 200$ kHz.

2 Bias measurements and calibration

The bias B_0 of the trap is generated by the “compensation” (C1, C2) and “dipole” (D1, D2) pairs of coils. The numbers of turns in these pairs of coils, with respect to their diameters, was chosen such that the bias propagated by the couple (C1, C2) should exactly compensate the bias created by the couple (D1, D2): meaning that when PSU2 is turned off, and all the coils have the same current flowing through them (cf. Figure C.3), the bias should be zero.

In practice, it is very difficult to achieve this: the fields created by (C1, C2) and (D1, D2) are large, and their compensation is extremely sensitive to the geometrical structure. Denoting $i_{\text{TOP}}/i_{\text{BOT}}$ the current generated by the top/bottom PSU, and β_C/β_D the first order coefficients for the dependence of the bias with the current in the compensation/dipole coils (linear approximation), we therefore have the following relations (expressed in frequency units):

$$\bar{B}_0 = \beta_C i_{\text{TOP}} + \beta_D (i_{\text{TOP}} + i_{\text{BOT}}) + \bar{B}_{\text{offset}} \quad (\text{C.1})$$

$$= \underbrace{(\beta_C + \beta_D)}_{\text{small}} i_{\text{TOP}} + \beta_D i_{\text{BOT}} + \bar{B}_{\text{offset}} \quad (\text{C.2})$$

where \bar{B}_{offset} is an additional contribution that results from the magnetisation of the surroundings (in the order of a few hundreds of kilohertz: cf. Figure C.4). The measurements of these coefficients are given in Figure C.5.

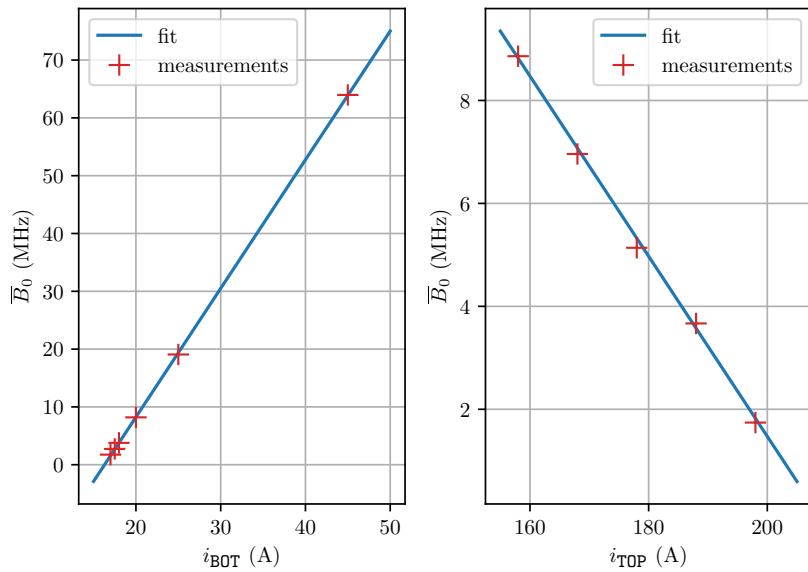


Figure C.5: Calibration of the bias \bar{B}_0 in MHz as a function of the current in the two PSUs. Calibration done after the overheating episode of October 2020. The first graph is obtained with a constant current $i_{\text{TOP}} = 198$ A on the left and gives $\beta_D = 2.226$ MHz A $^{-1}$. The second graph on the right is obtained with a constant current $i_{\text{BOT}} = 17$ A and gives $\beta_C + \beta_D = -0.175$ MHz A $^{-1}$. These slopes are rather stable, however the current i_{BOT}^0 corresponding to the zero bias is quite prone to change (in the range of 11 A to 16 A).

The bias to trapping frequency relation (Eq. (3.44)) is always valid, and

involves the same Λ constant. It is the current to bias relation that may vary with time (or some “mechanical” event such as the disassembly/re-assembly of the coils), in particular the zero-bias current. But when we witness a shift of the bias, we can always find a new value of the compression current to retrieve the same trapping conditions.

D

Blueprints

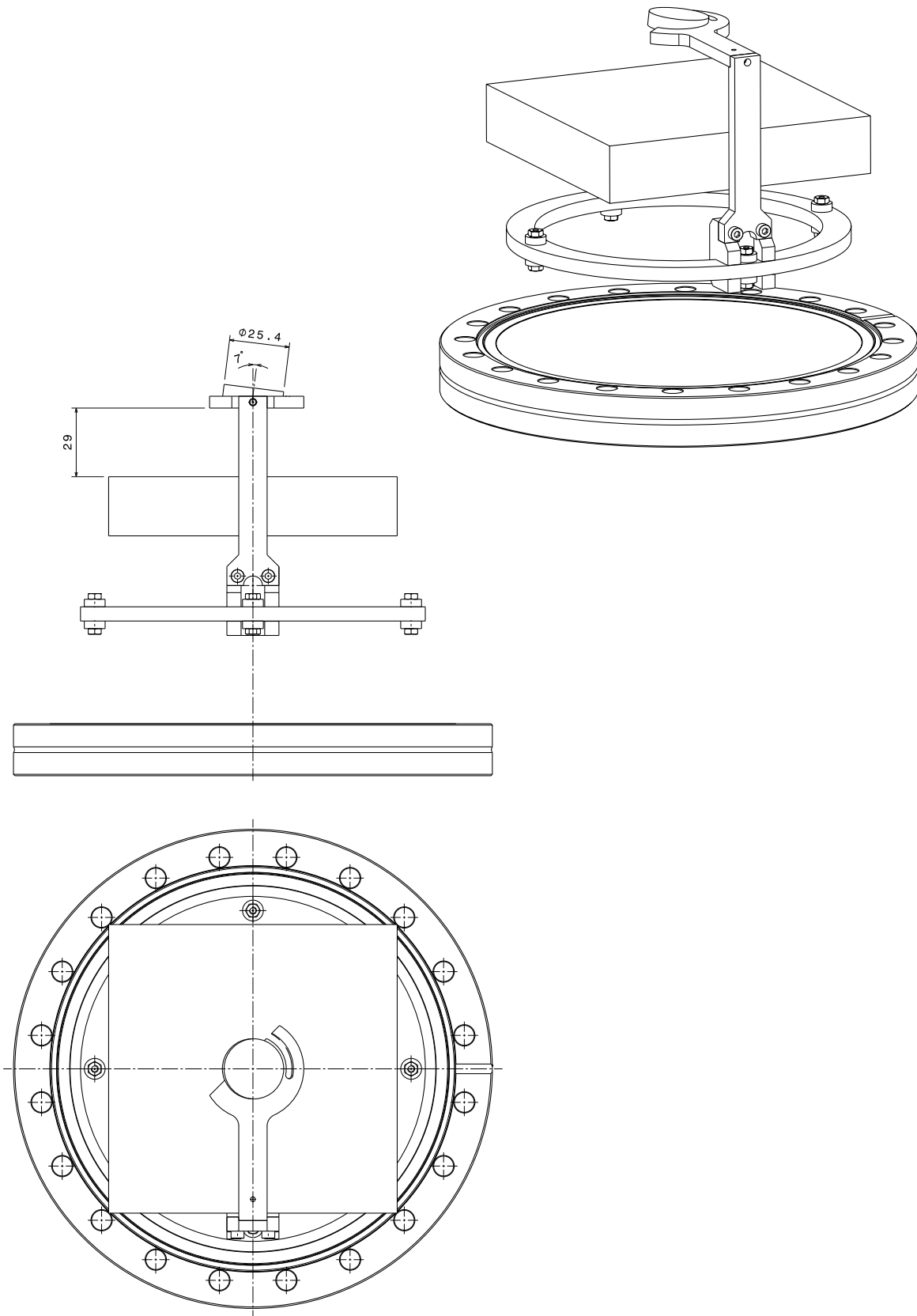


Figure D.1: Blueprint of the protective copper plate. Design by M. Jean-René Rullier, IOGS design office.

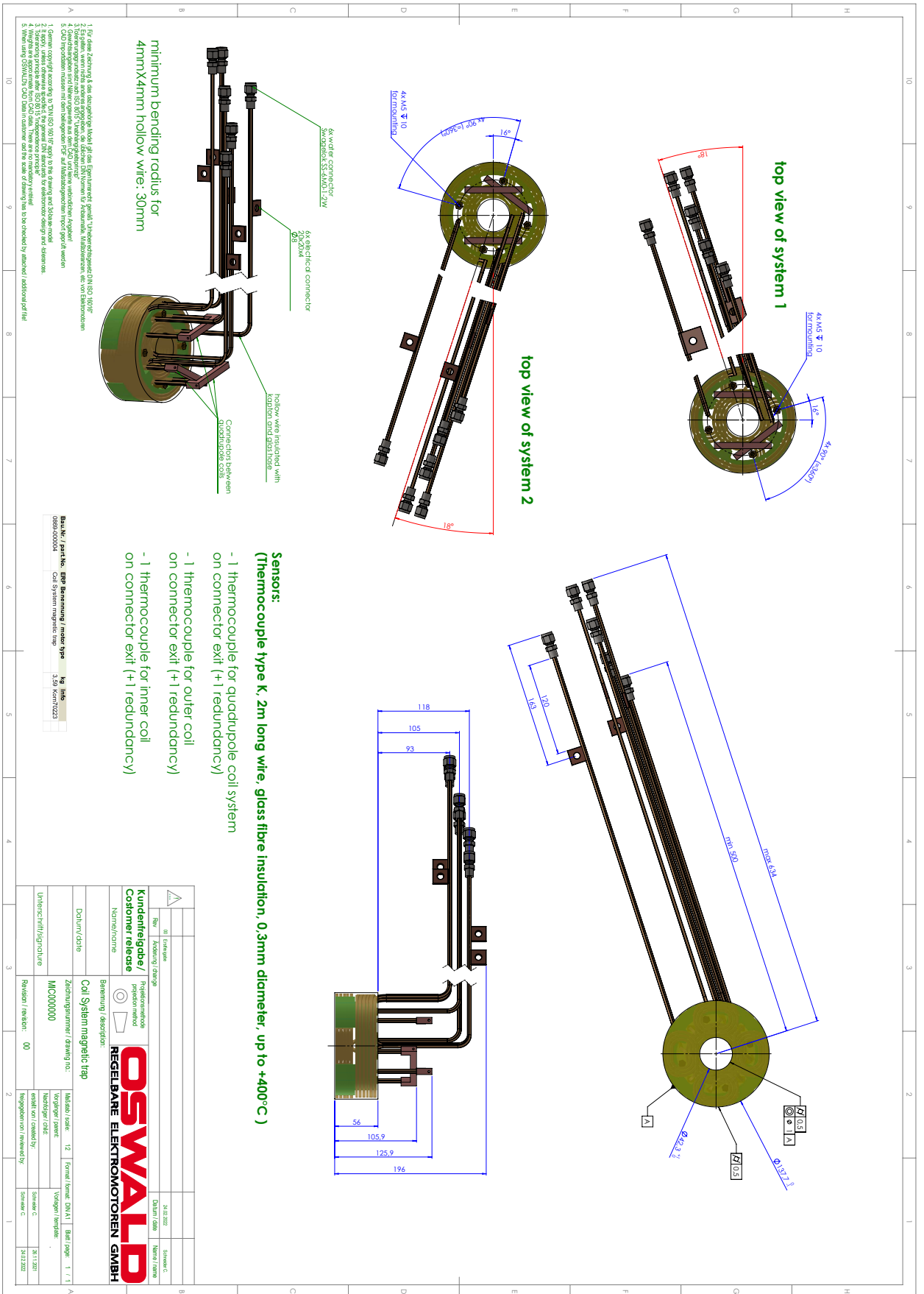


Figure D.2: Blueprint of the new Oswald® clusters of coils.

Bibliography

Here are the references in citation order.

- [1] M. D. Reid and D. F. Walls. “Violations of Classical Inequalities in Quantum Optics.” In: *Physical Review A* 34.2 (Aug. 1, 1986), pp. 1260–1276. DOI: [10.1103/PhysRevA.34.1260](https://doi.org/10.1103/PhysRevA.34.1260) (cited on pages vii, 6).
- [2] K. Kheruntsyan, J.-C. Jaskula, Piotr Deuar, Marie Bonneau, Guthrie Partridge, Josselin Ruaudel, Raphael Lopes, Denis Boiron, and Christoph Westbrook. “Violation of the Cauchy-Schwarz Inequality with Matter Waves.” In: *Physical Review Letters* 108 (Mar. 2012). DOI: [10.1103/PhysRevLett.108.260401](https://doi.org/10.1103/PhysRevLett.108.260401) (cited on pages vii, 6, 203).
- [3] Igor V. Volovich. “Cauchy–Schwarz Inequality-Based Criteria for the Non-Classicality of Sub-Poisson and Antibunched Light.” In: *Physics Letters A* 380.1-2 (Jan. 2016), pp. 56–58. DOI: [10.1016/j.physleta.2015.09.011](https://doi.org/10.1016/j.physleta.2015.09.011) (cited on pages vii, 6).
- [4] Tomasz Wasak, Piotr Szańkowski, Marek Trippenbach, and Jan Chwedeńczuk. “Cauchy–Schwarz Inequality for General Measurements as an Entanglement Criterion.” In: *Quantum Information Processing* 15.1 (Jan. 2016), pp. 269–278. DOI: [10.1007/s11128-015-1181-z](https://doi.org/10.1007/s11128-015-1181-z) (cited on pages vii, 6).
- [5] A. Perrin, H. Chang, V. Krachmalnicoff, M. Schellekens, D. Boiron, A. Aspect, and C. I. Westbrook. “Observation of Atom Pairs in Spontaneous Four-Wave Mixing of Two Colliding Bose-Einstein Condensates.” In: *Physical Review Letters* 99.15 (Oct. 12, 2007), p. 150405. DOI: [10.1103/PhysRevLett.99.150405](https://doi.org/10.1103/PhysRevLett.99.150405) (cited on pages vii, 6, 174, 176).
- [6] J.-C. Jaskula, G. B. Partridge, M. Bonneau, R. Lopes, J. Ruaudel, D. Boiron, and C. I. Westbrook. “Acoustic Analog to the Dynamical Casimir Effect in a Bose-Einstein Condensate.” In: *Physical Review Letters* 109.22 (Nov. 26, 2012), p. 220401. DOI: [10.1103/physrevlett.109.220401](https://doi.org/10.1103/physrevlett.109.220401) (cited on pages vii, 6, 174).
- [7] M. Bonneau, J. Ruaudel, R. Lopes, J.-C. Jaskula, A. Aspect, D. Boiron, and C. I. Westbrook. “Tunable Source of Correlated Atom Beams.” In: *Physical Review A* 87.6 (June 17, 2013), p. 061603. DOI: [10.1103/PhysRevA.87.061603](https://doi.org/10.1103/PhysRevA.87.061603) (cited on pages vii, 6, 174, 177, 190, 195).
- [8] Raphael Lopes. “An Atomic Hong-Ou-Mandel Experiment.” PhD thesis. Laboratoire Charles Fabry: Institut d’Optique Graduate School, Apr. 29, 2015. 182 pp. (Visited on 07/19/2022) (cited on pages vii, 6, 22, 84, 140, 144, 186, 187, 203).
- [9] Pierre Dussarrat, Maxime Perrier, Almazbek Imanaliev, Raphael Lopes, Alain Aspect, Marc Cheneau, Denis Boiron, and Christoph I. Westbrook. “Two-Particle Four-Mode Interferometer for Atoms.” In: *Physical Review Letters* 119.17 (Oct. 24, 2017), p. 173202. DOI: [10.1103/PhysRevLett.119.173202](https://doi.org/10.1103/PhysRevLett.119.173202) (cited on pages vii, 6, 148, 149, 195, 206, 209).

- [10] Roger Penrose, A. Ekert, and R. Jozsa. “Quantum computation, entanglement and state reduction.” In: *Philosophical Transactions of the Royal Society of London. Series A: Mathematical, Physical and Engineering Sciences* 356.1743 (1998), pp. 1927–1939. DOI: [10.1098/rsta.1998.0256](https://doi.org/10.1098/rsta.1998.0256) (cited on pages viii, 6).
- [11] Max Tegmark. “The Interpretation of Quantum Mechanics: Many Worlds or Many Words?” en. In: *Fortschritte der Physik* 46.6-8 (Nov. 1998), pp. 855–862. DOI: [10.1002/\(SICI\)1521-3978\(199811\)46:6/8<855::AID-PROP855>3.0.CO;2-Q](https://doi.org/10.1002/(SICI)1521-3978(199811)46:6/8<855::AID-PROP855>3.0.CO;2-Q) (cited on page 2).
- [12] Franck Laloë. “Comprenons-nous vraiment la mécanique quantique ?” In: 2011 (cited on page 2).
- [13] A. Einstein, B. Podolsky, and N. Rosen. “Can Quantum-Mechanical Description of Physical Reality Be Considered Complete?” en. In: *Physical Review* 47.10 (May 1935), pp. 777–780. DOI: [10.1103/PhysRev.47.777](https://doi.org/10.1103/PhysRev.47.777) (cited on pages 2, 69).
- [14] N. Bohr. “Can Quantum-Mechanical Description of Physical Reality be Considered Complete?” en. In: *Physical Review* 48.8 (Oct. 1935), pp. 696–702. DOI: [10.1103/PhysRev.48.696](https://doi.org/10.1103/PhysRev.48.696) (cited on page 2).
- [15] John S. Bell. “On the Einstein Podolsky Rosen paradox.” en. In: *Physics Physique Fizika* 1.3 (Nov. 1964), pp. 195–200. DOI: [10.1103/PhysicsPhysiqueFizika.1.195](https://doi.org/10.1103/PhysicsPhysiqueFizika.1.195) (cited on pages 3, 72).
- [16] D. Bohm. *Quantum theory*. Dover books on physics series. Dover Publications, 1951 (cited on page 3).
- [17] John F. Clauser, Michael A. Horne, Abner Shimony, and Richard A. Holt. “Proposed Experiment to Test Local Hidden-Variable Theories.” en. In: *Physical Review Letters* 23.15 (Oct. 1969), pp. 880–884. DOI: [10.1103/PhysRevLett.23.880](https://doi.org/10.1103/PhysRevLett.23.880) (cited on pages 3, 73).
- [18] John S. Bell. “Introduction to the hidden-variable question.” In: (1971) (cited on pages 3, 74).
- [19] John F. Clauser and Michael A. Horne. “Experimental consequences of objective local theories.” en. In: *Physical Review D* 10.2 (July 1974), pp. 526–535. DOI: [10/csfqv9](https://doi.org/10/csfqv9) (cited on pages 3, 91, 94).
- [20] Stuart J. Freedman and John F. Clauser. “Experimental Test of Local Hidden-Variable Theories.” In: *Physical Review Letters* 28.14 (Apr. 1972), pp. 938–941. DOI: [10.1103/PhysRevLett.28.938](https://doi.org/10.1103/PhysRevLett.28.938) (cited on pages 3, 13, 78).
- [21] Alain Aspect. “Proposed experiment to test the nonseparability of quantum mechanics.” en. In: *Physical Review D* 14.8 (Oct. 1976), pp. 1944–1951. DOI: [10.1103/PhysRevD.14.1944](https://doi.org/10.1103/PhysRevD.14.1944) (cited on page 4).
- [22] Alain Aspect, Philippe Grangier, and Gérard Roger. “Experimental Tests of Realistic Local Theories via Bell’s Theorem.” In: *Physical Review Letters* 47.7 (Aug. 1981), pp. 460–463. DOI: [10.1103/PhysRevLett.47.460](https://doi.org/10.1103/PhysRevLett.47.460) (cited on pages 4, 13, 78).
- [23] Alain Aspect, Philippe Grangier, and Gérard Roger. “Experimental Realization of Einstein-Podolsky-Rosen-Bohm *Gedankenexperiment* : A New Violation of Bell’s Inequalities.” en. In: *Physical Review Letters* 49.2 (July 1982), pp. 91–94. DOI: [10.1103/PhysRevLett.49.91](https://doi.org/10.1103/PhysRevLett.49.91) (cited on pages 4, 78).

- [24] Alain Aspect, Jean Dalibard, and Gérard Roger. “Experimental Test of Bell’s Inequalities Using Time-Varying Analyzers.” In: *Physical Review Letters* 49.25 (Dec. 1982), pp. 1804–1807. DOI: [10.1103/PhysRevLett.49.1804](https://doi.org/10.1103/PhysRevLett.49.1804) (cited on pages 4, 78).
- [25] Y. H. Shih and C. O. Alley. “New Type of Einstein-Podolsky-Rosen-Bohm Experiment Using Pairs of Light Quanta Produced by Optical Parametric Down Conversion.” en. In: *Physical Review Letters* 61.26 (Dec. 1988), pp. 2921–2924. DOI: [10.1103/PhysRevLett.61.2921](https://doi.org/10.1103/PhysRevLett.61.2921) (cited on page 4).
- [26] T. E. Kiess, Y. H. Shih, A. V. Sergienko, and C. O. Alley. “Einstein-Podolsky-Rosen-Bohm experiment using pairs of light quanta produced by type-II parametric down-conversion.” en. In: *Physical Review Letters* 71.24 (Dec. 1993), pp. 3893–3897. DOI: [10.1103/PhysRevLett.71.3893](https://doi.org/10.1103/PhysRevLett.71.3893) (cited on page 4).
- [27] J. G. Rarity and P. R. Tapster. “Experimental violation of Bell’s inequality based on phase and momentum.” en. In: *Physical Review Letters* 64.21 (May 1990), pp. 2495–2498. DOI: [10/dj6cp9](https://doi.org/10/dj6cp9) (cited on pages 4, 68, 80, 193).
- [28] B. Hensen, H. Bernien, A. E. Dréau, A. Reiserer, N. Kalb, M. S. Blok, J. Ruitenbergh, R. F. L. Vermeulen, R. N. Schouten, C. Abellán, W. Amaya, V. Pruneri, M. W. Mitchell, M. Markham, D. J. Twitchen, D. Elkouss, S. Wehner, T. H. Taminiau, and R. Hanson. “Loophole-free Bell inequality violation using electron spins separated by 1.3 kilometres.” en. In: *Nature* 526.7575 (Oct. 2015), pp. 682–686. DOI: [10.1038/nature15759](https://doi.org/10.1038/nature15759) (cited on pages 4, 72).
- [29] Marissa Giustina et al. “Significant-Loophole-Free Test of Bell’s Theorem with Entangled Photons.” en. In: *Physical Review Letters* 115.25 (Dec. 2015), p. 250401. DOI: [10.1103/PhysRevLett.115.250401](https://doi.org/10.1103/PhysRevLett.115.250401) (cited on pages 4, 72).
- [30] Lynden K. Shalm et al. “Strong Loophole-Free Test of Local Realism.” en. In: *Physical Review Letters* 115.25 (Dec. 2015), p. 250402. DOI: [10.1103/PhysRevLett.115.250402](https://doi.org/10.1103/PhysRevLett.115.250402) (cited on pages 4, 72).
- [31] Daniel M. Greenberger, Michael A. Horne, and Anton Zeilinger. “Going beyond Bell’s Theorem.” In: *Bell’s Theorem, Quantum Theory and Conceptions of the Universe*. Ed. by Menas Kafatos. Dordrecht: Springer Netherlands, 1989, pp. 69–72. DOI: [10.1007/978-94-017-0849-4_10](https://doi.org/10.1007/978-94-017-0849-4_10) (cited on page 4).
- [32] Gilles Brassard, Richard Cleve, and Alain Tapp. “Cost of Exactly Simulating Quantum Entanglement with Classical Communication.” In: *Physical Review Letters* 83.9 (Aug. 30, 1999), pp. 1874–1877. DOI: [10.1103/PhysRevLett.83.1874](https://doi.org/10.1103/PhysRevLett.83.1874) (cited on page 4).
- [33] Gilles Brassard, Anne Broadbent, and Alain Tapp. “Multi-Party Pseudo-Telepathy.” In: *Algorithms and Data Structures*. Ed. by Frank Dehne, Jörg-Rüdiger Sack, and Michiel Smid. Red. by Gerhard Goos, Juris Hartmanis, and Jan van Leeuwen. Vol. 2748. Lecture Notes in Computer Science. Berlin, Heidelberg: Springer Berlin Heidelberg, 2003, pp. 1–11. DOI: [10.1007/978-3-540-45078-8_1](https://doi.org/10.1007/978-3-540-45078-8_1). (Visited on 03/17/2022) (cited on page 4).
- [34] Klaus Mattle, Harald Weinfurter, Paul G. Kwiat, and Anton Zeilinger. “Dense Coding in Experimental Quantum Communication.” In: *Physical Review Letters* 76.25 (June 17, 1996), pp. 4656–4659. DOI: [10.1103/PhysRevLett.76.4656](https://doi.org/10.1103/PhysRevLett.76.4656) (cited on page 4).

- [35] Charles H. Bennett and Stephen J. Wiesner. “Communication via One- and Two-Particle Operators on Einstein-Podolsky-Rosen States.” In: *Physical Review Letters* 69.20 (Nov. 16, 1992), pp. 2881–2884. DOI: [10.1103/PhysRevLett.69.2881](https://doi.org/10.1103/PhysRevLett.69.2881) (cited on page 4).
- [36] Charles H. Bennett, Gilles Brassard, Claude Crépeau, Richard Jozsa, Asher Peres, and William K. Wootters. “Teleporting an Unknown Quantum State via Dual Classical and Einstein-Podolsky-Rosen Channels.” In: *Physical Review Letters* 70.13 (Mar. 29, 1993), pp. 1895–1899. DOI: [10.1103/PhysRevLett.70.1895](https://doi.org/10.1103/PhysRevLett.70.1895) (cited on page 4).
- [37] Dik Bouwmeester, Jian-Wei Pan, Klaus Mattle, Manfred Eibl, Harald Weinfurter, and Anton Zeilinger. “Experimental Quantum Teleportation.” In: 390 (1997), p. 5 (cited on page 4).
- [38] D. Boschi, S. Branca, F. De Martini, L. Hardy, and S. Popescu. “Experimental Realization of Teleporting an Unknown Pure Quantum State via Dual Classical and Einstein-Podolsky-Rosen Channels.” In: *Physical Review Letters* 80.6 (Feb. 9, 1998), pp. 1121–1125. DOI: [10.1103/PhysRevLett.80.1121](https://doi.org/10.1103/PhysRevLett.80.1121) (cited on page 4).
- [39] Committee on Technical Assessment of the Feasibility and Implications of Quantum Computing, Computer Science and Telecommunications Board, Intelligence Community Studies Board, Division on Engineering and Physical Sciences, and National Academies of Sciences, Engineering, and Medicine. “Chap. 2: Quantum Computing: A New Paradigm.” In: *Quantum Computing: Progress and Prospects*. Ed. by Emily Grumbling and Mark Horowitz. Washington, D.C.: National Academies Press, Mar. 27, 2019, pp. 24–56. DOI: [10.17226/25196](https://doi.org/10.17226/25196). (Visited on 03/17/2022) (cited on page 4).
- [40] John Preskill. “Quantum Computing in the NISQ Era and Beyond.” In: *Quantum* 2 (Aug. 6, 2018), p. 79. DOI: [10.22331/q-2018-08-06-79](https://doi.org/10.22331/q-2018-08-06-79) (cited on page 4).
- [41] Alain Aspect. “Preface to *Speakable and Unspeakeable*.” In: Cambridge University Press, 2004. Chap. Preface, pp. xvii–xxxix (cited on page 4).
- [42] Peter W. Shor. “Polynomial-Time Algorithms for Prime Factorization and Discrete Logarithms on a Quantum Computer.” In: *SIAM Review* 41.2 (1999), pp. 303–332. DOI: [10.1137/S0036144598347011](https://doi.org/10.1137/S0036144598347011) (cited on page 5).
- [43] Lov K. Grover. “A Fast Quantum Mechanical Algorithm for Database Search.” In: *Proceedings of the Twenty-Eighth Annual ACM Symposium on Theory of Computing - STOC '96*. The Twenty-Eighth Annual ACM Symposium. Philadelphia, Pennsylvania, United States: ACM Press, 1996, pp. 212–219. DOI: [10.1145/237814.237866](https://doi.org/10.1145/237814.237866). (Visited on 10/08/2022) (cited on page 5).
- [44] Charles H. Bennett and Gilles Brassard. “Quantum Cryptography: Public Key Distribution and Coin Tossing.” In: *Theoretical Computer Science* 560 (1984), pp. 7–11. DOI: [10.1016/j.tcs.2014.05.025](https://doi.org/10.1016/j.tcs.2014.05.025) (cited on page 5).
- [45] Artur K. Ekert. “Quantum Cryptography Based on Bell’s Theorem.” In: *Physical Review Letters* 67.6 (Aug. 5, 1991), pp. 661–663. DOI: [10.1103/PhysRevLett.67.661](https://doi.org/10.1103/PhysRevLett.67.661) (cited on page 5).

- [46] Stephen C. Wein, Juan C. Loredó, Maria Maffei, Paul Hilaire, Abdelmounaim Harouri, Niccolò Somaschi, Aristide Lemaître, Isabelle Sagnes, Loïc Lanco, Olivier Krebs, Alexia Auffèves, Christoph Simon, Pascale Senellart, and Carlos Antón-Solanas. “Photon-Number Entanglement Generated by Sequential Excitation of a Two-Level Atom.” In: *Nature Photonics* 16.5 (May 2022), pp. 374–379. DOI: [10.1038/s41566-022-00979-z](https://doi.org/10.1038/s41566-022-00979-z) (cited on page 5).
- [47] Antoine Browaeys and Thierry Lahaye. “Many-Body Physics with Individually Controlled Rydberg Atoms.” In: *Nature Physics* 16.2 (Feb. 2020), pp. 132–142. DOI: [10.1038/s41567-019-0733-z](https://doi.org/10.1038/s41567-019-0733-z) (cited on page 5).
- [48] Raphaël Lescanne, Marius Villiers, Théau Peronnin, Alain Sarlette, Matthieu Delbecq, Benjamin Huard, Takis Kontos, Mazyar Mirrahimi, and Zaki Leghtas. “Exponential Suppression of Bit-Flips in a Qubit Encoded in an Oscillator.” In: *Nature Physics* 16.5 (May 2020), pp. 509–513. DOI: [10.1038/s41567-020-0824-x](https://doi.org/10.1038/s41567-020-0824-x) (cited on page 5).
- [49] S. Debnath, N. M. Linke, C. Figgatt, K. A. Landsman, K. Wright, and C. Monroe. “Demonstration of a Small Programmable Quantum Computer with Atomic Qubits.” In: *Nature* 536.7614 (Aug. 4, 2016), pp. 63–66. DOI: [10.1038/nature18648](https://doi.org/10.1038/nature18648) (cited on page 5).
- [50] Christian D. Marciniak, Thomas Feldker, Ivan Pogorelov, Raphael Kaubruegger, Denis V. Vasilyev, Rick van Bijnen, Philipp Schindler, Peter Zoller, Rainer Blatt, and Thomas Monz. “Optimal Metrology with Programmable Quantum Sensors.” In: *Nature* 603.7902 (Mar. 24, 2022), pp. 604–609. DOI: [10.1038/s41586-022-04435-4](https://doi.org/10.1038/s41586-022-04435-4) (cited on page 5).
- [51] Akihiro Kuwahata, Takahiro Kitaizumi, Kota Saichi, Takumi Sato, Ryuji Igarashi, Takeshi Ohshima, Yuta Masuyama, Takayuki Iwasaki, Mutsuko Hatano, Fedor Jelezko, Moriaki Kusakabe, Takashi Yatsui, and Masaki Sekino. “Magnetometer with nitrogen-vacancy center in a bulk diamond for detecting magnetic nanoparticles in biomedical applications.” In: *Scientific Reports* 10 (Feb. 2020). DOI: [10.1038/s41598-020-59064-6](https://doi.org/10.1038/s41598-020-59064-6) (cited on page 5).
- [52] Christopher Gerry and Peter Knight. *Introductory Quantum Optics*. Cambridge University Press, 2005 (cited on pages 12, 18, 47, 176).
- [53] C. K. Hong, Z. Y. Ou, and L. Mandel. “Measurement of Subpicosecond Time Intervals between Two Photons by Interference.” In: *Physical Review Letters* 59.18 (Nov. 2, 1987), pp. 2044–2046. DOI: [10.1103/PhysRevLett.59.2044](https://doi.org/10.1103/PhysRevLett.59.2044) (cited on pages 13, 15).
- [54] P Grangier, G Roger, and A Aspect. “Experimental Evidence for a Photon Anticorrelation Effect on a Beam Splitter: A New Light on Single-Photon Interferences.” In: *Europhysics Letters (EPL)* 1.4 (Feb. 15, 1986), pp. 173–179. DOI: [10.1209/0295-5075/1/4/004](https://doi.org/10.1209/0295-5075/1/4/004) (cited on pages 13, 14).
- [55] Claude Cohen-Tannoudji, Bernard Diu, and Franck Laloë. *Mécanique quantique - Tome 3. Savoirs Actuels*. EDP Sciences ; CNRS Editions, 2017 (cited on pages 14, 69).
- [56] N. Somaschi, V. Giesz, L. De Santis, J. C. Loredó, M. P. Almeida, G. Hornecker, S. L. Portalupi, T. Grange, C. Antón, J. Demory, C. Gómez, I. Sagnes, N. D. Lanzillotti-Kimura, A. Lemaître, A. Auffèves, A. G. White, L. Lanco, and P. Senellart. “Near-Optimal Single-Photon Sources in the Solid State.” In: *Nature Photonics* 10.5 (May 2016), pp. 340–345. DOI: [10.1038/nphoton.2016.23](https://doi.org/10.1038/nphoton.2016.23) (cited on page 15).

- [57] Hui Wang, Yu-Ming He, T.-H Chung, Hai Hu, Ying Yu, Si Chen, Xing Ding, Ming-cheng Chen, Jian Qin, Xiaoxia Yang, Run-Ze Liu, Z.-C Duan, J.-P Li, Stefan Gerhardt, Karol Winkler, Jonathan Jurkat, Lin-Jun Wang, Niels Gregersen, Yong-Heng Huo, and Jian-Wei Pan. “Towards optimal single-photon sources from polarized microcavities.” In: *Nature Photonics* 13 (Nov. 2019). DOI: [10.1038/s41566-019-0494-3](https://doi.org/10.1038/s41566-019-0494-3) (cited on page 15).
- [58] Richard A. Campos, Bahaa E. A. Saleh, and Malvin C. Teich. “Quantum-Mechanical Lossless Beam Splitter: SU(2) Symmetry and Photon Statistics.” In: *Physical Review A* 40.3 (Aug. 1, 1989), pp. 1371–1384. DOI: [10/bjcf48](https://doi.org/10.1103/PhysRevA.40.1371) (cited on pages 16, 24, 27, 29, 30).
- [59] R. Lopes, A. Imanaliev, A. Aspect, M. Cheneau, D. Boiron, and C. I. Westbrook. “Atomic Hong–Ou–Mandel Experiment.” In: *Nature* 520.7545 (Apr. 2, 2015), pp. 66–68. DOI: [10.1038/nature14331](https://doi.org/10.1038/nature14331) (cited on pages 22, 148, 149, 195, 206, 209).
- [60] Maxime Perrier. “Interférences multiples avec atomes froids.” Theses. Université Paris Saclay (COMUE), Sept. 2018 (cited on pages 22, 83–87, 115, 128, 149).
- [61] K Yu Spasibko, F Töppel, T Sh Iskhakov, M Stobińska, M V Chekhova, and G Leuchs. “Interference of Macroscopic Beams on a Beam Splitter: Phase Uncertainty Converted into Photon-Number Uncertainty.” In: *New Journal of Physics* 16.1 (Jan. 17, 2014), p. 013025. DOI: [10.1088/1367-2630/16/1/013025](https://doi.org/10.1088/1367-2630/16/1/013025) (cited on page 24).
- [62] Maxime Perrier, Ziyad Amodjee, Pierre Dussarrat, Alexandre Dureau, Alain Aspect, Marc Cheneau, Denis Boiron, and Christoph Westbrook. “Thermal Counting Statistics in an Atomic Two-Mode Squeezed Vacuum State.” In: *SciPost Physics* 7.1 (July 3, 2019), p. 002. DOI: [10.21468/scipostphys.7.1.002](https://doi.org/10.21468/scipostphys.7.1.002) (cited on pages 25, 65, 177, 203, 204, 206).
- [63] Pascual Jordan. “Der Zusammenhang der symmetrischen und linearen Gruppen und das Mehrkörperproblem.” In: *Zeitschrift für Physik* 94.7–8 (1935), pp. 531–535 (cited on page 26).
- [64] Julian S. Schwinger. “On angular momentum.” In: *Unpublished Report* (Jan. 1952). DOI: [10.2172/4389568](https://doi.org/10.2172/4389568) (cited on page 26).
- [65] Bernard Yurke, Samuel L. McCall, and John R. Klauder. “SU(2) and SU(1,1) Interferometers.” In: *Physical Review A* 33.6 (June 1, 1986), pp. 4033–4054. DOI: [10.1103/PhysRevA.33.4033](https://doi.org/10.1103/PhysRevA.33.4033) (cited on page 27).
- [66] J. J. Bollinger, Wayne M. Itano, D. J. Wineland, and D. J. Heinzen. “Optimal Frequency Measurements with Maximally Correlated States.” In: *Physical Review A* 54.6 (Dec. 1, 1996), R4649–R4652. DOI: [10.1103/PhysRevA.54.R4649](https://doi.org/10.1103/PhysRevA.54.R4649) (cited on page 32).
- [67] Christopher C. Gerry. “Heisenberg-Limit Interferometry with Four-Wave Mixers Operating in a Nonlinear Regime.” In: *Physical Review A* 61.4 (Mar. 17, 2000), p. 043811. DOI: [10.1103/PhysRevA.61.043811](https://doi.org/10.1103/PhysRevA.61.043811) (cited on page 32).
- [68] *Bernoulli Trial*. In: *Wikipedia*. Oct. 21, 2021. (Visited on 05/18/2022) (cited on page 35).
- [69] Roy J. Glauber. “The Quantum Theory of Optical Coherence.” In: *Physical Review* 130.6 (June 15, 1963), pp. 2529–2539. DOI: [10.1103/PhysRev.130.2529](https://doi.org/10.1103/PhysRev.130.2529) (cited on pages 36, 196).
- [70] Roy J. Glauber. “Coherent and Incoherent States of the Radiation Field.” In: *Physical Review* 131.6 (Sept. 15, 1963), pp. 2766–2788. DOI: [10.1103/PhysRev.131.2766](https://doi.org/10.1103/PhysRev.131.2766) (cited on pages 36, 196).

- [71] Jianbin Liu and Yanhua Shih. “ N^{th} -Order Coherence of Thermal Light.” In: *Physical Review A* 79.2 (Feb. 18, 2009), p. 023819. DOI: [10.1103/PhysRevA.79.023819](https://doi.org/10.1103/PhysRevA.79.023819) (cited on pages 40, 197).
- [72] A. Heidmann, R. J. Horowicz, S. Reynaud, E. Giacobino, C. Fabre, and G. Camy. “Observation of Quantum Noise Reduction on Twin Laser Beams.” In: *Physical Review Letters* 59.22 (Nov. 30, 1987), pp. 2555–2557. DOI: [10.1103/PhysRevLett.59.2555](https://doi.org/10.1103/PhysRevLett.59.2555) (cited on page 47).
- [73] Jonas Kitzinger, Xin Meng, Matteo Fadel, Valentin Ivannikov, Kae Nemoto, William J. Munro, and Tim Byrnes. “Bell Correlations in a Split Two-Mode-Squeezed Bose-Einstein Condensate.” In: *Physical Review A* 104.4 (Oct. 27, 2021), p. 043323. DOI: [10.1103/physreva.104.043323](https://doi.org/10.1103/physreva.104.043323) (cited on pages 68, 90, 92, 93, 96).
- [74] B. P. Abbott et al. “Observation of Gravitational Waves from a Binary Black Hole Merger.” In: *Phys. Rev. Lett.* 116 (6 Feb. 2016), p. 061102. DOI: [10.1103/PhysRevLett.116.061102](https://doi.org/10.1103/PhysRevLett.116.061102) (cited on page 68).
- [75] J. C. Hafele and Richard E. Keating. “Around-the-World Atomic Clocks: Predicted Relativistic Time Gains.” In: *Science* 177.4044 (1972), pp. 166–168. DOI: [10.1126/science.177.4044.166](https://doi.org/10.1126/science.177.4044.166) (cited on page 68).
- [76] D. Bohm and Y. Aharonov. “Discussion of Experimental Proof for the Paradox of Einstein, Rosen, and Podolsky.” In: *Physical Review* 108.4 (Nov. 15, 1957), pp. 1070–1076. DOI: [10.1103/PhysRev.108.1070](https://doi.org/10.1103/PhysRev.108.1070) (cited on pages 69, 73).
- [77] C. W. Misner, K. S. Thorne, and J. A. Wheeler. *Gravitation*. 1973 (cited on page 69).
- [78] J. B. Hartle. *Gravity: An Introduction to Einstein’s General Relativity*. San Francisco: Addison-Wesley, 2003. 582 pp. (cited on page 69).
- [79] Alain Aspect. “Closing the Door on Einstein and Bohr’s Quantum Debate.” In: *Physics* 8 (Dec. 16, 2015), p. 123. DOI: [10.1103/Physics.8.123](https://doi.org/10.1103/Physics.8.123) (cited on page 72).
- [80] J. S. Bell and Alain Aspect. “Introduction to the hidden-variable question.” In: *Speakable and Unspeakeable in Quantum Mechanics: Collected Papers on Quantum Philosophy*. 2nd ed. Cambridge University Press, 2004, pp. 29–39. DOI: [10.1017/CB09780511815676.006](https://doi.org/10.1017/CB09780511815676.006) (cited on page 74).
- [81] N. David Mermin. “Extreme Quantum Entanglement in a Superposition of Macroscopically Distinct States.” In: *Physical Review Letters* 65.15 (Oct. 1990), pp. 1838–1840. DOI: [10.1103/PhysRevLett.65.1838](https://doi.org/10.1103/PhysRevLett.65.1838) (cited on page 79).
- [82] José L. Cereceda. “Mermin’s n -Particle Bell Inequality and Operators’ Noncommutativity.” In: *Physics Letters A* 286.6 (Aug. 2001), pp. 376–382. DOI: [10.1016/S0375-9601\(01\)00454-6](https://doi.org/10.1016/S0375-9601(01)00454-6) (cited on page 79).
- [83] Wiesław Laskowski and Marek Żukowski. “Detection of N -Particle Entanglement with Generalized Bell Inequalities.” In: *Physical Review A* 72.6 (Dec. 30, 2005), p. 062112. DOI: [10.1103/PhysRevA.72.062112](https://doi.org/10.1103/PhysRevA.72.062112) (cited on page 79).

- [84] Iman Esmaeil Zadeh, J. Chang, Johannes W. N. Los, Samuel Gyger, Ali W. Elshaari, Stephan Steinhauer, Sander N. Dorenbos, and Val Zwiller. “Superconducting Nanowire Single-Photon Detectors: A Perspective on Evolution, State-of-the-Art, Future Developments, and Applications.” In: *Applied Physics Letters* 118.19 (May 10, 2021), p. 190502. DOI: [10.1063/5.0045990](https://doi.org/10.1063/5.0045990) (cited on page 79).
- [85] Michael A. Horne, Abner Shimony, and Anton Zeilinger. “Two-Particle Interferometry.” In: *Physical Review Letters* 62.19 (May 8, 1989), pp. 2209–2212. DOI: [10.1103/PhysRevLett.62.2209](https://doi.org/10.1103/PhysRevLett.62.2209) (cited on page 79).
- [86] Matthew Dean Schwartz. “Spinor solutions and CPT.” In: *Quantum Field Theory and the Standard Model*. Cambridge ; New York: Cambridge University Press, 2014. Chap. 11, pp. 185–188 (cited on page 80).
- [87] Steven Weinberg. “Relativistic quantum mechanics.” In: *The Quantum Theory of Fields, Volume 1: Foundations*. Cambridge ; New York: Cambridge University Press, 1995. Chap. 2, pp. 62–74 (cited on page 80).
- [88] Alexander D. Cronin, Jörg Schmiedmayer, and David E. Pritchard. “Optics and Interferometry with Atoms and Molecules.” In: *Reviews of Modern Physics* 81.3 (July 28, 2009), pp. 1051–1129. DOI: [10.1103/RevModPhys.81.1051](https://doi.org/10.1103/RevModPhys.81.1051) (cited on page 82).
- [89] Almazbek Imanaliev. “Towards Testing Bell’s Inequality Using Atoms Correlated in Momentum.” Laboratoire Charles Fabry: Université Paris-Saclay, Mar. 30, 2016. 179 pp. (cited on page 84).
- [90] Pierre Dussarrat. “Expériences d’Optique Atomique Quantique, Interféromètres à 2 et 4 modes.” PhD thesis. Laboratoire Charles Fabry: Université Paris-Saclay, Nov. 20, 2017. 176 pp. (cited on pages 87, 174, 180, 181, 186, 203, 206).
- [91] T. C. Ralph, W. J. Munro, and R. E. S. Polkinghorne. “Proposal for the Measurement of Bell-Type Correlations from Continuous Variables.” In: *Physical Review Letters* 85.10 (Sept. 4, 2000), pp. 2035–2039. DOI: [10.1103/PhysRevLett.85.2035](https://doi.org/10.1103/PhysRevLett.85.2035) (cited on page 91).
- [92] S. S. Hodgman, R. G. Dall, L. J. Byron, K. G. H. Baldwin, S. J. Buckman, and A. G. Truscott. “Metastable Helium: A New Determination of the Longest Atomic Excited-State Lifetime.” In: *Physical Review Letters* 103.5 (July 30, 2009), p. 053002. DOI: [10.1103/PhysRevLett.103.053002](https://doi.org/10.1103/PhysRevLett.103.053002) (cited on pages 104, 105).
- [93] S. Moal, M. Portier, J. Kim, J. Dugué, U. D. Rapol, M. Leduc, and C. Cohen-Tannoudji. “Accurate Determination of the Scattering Length of Metastable Helium Atoms Using Dark Resonances between Atoms and Exotic Molecules.” In: *Physical Review Letters* 96.2 (Jan. 20, 2006), p. 023203. DOI: [10.1103/PhysRevLett.96.023203](https://doi.org/10.1103/PhysRevLett.96.023203) (cited on pages 104, 107).
- [94] P. Kapitza. “Viscosity of Liquid Helium below the λ -Point.” In: *Nature* 141.3558 (Jan. 8, 1938), pp. 74–74. DOI: [10.1038/141074a0](https://doi.org/10.1038/141074a0) (cited on page 104).
- [95] Donald C Morton, Qixue Wu, and G Wf Drake. “Energy Levels for the Stable Isotopes of Atomic Helium(⁴ He I and ³ He I).” In: *Canadian Journal of Physics* 84.2 (Feb. 1, 2006), pp. 83–105. DOI: [10.1139/p06-009](https://doi.org/10.1139/p06-009) (cited on pages 105, 106).

- [96] Dominik Z. Kandula, Christoph Gohle, Tjeerd J. Pinkert, Wim Ubachs, and Kjeld S. E. Eikema. “Extreme Ultraviolet Frequency Comb Metrology.” In: *Physical Review Letters* 105.6 (Aug. 2, 2010), p. 063001. DOI: [10.1103/PhysRevLett.105.063001](https://doi.org/10.1103/PhysRevLett.105.063001) (cited on page 105).
- [97] A. Robert, O. Sirjean, A. Browaeys, J. Poupard, S. Nowak, D. Boiron, C. I. Westbrook, and A. Aspect. “A Bose-Einstein Condensate of Metastable Atoms.” In: *Science* 292.5516 (Apr. 20, 2001), pp. 461–464. DOI: [10.1126/science.1060622](https://doi.org/10.1126/science.1060622) (cited on page 104).
- [98] F. Pereira Dos Santos, J. Léonard, Junmin Wang, C. J. Barrelet, F. Perales, E. Rasel, C. S. Unnikrishnan, M. Leduc, and C. Cohen-Tannoudji. “Bose-Einstein Condensation of Metastable Helium.” In: *Physical Review Letters* 86.16 (Apr. 16, 2001), pp. 3459–3462. DOI: [10.1103/PhysRevLett.86.3459](https://doi.org/10.1103/PhysRevLett.86.3459) (cited on page 104).
- [99] J. C. J. Koelemeij, R. J. W. Stas, W. Hogervorst, and W. Vassen. “Magneto-Optical Trap for Metastable Helium at 389 nm.” In: *Physical Review A* 67.5 (May 29, 2003), p. 053406. DOI: [10.1103/PhysRevA.67.053406](https://doi.org/10.1103/PhysRevA.67.053406) (cited on page 105).
- [100] Michael Keller, Mateusz Kotyrba, Florian Leupold, Mandip Singh, Maximilian Ebner, and Anton Zeilinger. “Bose-Einstein Condensate of Metastable Helium for Quantum Correlation Experiments.” In: *Physical Review A* 90.6 (Dec. 1, 2014), p. 063607. DOI: [10.1103/PhysRevA.90.063607](https://doi.org/10.1103/PhysRevA.90.063607) (cited on page 105).
- [101] Mitsutaka Kumakura and Norio Morita. “Visible Observation of Metastable Helium Atoms Confined in an Infrared/Visible Double Resonance Trap.” In: *Japanese Journal of Applied Physics* 31 (Part 2, No. 3A Mar. 1, 1992), pp. L276–L279. DOI: [10.1143/JJAP.31.L276](https://doi.org/10.1143/JJAP.31.L276) (cited on page 105).
- [102] R. P. M. J. W. Notermans and W. Vassen. “High-Precision Spectroscopy of the Forbidden $2^3S_1 \rightarrow 2^1P_1$ Transition in Quantum Degenerate Metastable Helium.” In: *Physical Review Letters* 112.25 (June 25, 2014), p. 253002. DOI: [10.1103/PhysRevLett.112.253002](https://doi.org/10.1103/PhysRevLett.112.253002) (cited on page 105).
- [103] R. van Rooij, J. S. Borbely, J. Simonet, M. D. Hoogerland, K. S. E. Eikema, R. A. Rozendaal, and W. Vassen. “Frequency Metrology in Quantum Degenerate Helium: Direct Measurement of the $2^3S_1 \rightarrow 2^1S_0$ Transition.” In: *Science* 333.6039 (July 8, 2011), pp. 196–198. DOI: [10.1126/science.1205163](https://doi.org/10.1126/science.1205163) (cited on page 105).
- [104] William C. Martin. “Energy Levels and Spectrum of Neutral Helium (4He I).” In: *Journal of Research of the National Bureau of Standards Section A: Physics and Chemistry* 64A.1 (Jan. 1960), p. 19. DOI: [10.6028/jres.064A.003](https://doi.org/10.6028/jres.064A.003) (cited on page 106).
- [105] Daniel G. Cocks, Ian B. Whittingham, and Gillian Peach. “Ultracold Homonuclear and Heteronuclear Collisions in Metastable Helium.” In: *Physical Review A* 99.6 (June 28, 2019), p. 062712. DOI: [10.1103/PhysRevA.99.062712](https://doi.org/10.1103/PhysRevA.99.062712) (cited on pages 107, 110).
- [106] Michał Przybytek and Bogumil Jeziorski. “Bounds for the Scattering Length of Spin-Polarized Helium from High-Accuracy Electronic Structure Calculations.” In: *The Journal of Chemical Physics* 123.13 (Oct. 2005), p. 134315. DOI: [10.1063/1.2042453](https://doi.org/10.1063/1.2042453) (cited on page 107).
- [107] Lev D. Landau and Evgeny M. Lifshits. *Quantum mechanics: non-relativistic theory*. 3d ed., rev. and enl. Their Course of theoretical physics v. 3. Oxford ; New York: Pergamon Press, 1977. 673 pp. (cited on page 107).

- [108] O. Sirjean, S. Seidelin, J. Viana Gomes, D. Boiron, C. I. Westbrook, A. Aspect, and G. V. Shlyapnikov. “Ionization Rates in a Bose-Einstein Condensate of Metastable Helium.” In: *Physical Review Letters* 89.22 (Nov. 12, 2002), p. 220406. DOI: [10.1103/PhysRevLett.89.220406](https://doi.org/10.1103/PhysRevLett.89.220406) (cited on page 108).
- [109] S Seidelin, O Sirjean, J Viana Gomes, D Boiron, C I Westbrook, and A Aspect. “Using Ion Production to Monitor the Birth and Death of a Metastable Helium Bose Einstein Condensate.” In: *Journal of Optics B: Quantum and Semiclassical Optics* 5.2 (Apr. 1, 2003), S112–S118. DOI: [10.1088/1464-4266/5/2/367](https://doi.org/10.1088/1464-4266/5/2/367) (cited on page 108).
- [110] S. Seidelin, J. Viana Gomes, R. Hoppeler, O. Sirjean, D. Boiron, A. Aspect, and C. I. Westbrook. “Getting the Elastic Scattering Length by Observing Inelastic Collisions in Ultracold Metastable Helium Atoms.” In: *Physical Review Letters* 93.9 (Aug. 27, 2004), p. 090409. DOI: [10.1103/PhysRevLett.93.090409](https://doi.org/10.1103/PhysRevLett.93.090409) (cited on pages 108, 111).
- [111] P. J. Leo, V. Venturi, I. B. Whittingham, and J. F. Babb. “Ultracold Collisions of Metastable Helium Atoms.” In: *Physical Review A* 64.4 (Sept. 13, 2001), p. 042710. DOI: [10.1103/PhysRevA.64.042710](https://doi.org/10.1103/PhysRevA.64.042710) (cited on pages 109, 110).
- [112] Wikipedia, The Free Encyclopedia. *Molecular term symbol*. Sept. 14, 2021. (Visited on 07/25/2022) (cited on page 109).
- [113] H. C. Maſtwijk, J. W. Thomsen, P. van der Straten, and A. Niehaus. “Optical Collisions of Cold, Metastable Helium Atoms.” In: *Physical Review Letters* 80.25 (June 22, 1998), pp. 5516–5519. DOI: [10.1103/PhysRevLett.80.5516](https://doi.org/10.1103/PhysRevLett.80.5516) (cited on page 110).
- [114] R. J. W. Stas, J. M. McNamara, W. Hogervorst, and W. Vassen. “Homonuclear Ionizing Collisions of Laser-Cooled Metastable Helium Atoms.” In: *Physical Review A* 73.3 (Mar. 14, 2006), p. 032713. DOI: [10.1103/PhysRevA.73.032713](https://doi.org/10.1103/PhysRevA.73.032713) (cited on page 110).
- [115] P. O. Fedichev, M. W. Reynolds, and G. V. Shlyapnikov. “Three-Body Recombination of Ultracold Atoms to a Weakly Bound s Level.” In: *Physical Review Letters* 77.14 (Sept. 30, 1996), pp. 2921–2924. DOI: [10.1103/PhysRevLett.77.2921](https://doi.org/10.1103/PhysRevLett.77.2921) (cited on page 111).
- [116] B. D. Esry, Chris H. Greene, and James P. Burke. “Recombination of Three Atoms in the Ultracold Limit.” In: *Physical Review Letters* 83.9 (Aug. 30, 1999), pp. 1751–1754. DOI: [10.1103/PhysRevLett.83.1751](https://doi.org/10.1103/PhysRevLett.83.1751) (cited on page 111).
- [117] Martijn Schellekens. “The Hanbury Brown and Twiss Effect for Cold Atoms.” PhD thesis. U.F.R. Scientifique d’Orsay: Université Paris 11, Aug. 30, 2007. 186 pp. (cited on page 113).
- [118] Hugo Cayla. “Measuring the momentum distribution of a lattice gas at the single-atom level.” Theses. Université Paris Saclay (COMUE), Nov. 2018 (cited on page 113).
- [119] J. Viana Gomes, A. Perrin, M. Schellekens, D. Boiron, C. I. Westbrook, and M. Belsley. “Theory for a Hanbury Brown Twiss Experiment with a Ballistically Expanding Cloud of Cold Atoms.” In: *Physical Review A* 74.5 (Nov. 7, 2006), p. 053607. DOI: [10.1103/PhysRevA.74.053607](https://doi.org/10.1103/PhysRevA.74.053607) (cited on page 125).
- [120] M. Schellekens, R. Hoppeler, A. Perrin, J. Viana Gomes, D. Boiron, A. Aspect, and C. I. Westbrook. “Hanbury Brown Twiss Effect for Ultracold Quantum Gases.” In: *Science* 310.5748 (Oct. 28, 2005), pp. 648–651. DOI: [10.1126/science.1118024](https://doi.org/10.1126/science.1118024) (cited on pages 125, 197).

- [121] W. Lu, M. D. Hoogerland, D. Milic, K. G. H. Baldwin, and S. J. Buckman. “A Bright Metastable Atom Source at 80 K.” In: *Review of Scientific Instruments* 72.6 (June 2001), pp. 2558–2561. DOI: [10.1063/1.1372169](https://doi.org/10.1063/1.1372169) (cited on page 127).
- [122] Robin Kaiser. “Manipulation par laser d’hélium méastable: effet Hanle mécanique, refroidissement sous le recul d’un photon.” Theses. Université Pierre et Marie Curie - Paris VI, Oct. 1990 (cited on page 127).
- [123] Guillaume Labeyrie. “Deux outils pour l’optique atomique : jet intense d’hélium méastable et miroir à onde évanescente exaltée.” PhD thesis. 1998, 215 P. (Cited on pages 127, 130).
- [124] Antoine Browaey. “Piegeage magnetique d’un gaz d’helium metastable : vers la condensation de Bose-Einstein.” PhD thesis. U.F.R Scientifique d’Orsay: Université de Paris-Sud, 2000. 163 pp. (cited on pages 128, 130, 134, 135).
- [125] Jean-Christophe Jaskula. “Création et étude de sources d’états non classiques pour l’optique atomique quantique.” Theses. Université Paris Sud - Paris XI, Dec. 2010 (cited on page 129).
- [126] E. L. Raab, M. Prentiss, Alex Cable, Steven Chu, and D. E. Pritchard. “Trapping of Neutral Sodium Atoms with Radiation Pressure.” In: *Physical Review Letters* 59.23 (Dec. 7, 1987), pp. 2631–2634. DOI: [10.1103/PhysRevLett.59.2631](https://doi.org/10.1103/PhysRevLett.59.2631) (cited on page 131).
- [127] Jean Dalibard. “Une brève histoire des atomes froids - Chapitre 2.” In: *Atomes et rayonnement - Cours 2014-15* (May 27, 2015) (cited on page 131).
- [128] Harold J. Metcalf and Peter Van der Straten. *Laser Cooling and Trapping*. Graduate Texts in Contemporary Physics. New York: Springer, 1999. 323 pp. (cited on page 131).
- [129] Mitsutaka Kumakura and Norio Morita. “Laser Trapping of Metastable H₃e Atoms: Isotopic Difference in Cold Penning Collisions.” In: *Physical Review Letters* 82.14 (Apr. 5, 1999), pp. 2848–2851. DOI: [10.1103/PhysRevLett.82.2848](https://doi.org/10.1103/PhysRevLett.82.2848) (cited on page 131).
- [130] Paul J. J. Tol, Norbert Herschbach, Eric A. Hessels, Wim Hogervorst, and Wim Vassen. “Large Numbers of Cold Metastable Helium Atoms in a Magneto-Optical Trap.” In: *Physical Review A* 60.2 (Aug. 1, 1999), R761–R764. DOI: [10.1103/PhysRevA.60.R761](https://doi.org/10.1103/PhysRevA.60.R761) (cited on page 131).
- [131] A. Browaey, J. Poupard, A. Robert, S. Nowak, W. Rooijackers, E. Arimondo, L. Marcassa, D. Boiron, C.I. Westbrook, and A. Aspect. “Two Body Loss Rate in a Magneto-Optical Trap of Metastable He.” In: *The European Physical Journal D - Atomic, Molecular and Optical Physics* 8.2 (Jan. 1, 2000), pp. 199–203. DOI: [10.1007/s100530050027](https://doi.org/10.1007/s100530050027) (cited on page 131).
- [132] F. Pereira Dos Santos, F. Perales, J. Léonard, A. Sinatra, Junmin Wang, F. Saverio Pavone, E. Rasel, C.S. Unnikrishnan, and M. Leduc. “Penning Collisions of Laser-Cooled Metastable Helium Atoms.” In: *The European Physical Journal D* 14.1 (Apr. 2001), pp. 15–22. DOI: [10.1007/s100530170228](https://doi.org/10.1007/s100530170228) (cited on page 131).
- [133] Wolfgang Petrich, Michael H. Anderson, Jason R. Ensher, and Eric A. Cornell. “Behavior of Atoms in a Compressed Magneto-Optical Trap.” In: *Journal of the Optical Society of America B* 11.8 (Aug. 1, 1994), p. 1332. DOI: [10.1364/JOSAB.11.001332](https://doi.org/10.1364/JOSAB.11.001332) (cited on page 132).
- [134] A. H. Abbas, X. Meng, R. S. Patil, J. A. Ross, A. G. Truscott, and S. S. Hodgman. “Rapid Generation of Metastable Helium Bose-Einstein Condensates.” In: *Physical Review A* 103.5 (May 21, 2021), p. 053317. DOI: [10.1103/PhysRevA.103.053317](https://doi.org/10.1103/PhysRevA.103.053317) (cited on page 132).

- [135] R. Chang, A. L. Hoendervanger, Q. Bouton, Y. Fang, T. Klafka, K. Audo, A. Aspect, C. I. Westbrook, and D. Clément. “Three-Dimensional Laser Cooling at the Doppler Limit.” In: *Physical Review A* 90.6 (Dec. 1, 2014), p. 063407. DOI: [10.1103/PhysRevA.90.063407](https://doi.org/10.1103/PhysRevA.90.063407) (cited on pages 132, 133).
- [136] M. Walhout, J. Dalibard, S. L. Rolston, and W. D. Phillips. “ $\sigma_+ - \sigma_-$ Optical Molasses in a Longitudinal Magnetic Field.” In: *Journal of the Optical Society of America B* 9.11 (Nov. 1, 1992), p. 1997. DOI: [10.1364/JOSAB.9.001997](https://doi.org/10.1364/JOSAB.9.001997) (cited on page 133).
- [137] Eite Tiesinga, Peter Mohr, David Newell, and Barry Taylor. 2018 CODATA RECOMMENDED VALUES OF THE FUNDAMENTAL CONSTANTS OF PHYSICS AND CHEMISTRY. en. 2019-06-03 04:06:00 2019. URL: https://tsapps.nist.gov/publication/get_pdf.cfm?pub_id=928211 (cited on page 133).
- [138] M.-O. Mewes, M. R. Andrews, N. J. van Druten, D. M. Kurn, D. S. Durfee, and W. Ketterle. “Bose-Einstein Condensation in a Tightly Confining DC Magnetic Trap.” In: *Physical Review Letters* 77.3 (July 15, 1996), pp. 416–419. DOI: [10.1103/PhysRevLett.77.416](https://doi.org/10.1103/PhysRevLett.77.416) (cited on page 134).
- [139] T. H. Bergeman, Patrick McNicholl, Jan Kycia, Harold Metcalf, and N. L. Balazs. “Quantized Motion of Atoms in a Quadrupole Magnetostatic Trap.” In: *Journal of the Optical Society of America B* 6.11 (Nov. 6, 1989), pp. 2249–2256. DOI: [10.1364/JOSAB.6.002249](https://doi.org/10.1364/JOSAB.6.002249) (cited on page 134).
- [140] Piet O. Schmidt, Sven Hensler, Jörg Werner, Thomas Binhammer, Axel Görlitz, and Tilman Pfau. “Doppler Cooling of an Optically Dense Cloud of Magnetically Trapped Atoms.” In: *Journal of the Optical Society of America B* 20.5 (May 1, 2003), p. 960. DOI: [10.1364/JOSAB.20.000960](https://doi.org/10.1364/JOSAB.20.000960) (cited on page 137).
- [141] O. J. Luiten, M. W. Reynolds, and J. T. M. Walraven. “Kinetic Theory of the Evaporative Cooling of a Trapped Gas.” In: *Physical Review A* 53.1 (Jan. 1, 1996), pp. 381–389. DOI: [10.1103/PhysRevA.53.381](https://doi.org/10.1103/PhysRevA.53.381) (cited on page 138).
- [142] A. Robert, O. Sirjean, A. Browaeys, J. Poupard, S. Nowak, D. Boiron, C. I. Westbrook, and A. Aspect. “A Bose-Einstein Condensate of Metastable Atoms.” In: *Science* 292.5516 (Apr. 20, 2001), pp. 461–464. DOI: [10.1126/science.1060622](https://doi.org/10.1126/science.1060622) (cited on page 138).
- [143] Chiara Menotti and Sandro Stringari. “Collective Oscillations of a One-Dimensional Trapped Bose-Einstein Gas.” In: *Physical Review A* 66.4 (Oct. 21, 2002), p. 043610. DOI: [10.1103/PhysRevA.66.043610](https://doi.org/10.1103/PhysRevA.66.043610) (cited on page 141).
- [144] F Gerbier. “Quasi-1D Bose-Einstein Condensates in the Dimensional Crossover Regime.” In: *Europhysics Letters (EPL)* 66.6 (June 2004), pp. 771–777. DOI: [10.1209/epl/i2004-10035-7](https://doi.org/10.1209/epl/i2004-10035-7) (cited on page 141).
- [145] D. S. Petrov, G. V. Shlyapnikov, and J. T. M. Walraven. “Phase-Fluctuating 3D Bose-Einstein Condensates in Elongated Traps.” In: *Physical Review Letters* 87.5 (July 16, 2001), p. 050404. DOI: [10.1103/PhysRevLett.87.050404](https://doi.org/10.1103/PhysRevLett.87.050404) (cited on page 141).

- [146] D. Gallucci, S. P. Cockburn, and N. P. Proukakis. “Phase Coherence in Quasicondensate Experiments: An *Ab Initio* Analysis via the Stochastic Gross-Pitaevskii Equation.” In: *Physical Review A* 86.1 (July 19, 2012), p. 013627. DOI: [10.1103/PhysRevA.86.013627](https://doi.org/10.1103/PhysRevA.86.013627) (cited on page 141).
- [147] Aviv Keshet and Wolfgang Ketterle. “A distributed, graphical user interface based, computer control system for atomic physics experiments.” In: *Review of Scientific Instruments* 84.1 (2013), p. 015105. DOI: [10.1063/1.4773536](https://doi.org/10.1063/1.4773536) (cited on page 168).
- [148] Bernd Lücke, Jan Peise, Giuseppe Vitagliano, Jan Arlt, Luis Santos, Géza Tóth, and Carsten Klempt. “Detecting Multiparticle Entanglement of Dicke States.” In: *Physical Review Letters* 112.15 (Apr. 17, 2014), p. 155304. DOI: [10.1103/PhysRevLett.112.155304](https://doi.org/10.1103/PhysRevLett.112.155304) (cited on page 174).
- [149] Helmut Strobel, Wolfgang Muessel, Daniel Linnemann, Tilman Zibold, David B. Hume, Luca Pezzè, Augusto Smerzi, and Markus K. Oberthaler. “Fisher Information and Entanglement of Non-Gaussian Spin States.” In: *Science* 345.6195 (July 25, 2014), pp. 424–427. DOI: [10.1126/science.1250147](https://doi.org/10.1126/science.1250147) (cited on page 174).
- [150] Karsten Lange, Jan Peise, Bernd Lücke, Ilka Kruse, Giuseppe Vitagliano, Iagoba Apellaniz, Matthias Kleinmann, Géza Tóth, and Carsten Klempt. “Entanglement between Two Spatially Separated Atomic Modes.” In: *Science* 360.6387 (Apr. 27, 2018), pp. 416–418. DOI: [10.1126/science.aao2035](https://doi.org/10.1126/science.aao2035) (cited on page 174).
- [151] D. K. Shin, B. M. Henson, S. S. Hodgman, T. Wasak, J. Chwedeńczuk, and A. G. Truscott. “Bell Correlations between Spatially Separated Pairs of Atoms.” In: *Nature Communications* 10.1 (Dec. 2019), p. 4447. DOI: [10.1038/s41467-019-12192-8](https://doi.org/10.1038/s41467-019-12192-8) (cited on page 174).
- [152] M. Greiner, C. A. Regal, J. T. Stewart, and D. S. Jin. “Probing Pair-Correlated Fermionic Atoms through Correlations in Atom Shot Noise.” In: *Physical Review Letters* 94.11 (Mar. 21, 2005), p. 110401. DOI: [10.1103/PhysRevLett.94.110401](https://doi.org/10.1103/PhysRevLett.94.110401) (cited on pages 174, 175).
- [153] Logan W. Clark, Anita Gaj, Lei Feng, and Cheng Chin. “Collective Emission of Matter-Wave Jets from Driven Bose–Einstein Condensates.” In: *Nature* 551.7680 (Nov. 2017), pp. 356–359. DOI: [10.1038/nature24272](https://doi.org/10.1038/nature24272) (cited on page 174).
- [154] Robert Bücke, Julian Grond, Stephanie Manz, Tarik Berrada, Thomas Betz, Christian Koller, Ulrich Hoheneßer, Thorsten Schumm, Aurélien Perrin, and Jörg Schmiedmayer. “Twin-Atom Beams.” In: *Nature Physics* 7.8 (Aug. 2011), pp. 608–611. DOI: [10.1038/nphys1992](https://doi.org/10.1038/nphys1992) (cited on page 174).
- [155] F. Borselli, M. Maiwöger, T. Zhang, P. Haslinger, V. Mukherjee, A. Negretti, S. Montangero, T. Calarco, I. Mazets, M. Bonneau, and J. Schmiedmayer. “Two-Particle Interference with Double Twin-Atom Beams.” In: *Phys. Rev. Lett.* 126 (8 Feb. 2021), p. 083603. DOI: [10.1103/PhysRevLett.126.083603](https://doi.org/10.1103/PhysRevLett.126.083603) (cited on page 174).
- [156] K. V. Kheruntsyan, J.-C. Jaskula, P. Deuar, M. Bonneau, G. B. Partridge, J. Ruaudel, R. Lopes, D. Boiron, and C. I. Westbrook. “Violation of the Cauchy-Schwarz Inequality with Matter Waves.” In: *Physical Review Letters* 108.26 (June 25, 2012), p. 260401. DOI: [10.1103/PhysRevLett.108.260401](https://doi.org/10.1103/PhysRevLett.108.260401) (cited on pages 174, 176).

- [157] S. S. Hodgman, R. I. Khakimov, R. J. Lewis-Swan, A. G. Truscott, and K. V. Kheruntsyan. “Solving the Quantum Many-Body Problem via Correlations Measured with a Momentum Microscope.” In: *Physical Review Letters* 118.24 (June 14, 2017), p. 240402. DOI: [10.1103/PhysRevLett.118.240402](https://doi.org/10.1103/PhysRevLett.118.240402) (cited on page 174).
- [158] R. Ghosh and L. Mandel. “Observation of Nonclassical Effects in the Interference of Two Photons.” In: *Physical Review Letters* 59.17 (Oct. 26, 1987), pp. 1903–1905. DOI: [10.1103/PhysRevLett.59.1903](https://doi.org/10.1103/PhysRevLett.59.1903) (cited on page 174).
- [159] Bahaa E. A. Saleh, Ayman F. Abouraddy, Alexander V. Sergienko, and Malvin C. Teich. “Duality between Partial Coherence and Partial Entanglement.” In: *Physical Review A* 62.4 (Sept. 19, 2000), p. 043816. DOI: [10.1103/PhysRevA.62.043816](https://doi.org/10.1103/PhysRevA.62.043816) (cited on page 174).
- [160] Jay E. Sharping, Marco Fiorentino, Ayodeji Coker, Prem Kumar, and Robert S. Windeler. “Four-Wave Mixing in Microstructure Fiber.” In: *Optics Letters* 26.14 (July 15, 2001), p. 1048. DOI: [10.1364/OL.26.001048](https://doi.org/10.1364/OL.26.001048) (cited on page 174).
- [161] L J Wang, C K Hong, and S R Friberg. “Generation of Correlated Photons via Four-Wave Mixing in Optical Fibres.” In: *Journal of Optics B: Quantum and Semiclassical Optics* 3.5 (Oct. 1, 2001), pp. 346–352. DOI: [10.1088/1464-4266/3/5/311](https://doi.org/10.1088/1464-4266/3/5/311) (cited on page 174).
- [162] Hiroki Takesue and Kyo Inoue. “Generation of Polarization-Entangled Photon Pairs and Violation of Bell’s Inequality Using Spontaneous Four-Wave Mixing in a Fiber Loop.” In: *Physical Review A* 70.3 (Sept. 30, 2004), p. 031802. DOI: [10.1103/PhysRevA.70.031802](https://doi.org/10.1103/PhysRevA.70.031802) (cited on page 174).
- [163] Karen Marie Hilligsøe and Klaus Mølmer. “Phase-Matched Four Wave Mixing and Quantum Beam Splitting of Matter Waves in a Periodic Potential.” In: *Physical Review A*. American Physical Society 71.4 (Apr. 12, 2005), p. 041602. DOI: [10.1103/PhysRevA.71.041602](https://doi.org/10.1103/PhysRevA.71.041602) (cited on pages 174, 177, 179).
- [164] Gretchen K. Campbell, Jongchul Mun, Micah Boyd, Erik W. Streed, Wolfgang Ketterle, and David E. Pritchard. “Parametric Amplification of Scattered Atom Pairs.” In: *Physical Review Letters* 96.2 (Jan. 19, 2006), p. 020406. DOI: [10.1103/PhysRevLett.96.020406](https://doi.org/10.1103/PhysRevLett.96.020406) (cited on pages 174, 179, 195).
- [165] Marie Bonneau. “Mélange à quatre ondes atomique dans un réseau optique.” PhD thesis. Laboratoire Charles Fabry: Université Paris 11, Dec. 16, 2011. 180 pp. (cited on page 174).
- [166] Josselin Ruau del. “Création et caractérisation d’une source ajustable de paires d’atomes corrélés.” PhD thesis. Laboratoire Charles Fabry: Institut d’Optique Graduate School, Dec. 11, 2013. 184 pp. (cited on pages 174, 176, 181).
- [167] Leonard Mandel and Emil Wolf. *Optical Coherence and Quantum Optics*. 1st ed. Cambridge University Press, Sept. 29, 1995. (Visited on 09/02/2022) (cited on pages 175, 176).
- [168] S.P. Walborn, C.H. Monken, S. Pádua, and P.H. Souto Ribeiro. “Spatial Correlations in Parametric Down-Conversion.” In: *Physics Reports* 495.4-5 (Oct. 2010), pp. 87–139. DOI: [10.1016/j.physrep.2010.06.003](https://doi.org/10.1016/j.physrep.2010.06.003) (cited on page 175).
- [169] W. H. Louisell, A. Yariv, and A. E. Siegman. “Quantum Fluctuations and Noise in Parametric Processes. I.” In: *Physical Review* 124.6 (Dec. 15, 1961), pp. 1646–1654. DOI: [10.1103/PhysRev.124.1646](https://doi.org/10.1103/PhysRev.124.1646) (cited on page 175).

- [170] L. Deng, E. W. Hagley, J. Wen, M. Trippenbach, Y. Band, P. S. Julienne, J. E. Simsarian, K. Helmerson, S. L. Rolston, and W. D. Phillips. “Four-Wave Mixing with Matter Waves.” In: *Nature* 398.6724 (Mar. 1999), pp. 218–220. DOI: [10.1038/18395](https://doi.org/10.1038/18395) (cited on page 176).
- [171] J. M. Vogels, K. Xu, and W. Ketterle. “Generation of Macroscopic Pair-Correlated Atomic Beams by Four-Wave Mixing in Bose-Einstein Condensates.” In: *Physical Review Letters* 89.2 (June 24, 2002), p. 020401. DOI: [10.1103/PhysRevLett.89.020401](https://doi.org/10.1103/PhysRevLett.89.020401) (cited on page 176).
- [172] J. M. Vogels, J. K. Chin, and W. Ketterle. “Coherent Collisions between Bose-Einstein Condensates.” In: *Physical Review Letters* 90.3 (Jan. 23, 2003), p. 030403. DOI: [10.1103/PhysRevLett.90.030403](https://doi.org/10.1103/PhysRevLett.90.030403) (cited on page 176).
- [173] Lev Petrovič Pitaevskii and Sandro Stringari. *Bose-Einstein Condensation and Superfluidity*. Updated edition. International Series of Monographs on Physics 164. Oxford: Oxford university press, 2016 (cited on page 177).
- [174] Charles Kittel. *Introduction to Solid State Physics*. In collab. with Paul McEuen. Global edition, [9th edition]. Hoboken, NJ: Wiley, 2018. 692 pp. (cited on page 180).
- [175] Neil W. Ashcroft and N. David Mermin. *Solid State Physics*. New York: Holt, Rinehart and Winston, 1976. 826 pp. (cited on page 180).
- [176] J Hecker Denschlag, J E Simsarian, H Häffner, C McKenzie, A Browaeys, D Cho, K Helmerson, S L Rolston, and W D Phillips. “A Bose-Einstein Condensate in an Optical Lattice.” In: *Journal of Physics B: Atomic, Molecular and Optical Physics* 35.14 (July 3, 2002), pp. 3095–3110. DOI: [10.1088/0953-4075/35/14/307](https://doi.org/10.1088/0953-4075/35/14/307) (cited on page 186).
- [177] A. Messiah. *Quantum Mechanics*. Quantum Mechanics vol. 1. North-Holland Publishing Company, 1961 (cited on page 186).
- [178] Klaus Mølmer, A. Perrin, V. Krachmalnicoff, V. Leung, D. Boiron, A. Aspect, and C. I. Westbrook. “Hanbury Brown and Twiss Correlations in Atoms Scattered from Colliding Condensates.” In: *Physical Review A* 77.3 (Mar. 4, 2008), p. 033601. DOI: [10.1103/PhysRevA.77.033601](https://doi.org/10.1103/PhysRevA.77.033601) (cited on page 197).

Special Terms

A

AOM acousto-optic modulator. 131, 142, 149, 151, 160, 161, 167, 168, 188

B

BCHSH Bell, Clauser, Horne, Shimony and Holt. 73, 78, 80, 86, 97

BEC Bose-Einstein condensate. xiii, xvi, xvii, 102–104, 108, 110, 124, 125, 138–141, 143–146, 151–155, 157, 158, 168, 173, 174, 176–186, 188–191, 197

BS beam splitter. 15, 48, 87

C

CCD charge-coupled device. 149

CFD constant fraction discriminator. xvi, 115–117

CH Clauser and Holt. xii, 67, 94, 95

CHSH Clauser, Horne, Shimony and Holt. xii, xv, 67, 72–74, 76, 79, 89, 91–97

CLI command line interface. 167

cMOT compressed magneto-optical trap. 132, 133, 162, 168

CPU central process unit. 166

D

DBR distributed Bragg reflector. 104

DCE dynamical Casimir effect. 158

DFB distributed feedback laser. 104, 159, 160, 162

DTPI Détection: Temps, Position, Image. 116, 117

E

EOM electro-optic modulator. 158

EPR Einstein, Polsky and Rosen. ix, xii, 2, 7, 67–69, 71, 72, 74

EPRB Einstein-Polsky-Rosen-Bohm. xv, 3, 69, 70, 73, 76

F

FWM four-wave mixing. 174, 176, 178, 181

G

GPIO general purpose interface bus. 165

GUI graphical user interface. 167–169, 171

H

HAL Helium Atom Locator. xvii, 169–172

HBT Hanbury Brown and Twiss. 125, 197

hODT horizontal optical dipole trap. 139, 140, 143, 154, 155, 158, 189

HOM Hong-Ou-Mandel. xi, xv, 11–15, 17–25, 31, 32, 37, 48, 66, 148, 187, 195, 209, 210

I

IGBT insulated gate bipolar transistor. xiv, xviii, 187, 206, 213, 219

IOGS Institut d'Optique Graduate School. 166, 224

L

LUMAT Lumière-Matière. 116, 117

M

MCP microchannel plate. xiii, xvi–xviii, 79, 83, 102, 106, 112–117, 119–123, 125–127, 129, 140, 143–145, 147, 149–158, 167, 169, 170, 189, 191, 192, 194, 195, 215

MOT magneto-optical trap. xviii, 101, 102, 104, 105, 110, 125, 126, 128–133, 136, 146, 149, 151, 152, 156, 159, 165, 206, 219

MPQ Max-Planck-Institute for Quantum Optics. 166

MT magnetic trap. xvi–xviii, 128, 135–140, 144, 154, 164, 165, 168, 170, 187, 219

N

nHOM n -particle Hong-Ou-Mandel. 24, 54

NIM Nuclear Instrument Module. 116, 118–120

NIST National Institute of Standards and Technology. 72, 176

O

OAR open area ratio. 113

ODT optical dipole trap. xvi–xviii, 102, 128, 138–140, 144, 149–152, 154, 157, 158, 164, 168, 185, 187, 188, 191

OI optical isolator. 149, 160

OM optical molasses. 132–134

P

PEEK polyether ether ketone. 156

PM photomultiplier. 79

PSD phase-space density. 132, 134, 137, 139

PSU power supply unit. xviii, 117, 135, 165, 166, 187, 206, 219, 220

Q

QED quantum electrodynamics. 104, 105

R

RF radio frequency. xvi, 104, 136–138, 149, 151, 160–163, 165, 166, 168, 188, 219

S

SCPI Standard Commands for Programmable Instruments. 167

SNSPD superconducting nanowire single-photon detector. 79

SPDC spontaneous parametric down-conversion. 174–176

SWIR short-wave infrared. 149

T

TDC time-to-digital converter. xvi, 115, 116, 119–122

TF Thomas-Fermi. 141

TMS two-mode squeezed vacuum state. xv, 11, 12, 25, 38, 40, 43, 47–50, 52, 53, 55, 60, 62, 64–66, 89, 145, 182, 195, 197, 202–204, 206

TOF time of flight. 133

TTL Transistor–transistor logic. 120, 164–168

V

vODT vertical optical dipole trap. 139, 143, 151, 152, 189

Titre : Optique atomique quantique avec hélium métastable

Mots clés : non-localité, atomes ultra-froids, mécanique quantique, inégalités de Bell, interférométrie atomique, helium métastable.

Résumé : Les propriétés de corrélation et d'intrication de certains états quantiques à multiples particules ont été mises en évidence à partir des années 80, dans le cadre de la photonique. Depuis lors, la production et caractérisation d'états non-classiques dans divers contextes est devenue une thématique de recherche très féconde, ainsi qu'un important enjeu pour le développement des technologies quantiques. Cette thèse présente une plateforme expérimentale permettant de préparer des atomes d'hélium dans des états d'impulsion fortement corrélés. Le dispositif de détection qui a été développé dans notre groupe (à trois dimensions et résolu à l'atome unique) permet de sonder efficacement ces propriétés de corrélation, ce qui est

en général difficilement réalisable pour la plupart des montages expérimentaux similaires.

Plus particulièrement, ce manuscrit contient une première partie théorique qui traite d'une part de la généralisation de l'effet Hong-Ou-Mandel dans un contexte à multiples particules, et d'autre part de la mise œuvre d'une expérience de test des inégalités de Bell pour des atomes intriqués en vitesse. Ces deux expériences pourraient être réalisées prochainement dans notre équipe. Une seconde partie expérimentale rend compte des récents progrès effectués sur la plateforme, ainsi que les derniers résultats expérimentaux concernant les propriétés de corrélation de la source atomique que nous avons mise en place.

Title : Quantum atom optics with metastable helium

Keywords : non locality, ultra cold atoms, quantum mechanics, Bell inequalities, atom interferometry, metastable helium

Abstract : Correlation and entanglement properties of multi-particle quantum states have been demonstrated since the 1980s in the context of photonics. Since then, the production and characterisation of non-classical states in various contexts has become a very fruitful research topic, as well as a burning issue for the development of quantum technologies. This thesis presents an experimental platform able to prepare helium atoms in strongly correlated momentum states. The detection technique that has been developed in our group (three-dimensional and resolved to the single atom) allows to efficiently probe these correlation properties, which is in general difficult to achieve for most

similar experimental setups.

In particular, this manuscript contains a first part of theoretical nature, which deals on the one hand with the generalisation of the Hong-Ou-Mandel effect (in a context where more than two particles are involved); and on the other hand with the implementation of an experiment testing the Bell inequalities for atoms entangled with respect to their velocities. Both experiments could be carried out by our team in the near future. A second experimental part reports on the recent progress made on the platform, as well as the latest experimental results concerning the correlation properties of the atomic source that we have set up.